University of Bradford eThesis

PROCESS FINGERPRINTING OF MICRONEEDLE MANUFACTURING USING CONVENTIONAL AND ULTRASONIC MICRO-INJECTION MOULDING

M. GULCUR

Ph. D.

UNIVERSITY OF BRADFORD

2019

Process Fingerprinting of Microneedle Manufacturing Using Conventional and Ultrasonic Micro-injection Moulding

Mert Gulcur

BSc MSc

Submitted for the Degree for

Doctor of Philosophy

Faculty of Engineering and Informatics

University of Bradford

2019

Abstract

Mert Gulcur

Process Fingerprinting of Microneedle Manufacturing Using Conventional and Ultrasonic Micro-injection Moulding

Keywords: Micro-injection moulding, microneedles, micromanufacturing, process monitoring, process fingerprinting, in-line monitoring, microarrays, data acquisition, replication, laser machining

This research work investigates the development and application of process fingerprinting for conventional micro-injection moulding and ultrasonic micro-injection moulding manufacturing of microneedle arrays for drug delivery.

The process fingerprinting method covers in-depth analysis, interrogation and selection of certain process data features and correlation of these features with product fingerprints which are defined by the geometrical outcomes of the microneedle arrays in micro scale. The method was developed using the data collected using extensive sensor technologies attached to the conventional and ultrasonic micromoulding machines. Moreover, a machine vision based microneedle product evaluation apparatus is presented. Micromachining capabilities of different processes is also assessed and presented where state-of-the-art laser machining was used for microneedle tool manufacturing in the work.

By using process fingerprinting procedures, conventional and ultrasonic micromoulding processes has been characterised thoroughly and aspects of the process that is affecting the part quality was also addressed for microneedle manufacturing. It was found that polymer structure is of paramount importance in obtaining sufficient microneedle replication. An amorphous polymer have been found to be more suitable for conventional moulding whereas semi-crystalline materials performed better in ultrasonic micromoulding. In-line captured micromoulding process data for conventional and ultrasonic moulding provided detailed insight of machine dynamics and understanding. Linear correlations between process fingerprints and micro-replication efficiency of the microneedles have been presented for both micromoulding technologies. The in-line process monitoring and product quality evaluation procedures presented in this work for micro-injection moulding techniques will pave ways for zero-defect micromanufacturing of miniature products towards Industry 4.0.

Table of Contents

List of Figures

List of Tables

List of Publications

Journal articles:

Gülçür, M., Brown, E., Gough, T., Romano, J. M., Penchev, P., Dimov, S., Whiteside, B. (2020) Ultrasonic micromoulding: Process characterisation using extensive in-line monitoring for micro-scaled products. Journal of Manufacturing Processes, Volume 58, pages 289 – 301.

Romano, J. M., Garcia-Giron, A., Penchev, P., Gulcur, M., Whiteside, B.R. Dimov, S., (2020) Lotus-leaf inspired surfaces: hydrophobicity evolution of replicas due to mechanical cleaning and tool wear. Journal of Micro and Nano Manufacturing, vol. 8, no. 1.

Romano, J. M., Sarasa, J. F., Concheso, C., Gulcur, M., Dashtbozorg, B., Garcia-Giron, A., Penchev, P., Dong, H., Whiteside, B., Dimov, S. (2020) Tool wear effects on hydrophobic polymer surfaces replicated using plasma treated and laser-textured stainless steel inserts. Tribology - Materials, Surfaces & Interfaces, 2020, pp. 1 – 13.

Romano, J. M., Gulcur, M., Garcia-Giron, A., Martinez-Solanas, E., Whiteside, B. R. and Dimov, S. S. (2019) Mechanical durability of hydrophobic surfaces fabricated by injection moulding of laser-induced textures. Applied Surface Science 476, 850-860.

Baruffi, F., Gülçür, M., Calaon, M., Romano, J.-M., Penchev, P., Dimov, S., Whiteside, B. and Tosello, G. (2019) Correlating nano-scale surface replication accuracy and cavity temperature in micro-injection moulding using in-line process control and high-speed thermal imaging. Journal of Manufacturing Processes 47, 367-381.

Four additional publications are currently in preparation from the work presented in this thesis.

Conference contributions:

Babenko, M., Whiteside, B. R., Gulcur, M., Masato, D. (2017). Study of the factors affecting the heating mechanism in ultrasound microinjection moulding. In: Europe Africa Conference Polymer Processing Society (PPS), Dresden, Germany.

Gulcur, M., Whiteside, B. R., Babenko, M. (2017). Effects of initial material shape and compaction routes on ultrasonic injection moulding of thermoplastic materials. *Oral presentation* in: Euspen Special Interest Group Meeting on Micro/Nano Manufacturing, Glasgow, UK.

Nair, K., Gulcur, M., Zhang, J., Liu, Z., Paradkar, A., Coates, P., Whiteside, B. R. (2018). Novel microneedle design, manufacture, and characterisation techniques of solid reservoir microneedles. In: The 5th International Conference on Microneedles (Microneedles 2018), Vancouver, Canada.

Gulcur, M., Whiteside, B.R., Nair, K., Babenko, M. (2018) Ultrasonic injection moulding of polypropylene and thermal visualisation of the process using a bespoke injection mould tool. *Oral presentation* in: Euspen 18th International Conference & Exhibition, Venice, Italy, p. 243-244.

Gulcur, M., Whiteside, B. (2018) Process fingerprinting for optimised production of thermoplastic microneedle arrays using ultrasonic microinjection moulding. *Oral presentation* in: 19th Annual Recent Appointees in Polymer Science Meeting, Bradford, UK.

Gulcur, M., Whiteside, B., Penchev, P., Romano, J. M., Dimov, S. (2018) Replication of laser structured surfaces using ultrasonic micro-injection moulding. *Oral presentation* in: Euspen Special Interest Group Meeting: Structured & Freeform Surfaces, Paris, France.

Baruffi, F., Gulcur, M., Calaon, M., Whiteside, B., Tosello, G. (2018) In-line monitoring of micro structured surface replication in micro-injection moulding. In: Euspen Special Interest Group Meeting: Structured & Freeform Surfaces, Paris, France.

Gulcur, M., Whiteside, B. (2018) New technologies and process fingerprinting for optimised production of thermoplastic microneedle arrays using ultrasonic microinjection moulding. *Oral presentation* in: P70 – Polymer Engineering International / UK-China AMRI, Bradford, UK.

Gulcur, M., Whiteside, B., Coates, P. D. (2019) Investigating the effect of the feedstock shape on ultrasonic microinjection moulding. *Oral presentation* in: Annual Technical Conference 2019 (ANTEC), Detroit, US.

Gulcur, M., Nair, K., Coates, P. (2019) Process fingerprinting for ultrasonic micromoulding. Poster presentation in: Annual Technical Conference 2019 (ANTEC), Detroit, USA.

Gulcur, M., Whiteside, B., Fook, P., Rickens, K., Riemer, O. (2019) Process and product fingerprint concept for microinjection moulding of thermoplastic microneedle arrays. Poster presentation in: Euspen 19th International Conference & Exhibition, Bilbao, Spain, p. 238-239.

Gulcur, M. (2019) New technologies and process fingerprinting for optimised production of thermoplastic microneedle arrays. *Oral presentation* in: MICROMAN Special Session at Euspen 19th International Conference & Exhibition, Bilbao, Spain.

Tosello, G., Gulcur, M., Whiteside, B., Coates, P., Luca, A., De Sousa Lia Fook, P., Riemer, O., Danilov, I., Zanjani, M.Y., Hackert-Oschätzchen, M., Schubert, A., Baruffi, F., Achour, S. B., Calaon, M., Nielsen, C. V., Bisacco, G., Cannella, E., Rasmussen, A., Bellotti, M., Saxena, K., Quan, J., Reynaerts, D., Santoso, T., Syam, W., Leach, R., Kose, S.K., Parenti, P., Annoni, M., Cai, Y., Luo, X., Qin, Y., Zeidler, H. (2019) Micro product and process fingerprints for zero-defect net-shape micromanufacturing. Poster presentation in: Euspen 19th International Conference & Exhibition, Bilbao, Spain, p. 98-99.

Gulcur, M., Brown, E., Gough, T., Whiteside, B. (2019) Process fingerprinting: in-line quality assurance and process monitoring for ultrasonic moulding of thermoplastic microneedle arrays. *Oral presentation* in: Polymer Process Engineering 2019, Bradford, UK.

Acknowledgements

Many people helped and supported me during the preparation of this thesis and I would like to thank for their help and contribution. I would say, being involved in such an excellent team and partners within MICROMAN consortium and Polymer IRC has been a truly wonderful experience.

First and foremost, I would like to acknowledge the guidance and help of my main supervisor Prof. Ben Whiteside and thank him for offering me this interesting research opportunity at Polymer MNT lab along with his endless support and encouragement. Ben's contribution to my progress while becoming a scientist has been at the highest level. I learned a lot from him, and I hope our joint work will go beyond this project in the coming years. Thank you very much Ben!

I thank my co-supervisors, Prof. Tim Gough, and Dr. Elaine Brown very much for their valuable guidance and ideas during my PhD. Their motivation and positive attitude are greatly appreciated and have been an important element of this work.

I also thank the director of Polymer IRC labs, Prof. Phil Coates for his support and encouragement. He also has in fact, a strong input in the success of this thesis by the way he manages the lab and work he has done over the years.

I thank Dr. Karthik Nair very much for sharing his knowledge and expertise in microneedles with me. Karthik has always been there to help when I needed guidance. I will always remember our trip to Vancouver for microneedles conference, which was the first time ever, me going over to Americas.

Many thanks indeed for the help and support of Dr. Cristina-Luminita Tuinea-Bobe during my time at Polymer IRC. Her valuable ideas and guidance in all aspects have always been greatly appreciated.

Our collaboration with University of Birmingham in the last 3 years has been a truly special one. I thank Dr. Jean-Michel Romano for exchanging ideas throughout this PhD and hosting me at University of Birmingham for laser machining of microneedle mould inserts. I would like also to thank Dr. Pavel

Penchev for sharing his expertise and ideas on laser machining during my secondment. I also thank Prof. Stefan Dimov from University of Birmingham for hosting me and my involvement in this excellent collaboration opportunity.

Many thanks to our technical support team, Mr. Lee Thomas, Mr. Nigel Smith, Mr. John Hornby, Mr. Steve Allan, Mr. David Barker and Mr. Glen Thompson for their excellent work and guidance regarding machining jobs.

This work was undertaken within MICROMAN network (“Process Fingerprint for Zero-defect Net-shape MICROMANufacturing”). MICROMAN is a European Training Network supported by Horizon 2020, the European Union Framework Programme for Research and Innovation (Grant agreement ID: 674801). I thank our project coordinator Dr. Guido Tosello for the management of this network. I also would like to thank my supervisors for secondments, Dr. Oltmann Riemer from University of Bremen, and Dr. Jun Qian from KU Leuven. I thank Mr. Francesc Rivillas and Alfonso Pasqual from Ultrasion for hosting me in Barcelona regarding ultrasonic micromoulding training.

I thank my mates; Mattia for hosting me at KU Leuven and Pablo & LFM team for their excellent work on diamond machining of diffraction grating inserts. I thank Bana Shriky for her review of the first chapters. Many thanks to my fellow ESRs for their friendship and for having good time together during workshops and events and more.

I thank all my good friends from Turkey, UK, Germany, and all over the world for their friendship!

Lastly, I would like to dedicate this thesis to my family. I thank my parents Neclâ - İsmail and my brother Murat (He also was a Marie-Curie Fellow before me) for raising and guiding me to this day and for their love. This work could not have been possible without their support and I am grateful to them.

“Science is the most real guide for civilisation, for life, for success in the world. To search for a guide other than science is absurdity, ignorance, and heresy.”

Mustafa Kemal ATATÜRK

1924, Samsun

Notation

ABS	acrylonitrile butadiene styrene
BNC	Bayonet Neill-Concelman type of connection
cm	centimetre
CNC	computer numerical control
CoV	coefficient of variance
COC	cyclic olefin copolymer
DAQ	data acquisition
DMA	dynamic mechanical analysis
DSC	differential scanning calorimetry
DoE	design of experiments
°C	degrees Celsius
EDM	electrical discharge machining
g	gram
Hz	hertz
HDPE	high-density polyethylene
InPb	indium antimonide
IR	infrared
J	joule
K	kelvin
kHz	kilohertz
kN	kilonewton
LCP	liquid crystal polymer
LDPE	low-density polyethylene
LED	light emitting diode
m	meter
MEMS	micro electro-mechanical systems
µm	micrometer
µs	microsecond
mg	milligram
mm	millimeter

ms	millisecond
ns	nanoseconds
N	newton
ps	picosecond
PC	polycarbonate
PDMS	polydimethylsiloxane
PEEK	polyether ether ketone
PE	polyethylene
PMMA	poly(methyl methacrylate)
POM	polyoxymethylene
PP	polypropylene
PS	polystyrene
PTFE	polytetrafluoroethylene
R^2	R squared
ROI	region of interest
RPM	revolutions per minute
S	second
SD	standard deviation
$\lambda\lambda$	wavelength
V	volt(s)
W	watt

CHAPTER 1: Introduction, Objectives and Scope of Research

1.1 Introduction

During recent decades, there has been an increasing trend in utilising the material properties in the micro and nano scale for improving optical, mechanical, and electrical properties of materials. This trend leads the technological sectors to the miniaturisation of the devices and products for energy, electronics, optics, and medical technologies. One of the biggest challenges in micro-nano manufacturing of high-value products is the quality assurance of products with extremely small dimensions or features which usually are in microns or even in nanometre range.

Even though the throughput of some of the mass-production manufacturing methods such as microinjection moulding is very high, the quality assurance requirements and post-process metrology of the products has been the bottleneck in implementing these micro-manufacturing technologies in industry. Hence, concepts and methods for 100% quality assurance of mass produced micro-nano products with high cost margins have become of great importance.

The purpose of process fingerprinting for micromoulding in particular is to find correlations between some aspects and features of the process data that are inherently characteristic to the micromoulding processes and dimensional quality criterion of the micromoulded part. By introducing such relationships, it will be possible to monitor or even predict the dimensional outcome of the micromoulded product, hence the time and money spent for off-line quality assurance procedures will be much reduced. The development of such in-line product quality assessment procedures and methods is essential and will contribute in dealing with the big-data obtained from the manufacturing processes. These methods will also contribute to the movement towards an Industry 4.0 approach for digital manufacturing.

The aim of this work is to present extensive process fingerprinting and product characterisation methods for microneedles alongside complementary tool manufacturing technologies and to introduce a complete manufacturing cycle for microneedle arrays for drug delivery. The ultimate goal of process fingerprinting is to address and present robust in-line process monitoring procedures for micro-scaled products in micromoulding process environments.

1.2 Objectives of the project

i) To study and optimise process conditions for conventional and ultrasonic micromoulding of microneedle arrays.

ii) To implement state-of-the-art process monitoring and data acquisition solutions for ultrasonic and conventional micro-injection moulding technologies.

iii) To interrogate process characteristics and challenges of micromoulding techniques for microneedle manufacture.

iv) To present correlations between process measurements and geometric outcome of the microneedles.

v) To demonstrate machine vision-based, fast and reliable inspection apparatuses for microneedle quality assessment.

1.3 Micro and nano-scaled polymeric products

Technological advancements in micro-nano manufacturing enables the mass production of very small components or devices in cost-effective routes. Polymers in that sense, are quite suitable since they could be shaped, structured and functionalised in a variety of methods e.g. hot embossing and micro-injection moulding (Heckele and Schomburg 2004). Extremely small polymeric components could be in either monolithic forms such as gears, connectors, housing, and cantilevers, or in thin sheets with micro and nano functional surfaces or features. That signifies the need for different manufacturing methods for different shapes of final products. Two of the main established manufacturing methods for polymers in microsystem applications are micro - injection moulding and hot embossing (Worgull 2009).

Micro-injection moulding is a highly automated process which was developed from the insight and knowledge of injection moulding technologies which enables the mass production of extremely small polymeric components. The applications of these polymeric products require replication of micro-nano surface features and dimensional tolerances include optics, medical technologies, and micro electro-mechanical systems (MEMS). A detailed overview and principles of this technology will be given in Chapter 2.

Hot embossing is another cost-effective replication technology for producing functional surfaces with micro-nano features. Unlike micro-injection moulding, hot embossing is analogous to stamping techniques where the cost effectiveness arises from the technique’s large scale micro-nano feature replication capability up to 20 x 20 cm^2 (Kolew et al. 2011). The applications of polymeric hot embossing products include large-scale functional surfaces for optics (Schneider et al. 2014), self-cleaning surfaces (Röhrig et al. 2014) and photovoltaics (Schauer et al. 2018).

1.4 Microneedle technology

Miniaturisation trends of technological products also manifests itself in the medical and pharmaceutical sectors. Scaling down of medical components and devices allow new concepts to be considered such as body monitoring and novel drug delivery systems (Mirza et al. 2017; Vranić et al. 2020). Currently, transdermal drug delivery is carried out with hypodermic needles that are usually made of metals and substantially large geometries that cause pain and fear amongst patients. However, transdermal delivery of the drugs is limited by the inability of most of the drugs to cross the skin and reach the veins in order to be effective. To create more pores at the skin’s outer layer, micron-sized needles can be used and transportation of the delivered drugs can be more effective and efficient (Prausnitz 2004). The pores on the skin that are created by these microneedles are usually a few hundred µm in diameter so that there is enough space for large molecules to be transported across the skin.

The microneedles are designed and fabricated in arrays that have usually 25 - 100 microneedles on one patch. The microneedle heights are typically within the range of 100 - 1000 µm (van der Maaden et al. 2012). The main purpose of microneedles is puncturing of stratum corneum layer of the skin which is typically 10-20 µm thick without going deeper and contacting the nerves that could cause pain to the administered person. The stratum corneum layer can also have variable thicknesses in different parts of the human body which also proves that manufacturing a range of different heights of microneedles is also of interest (Prausnitz 2017).

Another important design consideration of the microneedles is the tip radii as they have a direct impact on the penetration forces. Generally, it becomes easier for the needle to puncture the skin with smaller tip radii causing less pain. An ideal tip radius between 1-10 µm has been reported as desirable by Prausnitz, however, microneedles tip radii of up to 60 µm have been studied depending on their application (Davis et al. 2004; Prausnitz 2017). Nalluri investigated the permeation enhancement of a 5x5 microneedle array with 556 ± 30 µm average height and tip radii 32 ± 8 µm using polyether ether ketone (PEEK) on pig skin (Nalluri et al. 2017). The micrographs and images presented in the work show that the needles successfully punctured the skin.

Although the ideal tip radius for microneedles is reported to be between 1 – 10 µm by Prausnitz, from manufacturing perspective this can pose problems. The sharper tip radii towards 1 µm would mean that the demoulding will become a problem for thermoplastics and also the handling and packaging of the needles will be challenging due to the damage that can occur at the tips. Moreover, the technological requirements for achieving tip radii towards 1 µm demand usage of low-throughput and laborious processes such as lithography and etching (Larrañeta et al. 2016). Hence, due to the practicalities and the trade-off between the demoulding phase and achievement of sharp tips a tip radii between5 – 15 µm can be considered as an ideal range for micromoulding of microneedle arrays.

Operation of hypodermic needles must be administered by competent healthcare professionals with a scarcity in numbers in developing countries (Drain et al. 2003; Prausnitz 2017). Puncturing the outer layer of the skin by a hypodermic needle also often causes pain to the patients inducing needle phobia, which makes it difficult to deliver vaccines (Gill et al. 2008). In addition, vaccine deliveries using hypodermic needles are not efficient since nearly half of the vaccine material is wasted (Drain et al. 2003). Microneedle arrays or microneedle patches are one of the emerging medical technologies for the near future and this technology attempts to tackle those problems mentioned above.

There have been different methods and approaches for drug delivery using microneedles (Prausnitz 2017). The first and one of the most common ways is to use solid microneedles to create pores on the skin's outer layer - stratum corneum followed by application of a patch or a droplet of drug on the pores to achieve drug delivery. The second approach is to coat the solid microneedles with drugs, then apply to the patient's skin for a designated period of time. Subsequently, the microneedle patch is to be removed and disposed. Another common concept is to create microneedles with dissolvable tips or shafts. After insertion, the dissolvable parts break and stay in the skin, delivering the drug. The schematic representation of these different approaches is given in Figure 1-1.

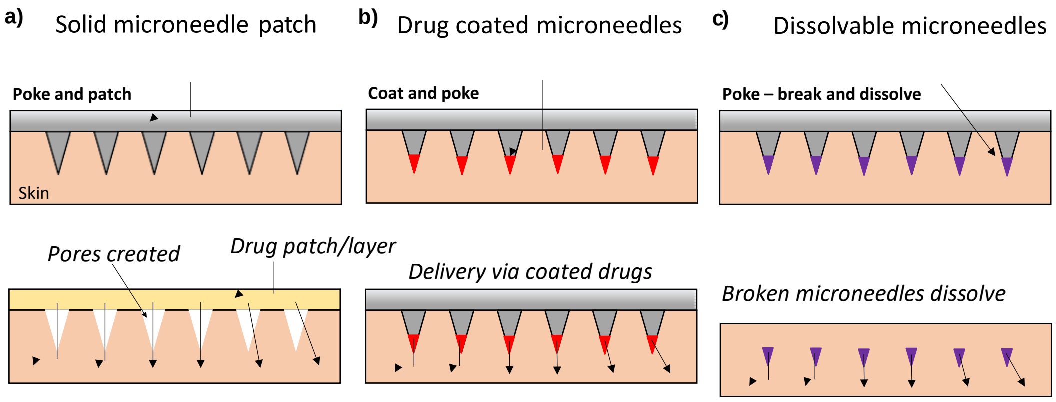

Figure 1-1. Different approaches on drug delivery using microneedles. a) drug delivery using solid microneedles and creation of pores, b) drug-coated microneedles, c) dissolvable microneedles. Based on the information provided by the reference (Prausnitz 2017).

In this work, solid microneedle design has been adopted and high-quality microneedles have been manufactured using conventional and ultrasonic micro-injection moulding techniques. Since the focus of the work was to carry out process fingerprinting and demonstrate production scenarios for microneedles, drug delivery and skin penetration studies have not been covered.

1.5 Micro-injection moulding for microneedle patches

One of the important challenges for microneedles is to manufacture them in large volumes while maintaining the functionality alongside reduction in the unit cost. Microneedle technology requires highly demanding advanced manufacturing technologies for the manufacturing of challenging geometries and features such as high aspect ratios and sharp tips. In this sub-section, a short overview on manufacturing technologies of microneedle arrays is provided and the reasons why conventional micromoulding stand out as one of the more suitable and viable technique for mass production are given. Moreover, a short discussion on ultrasonic micromoulding also has been given signifying potentials of this recently commercialised technology.

The literature on microneedles shows that the manufacturing methods for microneedle arrays mostly originate from MEMS industry including lithography, etching, polydimethylsiloxane (PDMS) moulding and printing techniques (Henry et al. 1998; Allen et al. 2016; Larrañeta et al. 2016). Tarbox et al. published a review summarising manufacturing and coating methods for microneedles (Tarbox et al. 2018). In most of these articles, micromoulding term is often associated with PDMS casting routes which allows replication of microneedle features, however, most of these manufacturing routes are far from successful up-scaling as they are multi-step batch processes (Demir et al. 2013; Bediz et al. 2014; Wang et al. 2017). The PDMS micromoulding method comprises 3 steps where a PDMS mould with microneedle cavities are formed using a metal or silicon master mould, then a PDMS mould is used for forming and casting of the microneedle patches. Although this method is beneficial for experimenting with new microneedle geometries and drugs for delivery, it does not provide a commercial solution for microneedle manufacture. To summarise, microneedle patches must be produced in large numbers for accessibility of vaccination and other drugs for all regions of the world. Due to this reason, although there have been significant improvements in research on vaccines and drug delivery using microneedles, the techniques used for fabricating those microneedle patches remain unscalable and obscure from a manufacturing point of view.

Due to its high repeatability, short cycle times and micro-nano replication capabilities, micromoulding technique fits well to demanding manufacturing requirements for a microneedle mass production cycle (Whiteside et al. 2003; Nair et al. 2015). The sharp-pointy tips and high aspect ratios make manufacturing of microneedles a challenging task. However, microinjection moulding can offer extremely high injection speeds, tight control of melt and mould temperatures and capability of applying holding pressures after the microneedle cavities are filled. Due to these advantages, a wide range of polymers with sufficient mechanical strength and chemical inertness can be used for manufacturing microneedles using micromoulding.

Micro-injection moulding should be considered in conjunction with complementary technologies for tooling such as electrical discharge machining (EDM), laser machining and micro-milling for microneedle tool manufacturing as most of the investment is required for the tooling and machinery. One other advantage of micro-injection moulding is that the tooling is an only one-time investment since a mould tool for microneedles can perform more than tens of thousands cycles in its lifetime.

A recent review article on microfabrication of microneedle arrays report that there are limited amount of reports in the literature that use injection or micro-injection moulding as a manufacturing method for microneedle arrays (Juster et al. 2019). Work was carried out for injection moulding of a single microneedle device with microchannels for liquid extraction (Sammoura et al. 2007). The authors manufactured 600 μm long needles with cyclic olefin polymer (COC) and carried out insertion tests to biological samples.

Hamilton presented mould manufacturing procedures and injection moulding of polymeric microneedle arrays (Hamilton 2011). The author used computer numerical control (CNC) milling and engraving methods to produce microneedle cavities with 600 μm depth and approximately 10 μm of tip sharpness. Polystyrene (PS), COC, liquid crystal polymer (LCP) and polyarylamid (PARA) have been used for manufacturing microneedles with a conventional injection moulding machine.

Attempts were made to utilise laser machining processes for microneedle cavity generation on tool surfaces and application of resulting tooling for microneedle production (Dimov et al. 2011; Steglich et al. 2012). Yung et al. used picosecond laser machining for microneedle cavities for tooling and manufactured hollow microneedle arrays using polyoxymethylene (POM) (Yung et al. 2012). PEEK and polycarbonate (PC) solid microneedles were manufactured by Nair et al. and plasma treatment effects on microneedles were also investigated (Nair 2014).

Although conventional micro-injection moulding stands out as a viable manufacturing method, there could be some drawbacks related to the way of processing the material using this manufacturing method. First, micromoulded products are usually very small and each shot of the material is a very small fraction of the material inside the plastication barrel at elevated temperatures. This in turn, results in degradation of the polymer over time and deterioration of chemical and physical properties. Moreover, pharmaceutical grade polymers are usually expensive and there could be drawbacks regarding degradation while incorporating active ingredients to the polymer for drug delivery purposes. Recent developments in micromoulding technologies address these issues and provide solutions to overcome these drawbacks.

Ultrasonic micro-injection moulding could be an alternative to micro-injection moulding for tackling aforementioned issues regarding polymer and active ingredient degradation for innovative approaches (Janer et al. 2020). Ultrasonic micromoulding process have some unique capabilities and advantages over the conventional micromoulding technology. The feedstock is being melted by means of ultrasonic energy and the melt is exposed to high temperatures only a few seconds which could be advantageous for preventing degradation problems. Moreover, only the amount of material is melted and injected to the mould cavity where material savings could be crucial for pharma-grade materials. The theory behind ultrasonic micromoulding, experimental campaign and results for this particular technology will be discussed in Chapter 2 and Chapter 6.

Microneedles are poised for commercialisation since some drug delivery tests and vaccinations including phase-1 in-human trials have already been carried out (Rouphael et al. 2017). Micro-injection moulding techniques have the opportunity and capability to provide demanding manufacturing requirements for mass production of microneedles. The technology also offers excellent possibilities for research as both conventional and ultrasonic micromoulding techniques can process a wide range of polymers and pharmaceutical materials. Moreover, process monitoring aspect of microneedle manufacture has been overlooked, where no reports regarding extensive process monitoring of a microneedle production scenario are present in the literature.

Conventional micro-injection moulding can be considered as an established technology for its capability and repeatability for manufacturing micro-nano components in large volumes, whereas ultrasonic micromoulding can offer certain advantages when processing temperature-sensitive materials. There are reports in the literature showing the benefit of having sonication during replication processes (Sato et al. 2010; Jung and Park 2014). When ultrasonic micromoulding is considered, usage of sonication while moulding would provide significant advantages during filling of the mould cavities due to sustained temperatures after filling and at lower viscosities (Sacristán et al. 2014). These advantages make ultrasonic micromoulding also a promising candidate for microneedle manufacture.

1.6 The need for process fingerprinting in micromanufacturing

Recent reports from independent market analysis and strategic guidance companies such as Yole Développement and IHS Technology indicate the importance of emerging micro and nano technologies. A report which Yole Développement released suggest that microsystem and microfluidics industry is maturing, and new companies are founded, and they expect growth (Yole Développement 2015). Another study from IHS Technology discusses high-value MEMS and internet of things devices and reports that a 9.4% increase was expected from 2013 to 2018 in compound annual growth rate (Bouchaud and Dixon 2015). Between 2010 – 2014 a 5.5% of growth rate was reported previously by the authors.

The analyses from these companies signify that future micro and nano manufacturing technologies will have increased market shares and impact on our lifestyles in the coming years. One of the biggest requirements in micromanufacturing is that these technologies need intricate, yet simple and cost-effective quality assurance and mass production processes. In that sense, process fingerprinting concept will provide a thorough characterisation of micro-injection moulding processes for microneedle manufacture which is expected to be commercialised in the near future.

1.7 Scope of the research

In Chapter 1, a general overview on polymeric micro-nano products, microneedle arrays and suitability of micromoulding technologies for manufacturing microneedles have been discussed. Significance of micromanufacturing methods and general trends for the markets have also been given.

An overview of polymers and their viscoelastic behaviour are given in Chapter 2. Conventional and ultrasonic micromoulding are also introduced and main principles of the processes will be discussed in that chapter. A short summary on ultrasonics theory and interaction of ultrasonic energy with polymers is also discussed.

Before introducing the process fingerprint concept, detailed information is provided in Chapter 3 on process monitoring devices used for micromoulding processes. First, examples from literature are given for process monitoring of micromoulding processes. Then, the equipment and methods that are used in this work described comprehensively.

Building on the process monitoring methods given in Chapter 3, Chapter 4 introduces the process fingerprint concept which is one of the main focuses in this thesis. In the chapter, process and product fingerprints are defined, and measurement methods for both micromoulding processes and product dimensions are also discussed.

Chapter 5 covers the conventional micromoulding of microneedle arrays with extensive process monitoring and evaluation of microneedle quality. Process characteristics are explained and process fingerprint analysis is carried out for microneedle arrays.

Ultrasonic micro-injection moulding experiments for manufacturing of microneedles and process fingerprinting analysis are investigated in Chapter

6. Correlations between process and product fingerprints are studied in detail. Moreover, process data taken from a variety of sensors are analysed and the process is characterised accordingly.

Chapter 7 summarises the work and provides a global discussion and comparison between conventional and ultrasonic micromoulding processes. Concluding comments and the most significant outcomes are also presented. Ways of improvement and recommendations for future work are also given.

1.8 Summary

This chapter has introduced the need and importance of micro and nano scaled polymer components and particularly, microneedle arrays. A short review on the manufacturing methods is provided and the selection of micro-injection moulding for manufacturing of microneedles is justified with examples from literature. The need and current trends for micro and nano technologies have been also discussed briefly. The scope of the work and project aims have been summarised.

CHAPTER 2: Micro-injection Moulding Background

2.1 Introduction

This chapter provides the theoretical background for conventional and ultrasonic micro-injection moulding by briefly discussing the development of both technologies over the last few decades and explaining the current state-of-the-art. A review on process characteristics, microfeature replication capabilities and process challenges of micromoulding methods are given in detail. Since micromoulding techniques are derived from the injection moulding principles, main aspects of this process are also discussed. First, a theoretical background for polymers is given as the main focus of the work is thermoplastic microneedle arrays.

2.2 Polymeric materials

2.2.1 Classification of polymers

The term polymer is a combination of two different Ancient Greek words “poly” meaning many and “mer” meaning part. Polymers are long-chain molecules that consist of one or more repeating subunits called “mers”. Thermal and physical properties of polymers are determined by their repeating unit, length of the chain and intermolecular forces. Classifications of polymers are commonly presented as:

i) Thermoplastic and thermosets: Thermoplastic polymers are softened through application of heat and can be heated and cooled repeatedly due to their molecular arrangements. On the contrary, thermoset materials have strong covalent bonds within their chains formed during polymerisation reactions or thermal process. These covalent bonds lead to a cross-linking of the polymer, preventing it from cyclic thermal processing.

ii) Natural and synthetic polymers: There are natural polymers available such as proteins and cellulose, whereas many polymeric materials are synthetically produced e.g. polystyrene, polypropylene and nylon.

iii) Classification according to the mechanism of polymerisation: For some polymers, the addition of monomers can be sequential, e.g. polystyrene from styrene monomers. These types of reactions are called addition polymerisations. There are reactions that include ring opening reactions where the carbon ring is opened and polymerisation is facilitated through sterically strained cyclic monomers, e.g. POM from trioxane.

iv) Classification according to polymer structure: Homopolymers consist of only one type monomers whereas there are more than one repeating units in copolymers.

v) Classification according to crystallinity: Generally, polymers can be classified in two different groups in terms of their crystal structure: amorphous and semi-crystalline polymers.

2.2.2 Amorphous and semi-crystalline polymers

Semi-crystalline polymers incorporate ordered and amorphous regions where the latter could be in small or large percentages depending on the processing, e.g. cooling rate. Long polymer molecules cannot form lattice structures but instead they fold, and form densely packed regions in comparison to amorphous regions. Crystalline regions in polymers are closely packed fragments of the molecules where rigidity and density properties are quite profound whereas amorphous regions provide more mechanical flexibility and less dense molecular packing. Molecular arrangements in polymers and their semi-crystallinity are of critical importance for micromoulding of extremely small products, such as microneedles as they affect the flow, cooling behaviour and mechanical properties of the resulting product. Therefore, in this subsection, amorphous and semi-crystalline polymers will be discussed briefly, and their significance will be emphasised particularly for micromoulding applications.

Molecular structure and intermolecular forces play an important role in deciding whether a polymer will form crystallites or stay in an amorphous structure. If a chain of a polymer molecule is symmetric and regular which makes folding of chains and arrangements easier, it is more likely that it will form a semi-crystalline structure (e.g. polyethylene - PE). However, if the polymer chain has attached groups that disrupts the symmetry, causing asymmetries along the polymer backbone, the resulting structure will likely to be an amorphous state. The resulting structure is a randomly distributed molecular entanglements of long molecules, which, to some extent, also restricts the flow of the material. In some cases, e.g. Nylon 6,6, intramolecular hydrogen bonds help the chains to align and stay closer, resulting in a crystalline structure. Therefore, symmetry, regularity of the polymer chain and intermolecular forces between the chains are some of the factors that play important role for a polymer to form crystals.

The level of interaction between the polymer chains and degree of crystallinity affect the critical temperatures for polymers. Amorphous polymers have disordered molecular structures as mentioned above and show a thermal behaviour where a glass transition temperature (T_g) is observed. Below T_g, amorphous polymers are in a rigid physical state. When the amorphous polymers are heated above their T_g, the polymer changes shape under deformation or shear and becomes a rubbery material. Crystalline polymers have both T_g and melting point (T_m), and the latter being at higher values. T_g is the temperature at which long range movements of lengthy chains start for semi-crystalline polymers. At T_m, the crystalline regions lose their integrity and polymer completely becomes an amorphous flowing melt.

Properties of polymers are greatly affected by the way they are processed and associated with the thermal and structural features discussed above. Most of the polymer products are, at least once in their lifetime, exposed to a screw extrusion process for blending or pelletising to be prepared as semi-finished industrial products. These processes are usually carried out at elevated temperatures above either T_g or T_m for forming. Cooling of a polymer from elevated temperatures determines its microstructure where crystalline and amorphous regions can be formed in different proportions.

If a semi-crystalline polymer is considered for cooling behaviour, fast and slow cooling rates will induce different crystallite amounts and hence different mechanical and optical properties. Polyethylene (PE) is a very good example for semi-crystalline polymers in which the degree of crystallinity changes considerably depending on the processing conditions. During cooling of PE, slower cooling rates will result in smaller free volumes for the same amount of mass with allowance of more time for the molecules to find favourable places to form crystallites whereas faster cooling rates will result in larger free volumes. Larger volumes result in smaller densities because of the abundance of amorphous zones where the polymer molecules are entangled and occupying more volume. The abundant crystalline regions in the slow cooling scenario contribute to mechanical strength of the semi-crystalline polymer. In addition, crystalline and amorphous zones have different refractive indices, resulting in opaqueness in the case of more crystallites and transparency for fast-cooled amorphous dominant PE. Fast and slow cooling rate scenario for PE and volume - temperature relation is given in Figure 2-1.

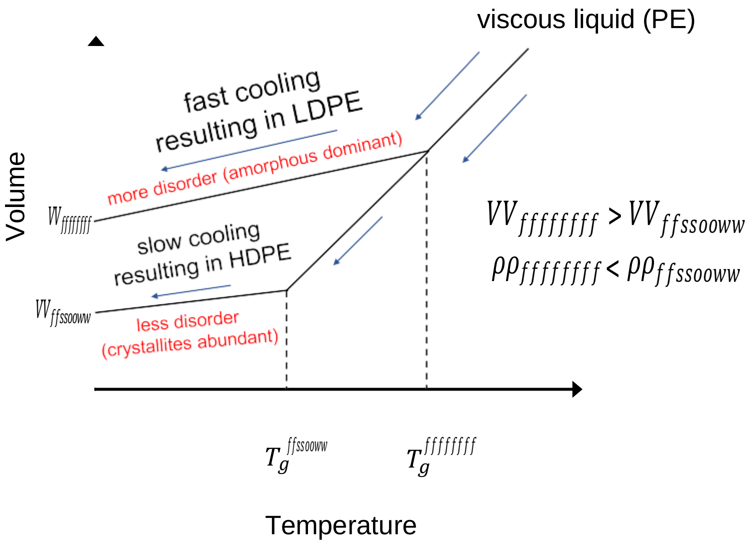

Figure 2-1. Cooling behaviour of a viscous melt or liquid (polyethylene - PE used as an example). Volumes and glass transition temperatures are indicated with V and T_g respectively for slow and fast cooling rates. Fast cooling of a viscous liquid results in entanglement of molecules and high volumes whereas in slow cooling rates material tends to form ordered crystallites. Fast cooling results in low-density polyethylene (LDPE) and slow cooling in high-density polyethylene (HDPE). The terms are defined as following: $VV_{ffffffff}$ = final volume achieved by fast cooling rate, $VV_{ffssooww}$ = final volume achieved by slow cooling rate, $\rho\rho_{ffffffff}$ = Final density achieved by fast cooling rate, $\rho\rho_{ffssooww}$ = Final density achieved by slow cooling rate.

The flow and the ability of material to fill intricate micro-nano features is heavily influenced by the molecular characteristics and arrangements of the material in micromoulding. For a polymer, being amorphous or semi-crystalline is also important since semi-crystalline polymers usually exhibit shrinkage due to their significant volume change during solidification. Considering the very small and intricate micro-nano features of the moulds, this could be a disadvantage since the functional surfaces lose their flatness with shrinkage marks. On the other hand, amorphous polymers exhibit a T_g range and the free volume change for these materials are less pronounced, often resulting in negligible shrinkage effects.

Plasticising polymers using ultrasound waves differs from the heating and melting the feedstock in conventional micromoulding. Crystalline structure of the polymer has a clear effect on ultrasonic processes since the heat generation is facilitated by both external friction of the feedstock and internal friction on molecules due to damping of ultrasonic waves. For instance, if a semi-crystalline material such as polypropylene (PP) is ultrasonically moulded, inhomogeneities are commonly seen in heating as the materials have a sharp melting point and it is difficult to distribute the sonication evenly during melting. The elastic nature of the material allows for absorption or insulation of the sonication until sufficient energy is provided for overcoming the heat of fusion barrier to break down the semi-crystalline structure in order to allow the flow of material. A combination of uneven temperature distribution in the melt and significant volume change during moulding is seen in turn. These effects result in local viscosity differences and cause even poorer shrinkage marks then conventional micromoulding, affecting the replication of micro and nano features.

To summarise, although polymers show lower mechanical and thermal properties than of metals and ceramics, their flexibility and cost effectiveness in processing make them one of the most important types of engineering materials. By tuning the cooling rates, melt temperatures and moulding profiles in micromoulding, the percentage of crystalline structures can also be modified for different purposes. In contrast with their limited material properties compared with other classes, some polymers can offer relatively high mechanical stiffness and operation temperatures for certain applications. Polymer products are and will be used in a wide variety of due to the increased needs for miniaturised, low-cost, and functional devices.

2.3 Injection moulding

Injection moulding is a manufacturing method that allows high volume and precision manufacturing of thermoplastics with net shape forming meaning that the manufactured part does not need any additional finishing treatment after the process, as they are ready to use. The main principle of injection moulding is that the polymer pellets are fed into a hopper which is connected to a barrel with a rotating screw inside and external heating elements that plasticise the material, and which then the molten material is conveyed, via the movement of the screw system, to the mould. Main parts of an injection moulding machine are presented in Figure 2-2.

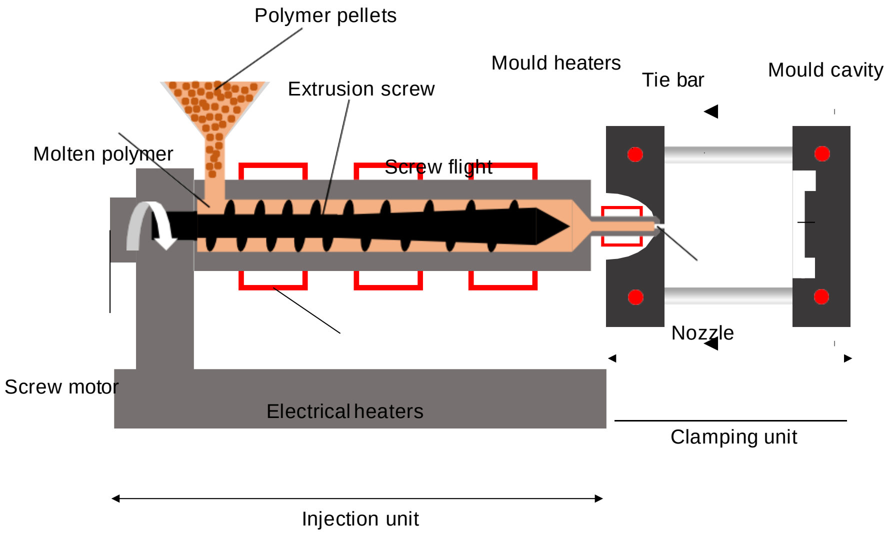

Figure 2-2. Schematic representation of an injection moulding machine.

The technique generally uses sufficiently high temperatures and pressures to make sure that the mould cavity is filled rapidly to supress the effect of cooling and solidification since there is a big temperature gradient between the melt and the polymer.

Injection moulding machines are usually defined by 2 main units; the first one being the plasticising unit that facilitates the melting of the polymer feedstock and conveying the melt for injection into the mould, and the second one is called the clamping unit which governs the movement of the mould and ejection of the moulded parts. An injection moulding process can be described in 5 different stages:

i. Clamping of the mould and injection of the polymer melt by the movement of the screw to the mould tool. Additional injection pressure is applied for a certain time to compensate for shrinkage and to complete filling of the mould.

ii. Backward motion of the screw that facilitates the metering of the material which will be used for next shot.

iii. Retraction of either of the clamping unit and the mould halves or the plasticising unit.

iv. Opening of the mould for the preparation of the ejection phase. The part is usually stuck in the moving half of the injection mould tool where the cavity is placed.

v. Ejection of the part using the ejector assembly placed in the injection mould tool (Figure 2-3).

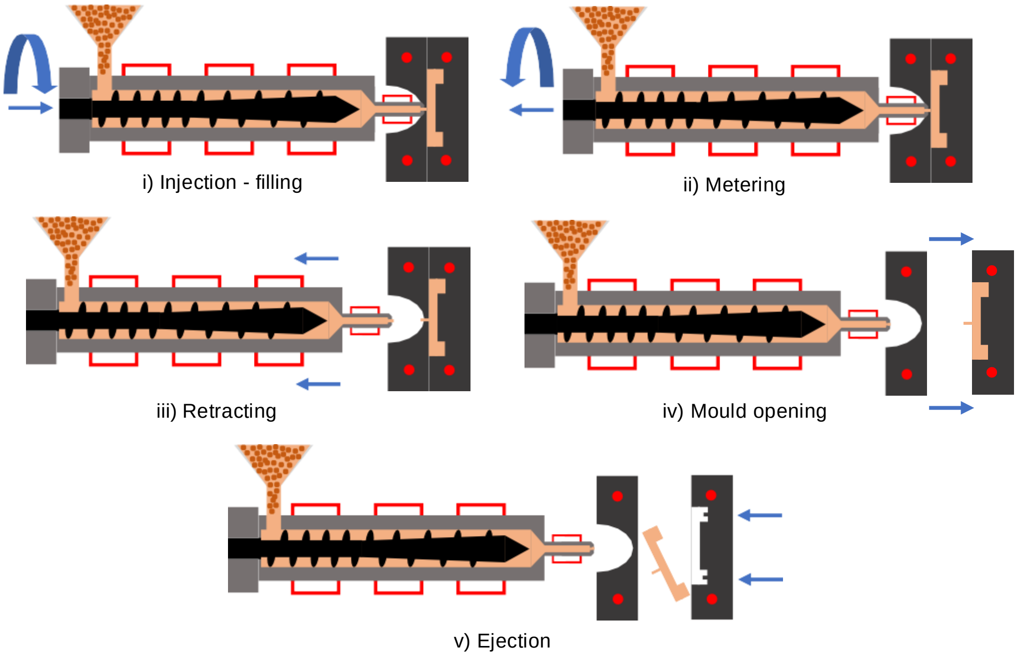

Figure 2-3. Schematic depicting the 5 main phases of injection moulding process.

As described in the steps above, it is crucial to have a packing phase in an injection moulding process for the moulded part in order to compensate for the shrinkage effect of the solidifying polymer and apply some additional pressure for filling the mould cavity better. In the first stage, the filling process is dominated by the injection speed of the molten polymer. If this high speed of injection is sustained until the cavity becomes full, there will be a sudden increase in the cavity pressure as the material no longer flows and is simply compressed. In order to avoid this problem, the cavity is part filled to around 98-99%, and at that time the process is shifted to a pressure-controlled regime to fill the remainder of the mould cavity. Then, this pressure is sustained for a certain amount of time so that the shrinkage of the frozen material can be compensated since there will be a change in volume while the molten polymer solidifies.

Because of the limitations in manufacturing smaller reciprocating screws and the need for the usage of pellets as the polymer feedstock shape, the screw diameter can be no smaller than 14 mm practically (Michaeli et al. 2002). Although conventional injection moulding is one of the widely used net-shape forming manufacturing technique for high volume production, it is difficult to implement this technology into micromanufacturing of polymeric parts because of the high volumes of melts in the screw systems and precision of these screw based injection units (Whiteside et al. 2003). Another difficulty of using big screws and plasticising units for producing micromoulding of extremely small parts is that the residence times for unit volume of molten polymer is increased which will be problematic when using temperature sensitive materials needed for medical applications. Therefore, microinjection moulding machines are developed on the main principles of conventional injection moulding to find solutions for the problems of injection of small shot sizes with high velocities and without premature solidification of the molten polymer into the mould cavity to produce micro-nano scaled parts.

2.4 Micro-injection moulding

Micro-injection moulding is a net-shape manufacturing technology to produce high volumes of mainly polymeric micro components with high precision and accuracy. The technique originates from the principles of conventional injection moulding as mentioned in Section 2.3. One of the main challenges in micro-injection moulding is the melting and injection of the extremely small amount of polymer melt into the mould cavity without premature solidification. As the injected parts get smaller, the surface effects become more pronounced in micromoulding since the surface area to volume ratio for final parts increase considerably as compared with conventional injection moulding. That situation results in extreme cooling rates and poses challenges in complete filling of the micro featured mould surfaces. The definitions of micromoulded parts change in the literature but the most appropriate definition of a micromoulded part has been given by Kukla et. al (Kukla et al. 1998):

i. Extremely small, moulded parts that weigh only few milligrams;

ii. A component produced by conventional injection moulding or other moulding techniques, but its functionality depends on the microfeatures that it incorporates;

iii. A part that can be of any size, but with tolerances on the order of micron scale.

The fact that the conventional injection moulding uses a screw system for both conveying and melting the material means that it is hard to achieve the shot sizes required by micro components which are sometimes a few milligrams. Thus, most micro-injection moulding machines are designed in the way that the plasticisation and injection units are separated. One of the first microinjection moulding machines that used this approach is Microsystem 50 from the Austrian company Battenfeld. In Microsystem 50, the plasticisation phase is facilitated with a reciprocating screw that is positioned 45° to the horizontal axis and with 16 mm screw diameter which is considerably smaller than in conventional injection moulding machines. After obtaining the molten polymer in the plasticisation unit, a secondary dosing piston is used and the amount of material to be injected is dosed inside another chamber. The injection phase is completed with the transfer of the material in front of the injection piston which is positioned horizontally and connected to the mould by a nozzle. The micromoulding process is then accomplished through these three phases and the part is ejected by an ejector assembly located in the mould’s moving half.

Microsystem 50 was the state-of-the-art of the micro-injection moulding machines of 2000’s, having the capability to manufacture microparts efficiently and in-line inspection of the moulded parts using a machine vision system for quality control. However, the presence of a separate dosing unit for the process adds additional complexity to the process and cleaning of the metering chamber, barrel and injection piston was difficult, especially when using medical materials which are very sensitive to contamination. The technology was enhanced further by Wittmann - Battenfeld Group and significant improvements made over the old technology with the introduction of Micropower 15 microinjection moulding machines.

Micropower 15 differs from the old technology by using a two-phase moulding approach rather than three-phase moulding which was used in Microsystem 50. The new technology uses only the plasticising screw for both metering and melting of the polymer feedstock and injection is facilitated by an injection plunger. The screw diameter in Micropower 15 is 14 mm and can melt the standard pellet shaped feedstock. The metering accuracy is reported as 5 mg and shot sizes as small as 50 mg can be injected. The injection velocities can go up to 750 mm/s with approximately 3000 bars of injection pressures depending on the injection plunger diameter (Naitove 2010). With updates on both hardware and machine controls in the newer generations of this brand, Micropower 15 is regarded as the state-of-the-art of micro-injection moulding technology. In this work, Micropower 15 was used for manufacturing of microneedle patches and comparisons were made with recently developed ultrasonic microinjection moulding technology. A schematic description of the injection and dosing unit of Micropower 15 is given in Figure 2-4.

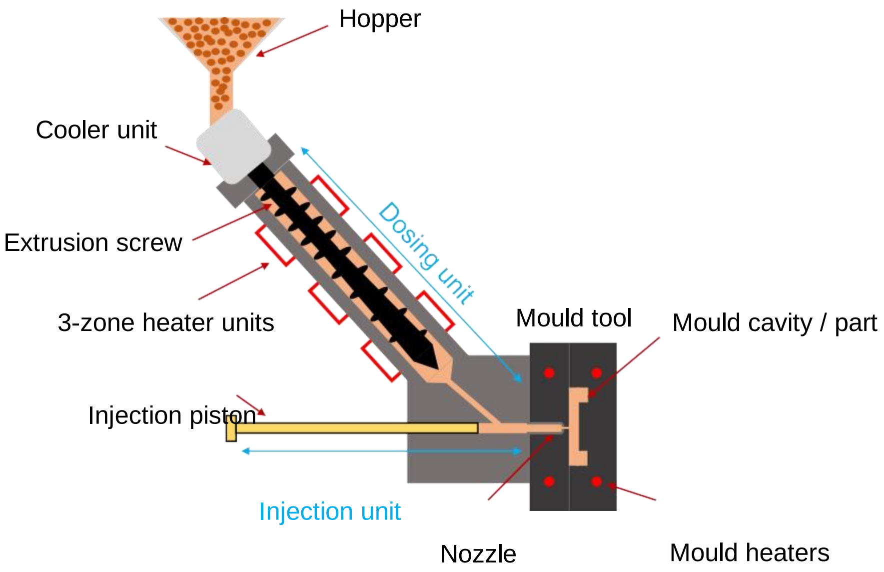

Figure 2-4. Schematic representation of the dosing and injection unit of Wittmann-Battenfeld Micropower 15 microinjection moulding machine.

Micropower 15 is an all-electrically controlled machine in both clamping and injection units for high precision and accuracy. It has been designed for extendable production lines and is also suitable for clean-room environments. The clamping unit consists of a highly precise servo motor for clamping force detection and mould safety device. The unit also incorporates a rotary plate that allows attachment of two moulds which effectively halves the cycle time. 14 mm 3-zone screw is used in the plasticising unit. 5 mm injection plunger was used for injection of small amounts in this work, as low as ~300 mg for microneedle patches. The main specifications of Witmann-Battenfeld Micropower 15 are given in Table 1.

Table 1. Main specifications of Wittmann - Battenfeld Micropower 15 microinjection moulding machine

Feature/specification	Value & units
Clamping force	150 kN
Dosing screw diameter	14 mm
Injection plunger diameter	5 mm
Maximum rotational screw speed	200 RPM
Maximum injection speed	750 mm/s
Maximum injection pressure	3000 bars

2.4.1 Micro-injection moulding process parameters

In micromoulding, there are many parameters to be tuned for a successful product and each of them has significant impacts on the overall part quality.

Although most of the process parameters for injection moulding have similar impacts on micro-injection moulding, the scaled down version has significant differences and phenomena such as very high surface to volume ratios of the micromoulding cavity and shear heating effects. The most important process parameters include the melt temperature, mould temperature, injection speed, injection pressure and holding pressure (Packianather et al. 2015). During a process optimisation stage, these parameters can be regarded as independent variables.

Melt temperature is one of the most influential factors in a micromoulding process since the flow properties and viscosity of the molten material inside the barrel are strongly affected by the temperature of the melt. There are reports in the literature that higher melt temperatures lead to a better filling of the micro-nano structured mould surface features for polymers (Mnkknen et al. 2002; Sha et al. 2007). Alongside its advantages, it should also be noted that the higher barrel or melt temperature for polymers also can be problematic because of the residence times which could lead to degradation of the molten polymer.

The rapid cooling of the moulded parts due to high surface area to volume ratios in micro-injection moulding is an important aspect of the process and it is mostly affected by the mould temperature ($\mathrm{T_{mould}}$). The temperature difference between the melt and the mould causes the injected polymer to cool down at very high rates. $\mathrm{T_{mould}}$ is one of the parameters that directly influence not only the filling and replication properties but also the internal morphology of the moulded part (Whiteside et al. 2004). Ideally, the mould temperature could be set above the glass transition or melt temperatures of the polymers, however, using high mould temperatures results in elongated cycle times and problems in ejection of the parts from the mould cavity. Depending on the heat deflection temperature of the micromoulded polymer, the part also could deform under ejection forces. Hence, a good balance between the critical temperatures of the polymer and mould temperature should be maintained in order to optimise the micromoulding process. Mould temperature affects the ejection of the part in micromoulding and cycle and cooling times can be critical. A cycle time of ~22 s has been read from the machine screen in this work which could be effectively reduced to ~11 s by using the two platen system for higher throughput.

Injection speed or velocity is also another critical parameter to consider in micro-injection moulding since the premature freezing of the polymer melt could be eliminated by injecting the shot to the mould cavity rapidly. In terms of filling the high aspect ratio structures and small micromoulding cavities high injection speeds could be favourable, however it should be noted that polymers undergo a shear heating effect which would cause the polymer melt to heat even more during injection which could lead to degradation problems (Griffiths et al. 2007). The other phenomena related to this behaviour is known as the Diesel effect where the hot air trapped inside the micromoulding cavity can cause combustion of the material due to extremely high injection speeds (Giboz et al. 2007).

Pressure measurements and control in micro-injection moulding is also important since, depending on the machine design, a moulding process becomes pressure controlled after the majority of the cavity is filled. The compensation of the shrinkage and complete filling of the part is achieved by the holding pressure or switch-over pressure. Zhang et al. studied the velocity to pressure control for a micro-injection moulding machine which as a screw-based injection system (Zhang et al. 2011; Zhang and Gilchrist 2014). The authors have reported that velocity controlled regime influenced the process measurements. Moreover, they signify the importance of timing and machine control while the transition from velocity to pressure controlled is being carried out. It has been also reported that the cavity pressure can be used as an indicator of process variation and is of great importance for a micro-injection moulding process (Packianather et al. 2015). In conclusion, both injection and cavity pressure measurements are crucial and must be understood thoroughly for better understanding of a micromoulding process.

2.5 Ultrasonic micro-injection moulding

In this section and sub sections, the recently commercialised ultrasonic micromoulding is discussed and historic development of the technology is also covered. To discuss all aspects of this new process, a short review on theory of ultrasonic waves and wave motion in elastic media, ultrasonic energy transfer and heating of the polymers using ultrasound are presented. In Subsection 2.5.5, a review of the literature present for ultrasonic micromoulding is given and details of a state-of-the-art equipment is also available.

2.5.1 Generation of ultrasonic waves

Ultrasonics is the field of study related to the usage of ultrasound or ultrasonic waves. The term “ultrasonics” refers to the mechanical sound waves having frequencies above the normal sound waves which are usually defined above 20 kHz that corresponds to the human hearing threshold.

Sound wave is a mechanical wave and is formed by the oscillations of particles in elastic media from their equilibrium positions induced by an external impact. Any oscillating force in an elastic medium could induce a mechanical or acoustic wave. However, ultrasonic waves have frequencies above 20 kHz and for generation of these waves high frequency signal generators should be used. For this purpose, the piezoelectric effect is exploited. Piezoelectricity is a phenomenon whereby, the material, when deformed under a force, generates a voltage and was discovered by Curie Brothers (Curie and Curie 1882). The opposite is also possible, where the shape of the crystal changes with applied voltage. Therefore, when an alternating voltage is applied to a piezoelectric material, it will change shape according to the frequency of the voltage, causing vibration or oscillating movement of the transducer in the ultrasonic range. In other words, transducers are devices that convert electrical energy into acoustic energy via mechanical vibrations. The mechanical displacement of the crystal induces mechanical, and hence ultrasonic waves when high frequencies are applied.

Quartz is one of the most widely known piezoelectric materials and there are also other piezoelectric material available e.g. PZT, $BaTiO_3$ and, recently discovered, graphene (Wei et al. 2018). This particular crystal is one of the polymorphs of silica and is composed of silicon and oxygen atoms with the chemical formula of SiO_2. The origins of the piezoelectric effect in quartz are the disruption in the symmetry of charges within the crystal structure. Under mechanical compression or electrical field, the positions of the negative and positive ions are altered resulting in charge distribution changes. External electric field induces strain and displacement within the crystal whereas mechanical force generates electrical fields or voltages. A schematic representation of charges in a quartz crystal is depicted in Figure 2-5.

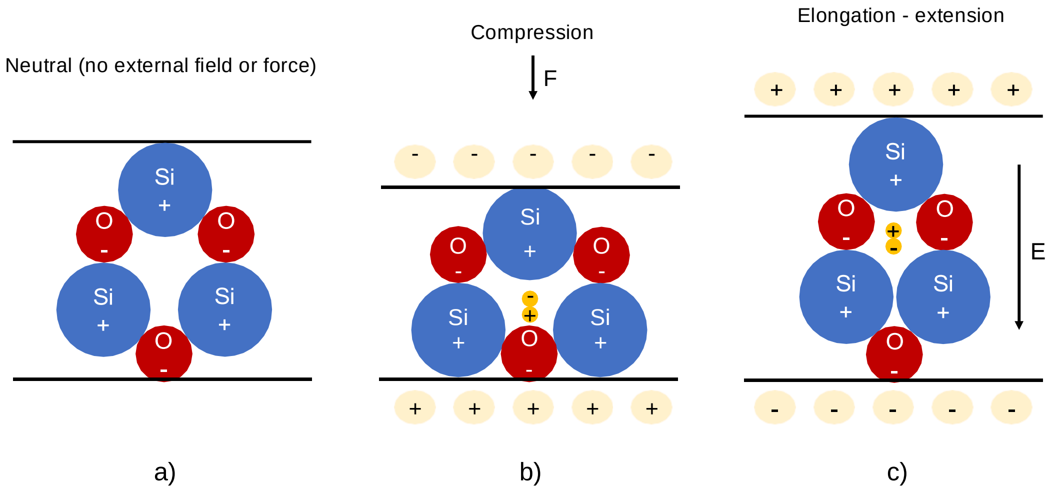

Figure 2-5. Schematic representation of charges in a quartz crystal. a) Charge neutrality in the lattice under no external electrical field or force, b) Charge distribution changes due to compression with force, F, c) Elongation in the lattice due to change in charge distribution under electric field, E. Centres of gravity change for positive and negative ions under external force or electrical field.

For generating ultrasonic waves transducers are used. An ultrasonic transducer usually consists of a piezoelectric crystal, metal contacts and housing. Application of high frequency (e.g. ⩾ 20 kHz) electric field induces extremely fast mechanical displacements in the crystal. The resultant ultrasonic wave can be adjusted to certain amplitudes and frequencies by modifying the electrical signals and the ultrasonic stack as will be discussed in Subsection 2.5.3.

2.5.2 Main characteristics of ultrasonic waves

In order to understand how the ultrasonic waves interact with polymers, the wave motion and characteristics must be understood. In theory, all the waves follow certain physical rules as they are travelling or propagating through a medium e.g. electromagnetic waves or mechanical waves travelling through air. For longitudinal waves, these are periodic motions that repeat along a propagation direction, e.g. oscillations of particles along a direction in an elastic matter.

Ultrasonic waves have sinusoidal vibratory motions. Like all other wave types, ultrasonic wave can be characterised by their wavelength or frequency, amplitude, and velocity. They have been classified as a mechanical wave as they oscillate the particles within a media and transfer energy. A sinusoidal transverse wave its main properties are depicted in Figure 2-6.

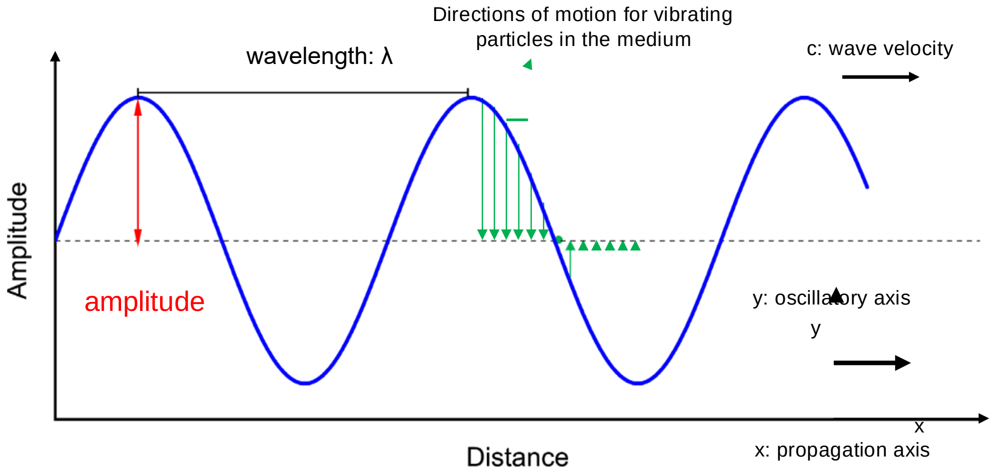

Figure 2-6. Example of a typical sinusoidal wave. Ultrasonic waves generally follow the similar sinusoidal behaviour.

As depicted in the Figure 2-6, the amplitude defines the energetic strength of any wave and shows the displacements of individual particles as the wave is passing through the medium. The distance between the two maxima points of a wave is the wavelength ($\lambda\lambda$). The frequency of an ultrasonic wave is defined as the number of waves that pass within unit time, namely one second. The unit for frequency is Hertz (Hz) and 1 Hz corresponds to one pass of a wave in 1 second. The relationship between frequency (VV) and wavelength of a wave is given by the wave velocity (cc):

$$cc = \lambda\lambda \cdot VV \tag{2.1}$$

It should be noted that cc will change for different materials since the bonding within atoms and intermolecular forces will be altered. The implication of this is to have different elastic constants in different media that would affect the propagation velocity of the ultrasonic wave. A variety of polymers with different molecular structure and arrangements result in different elastic constants and mechanical behaviours so that the propagation of the ultrasonic wave will be changed. For that, velocity of an ultrasonic wave within an isotropic medium where all the material properties are the same for different lattice directions has to be discussed as follows.

Ultrasonic waves-material interactions can be better understood if an elastic-isotropic medium is considered. During the propagation of an ultrasonic wave, there will be stresses acting on each atom and the velocity of propagation can be derived from stress and strain relationships.

The stress - strain relationships in elastic materials are governed by the elastic constants of Young's modulus (EE) which is a measure of rigidity, bulk modulus - a volumetric fractional change due to hydrostatic pressure and shear modulus - a ratio of shear stress and shear strain are by:

$$EE = \frac{\sigma\sigma}{\varepsilon\varepsilon} \tag{2.2}$$

Where: $EE =$ Modulus of elasticity (Young's Modulus) [N/m^2]
$\sigma\sigma =$ uniaxial stress or force per unit area [N/m^2]
$\varepsilon\varepsilon =$ strain, induced by the uniaxial stress, dimensionless

Elastic modulus of a material is determined by a variety of different factors such as intermolecular forces, crystal structure, and the thermal history of the material. Polymers are of interest in this work and it can be commented that these factors change drastically from one polymer to another, and it is expected that the transmittance of ultrasonic energy to the polymer for USM process will be different and depend on many different process and feedstock related factors such as initial shape of the material and amount of interfaces.

The energy of a sound wave exerted on a medium is associated with the kinetic energy of the particles which are subject to these disturbances caused by the ultrasonic wave. The energy and power transmitted by a sound wave can be derived using a sinusoidal displacement and integration of the pressure component associated with this sinusoidal displacement. Energy density of sound ($\epsilon\epsilon$) for a unit volume is defined as following (Gooberman 1968):

$$\epsilon\epsilon = \frac{\pi\pi \cdot \omega\omega \cdot \sigma\sigma \cdot cc \cdot \varepsilon\varepsilon^2}{xx} \tag{2.3}$$

Where: $\omega\omega =$ angular frequency of the sinusoidal wave [rad/s]

$cc =$ associated speed of the wave [m/s]

x = length, distance in x direction [m]

Equation 2.15 can also be expressed in power units by the energy intensity I - the amount of energy transmitted in one second through unit area:

$$I = E \cdot c = \frac{\pi \cdot \omega \cdot \sigma \cdot c^2 \cdot \varepsilon^2}{x} \tag{2.4}$$

As can be seen from equation 2.3 and 2.4, the energy of an acoustic wave is proportional to its frequency, strain, and amplitude factors. Amplitude can be an important parameter to consider for ultrasonic plasticising of polymers, as it has square dependence on the energy exerted per unit time. Additionally, frequency also has a linear relationship with energy intensity, where sonication frequency during ultrasonic melting of a polymer could be of interest for ultrasonic micromoulding.

This subsection has described the general characteristics of ultrasonic waves including their interaction with elastic mediums. Mathematical terms for sound wave velocities and energy relations of ultrasonic waves have been summarised. The information and theoretical background in the following subsections will be built upon the insight given here.

2.5.3 Ultrasonic energy transfer in polymers

Ultrasonic micromoulding technology uses sonication energy to plasticise the polymer, therefore origins of heat generation and energy transfer in polymers by ultrasonic waves is crucial for understanding the process. There has been both experimental and numerical attempts to study the viscoelastic heating of polymers in the literature and in this subsection, a general overview of heat generation mechanisms for polymers will be given and examples from literature will be discussed.

When an ultrasonic wave travels through a medium, e.g. polymers, the energy associated with its amplitude or intensity will be dissipated as heat energy due to absorption within the internal structure. This absorption process in polymers is directly related to the viscoelastic behaviour of the polymer where the material shows different stress-strain response due to its internal structure. Viscoelasticity mainly defined as the material’s elastic and viscous behaviour occurring simultaneously in general terms and its strain rate dependant mechanical properties. The amount of heat dissipated is directly related to the molecular arrangement of the polymer at that particular state. These states could be glassy, viscous, and rubbery and in each of these states the dominant intermolecular forces are different and heat generation upon sonication changes accordingly.

Ultrasonic energy is directed into polymers for plasticising the material either locally or volumetrically by a set of different piezoelectric components named an ultrasonic stack. For plasticising of polymers using sonication energy, an ultrasonic stack that consists of a transducer, booster and sonotrode is used. As previously discussed in 2.5.1, the transducer is the device which converts the alternating electrical signals to mechanical displacement where it is connected to an external signal generator source. The transducer is inside a metal housing and connectors and this component is called a converter as a whole. For modifying the amplitude of the displacement signal that is generated by the transducer, a booster is used. Finally, a horn or sonotrode is attached to the booster which makes actual contact with the polymer to be plasticised. The resonant frequency of an ultrasonic transducer is defined in the manufacturing stage and is typically 10 - 100 kHz for ultrasonic welding, riveting and moulding applications. Tuning is done in the ultrasonic stack design stage where the booster and horn lengths are set and applied voltage and current drawn by the transducer set in phase. Horn or sonotrode lengths are determined by the speed of sound and resonant frequency of the transducer. Also, the speed of sound for the booster and sonotrode should be considered in the tuning stage of an ultrasonic stack. A schematic of an ultrasonic stack is given in Figure 2-7.

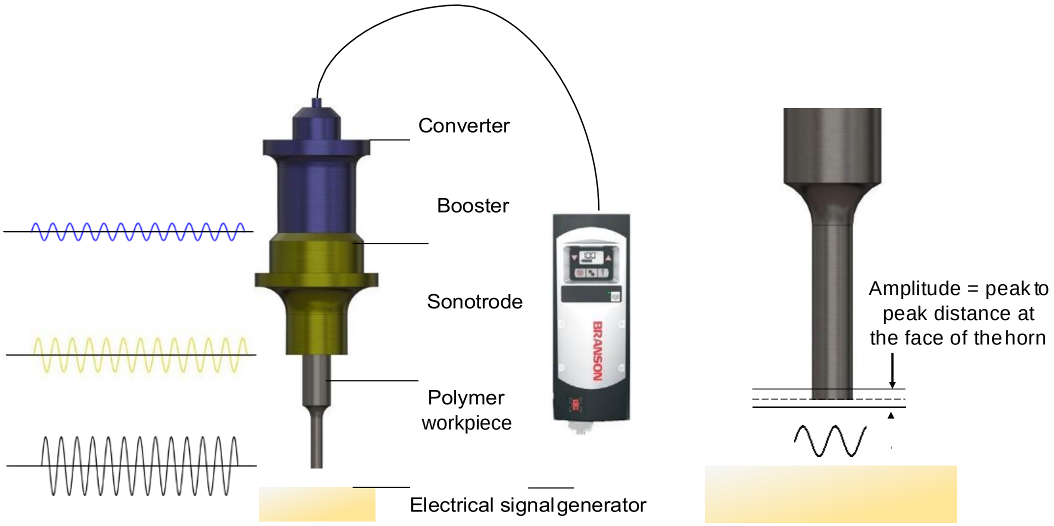

Figure 2-7. a) Schematic representation of ultrasonic stack, b) Ultrasonic amplitude depiction that corresponds to the peak to peak distance of the horn during sonication.

After application of sonication onto polymer, ultra-fast displacements or strains on the surface induce stress in the material. The absorption of this sonication energy is facilitated by the two mechanisms that have been reported for heat generation during plasticising of the polymer (Tolunay et al. 1983). The first one is interfacial friction which involves rapid heating of the polymer by its surface asperities that are in contact with interfaces such as other granules, mould walls or the sonotrode itself. The second heating mechanism for plasticising is volumetric or more commonly, viscoelastic heating which is due to the damping of ultrasonic vibrations within the polymer chains. Viscoelastic heating is more of an internal heating mechanism and it is directly related to the intermolecular bonds, flow properties and loss modulus of the material. This mechanism is directly in conjunction with the polymer's mechanical properties under oscillatory induced strains and reported as the main heating and energy transfer during an ultrasonic plasticising process (Tolunay et al. 1983).

For better understanding of viscoelastic heating behaviour, dynamic-mechanical behaviour of polymers has to be analysed. This summary will provide descriptions for complex or dynamic modulus which consists of real and imaginary parts and explains the elastic and viscoelastic behaviours, respectively.

An ultrasonically applied strain which is associated with the amplitude of the sonotrode can be written in a sinusoidal form as:

$$\varepsilon\varepsilon = \varepsilon\varepsilon_0 \sin\,(\omega\omega tt) \qquad (2.5)$$

Where: $\varepsilon\varepsilon_0$ = amplitude of the applied sonication or strain induced.

Angular frequency can also be written as:

$$\omega\omega = 2\pi\pi ff \qquad (2.6)$$

The sinusoidal strain will also induce a stress with a phase delay ($\delta\delta$) on the material which can be generalised in sinusoidal form:

$$\sigma\sigma = \sigma\sigma_0 \sin\,(\omega\omega tt + \delta\delta) \qquad (2.7)$$

Where: $\sigma\sigma_0$ = amplitude of the stress induced by the strain.

$\delta\delta$ is the phase difference or lag between $\varepsilon\varepsilon_0$ and $\sigma\sigma_0$ which are in sinusoidal forms. For ideal elastic materials, the stress response follows the shape of the strain function without any lag and the phase difference becomes $\delta\delta = 0$ which indicates that they are in phase. That implies that the material follows the applied strain by the stresses induced on itself. Also when $\delta\delta$ is zero or close to zero, it means that the material can deform and recover to its initial position without permanent deformation. In other words, the material follows a spring-like behaviour. However, in the case of $\delta\delta = \pi\pi/2$, stress and strain functions are completely out of phase and the material behaves equal to an ideal viscous liquid. Viscoelastic materials have a phase difference between applied strain function (Eq. 2.5) and stress response (Eq. 2.7) in the range of $0 - \frac{\pi\pi}{2}$ and they show elastic and viscous behaviour in depending on different molecular arrangements and phases. Viscoelastic materials' flow or stress response is also affected by the frequency of the load, temperature and strain rate. This also has implications that for the same sonication source, behaviour of different viscoelastic materials, namely polymers, could be significantly distinct in terms of their heat dissipation and flow properties. An example for applied strain and stress response of an ideal viscous fluid with a phase difference of $\frac{\pi\pi}{2}$ is given in Figure 2-8.

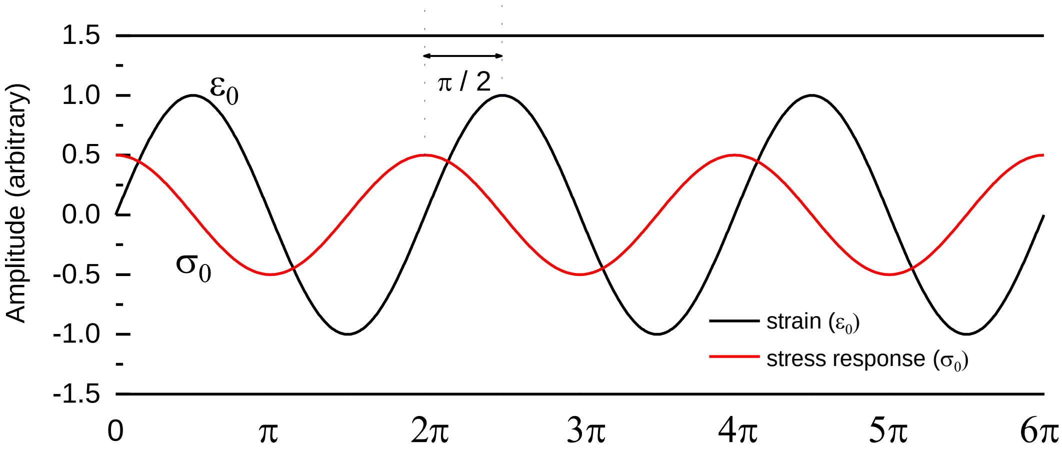

Figure 2-8. Graphical depiction of a strain function (black curve) and stress response (red curve). A phase difference of $\frac{\pi}{2}$ is present between stress and strain ($\sigma_0 = 0.5\varepsilon_0$).

A better way of interpreting sinusoidal waves is to write them in complex forms, hence the strain function in Eq. 2.5 becomes:

$$\varepsilon^* = \varepsilon_0 \exp(i\omega t) \text{ where } i = \sqrt{-1} \tag{2.8}$$

Likewise, the stress response with phase difference or lag in Eq. 2.7 can be written as:

$$\sigma^* = \sigma_0 \exp[i(\omega t + \delta)] \tag{2.9}$$

From Hooke's law in Eq. 2.2, the complex modulus can be deduced as following:

$$E^* = \frac{\sigma^*}{\varepsilon^*} = \frac{\sigma_0}{\varepsilon_0} \exp(i\delta) \tag{2.10}$$

Using Euler's formula, the term can be expanded into:

$$E^* = \left(\frac{\sigma_0}{\varepsilon_0}\right) \cos\delta + i \left(\frac{\sigma_0}{\varepsilon_0}\right) \sin\delta \tag{2.11}$$

The first term on the right side of the equation is called the storage modulus of the material given as:

$$E' = \left(\frac{\sigma_0}{\varepsilon_0}\right) \cos\delta \tag{2.12}$$

The loss modulus is the second term of the right-hand side of Eq. 2.11 given as following:

$$E'' = \left(\frac{\sigma_0}{\varepsilon_0}\right)\sin\delta \tag{2.13}$$

Hence, the dynamic or complex modulus can be generalised:

$$E^* = E' + E'' \tag{2.14}$$

The complex modulus characterises the mechanical behaviour of the material under vibratory or cyclic mechanical stresses. E' is associated with the elastic behaviour of the material whereas E'' represents the viscoelastic characteristics and heat dissipation. E^* can be determined empirically by using dynamical mechanical analysis (DMA) methods. E' is also called the storage modulus since it represents the materials capability to store energy in elastic manner. E'' termed as the loss modulus as it is associated with the heat dissipation and damping properties.

The ratio of E'' and E' is a measure of energy dissipation of the material under cyclic load (also called damping), given as following:

$$\frac{E''}{E'} = \frac{\sin\delta}{\cos\delta} = \tan\delta \tag{2.15}$$

The complex modulus reveals that, if a stress is applied on a polymer, some fraction of this load will be dissipated as heat and some part will be stored within the material. The material recovers from the deformation and releases the energy by returning to its initial shape, which corresponds to the elastic behaviour. Any heat released or dissipated will be dependent on the $\tan\delta$ term. Since this subsection involves the ultrasonic energy transfer and melting mechanisms of the polymer using sonication, E'' will be explained in detail.

The ability of the polymer to dissipate heat energy depends on its molecular arrangements. As discussed previously in Subsection 2.2.2, polymers can be in amorphous and semi-crystalline forms and they generally show glassy (or solid for semi-crystalline polymers), rubbery and viscous behaviour as they are heated. For these different states or phases, polymers show uniquely different storage and damping properties.

In the rigid or glassy state, polymers show elastic behaviour and tend to deform and recover from applied cyclic deformations. Semi-crystalline polymers in particular show pronounced elasticity, because of the crystalline regions and their high storage modulus. Semi-crystallinity in such materials results in a sharp T_m and in order to break the bonds within crystalline regions usually highly energetic sonication is needed. In that state, the loss modulus is small and there is no significant heat dissipation.

After surpassing T_m or T_g range for amorphous polymers, the interactions between polymer chains become weaker and the material loses its rigidity. In this phase, polymer becomes semi-rigid and is able to induce frictions within its molecular chains resulting in a high loss modulus and therefore high amount of heat dissipation. This behaviour is called volumetric or viscoelastic heating and is the main mechanism of heating in polymers under sonication. Subsequently, polymer reaches its rubbery state and loses its complete rigidity. Polymer chains no longer exhibit intermolecular frictions resulting in less heat dissipation and low loss modulus.

Some of the early attempts to investigate the heating and bonding mechanisms for polymers during ultrasonic welding include temperature measurements at or near the interface of the welding. Frankel and Wang discussed a model and proposed empirical equations for characterising the increases in temperature and mechanical strength of the joints during ultrasonic welding of Acrylonitrile butadiene styrene (ABS) (Frankel and Wang 1980). The authors witnessed the notable temperature increase near T_g signifying the viscous heating phenomenon. Similar work was done by Tolunay et.al. on studying the heating and bonding mechanisms in ultrasonic welding by attachment of thermocouples at the weld interface (Tolunay et al. 1983).

Viscoelastic heating effect in ultrasonic welding is modelled and verified by experiments in the literature (Zhang et al. 2010). The authors have shown that the simulation results are in accordance with the experimental findings. Their report also indicates the importance of energy directors of different shapes at the interface which results in nonuniform temperature distributions. They also acknowledge the interfacial effects that contribute to the heating.

Jiang and colleagues have carried out work to quantify the heat generation rate by viscoelastic heating for Poly(methyl methacrylate) (PMMA) (Jiang et al. 2016). The viscoelastic heating effect was studied by experimenting with different ultrasonic amplitude and frequencies alongside computational results. The work signifies the high rates of heating as large as 125°C/s in the glass transition regions. Authors use the generalised heat generation rate (QQ) as a function of ultrasonic frequency, amplitude and loss modulus with the equation given below for ultrasonic processes:

$$QQ = VV\pi\pi\varepsilon\varepsilon_0{}^2 EE'' \quad (2.16)$$

Eq. 2.16 is a more refined form of Eq. 2.4 and it can be seen that QQ shows a square dependence on the amplitude of the sonication, hence, during plasticisation this parameter will be decisive on the energy exerted by sonication onto polymer.

Another way of energy transfer and heat generation in polymers during ultrasonic processes is the interfacial friction between the polymer interfaces, sonication chamber and sonotrode area. However, one of the reports suggest that the surface microstructure is also of importance for initiating the ultrasonic welding process and surface asperities act as small energy directors during sonication (Tolunay et al. 1983). Authors also report that temperatures as high as 250°C were measured at the weld interfaces that result from the friction between surfaces due to sonication.

Work has been carried out in literature to quantify and investigate the effect of interfacial heating by sonication on PMMA discs (Wu et al. 2017). The authors modelled an ultrasonic plastication chamber with spherical PMMA pellets under certain assumptions. Their calculations using ANSYS package indicate that interfacial friction is a transient process and a temperature increase of ~100°C was observed in a time period of only ~0.06 s. It has been seen that the interfacial friction occurs until the interfaces of the pellets disappear and some damping from the viscoelastic heating is needed to heat the polymer volumetrically.

In this subsection, ultrasonic energy transfer in polymers has been discussed considering sinusoidal stress - strain relations and complex modulus. Heating mechanisms of polymers using sonication have been introduced and examples from literature have also been given. The subsection can be summarised by emphasising the most significant points as following:

- Viscoelastic heat generation is dependent on the molecular arrangements of the polymer and the polymer’s ability to dissipate heat. One has to analyse the loss modulus of the material to have more insight on damping or heat dissipation of polymers.
- Ultrasonic amplitude is the most effective parameter to introduce more energy into the system for plasticising the polymer. Other significant entities are sonication frequency and loss modulus.
- Interfacial friction plays an important role also by initiating the heating and melting process by means of lateral movements of pellets. Melting phase for ultrasonic moulding process can be assisted by introducing greater interfacial areas.

2.5.4 Ultrasonic micromoulding process

Ultrasonic plasticising of polymers was of interest for decades due to the extensive usage of ultrasonic welding and riveting processes in the industry. Due to the advancements of micro and nanotechnologies starting from late 90’s, ultrasonic melting and moulding of polymer materials was thought to be an alternative for conventional injection moulding and newly developed microinjection moulding machines starting from early 2000’s.

When microsystems applications are considered, plasticising the polymers using screw systems could introduce degradation problems due to residence times. Also, microparts usually form only 1% of the shot, which is injected to the mould cavity, and more than 90% of the polymer will be wasted. Moreover, with the advancement of medical technologies, the degradation of the polymers due to residence times became an even bigger problem for pharma-grade polymers which usually have high cost. Therefore, direct ultrasonic melting and injection opened new paths in order to overcome these problems related to dosing and degradation.

The first attempts on ultrasonic moulding of polymers used commercial ultrasonic welder machines in which the sonotrode plasticises the polymer in powder form and the material is injected via the decrease in viscosity under pressure. Paul and Crawford published the first report on ultrasonic moulding of polymers and moulded tensile bar shaped samples in 1981, however the first application for compacting the polymer powders was reported by Fairbanks in 1974 (Fairbanks 1974; Paul and Crawford 1981). Fairbanks adopted sonication to compact both thermosetting and thermoplastic polymers using a sonication chamber both in vertical and horizontal configurations. In Paul and Crawford’s report, a conventional ultrasonic welder with 20 KHz sonication frequency was used. In the work, mechanical properties of the moulded samples were tested, and morphologies of the fused polypropylene powders were investigated. These are the first reports on ultrasonic moulding of thermoplastic materials and shot sizes of as low as 0.5 g had been achieved.

One of the main advantages of an ultrasonic moulding process would be having shorter residence times than in conventional micromoulding, which could open new paths to process pharma-grade materials with active drugs without degradation. The first and only report on this approach using ultrasonic moulding of tablets was published in 1997 by Kellomäki and Törmälä where bio-absorbable polymers tablets were moulded with furosemide and caffeine (Kellomäki and Törmälä 1997). Authors present that distribution of the drugs have not been very homogenous, however, ultrasonically moulded tables has shown good mechanical properties in punch tests.

Michaeli et. al. introduced the ultrasonic plasticising concept for microinjection moulding processes and have been one of the first research groups to investigate ultrasonic microinjection moulding systematically (Michaeli et al. 2002). The authors main goal was to prove that eliminating the screw-based plasticising was possible using an ultrasound-based melting of the polymer and adjusting the dosage for the micropart to be injected. Benefits of using a dedicated ultrasonic plasticisation unit are that the polymer degradation can be eliminated and decreasing the shot sizes were potentially possible as indicated in the literature by previous authors. The paper introduces a prototype ultrasonic microinjection moulding machine for the first time for microsystems applications in the literature. In the first prototype, the injection of the molten material was achieved by the downward movement of the sonotrode. The authors report that the ultrasonic plasticisation technique made it possible to plasticise materials for typical micro cavities below 1 s.

Further work was carried out by the same group by using polyoxymethylene (POM) for ultrasonic microinjection moulding process (Michaeli and Opfermann 2006). The equipment used was a commercial ultrasonic welder with a plasticising chamber and mould tool attached. The authors reported a processing window for POM using different holding force and ultrasonic amplitude combinations. They also emphasize that the plasticising times can be reduced up to 50% by using higher forces and ultrasonic amplitudes. Michaeli et. al. investigated the ultrasonic moulding process further by implementing data acquisition modules for temperature control and displacement sensing during the ultrasonic moulding process (Michaeli et al. 2011). Work also focuses on the mixing properties of the process reporting that a certain amount of sonication amplitude (49 µm) is required to obtain a homogenous polypropylene melt.

2.5.5 Ultrasonic microinjection moulding state-of-the-art

For commercialisation of the ultrasonic microinjection moulding process, a European Union (EU) funded project named SONOPLAST started in 2007, and the first design of an ultrasonic micro injection moulding machine as a prototype was developed (*Sonoplast project report* 2010). Colavizza et. al summarised the outcomes of the project and main features of ultrasonic moulding technology as following (Colavizza et al. 2010):

- A significant amount of reduction achieved in the sprue size of the micromoulded product at around 50%.
- Plastication of polymers using ultrasound results in reduced energy consumption for the processes as the new technology is not a screw-based system and do not use conventional cartridge heaters. Moreover, shorter cycle times also can benefit from energy savings (Zeng et al. 2014).
- It has been reported that there was no degradation for PP samples according to the dynamical-mechanical thermal analysis.

Based on the results of this work, another EU project called SONO”R”US was launched in late 2000’s for developing a ready-to-market ultrasonic microinjection moulding machine (*SONORUS: New Machine for Microparts Moulding base on Ultrasound Excitation* 2011). Following this activity, a Barcelona based company Ultrasion s.L was founded and Sonorus 1G ultrasonic microinjection moulding machine made available commercially. Recently, Sonorus 1G can be regarded as the state-of-the-art and it is the only commercial ultrasonic injection moulding machine available in the market (*Ultrasion s.L website* 2019).

Sonorus 1G uses a power supply (Branson DCX-S) that is connected to the transducer to provide electrical signals for inducing contracting and expanding movement in the quartz crystal. Electrical signals are converted to mechanical displacements by the transducer and the amplitude of the sonication is tuned by a booster. Finally a stepped sonotrode with a radius of 8 mm applies the sonication onto the polymer feedstock for plastication of the polymer material. The ultrasonic stack has been tuned to 30 kHz by the manufacturer and the operation limit has been set to 29250 – 30250 Hz as a safety measure and to protect the transducer.

Sonorus 1G has an upright configuration and vertical injection axis where the polymer feedstock is melted in the cylindrical sonication chamber located between the 8 mm sonotrode and injection plunger. The movement of the sonotrode and upper mould is facilitated by different motors as well as the injection plunger. The lower half of the mould is attached to the main base plate of the machine where the surface position is used for referencing the positions of the mould halves, sonotrode and injection plunger. Polymer pellets are either fed manually or by the dosing unit which counts the numbers of the pellets using a laser and electromagnet apparatus. A pneumatic ejector system is used for ejecting the parts. The mould heating can be provided according to the demands of the mould design and the need for additional cooling systems. A schematic of the main features of Sonorus 1G is given in Figure 2-9.

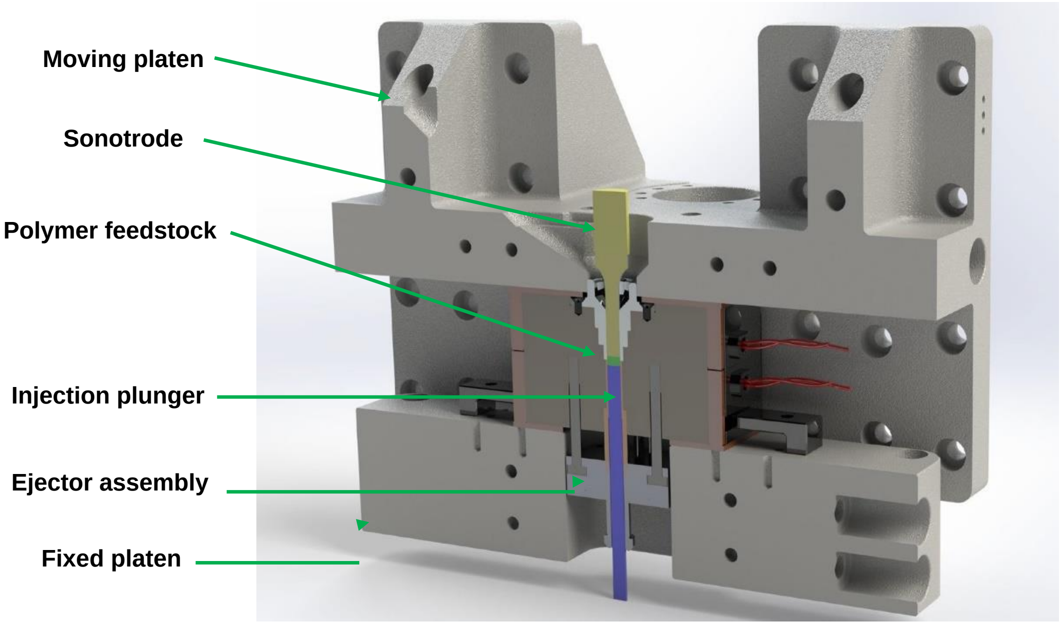

Figure 2-9. Main features of Sonorus 1G ultrasonic micromoulding machine.

As depicted in Figure 2-9, the moving platen holds the upper mould and closes the mould during operation. The sonotrode is attached to another motor and positioned 2 mm above from the zero-point line where the upper and lower moulds meet. The horn vibrates at 30 kHz and remains fixed during the micromoulding. Polymer feedstock is compressed against the vibrating sonotrode via the injection plunger which is depicted in blue. Ejection of the part is facilitated using the ejector assembly, where the ejector pins are located. Fixed platen at the bottom of the machine assembly is the fixed reference for position which the movement of other components is controlled.

Melting and injection phases are carried out simultaneously in ultrasonic micromoulding. The machine lacks the capability of a pressure-controlled switchover and each phase of the micromoulding is controlled by the position of the piston below the zero-point line. Although machine control allows changing the plunger velocity, there are compaction phase and melting initiation phases in which the injection plunger stay fixed and compresses the pellets. In that case, the actual velocity of the plunger is way below then the value which is set in the machine control. Ultrasonic amplitude, plunger force and sonication time are parameters that can be changed and tuned accordingly. It is important to note that different cavity volumes require significantly different parameters. For instance, gate design is very important for ultrasonic moulding where sharp edges and corners must be avoided in order not to hinder the flow of the material. Smaller and narrow gate and runners result in difficulties in ultrasonic micromoulding.

The process takes place in following steps:

- Feeding of the material – typically, a few hundreds of milligrams inside the sonication chamber, between the sonotrode and injection plunger:
- Compression of the feedstock against vibrating sonotrode to initiate melting:
- Conveying and compression of molten polymer towards the mould cavity happens simultaneously as the material near the sonotrode plasticised early on:
- After the mould cavity is filled, sonication is sustained and packing of the molten polymer takes place. Sonication at this stage generally results in higher temperatures towards the main micromoulding cavity and aids better replication within the regions of interest. The process steps are depicted schematically in Figure 2-10.

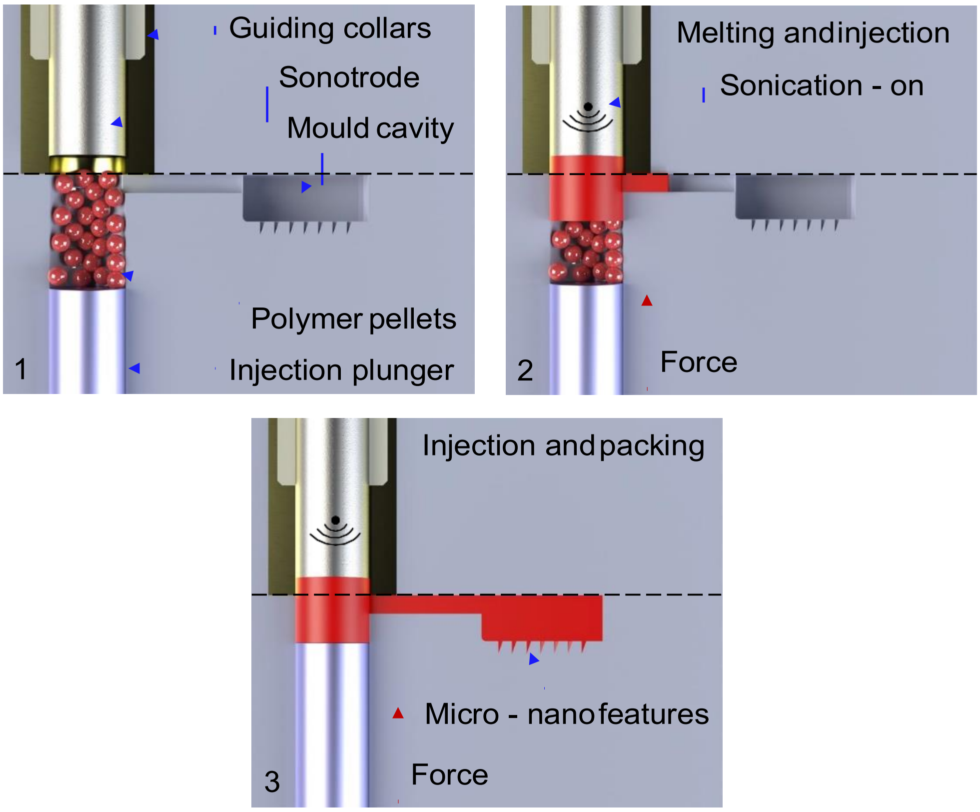

Figure 2-10. Ultrasonic micromoulding process details. 1) polymer pellets are placed inside the sonication chamber, above the injection plunger, 2) Sonication is on and polymer pellets are being compressed against the vibrating sonotrode, 3) Micromoulding cavity is completely filled. Sonication and plunger force are sustained for better packing.

It is important to note that the sonotrode stays at a fixed position during compression, melting and filling phases. Depending on the injection forces applied by the plunger, this position could change due to the stretching of the elastic belt which the sonotrode unit is connected. Another important feature is the guiding collars which are made out of brass and PEEK. Inner PEEK collar holds the sonotrode with sufficient tightness in order to maintain its centre position. There is a very tight tolerance of 50 μm for the outer brass collar which guides the sonotrode to its vibration position.

2.5.6 Ultrasonic microinjection moulding parameters

For producing complete and high-quality micromoulded parts with ultrasonic moulding, the process parameters need to be carefully selected. The process parameters to be used for ultrasonic micromoulding also change significantly depending on the molecular structure of the polymer and also the size of the mould cavity. As discussed in Subsection 2.5.3, amorphous and semi-crystalline polymers transmit and interact with ultrasonic waves differently and this results in a variety of ultrasonic amplitudes and sonication times in practice. Glassy structure of amorphous materials allows them to be melted over a wide range of ultrasonic amplitudes whereas the sharp melting points of semi-crystalline materials usually require higher amplitudes. Various parameters can be modified accordingly for different materials and feedstock shapes from the control screen of Sonorus 1G (Figure 2-11).

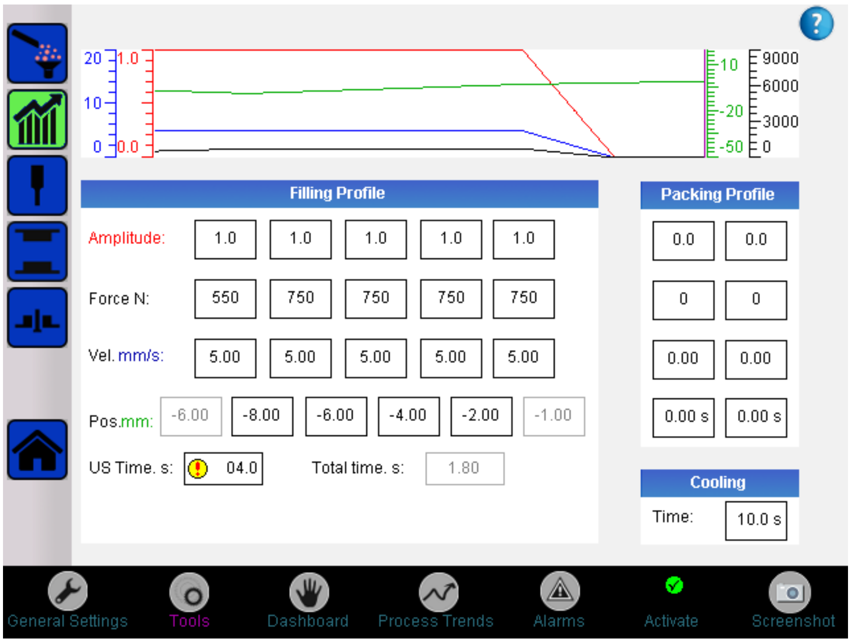

Filling Profile

Amplitude:		1.0	1.0	1.0	1.0	1.0
Force N:		550	750	750	750	750
Vel. mm/s:		5.00	5.00	5.00	5.00	5.00
Pos.mm:	-6.00	-8.00	-6.00	-4.00	-2.00	-1.00

US Time. s: 04.0
Total time. s: 1.80

Packing Profile

0.0	0.0
0	0
0.00	0.00
0.00 s	0.00 s

Cooling

Time: 10.0 s

Figure 2-11. The control screen of Sonorus 1G for process parameters.

Machine control also allows application of packing forces without sonication to compensate shrinkage effects. Although the process is divided into two different stages of packing and filling profiles, for most of the materials it is possible to get full parts without additional packing as the sustaining the sonication after the part is filled also acts as a packing phase.

When optimising an ultrasonic micromoulding process, the total energy input that will be given to the feedstock to be plasticised should be considered. The most important parameters that are decisive on melting of the feedstock properly are the sonication time (t_{sonic}) and ultrasonic amplitude. t_{sonic} should not either be prolonged or very short, as force acts from the injection plunger constantly during sonication and this causes the sonication frequency to change. The ultrasonic stack used for the machine has a resonant frequency of 30 kHz. As a safety measure it has been designed so that it operates between 29.25 – 30.75 kHz in order not to overload the transducer. Any fluctuation in the frequency outside this range causes the machine to stop immediately.

Sonication amplitude is more of a material specific parameter and it is not changed throughout the process once set. Longer sonication times allow constant energy input for melting the material as the molten material already conveyed by plunger which will result in a continuous flow towards the cavity. It should also be noted that prolonged sonication of the feedstock is not always possible, as the applied force results in excessive damping and a change in the resonant frequency of the ultrasonic stack leading to overload of the transducer. Because of overload, the machine ceases its operation instantly and the moulding cycle is stopped. This results in variability in the product quality and difficulties in assessment of the process characteristics.

Another important parameter is the plunger force or injection force (F_i), which is applied to compress the polymer feedstock against the vibrating sonotrode and provide conveyance of the molten material towards the runner. Using excessively high forces will result in overloads, as discussed before and lowest forces should be carefully chosen in order not to overload the sonotrode and provide a steady flow for the plasticised material. This careful adjustment of injection force results in much lower flow rates when it is compared with conventional micromoulding.

T_{mould} is very critical for ultrasonic microinjection moulding since the injection pressures and flow rates are considerably lower than microinjection moulding. Higher mould temperatures are always beneficial for the flow of the material, although, thermal expansion effect should also be considered as the resonant frequency of the ultrasonic stack might be changed. Moreover, the upper limit for mould temperatures should be set carefully as some of the polymer heat deflection and glass transition temperatures could be in the region of 100°C. As the flow rates are significantly lower than of conventional micromoulding, slightly higher mould temperatures are used for the same materials in ultrasonic microinjection moulding to overcome premature solidification effects. Mould temperature also affects the cycle time as the moulded part has to be at temperatures lower than its heat deflection point. The typical cycle time of ultrasonic micromoulding process found to be between 20-30 s depending on the mould temperature and material used.

2.6 Summary

This chapter has provided theoretical background on polymer materials, conventional and ultrasonic microinjection moulding techniques and ultrasonic energy transfer which is specific for ultrasonic microinjection moulding. The differences between amorphous and semi-crystalline polymers have been discussed in detail since there will be significant differences in melting and moulding phases in ultrasonic moulding processes in microneedles. A short overview of conventional injection moulding and micromoulding technologies have established the fundamentals for understanding the processing conditions of microneedles. Critical process parameters are also discussed.

For understanding the ultrasonic moulding process better, the generation of ultrasonic waves and ultrasonic heating and energy transfer in polymers have also been covered. Wave motion and fundamental wave properties, alongside with complex modulus and power dissipations are formulated.

Lastly, state-of-the-art machines for both conventional and ultrasonic microinjection moulding technologies have been reported and operating mechanisms and conditions are also explained. The state-of-the-art micromoulding machines of Micropower 15 and Sonorus 1G have been used throughout this project.

CHAPTER 3: Materials, Tooling and Process Monitoring for Micro-injection Moulding Techniques

3.1 Introduction

This chapter provides and covers the tools, equipment and materials used for extensive process monitoring that has been used experimentally for conventional and ultrasonic micromoulding. First, it starts with an introduction to machining technologies for micromoulding tool making and explains the mould tools have been used in this work in detail. Then, it discusses flow visualisation, thermal imaging, and extensive data acquisition methods for both conventional and ultrasonic microinjection moulding techniques.

In this thesis, state-of-the-art of mould manufacturing processes for microinjection mould tools and microneedle cavities have been covered particularly by presenting attempts made throughout the project. Mould tool designs for conventional and ultrasonic micromoulding will be explained in detail.

Data acquisition is one of the most important tools for real-time monitoring of micromoulding processes and state-of-the-art sensors and programmable interfaces used in the work are described here. Specifications and properties of both built-in machine sensors and external devices have been summarised. The methods used for data acquisition in this chapter provide the foundations of the fingerprint concept that will be introduced in Chapter 4 and used extensively in later chapters.

At the end of the chapter, physical properties of the materials used for micromoulding experiments have been included and material selection reasons are discussed. This chapter provides all the theoretical and practical background for state-of-the-art process monitoring technologies used for conventional and ultrasonic microinjection moulding processes.

3.2 Microinjection moulding tools

Tooling for micromoulding applications is an important aspect of the technology as they can cost significant amounts which is sometimes comparable with the cost of the moulding machine itself. Despite the high price, mould tools are usually one-time investments for particular products and their lifetime is on the order of tens of thousands of cycles. With the advancements in machining technologies, the tooling costs will go down and extremely small features within the moulds can be easily manufactured.

In micromoulding, a mould cavity with extremely small features is often machined onto an interchangeable die plate or mould insert for modularity. This helps to keep the tooling costs low as rather than building new moulds and ejector assemblies manufactured for each product, only mould inserts are machined so that different products could use the same mould configuration as much as the design allows. The micromoulding tools can be manufactured from a variety of materials, most commonly, stainless steels with sufficient wear resistance (Romano et al. 2019). For instance, Stavax® ESR is a commercial stainless tool steel with wear resistance combined with good machinability and it has been used for manufacturing microneedle mould inserts. For certain areas of application such as freeform optics and high quality lens manufacture, nickel silver (German silver) is another common material with excellent machinability used in diamond cutting and turning methods (Holthusen et al. 2017).

3.3 Tool manufacturing techniques for microneedle cavities

A number of high-tech mould manufacturing techniques has been utilised for the purpose of having high-quality microneedle cavities. The manufacturing trials of the mould inserts was carried out at different institutes from UK and Europe (University of Birmingham and KU Leuven). This subsection summarises the theory behind these micromanufacturing techniques and gives a short summary on the samples manufactured and attempts made for microneedle mould inserts.

Heckele et. Al summarised the tool manufacturing techniques for micromoulding in the early 2000’s and significant improvements in machining technologies have been achieved since then (Heckele and Schomburg 2004). In the following, a summary of the most advanced mould machining techniques such as micro-electrical discharge machining, laser machining, micro milling and diamond cutting has been provided. Each technology has been explained with their capabilities for producing micro-nano mould features and some experimental attempts also have been given.

3.3.1 Micro-electrical discharge machining

The micro-electrical discharge machining (μEDM) process is the scaled down version of conventional EDM for manufacturing of micro-scaled features by means of eroding the material using electrical discharges between the workpiece and the electrode or tool within a dielectric liquid. The technology is contactless, and it has been carried out using a high temperature plasma formed between the workpiece and tool. The plasma channel is formed by the electrical pulses first and each pulse melts and evaporates a small amount of material from the workpiece. With each pulse, contaminants within the dielectric fluid are attracted and concentrated with the electric field. When the voltage increased, these microscopic particles ionise and form a high temperature plasma resulting in melting and evaporation of the material from the surface of the workpiece. As a result, a small crater is formed, and machining process is carried out accordingly. There are different approaches and tool shapes for carrying out μEDM for a variety of purposes as given following:

- μEDM milling: a tubular electrode with diameter down to 10 μm is achieved using dressing methods and three-dimensional (3D) cavities can be machined with computer aided machining software.
- μ-wire EDM: a technique which uses a continuous wire fed as an electrode for precision cutting of workpieces.
- μEDM drilling: similar to milling process a tubular electrode is used for machining blind or through holes on workpieces.
- Die-sinking μEDM: A method that uses a patterned die as an electrode to create its negative shape on the workpiece.

μEDM is capable of machining 3D high-aspect ratio cavities, e.g microneedle cavities, although the sharpness of the conical or pyramidal shapes are limited by the shape of the tool. The tool or the electrode is dressed for machining of microneedle cavities until the diameter of the tool reduced down to on the order of 10 μm. The dressing process is itself a challenge since working with such small diameters usually result in breakages of the electrode tips. Moreover, microneedle mould inserts usually consist of arrays of needle cavities, typically 25 to 100, where for each cavity the tool needs to be dressed again and machine the desired cavity. Because of these reasons, the costs of µEDM machined microneedle mould inserts are very high and need a lot of care and effort needs to put into the machining work.

To evaluate the microneedle mould making capabilities of µEDM, a secondment work has been carried out at Katholieke Universiteit Leuven (KU Leuven) – Department of Mechanical Engineering. A state-of-the-art SARIX® SX-100 µEDM machine was used for attempting to machine conical shapes on the sides of stainless mould steel (Uddeholdm - Stavax® ESR) surfaces for laminated moulds for microneedle geometries. The details of laminated microneedle mould tools can be found in the work Nair carried out (Nair 2014). Laminated approach requires the milling of a flat laminate from the sides and these laminates with arrays of microneedles stacked together for forming a microneedle cavity. Conical needle shapes of 500 µm in base and 700 µm in height have been machined on flat Stavax® surfaces. The resulting grooves were inspected using a Sensofar® S lynx microscope in confocal mode with 10x objective lens. An image of the conical shape machined and a schematic showing the laminated approach can be seen in Figure 3-1.

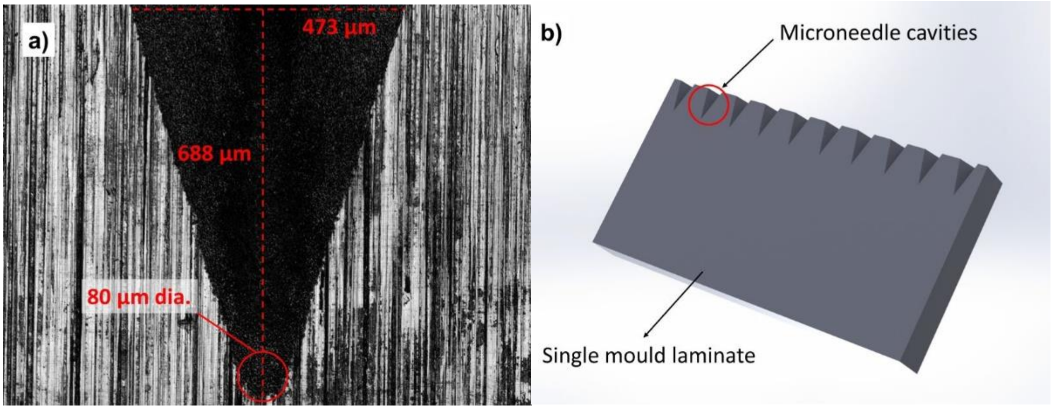

Figure 3-1. a) µEDM machined conical microneedle shape on Stavax® laminate. Base width, height and tip diameter of the shape are indicated. The depth of the cavity along the reading axis is measured to be ~40 µm, b) Computer generated image of a laminate structure and microneedle cavities to be machined from the side.

The confocal microscope measurements showed a tip radius of 40 µm was achieved on the stainless-steel surface which is not ideal for microneedles since radii below 20 µm is favoured for better penetration of the microneedles. The dressed electrode tip had a radius of approximately 40 µm and it manifested itself in the smallest achieved tip radius according to the inspections carried out. The characteristic surface roughness induced by the spark erosion process was also evident and has been seen on the sides of the cavity. With this result in hand, other avenues for obtaining better microneedle cavities were considered during the project as will be discussed in later sections.

Amongst the micro-mould manufacturing techniques, µEDM offers good microneedle cavity quality however the sharp features of the microneedles will be limited by the tool or electrode diameter. Machining of multiple cavities with additional dressing steps make it difficult to automate and laborious for machining microneedle features. Yet, with specialised operators and expertise in dressing of the electrodes, the technique could become an a major complementary micromanufacturing technology for micromoulding.

3.3.2 Laser machining (milling)

Within advanced mould machining methods, laser machining has become a prominent technique due to its applicability for creating micro and nano sized large-area functional surfaces. The applications of these laser machined metallic surfaces and their negative replicas include optical surfaces, anti-microbial and self-cleaning surfaces (Baruffi et al. 2019; Romano et al. 2019). The technique includes a laser source with a set of intricate opto-mechanical components for high precision machining and patterning of micro-nano features and larger scale milling of engineering materials for a variety of purposes. 3D computer aided design/manufacturing (CAD - CAM) software create the required paths or layer by layer machining routes for the laser to carry out the machining process.

Ablation of metal surfaces using lasers takes place when the laser pulses are focussed onto the workpiece and absorbed by the surface. As a result of absorption, a number of different thermal phenomena occur such as softening, melting, plasma formation and evaporation. Pulse duration is decisive on the laser power or energy for ablating the material, as the lower power pulses result in only local heating of the workpiece. The laser machining process is characterised by 5 different steps: heating, surface melting, surface vaporisation, plasma formation, ablation (Chryssolouris et al. 2015).

Optimisation and selection of the correct laser ablation process of micromoulding inserts are crucial in order to achieve high-quality micro-nano surface features. Scholz et al. discusses the importance of pulse duration by using µs, ns and ps lasers for structuring for bio-mimetic surfaces on mould inserts (Scholz et al. 2012). They report superior machining quality of microstructures when using ps lasers over µs at the expense of longer machining durations up to 60 times. It also has been pointed out that there is a compromise between the pulse duration and the quality of the machined intricate microstructures.

Dimov et al studied the tool making capabilities of laser machining for biomimetics and microneedle cavities (Dimov et al. 2011). They report solid-microneedle cavities machined using ns and ps laser ablation and cavities and polymer replicas were manufactured as deep as 1000 µm with 600 µm base. One significant outcome of their work was the limitation of laser machining that the beam shape was decisive on the final microneedle cavity shape. They attempted to machine core pin structures within the needle cavities, however, due to the beam shape and shadowing effect it was not possible to obtain straight side walls for such pins for hollow microneedle structures. Steglich et al. focused on the characterisation of the microneedles manufactured using a focus variation microscope (Steglich et al. 2012). Their report presents that the 3D generated images from the optical measurements of microneedles has significantly rough side walls for microneedles were present that time.

Nowadays, femtosecond (fs) lasers provide ultrashort pulses for machining of extremely small features by creating very small heat affected zones and thus removal of the material. That allows formation of smoother and sharper edges as compared with ns and ps lasers. Our joint work with Advanced Manufacturing Technology Centre - University of Birmingham present the patterning mould inserts by a state-of-the-art laser machining equipment (Lasea) with a wide range of micro-nano surface structures and eventual replication of the mould inserts in Centre for Polymer Micro-Nano Technology at University of Bradford (Romano et al. 2019). In the article, arrays of holes (~200 nm in diameter), laser induced periodic surface structures (~900 nm pitch length) and micro-grids were manufactured on mould inserts. Then, the mould inserts were installed on the micromoulding machines for manufacturing polymer replicas that have hydrophobic properties.

The same equipment with fs laser with 310 fs pulse duration and 1032 nm wavelength was employed for microneedle cavity fabrication on mould surfaces in a secondment work during the project in October 2018 at University of Birmingham. Solid microneedles cavities with ~930 μm in depth and ~630 μm in base diameter were machined on Stavax$^{\circledR}$ ESR mould inserts employing a layer-based machining method. A photograph of the mould insert (a) and SEM image (b) can be seen from Figure 3-2.

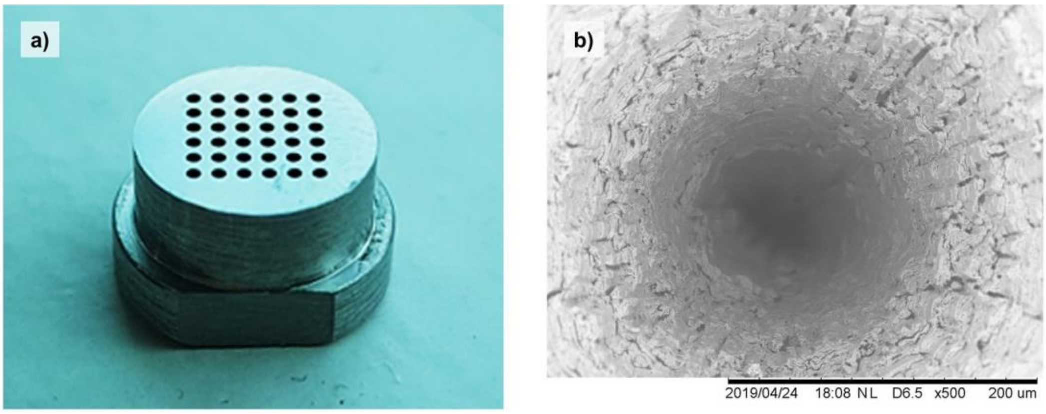

Figure 3-2. a) Laser machined mould insert, b) an SEM image showing the machining marks on the walls of a microneedle cavity.

The SEM image in Figure 3-2b show the laser machining marks clearly. No severe cracking effects have been seen on the walls and the features seemed to be consistent for all 36 microneedle cavities. Moreover, machining marks on the walls are quite periodic and no severe thermal cracking problems are seen on the mould walls after the machining process.

The mould insert accommodates 36 microneedles in 6x6 configuration with 1 mm pitch distance. For assessing the dimensions of the insert, a PDMS replica method was used. The PDMS resin and hardener was mixed at 10:1 ratio and viscous mixture was poured on the insert using an additional brass collar for preventing the flow of the resin to the sides. The curing process was done inside a desiccator to remove any air bubbles forming and left for curing at room temperature. Figure 3-3 shows an image taken with a low-vacuum scanning electron microscope (SEM, Hitachi - TM3030) of the

PDMS replica obtained from the laser machined microneedle insert. The SEM images taken from the PDMS microneedles are shown in Figure 3-3.

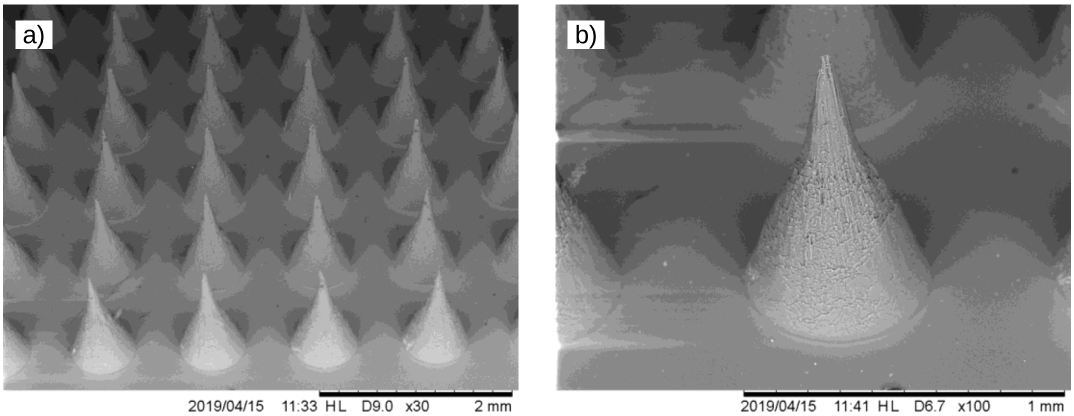

Figure 3-3. SEM images of the PDMS replica of the laser machined mould insert. Images were taken at a 45° over the array of microneedles (a), and a single microneedle (b).

Of the processes that having potential of machining high-aspect ratio microneedle cavities, fs laser machining showed excellent capability in producing cavities as deep as ~1000 μm with tip radii changing between 3 - 10 microns, which the latter being important for penetration of the microneedles to the skin. The machining times for producing 36 microneedle cavities were as low as ~40 minutes which is way lower than producing it in a laminated structure with μEDM technique. Therefore, with recent advancements in optomechanical components and laser technologies, laser machining stands out as a viable method for manufacturing microneedle tooling for high-volume microneedle drug delivery devices.

3.4 Microinjection mould tool assembly for microneedles

As the polymer melt being injected for micromoulding, it first passes through the nozzle and then enters the tool where the temperature is significantly lower. After the part is cooled down it needs to be ejected in order to be collected. A mould tool mainly comprises of a micromoulding cavity on the main die and an ejector assembly for ejecting the moulded part.

Microinjection mould tools for Micropower 15 consist of two main parts, the first one being the fixed half which stays fixed during the process it is the part where the nozzle is located in the middle. The moving half is attached to the clamping unit of Micropower 15. It also accommodates the cavity plate and ejector assembly. The cavity plate has a modular design and different inserts can be used without changing the structure of the mould. The ejector assembly is located at the back side of the moving half where the ejector and push-back pins are attached to a pair for ejector plates. Generally, the moving half also houses the channels or cavities for temperature or pressure sensors. A 3D rendered image of the mould tool and details of the mould assemble can be seen in Figure 3-4.

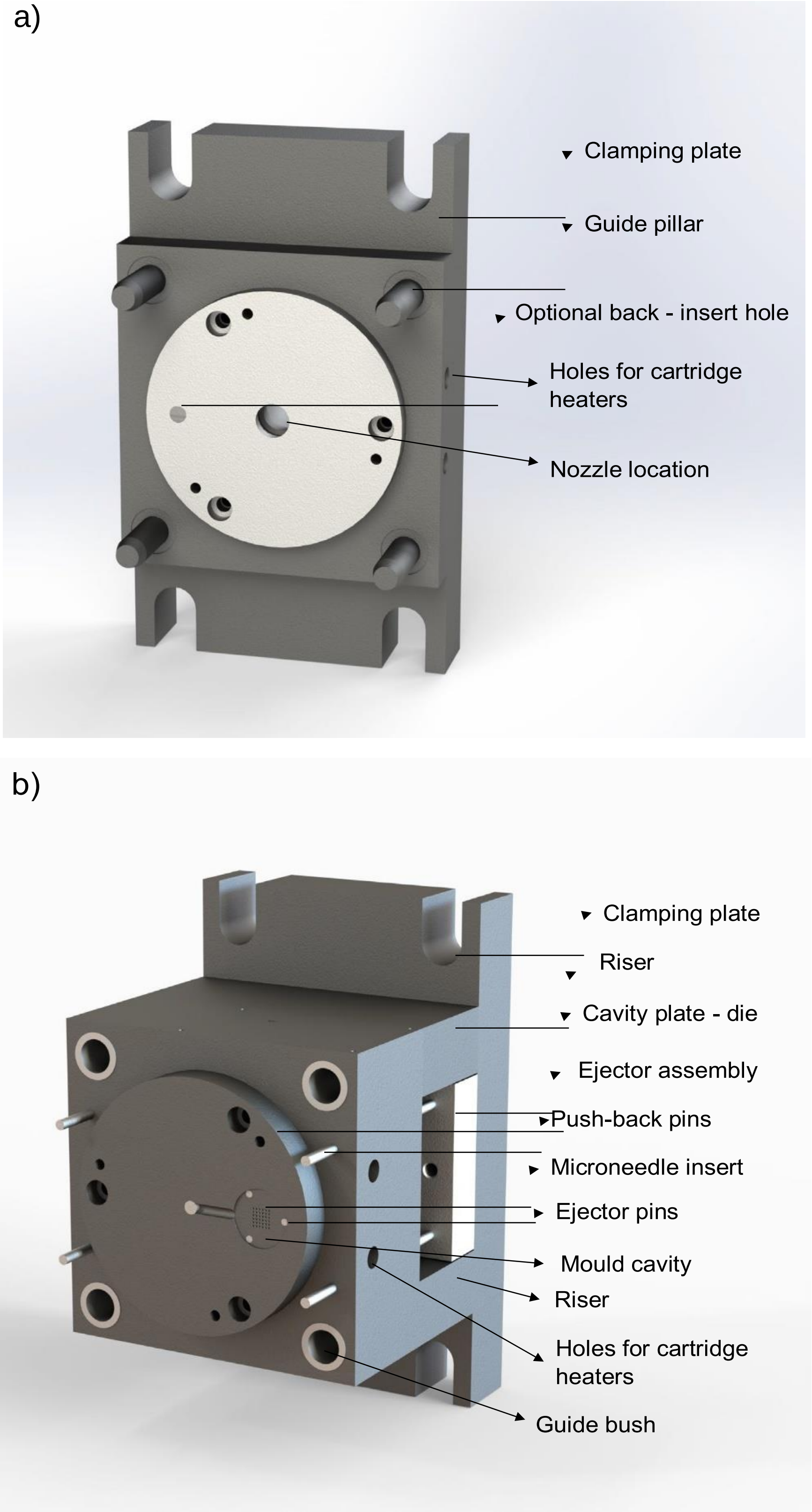

Figure 3-4. The fixed (a) and moving (b) halves of the mould tool used for conventional microinjection moulding experiments.

As can be seen from Figure 3-4b, the circular mould cavity is connected with a semi-spherical straight runner to carry out moulding process. The cavity plate can hold interchangeable mould inserts. Temperature control of the moulds were facilitated by J-type thermocouples and cartridge heaters. Ejection of the part is done by four ejector pins; three on the main mould cavity and one on the sprue called the z-pin. This z-pin has an undercut at its tip which has a function to keep the moulded part onto the moving half while the mould is opening. The heating of the moulds is carried out using a pair of cartridge heaters and a J-type thermocouple.

3.5 Flow visualisation mould tool for ultrasonic micromoulding

The flow of ultrasonically plasticised polymers is significantly different and complex compared with conventional micromoulding. The polymer melt in conventional micromoulding is homogeneously plasticised in the barrel which in turn results in a symmetric and uniform progression of the flow front towards the cavity during injection (Babenko et al. 2018). In contrast, the simultaneous melting and injection phases in ultrasonic micromoulding causes melt progression to be asymmetric and quite complex (Whiteside et al. 2016; Gulcur et al. 2018). Flow visualisation using thermal imaging is a powerful tool to characterise the consistency of the flow front progression and carry out temperature measurements of the polymer melt.

A mould tool that allows the imaging of flow of the ultrasonically processed material is designed and created for process fingerprinting purposes which will use temperature readings from the mould cavity. Thermal imaging of the conventional micromoulding flows have been already characterised in detail by other researchers from the group (Spares et al. 2013; Babenko et al. 2018). Thus, thermal imaging have been exploited only for ultrasonic micromoulding in this work.

Tooling for ultrasonic micromoulding is also similar to conventional microinjection moulding from design point of view with some key differences on the sprue/injection regions. Firstly, the mould is vertically oriented due to the machine design. Secondly, the ultrasonic micromoulding tool has a viewing channel in its upper half and a sapphire window on the upper die allowing the visualisation of the flow of the melt during the micromoulding event. This allows high-speed thermal and high-speed optical imaging techniques can be used to characterise the micromoulding flows. Lastly, the upper half also houses the PEEK and brass guides for the sonotrode for maintaining the centring during sonication.

The main cavity plate or die is attached to the lower mould. Similar to the conventional micromoulding tool, modular cavity plate allows using of different mould inserts. The circular mould cavity is connected to the sonication chamber with a straight runner with rounded edges at the contact points with the sleeve of the plunger to provide a smooth pathway to the material being melted by the sonotrode. This eliminates the risk of restricted flow of the molten polymer and overload of the ultrasonic generator. An ejector assembly is also attached to the lower mould and it is operated with a pneumatic drive from the machine. The ejector unit is located beneath the reference plate of the machine and there is limited amount of space for additional sensor attachments. A channel is also machined under the lower plate for wiring of the sensor attachments that can be used. Mould heating is carried out using two pairs of 200 W heaters. A rendered image of the flow visualisation mould tool for ultrasonic micromoulding is given in Figure 3-5.

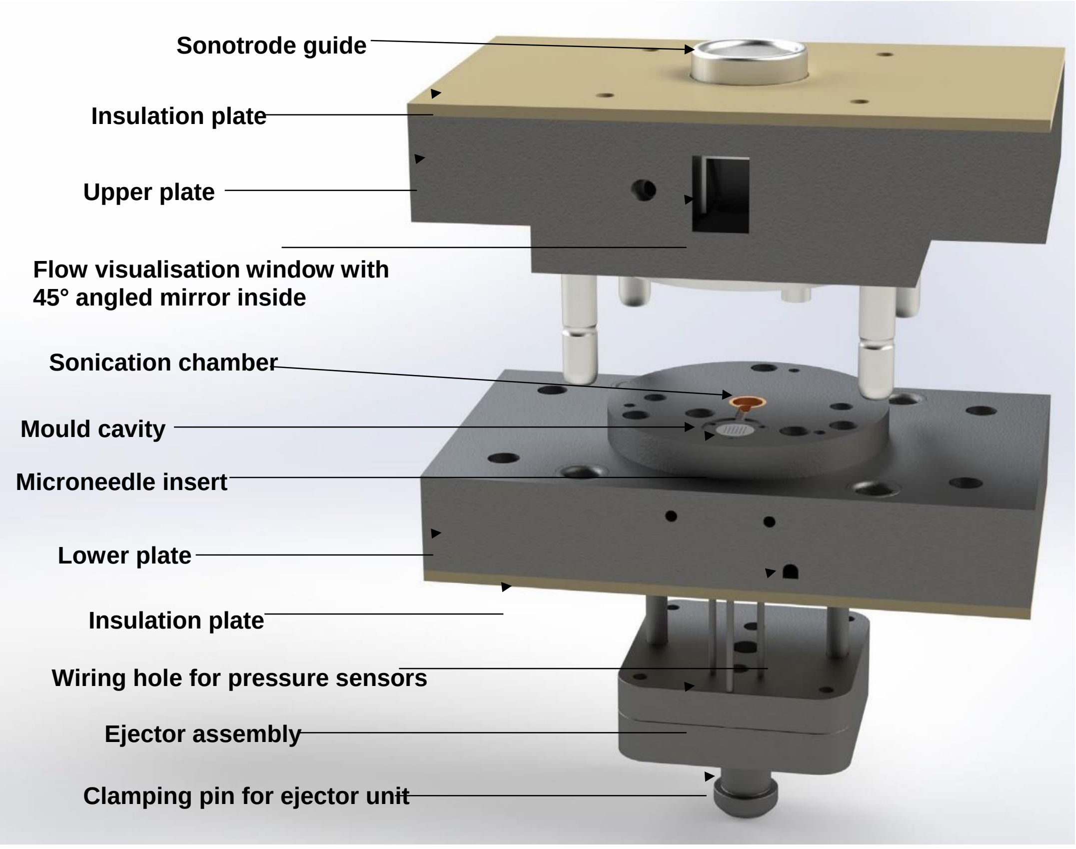

Figure 3-5. Flow visualisation mould tool for ultrasonic micromoulding.

3.6 Part geometry and microneedle mould inserts

In this section the part geometries and dimensions of the mould inserts and microneedle features will be given in detail.

3.6.1 Microneedle mould inserts

Two microneedle mould inserts have been used in this work. The first was EDM machined at an external company and has been used for a previous research work in the group (Nair et al. 2015). The machining steps included multiple dressing of the tools and machining of 25 microneedles in a 5x5 array configuration. The depth of the microneedle cavities was approximately 550 μm with slight differences due to spark erosion. The cavities were machined in conical shapes and the tip radius was measured to be approximately 30 μm. The base of the conical cavity has been measured to be 300 μm. No core pins or other channel inducing geometries were present for this particular design and the resultant microneedles from the insert have solid microneedle configuration. The dimensions and details of the mould insert are given in Figure 3-6. This insert has only been used for initial experimentation of ultrasonic micromoulding and the majority of the work in this work has been done using the second insert.

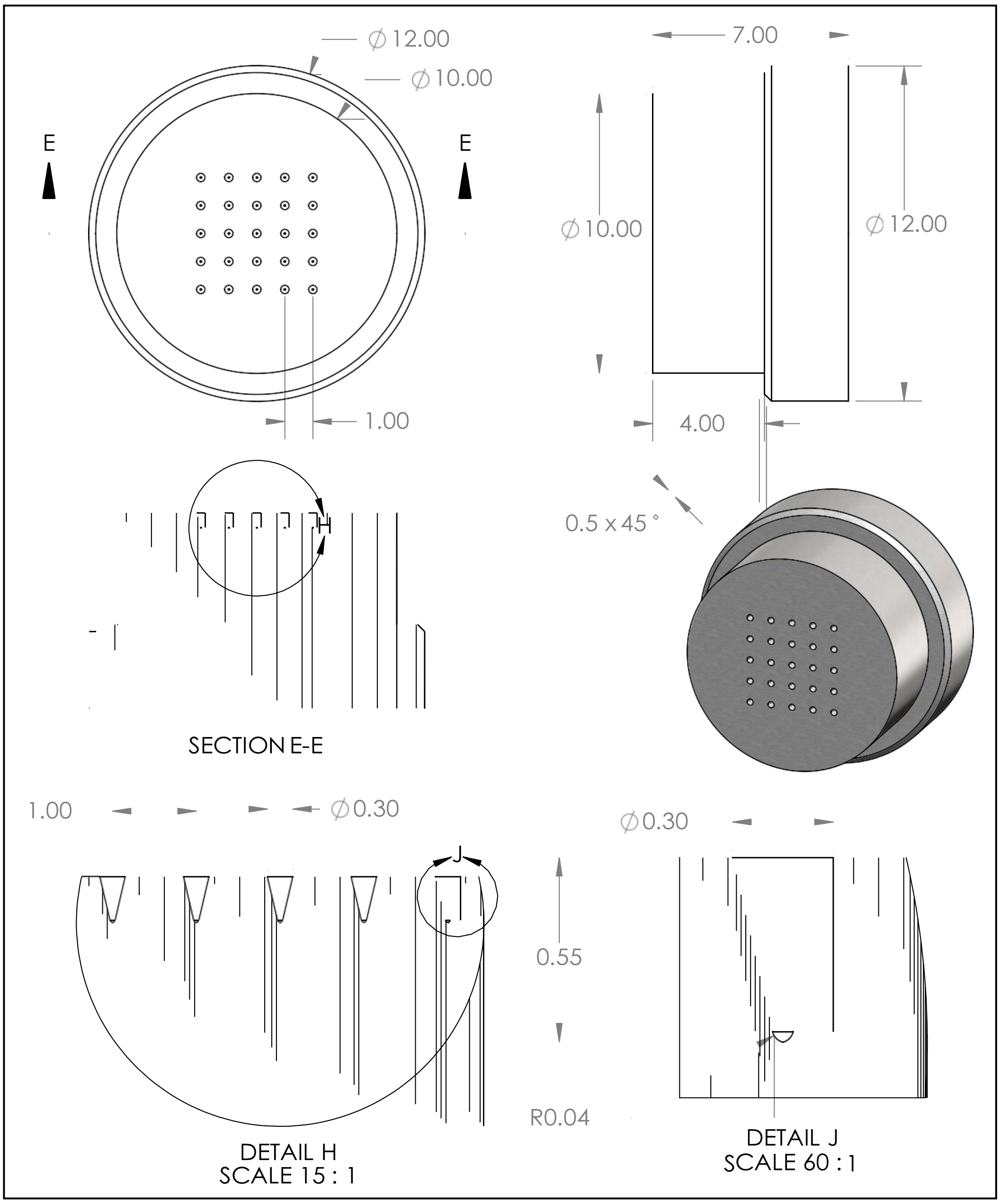

Figure 3-6 Dimensional details of the 5x5 EDM machined microneedle insert. All dimensions are given in mm unless otherwise specified.

The second microneedle insert used in this work has been laser machined at the University of Birmingham as described in 3.3.2. The cavities on laser machined insert are both wider in base and deeper as compared with EDM one. Moreover, the needle structures also have a taper of 15° from the cone that forms the base of the cavities. According to PDMS replicas made from this particular insert, the average needle height was found to be approximately 930 μm with tip radii going below 5 μm. The details of the laser machine insert is given in Figure 3-7.

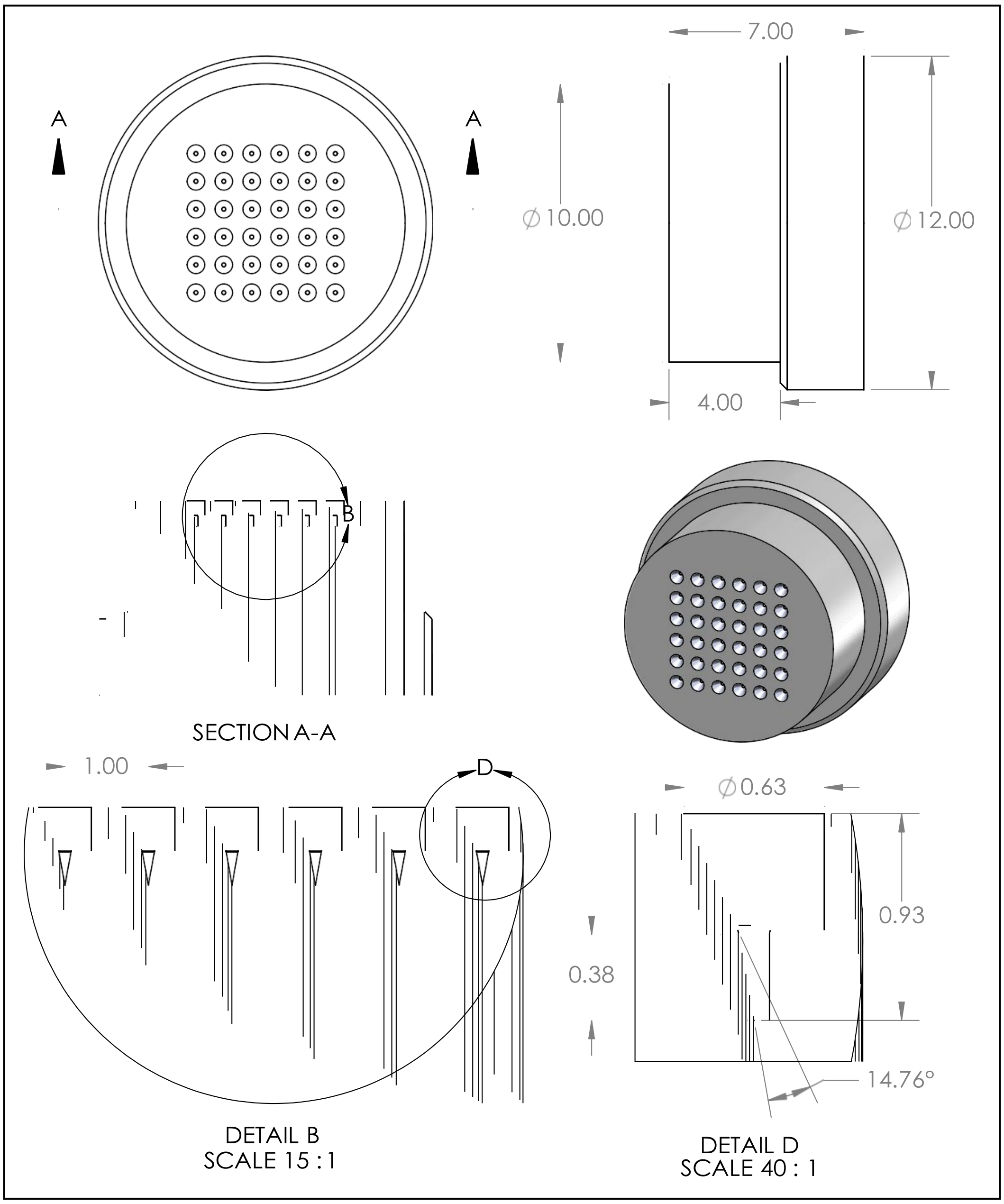

Figure 3-7. Dimensional details of the 6x6 laser machined microneedle insert. All dimensions are given in mm unless otherwise specified.

The tapered design of the microneedle cavities makes it more challenging to fill the whole structure for the molten polymer allowing to see the implications of changes in the process measurements and features on the final product quality.

3.6.2 Dimensions of the parts

Slight differences are present between the microneedle geometries manufactured with conventional micromoulding and ultrasonic micromoulding. The first difference is the sprue diameter where it is 5 mm for conventional and 8 mm for ultrasonic micromoulding. The ultrasonically moulded part also has a wider runner of 3 mm to provide more space for progressively plasticised material whereas the conventional micromoulding part uses a 2.5 mm wide runner. The circular cavities are 0.5 mm thick and the surface which the microneedles standing on is slightly proud on the main circle by 0.1 mm. Detailed dimensions of the parts are given in Figure 3-8.

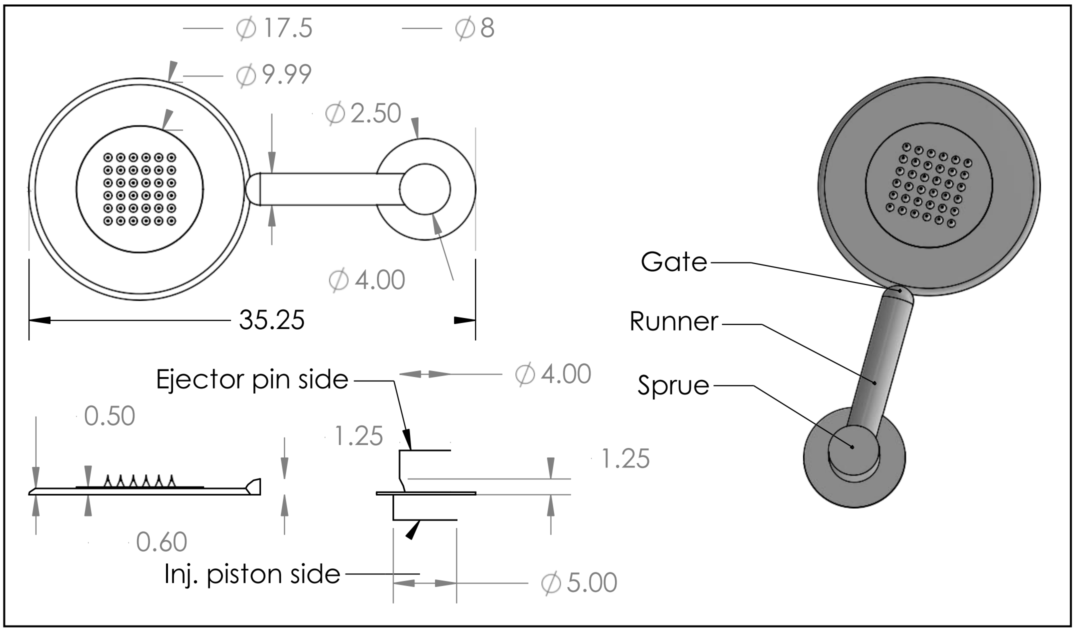

Figure 3-8. Dimensions of the microneedle component for conventional micromoulding tool design.

Ultrasonically micromoulded part has a sprue that is usually 2 – 2.5 mm in thickness which results from the minimum injection position of the sonotrode and maximum injection distance of the injection plunger. Flow visualisation for ultrasonic micromoulding is carried out on the inner circle which forms the base for the microneedles a majority of the cavity surface can be imaged using the thermal camera.

3.7 Thermal imaging of micromoulding flows

Thermal imaging of microinjection moulding flows has been a powerful method to investigate the filling behaviour and temperature distributions of the melt. Extremely small micromoulding cavities fill rapidly and high-speed infrared (IR) imaging capabilities are needed in order to capture the flow of the polymer. Nowadays, highly sensitive focal-plane arrays of sensors have been utilised for this purpose in thermal cameras to monitor the events with high capture speeds.

A high-speed IR camera has been employed in this work for monitoring the temperature distributions during ultrasonic micromoulding of microneedle patches. Visualising the flow of the melt using IR imaging and extracting temperature information from thermographs contain essential information for characterising the process. This will be achieved by extracting certain fingerprint information from the thermal images taken during ultrasonic microinjection moulding events.

Visualisation of micromoulding flows using either of conventional or thermal imaging require a transparent window on one side of the mould cavity so that the IR photons can be passed through an optical path and collected by a sensor. Sapphire provides a decent transmission range of 0.17 – 6.5 μm in IR part of the spectrum for micromoulding flow visualisation. The other important criteria to consider is the thermal conductivity and heat capacity for the transparent windows. Sapphire has comparable values with P20 tool steel for both criteria and has been selected to be used in the research group as following.

Work has been done in the group previously to visualise micromoulding process by modifying an older and a more recent high-speed thermal camera (Spares et al. 2009; Spares et al. 2013). In these studies, calibration procedures for thermal cameras and cooling curves have been presented. Authors also report some phenomena that occurs during filling stages such as super-heating and shear heating effects. Whiteside et. Al. visualised and studied the temperature evolution during ultrasonic moulding process (Whiteside et al. 2016). Their report emphasises that highest surface temperatures seen after filling of the mould cavity as a result of sustaining the sonication. Finally, a state-of-the-art thermal camera was employed to study the heat transfer coefficients during microinjection moulding (Babenko et al. 2018). Thermal imaging was used to measure the surface temperature of the polymer melt and for investigating the cooling behaviour. In the work, carbon black filled polymers are used in order to measure more accurate temperatures and block the IR photons coming from the mould surface for better measurements.

In the following, a brief introduction to the IR imaging will be given and experimental equipment used for this purpose will be presented with examples. In this thesis, thermal imaging experiments have been carried out only for ultrasonic moulding experiments.

3.7.1 Thermal imaging background

Heat energy is transmitted by three different ways, namely; conduction, convection, and radiation. Radiation involves emission of photons from a source and thermal imaging is developed by analysing the wavelength or the energy of these emitted photons for measuring the temperature of the source. These emission processes occur in the form of IR photons.

William Herschel first discovered the existence of IR by performing an experiment with a prism and placing thermometers at the locations where different colours separated in 1800 (Ring 2016). He measured highest temperatures beyond the visible red which meant that there are invisible rays that give rise to the increase in temperatures. This invisible IR region of the electromagnetic spectrum corresponds to wavelengths between 750 nm and 1 mm.

All materials emit electromagnetic radiation in IR given that if they have temperature above absolute zero, 0 K. When an electromagnetic wave changes a propagation medium, there are three processes that occur and the percentage of each change depending on the characteristics of the medium and electromagnetic wave. Reflection is the change of the direction of the wave front when an electromagnetic wave hits a surface. The passage of electromagnetic waves through a medium is called transmission. The third phenomena are the absorption where the incoming electromagnetic wave can be absorbed by the medium. These three effects are quantified by reflectivity ($\sigma\sigma$), transmittance ($\tau\tau$) and absorbance ($\alpha\alpha$). The sum of these three are unity and can be stated as following:

$$\sigma\sigma + \tau\tau + \alpha\alpha = 1 \tag{2.17}$$

For better understanding the absorption and emission processes, the black body concept has to be understood. A black body can be considered as a box that does not reflect any of the incoming electromagnetic waves, but instead it absorbs them. In thermal equilibrium conditions where the temperature of the environment and the black body are the same, the black body cannot keep absorbing all the incoming electromagnetic energy as it will get hotter and hotter. This situation violates the second law of thermodynamics which states that heat energy cannot be transferred from one body to a hotter body. Thus, the black body starts to emit electromagnetic energy as much as it absorbs. This situation can be explained by the photon emission of electrons when an incoming photon is absorbed by an electron, it will be excited to a higher energy state. The electron spontaneously falls back to its initial state which is more favourable energetically by emitting a photon with the same energy it once absorbed. Hence, for black bodies the absorbed amount of energy is also emitted in the form of electromagnetic waves.

Emissivity (ϵ) is defined as the capability of a body to emit electromagnetic energy. The black body is considered as a perfect absorber and emitter in the idealised case and the emissivity (ϵ) value equals to 1. Real materials have emissivity values below between 0 and 1 and hence they are called grey bodies. Polymers have emissivity values between 0.9 – 0.95 and appropriate emissivity values has been used for thermal imaging of ultrasonic moulding experiments (Spares et al. 2013).

3.7.2 Thermal imaging equipment

A high-speed thermal camera (FLIR X6540SC) has been used for visualising ultrasonic micromoulding flows in this work. The camera is capable of recording 640 x 512 pixels with a maximum frame rate of 126 Hz. Detector consists of a focal plane array type of sensor made out of InSb. The IR operation range of the camera has been reported as 1.5 – 5.5 μm by the manufacturer which is also in correspondence with IR transparency of sapphire window. The InSb IR detector is capable of detecting the photons from that particular spectrum (1.5 – 5.5 μm) and the results are extrapolated for photons with wavelength outside of this range.

The thermal camera has been mounted on a 3-axis tripod and an x-y translational stage to be able to focus and adjust the thermal scene. To be able to understand the optical path of the IR rays, it is worth to remind that the ultrasonic micromoulding tool is in a vertical configuration. The optical train for thermal imaging purposes has been formed by the mould insert surface where the polymer melt is being imaged through a sapphire window on top of the upper mould just above the mould cavity followed by a mirror at 45° located at the end of the viewing channel. The IR rays can then be focused on the germanium lens of the thermal camera. Figure 3-9 shows the cross section of the flow visualisation mould tool and optical train.

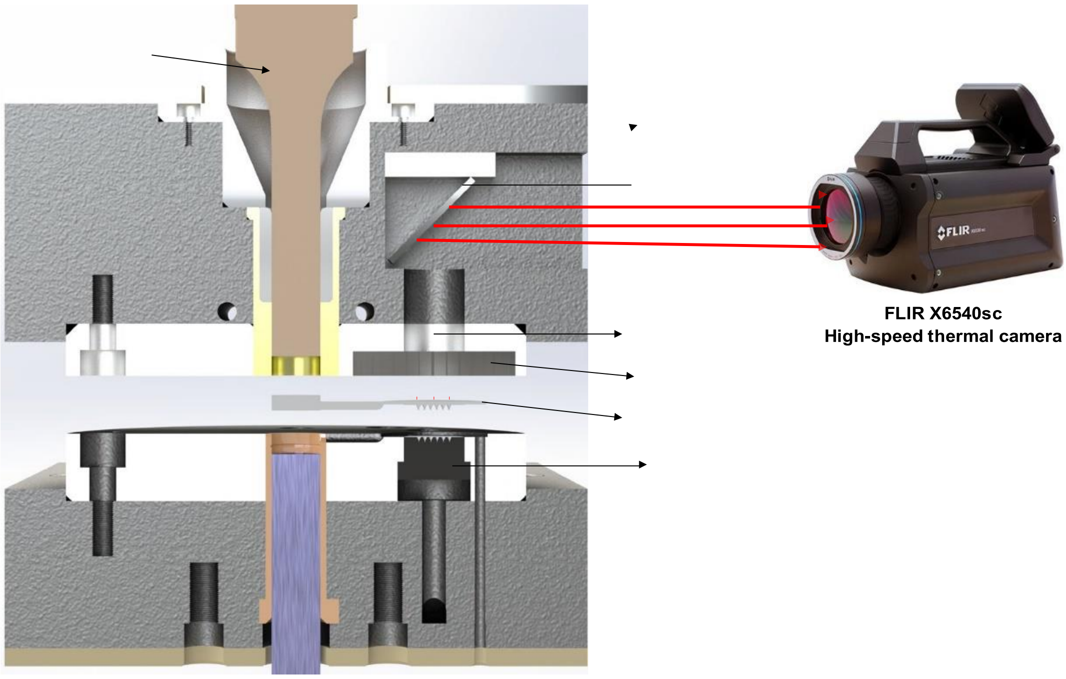

Figure 3-9. A rendered image of mould tool cross section and schematic representation of the optical train used for thermal imaging of ultrasonic moulding experiments. Infrared emissions from the moulded part continuously recorded as the melt fill the cavity. The image is not to the scale of the objects.

In the current tooling dimensions and camera specifications, it is possible to visualise the whole 6x6 microneedle array and the majority of the circular mould cavity. The 640 x 512 pixel image corresponds to an area of 7 x 9 ≈ 63 mm^2. The calibration and calculation of the area have been done using Vision Assistant 2019 software which is available in the LabVIEW package.

3.7.3 Thermal imaging measurement details and settings

Carrying out fine adjustments for thermal imaging is very important as the technique is quite intricate and a variety of different processes going on simultaneously while the polymer melt is emitting IR. When using thermal imaging, the emissivity and additional reflection effects must be considered for better understanding the temperature being measured.

The thermal camera is controlled via a software that gives access to the camera settings. First, the spectral range for the acquisitions was adjusted. An integration time of 50 µs has been set to have accurate measurements for the range of 128.1 – 266.5°C. Above and below that range, the measurement has been extrapolated by the software. Fine adjustments regarding the positioning of the camera and also flat field corrections for the signals obtained by the imaging sensor have been carried out. A carbon tape has been sticked at the outer surface of the mould as it is the best emitter available because of its colour. Following that, a cool and a hot scene for the thermal camera has been prepared by having measurements from the surface carbon tape at room temperature and 60 – 80°C by mould heaters. Then the pixel corrections have been made by the software automatically. Figure 3-10 shows the experimental setup for thermal imaging and an example thermal image of the mould surface.

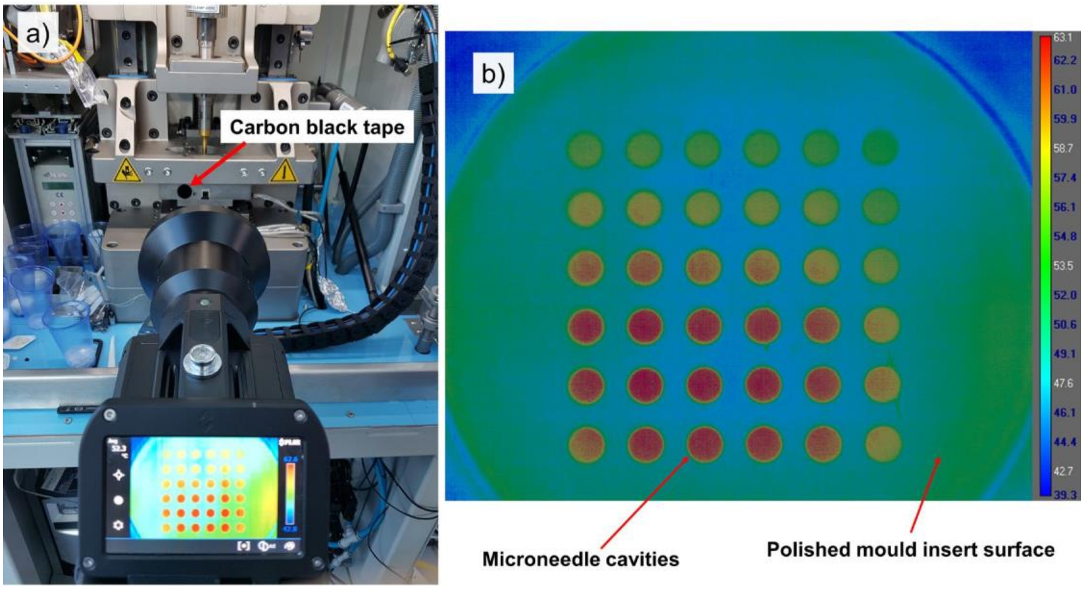

Figure 3-10. a) Thermal imaging setup, b) thermal image of the microneedle mould insert surface. Notice the relative temperature scale.

Microneedle cavities can be spotted easily from the thermal images (Figure 3-10b) and they are seen as the hottest spots in the thermal image due to the multiple reflection and emission processes within these narrow cavities. It can also be seen from the figure on the right that although the temperature of the mould was set to 70°C, a range of temperatures from 51 to ~40°C have been read from the mould surface according to the scale. The first reason for this is that the absorption of the sapphire window is not taken into account due to experimental difficulties caused by the machine design. Moreover, the insert surface was polished before laser machining process and reflectivity of the surface was quite high. In that sense, rather than being a good emitter, the polished mould surface tends to reflect the cooler IR radiations that results in reading lower temperatures than expected. Another effect has been seen that not all of the microneedle cavities show the same temperatures. This is due to the cartridge heaters of the mould where their hot-heating spots were localised at times and thermocouple measurements confirmed that there were some temperature differences between the regions near the gate and the end. Alignment of the camera also escalates this effect.

3.8 Data acquisition for micromoulding technologies

Data acquisition (DAQ) tools and interfaces provide reading and recording environment for process monitoring and is of great importance for microinjection moulding processes in order to understand what is happening during the process in very small time scales and extreme conditions. The equipment and methods for DAQ extensively used in both industry and research for different purposes. DAQ systems usually consist of the following components for micromoulding applications:

- Sensors for measuring changes in physical phenomena happening during the process. These could be pressure, force, temperature changes or displacement that are transient.
- Charge amplifiers for amplification of signals. A majority of force and pressure sensors require amplification of signals as often times very small amounts of charge or current is generated by small piezoelectric transducers.
- A board or chassis. These devices provide ports for inputs and outputs for the measurements.

- Software interfaces. A variety of programme languages and interfaces can be used for systematic DAQ and analysis. Any triggering or synchronisation procedures can also be done through coding.

Extensive DAQ equipment and software has been used in the group for monitoring state-of-the-art micromoulding machines previously including force, pressure and temperature sensors, ultrasonic sensors and optical techniques (Whiteside et al. 2005a; Whiteside et al. 2005b; Whiteside et al. 2008). The purpose of DAQ in micromoulding is to record the physical quantities during a moulding cycle and analyse it to find out how the machine dynamics and process conditions affect these measurements and quality criteria of the micromoulded products. For instance, injection and cavity pressure values has been recorded for 750 cycles and correlated to the micro-part features previously (Whiteside et al. 2005b). Other possibility for benefitting from the DAQ systems is to use a feedback loop to tune the process conditions for ensuring that the moulded product meets the quality requirements.

In this work, a National Instruments cDAQ – 9185 ethernet chassis has been used as a network device for obtaining the measurement signals from several sensors and machine outputs. The chassis allows plugging four different National Instruments (NI) conditioned modules.

Acquisition of the process data from Micropower 15 and Sonorus 1G was carried out using two NI-9215 BNC (Bayonet Neill-Concelman type of connection) modules for measuring voltages from the sensors. Process data have been recorded using a LabVIEW code for multiple channels where needed. The DAQ chassis and physical details of the unit can be seen from Figure 3-11.

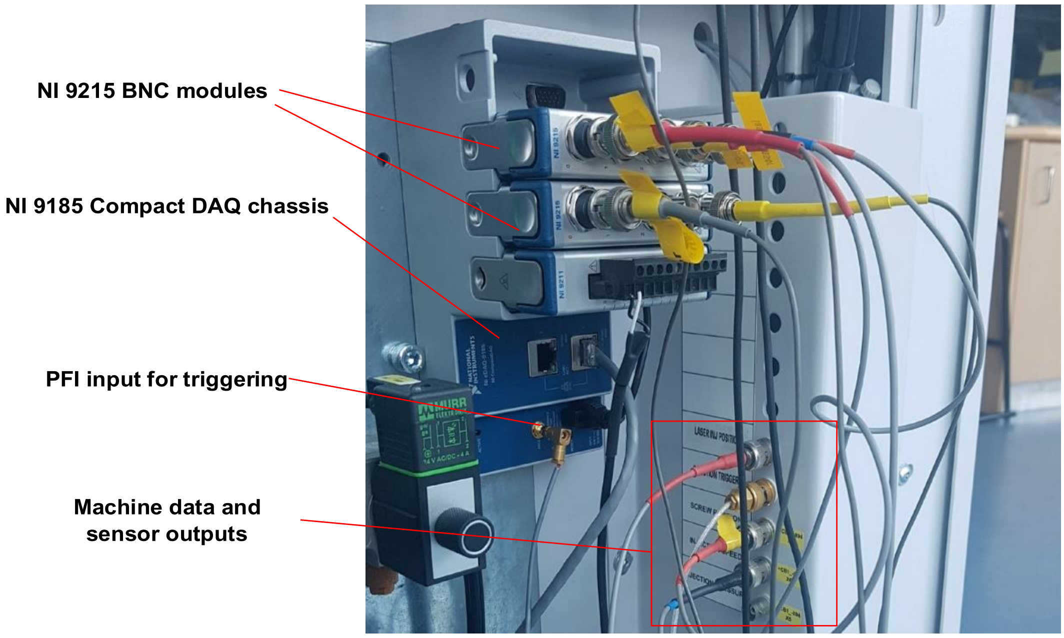

Figure 3-11. DAQ hardware installed at the rear of Micropower 15. One of the BNC modules was also used for Sonorus 1G cavity pressure measurements.

DAQ assistant visual instrument (VI) block codes have been used to develop a user-friendly software as it can be to capture conventional micromoulding process data within the framework of this project. A similar code has been also used to capture only cavity pressures from ultrasonic micromoulding machine as this is the only channel connected to the DAQ chassis. An acquisition rate of 100 Hz with 10 samples to be read at a time has been set initially for DAQ. However, it was seen that some micromoulding experiments required extremely high injection speeds and capturing of the process data at much higher speeds. For that reason, the majority of the data acquisitions have been carried out at 1000 Hz. The triggering of DAQ from Micropower has been carried out using a 24 V signal. The signal turns on when the mould starts to close before the injection starts. It has been converted to a 5 V signal and has been tapped to the programmable function interface (PFI) input and has been configured as the trigger signal from the software. The software uses the digital increasing edge of the trigger signal to start the acquisition. A similar procedure has been carried out for ultrasonic micromoulding machine where an analog signal input for the trigger has been acquired when the sonotrode starts sonication. The screen capture of the DAQ software user interface is given in Figure 3-12.

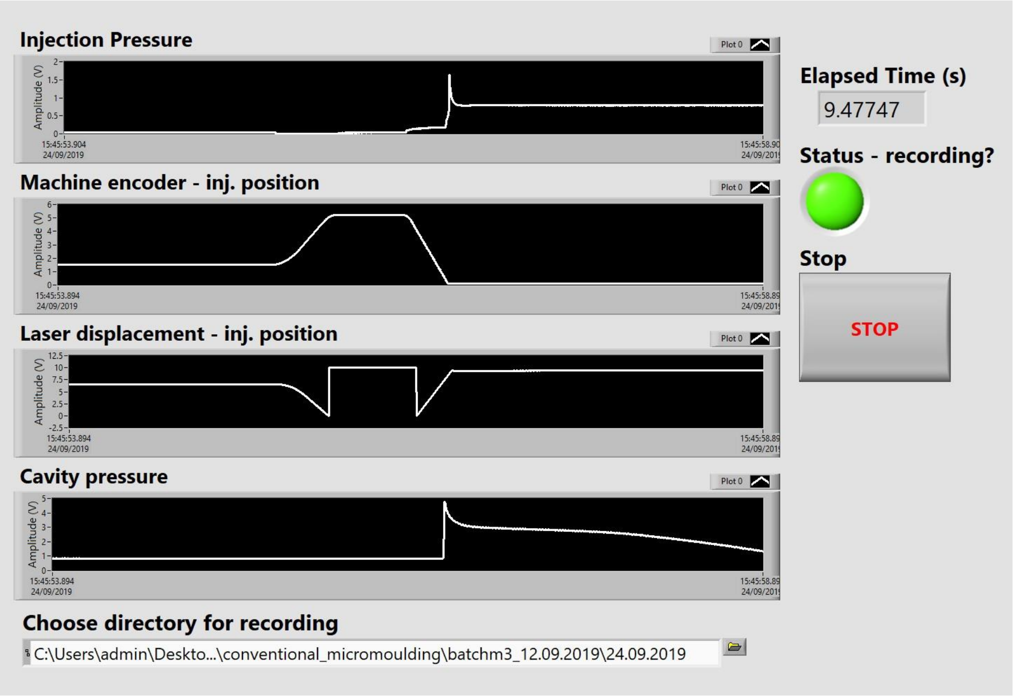

Elapsed Time (s): 9.47747

Choose directory for recording: C:\Users\admin\Deskto...\conventional_micromoulding\batchm3_12.09.2019\24.09.2019

Figure 3-12. Software user interface written using LabVIEW for DAQ recordings.

The LabVIEW script written captures the data in 4 different channels (injection pressure, injection speed, injection position, laser displacement information) by forming a time axis using a reference time from the computer clock and generating the files automatically for each cycle.

3.8.1 Built-in sensors for conventional micromoulding machine

The conventional microinjection moulding machine used for this work has 3 BNC outputs for recording injection pressure, injection speed and screw position. The first of the BNC ports is connected to the injection pressure sensor (X-sensors, XB-120-1500) which is located at the back of the injection piston. This sensor and measurement of injection pressure is of paramount importance as the machine controls the process with a feedback loop by reading the pressure values. Pressure-controlled switch over for packing is carried out by controlling these pressure values.

When using a 5 mm plunger, the sensor measures 0 – 600 kg of force within 0 – 10 V output range. This has been converted to the pressure unit of bars using the holding pressure values that were read from the machine screen. Since the machine controls itself in a feedback loop using this holding pressure information, this has been considered as the most appropriate way of doing a linear calibration for the sensor data.

Injection piston position data from the encoder and injection speed are calculated using complex conversions from servo position and gearbox revolutions per minute (RPM) values. The detailed calculations and conversion charts are confidential to the manufacturer company. Each of these channels have been connected to a charge amplifier and the signals have been recorded using the DAQ interface as voltage outputs.

3.8.2 Laser displacement sensor for injection position

Microinjection moulding processes require high specification mechanical and servo-electric systems for moulding of extremely small components and controlling the process. For avoiding premature freezing and filling the cavity as rapidly as possible usually extremely high injection speeds are required as covered previously. As will be discussed in detail in Chapter 4, a part filling of the cavity and pressure switch-over from velocity controlled injection process is dominantly favoured in most of the injection moulding processes for avoiding pressure overshoots and potential damages to the tool and injection unit. This is a very challenging feature to implement in microinjection moulding machines as there are strict physical requirements for rapid acceleration and deceleration of the injection piston unit in order to switch to a pressure controlled regime in such a small time scale measured by milliseconds.

Servo-electric motors provide required precision and accuracy in terms of positioning. However, due to the mechanical components in the injection unit such as the drive belt, gears and frictional forces actual behaviour of the injection unit could be different from what the machine considers where it should be. For assessment of errors or deviations that could take place during injection, an ultra-high-speed laser displacement sensor (Micro-Epsilon, OptoNCDT 2300-100) has been installed at the rear of the injection unit. It is one of the laser sensors from the that is available in the market with highest performance products with 49.14 kHz measuring rate. The sensor is capable of detecting the smallest displacements (0.8 μm at 20 kHz) of the injection piston with high accuracy. A flexible target for the laser spot has been attached to the platen of the injection plunger for displacement measurements. The sensor has a measurement range of 10 cm and positioned carefully. The measurement principle is based on the triangulation of the laser beam reflected by the surface at a particular distance. Details of the injection unit and position of the laser displacement sensor alongside with a schematic showing the measurement principles of laser triangulation is given in Figure 3-13.

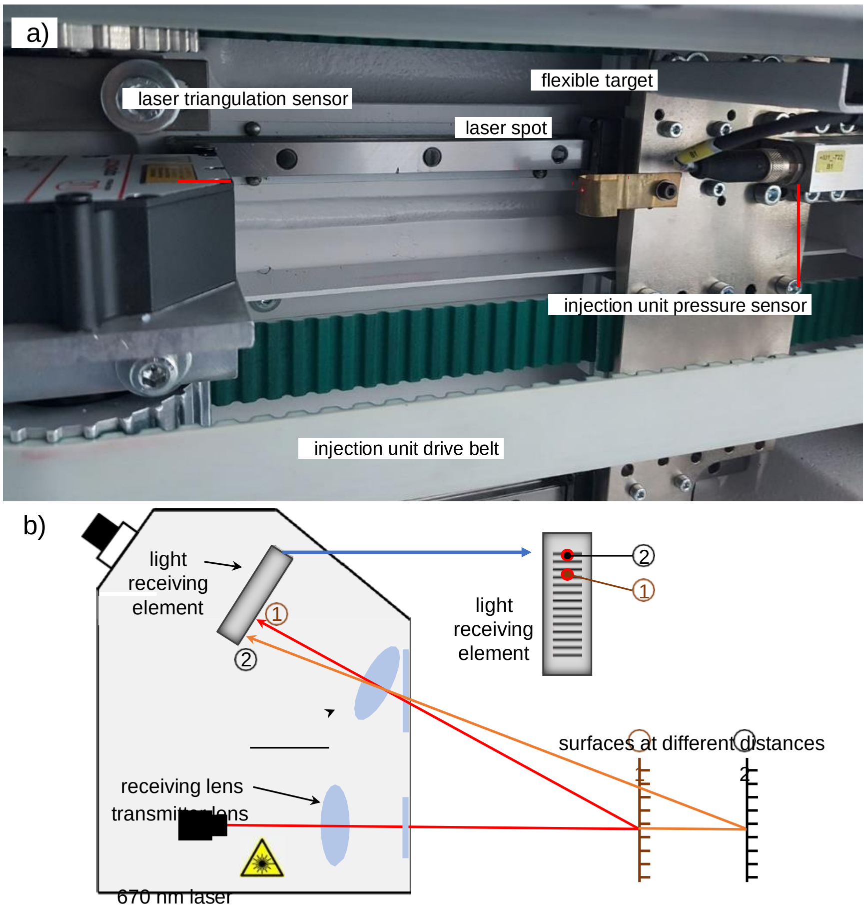

Figure 3-13. Laser displacement sensor attachment at the back of the Micropower 15 injection unit. (a) shows the injection unit of the machine. (b) depicts the physical principles behind the laser triangulation measurements.

A flexible brass target for the laser spot have been cut and attached to the injection unit initially. The target is flexible in the sense that it is made of a thin brass sheet for protecting the sensor from damage that could occur from injection unit's backward movement. Because of its flexibility the target starts vibrating as the injection piston rapidly decelerates and switches over to pressure control. These vibrations have been confirmed with the harmonics in the position measurements. Sensor voltage output has been connected to the NI-9215 BNC unit alongside with other process data. Measured voltages between 0 to 10 V correspond to a range of 0 – 10 cm and conversions have been done accordingly.

A more rigid and thicker target have been machined and a set of experiments have been performed to test the effects of the target flexibility on the measurements. This particular target is made of a thicker brass (~1 mm) rather than using a foil for dimensional stability and avoiding vibrational modes of the target. Injection cycles have been performed at 50, 200, 400 and 760 mm/s (maximum) injection velocities and laser displacement data have been recorded for comparison. The data is given in Figure 3-14.

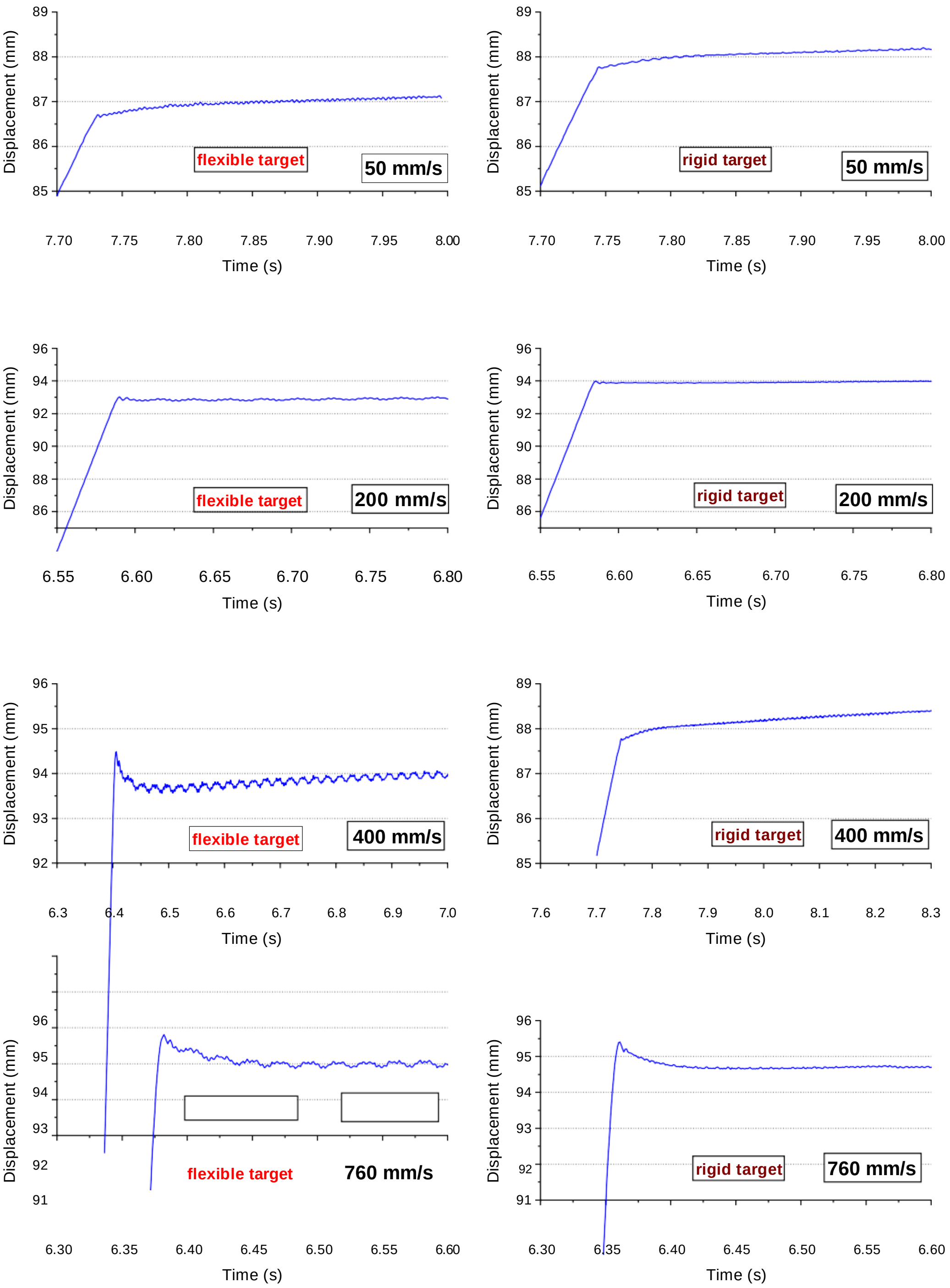

Figure 3-14. Laser displacement sensor data for flexible (left column) and rigid (right column) targets. 50, 200, 400 and 760 mm/s injection velocities have been presented in

different rows.

The left column in Figure 3-14 show the obvious harmonics present because of the vibrations on the flexible target. The amplitude of the oscillations increase with higher injection velocities where the effect becomes more detrimental for measurement purposes. The causes of these vibrations are mainly the deceleration that the target is experiencing while the unit switches over to pressure control. The injection unit retracts itself because of the very high injection speeds of 400 and 760 mm/s as can be seen from the peaks. The rigid target resulted in considerably better results as presented on the right column in Figure 3-14, as the oscillations in the displacement data nearly diminished nearly completely. As a result, although flexible targets are beneficial for protecting the sensor from possible mechanical damage, there is a compromise in the accuracy of the sensor data. It has been seen that the rigid target provided better results and they have been used for conventional micromoulding experiments for data acquisition.

3.8.3 Built-in sensors for ultrasonic micromoulding

The software interface provided with Sonorus 1G ultrasonic micromoulding machine allows the user to monitor and record injection force, sonication frequency, power consumption and plunger position. Sonication frequency and power consumption of the sonotrode are recorded from the Branson generator analog output. Injection force is determined by reading the servomotor torque. Lastly the position information has been extracted by the injection plunger motor turns. Position is calculated by the motor position (revolutions) and the transmission ratio. The details of the calculations and conversion charts are not disclosed by the company.

3.8.4 Cavity pressure measurements

Micro-nano replication and dimensional stability of the micromoulded products depend on machine dynamics and thermomechanical history of the polymer melt. In that sense, cavity pressure has been known as a reliable measurement that can be carried out for process monitoring purposes for understanding process dynamics alongside with the filling behaviour of the polymer.

Several papers published in the literature that signify the importance of cavity pressure measurements for micromoulded products. Cavity pressure data have been reported to be the most indicative process measurement in terms of variation in the micromoulded part quality as reported previously by the group using a state-of-the-art micromoulding machine (Battenfeld

Microsystem 50) at the time (Whiteside et al. 2005b). The work included the study of a sub-milligram micro-component and the quality of the parts are remarkably sensitive to the variations in the process that manifest themselves on cavity pressure.

Griffiths et. Al. investigated the effects of process parameters on cavity pressure and studied different features of the cavity pressure curves for a microfluidic component (Griffiths et al. 2011). The authors extracted maximum pressure peak, pressure work and pressure increase rate values for each cycle for process monitoring purposes. It has been reported that the cavity pressures are heavily dependent on the melt temperature, material characteristics and machine dynamics. Although the direct correlations and analysis of these cavity pressures in conjunction with the part quality criterion is missing in the work, the paper has been one of the examples of how process fingerprinting could be carried out for micro-injection moulding process interrogation.

As the melt enters and fills the micromoulding cavity, pressures at specific locations in the cavity increase. In addition to the built-in machine sensors and other process monitoring methods, cavity pressure measurements have also been carried out for both micromoulding technologies in this thesis. Cavity pressure measurements are commonly made by piezoelectric transducer based force or pressure sensors. As indicated in Chapter 2, transducers have piezoelectric crystals that convert externally applied pressures to charges or voltages. For micromoulding applications, there are two methods for measuring cavity pressures. The first one being the direct cavity pressure measurements where the pressure sensor is flush-mounted with the mould cavity. Polymer melt is in direct contact with the melt in this method and measures the pressure induced by the polymer.

The second method is to measure the cavity pressure indirectly using a force sensor by installing it at the back of an ejector pin or measurement pin that is in contact with the polymer melt during moulding. Measuring the cavity pressure indirectly have slight disadvantages over the direct measurements. The measured pressure is a combination of the applied force by the polymer melt and frictional forces that arise between the pin and the mould. However, indirect method allows accurate measurements of ejection forces which could be useful for optimising the dimensional stability of the micromoulded product. Work carried out on characterising the main features of the of the ejection force curves using a miniature sensor and determining optimum process conditions for polymer replication (Griffiths et al. 2015). In this thesis, an indirect measurement technique is adopted as the direct measurement sensors could be damaged with the sonication during ultrasonic micromoulding experiments. The same sensor attachment procedures have been carried out for both mould tools.

To our knowledge, no detailed study has been reported in the literature for cavity pressure monitoring for thermoplastic microinjection moulded microneedles and ultrasonic micromoulding. For achieving this task, a miniature indirect pressure sensor (Kistler 9210AA) has been installed on the ejector plates of both conventional and ultrasonic micromoulding mould tools. The sensor casing is only 3.5 mm in diameter and has a measuring range of 0 – 250 N and depending on the measuring pin dimensions, maximum measurable pressure values are reported up to 3000 bars.

A recess in the shape the sensor at 45° has been machined on the back ejector plates for both mould tools so that the sensor can sit just behind the pin which is located at the far end of the cavity. Cross section of the ejector plate and sensor recess are given in Figure 3-15. For preventing interference of the sensor signal, electromagnetic shielding has been achieved by using aluminium adhesive tapes for the wiring of the sensor. The details of the cavity pressure measurements and process fingerprint analysis will be covered in Chapter 4.

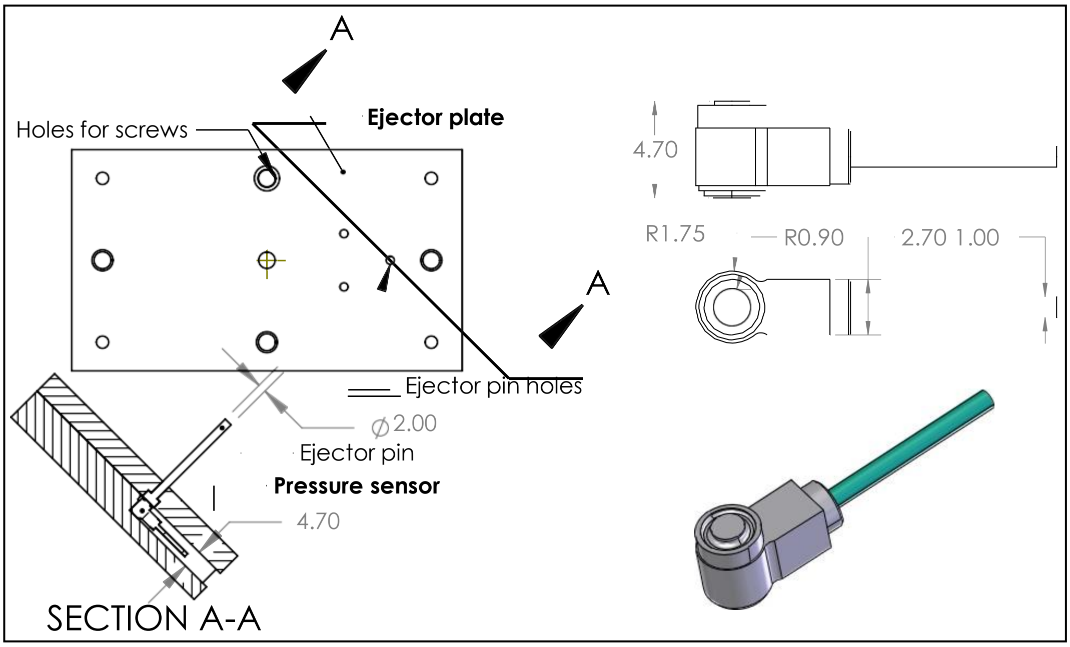

Figure 3-15. Dimensional details and cross section drawings of the ejector plate for the attachment of the Kistler 9210AA sensor. The sensor sits behind the ejector pin to measure cavity pressures. All dimensions are in mm unless otherwise specified.

3.9 Materials

Although extensive work has been carried out for micromoulding processes using wide-range of polymers in the literature, there are a limited number of articles and knowledge available for ultrasonic micromoulding of different thermoplastic materials. There are some reports on ultrasonic moulding of PP, PLA, PE and PEEK, however, most of these studies lack the replication assessment of the technology at micro and nano scale (Sacristán et al. 2014; Sánchez-Sánchez et al. 2017; Dorf et al. 2018; Masato et al. 2018). Therefore, for having a well-defined starting point, two widely-used polymers namely polypropylene (PP) and acrylonitrile butadiene styrene (ABS) for injection moulding have been selected. This selection also will allow the comparison of semi-crystalline and amorphous materials for both micromoulding technologies.

3.9.1 Polypropylene (PP)

A generic polypropylene resin (Ineos PP 100 - GA12) has been chosen for one of the materials for this work. The material shows good flow properties and has been designed for injection moulding applications. Processing of PP in injection moulding is relatively easy and predictable hence providing a good starting point when using new micromoulding cavities. PP is a semi-crystalline polymer that has a sharp melting point in the vicinity of 165°C. The exact melting temperature of the material used and viscosity will be discussed in the following sub-sections. Some of the important physical properties of PP used in this work is given in Table 2.

Table 2. Physical properties of Ineos 100-GA12 PP resin.

Properties	Value & units
Melt flow rate at 230°C/2.16 kg	12 g/10 min
Tensile strength at yield	34 MPa
Heat deflection temperature at 0.45 MPa	90°C
Shrinkage (Fischer 2003)	1 - 2.5%

3.9.2 Acrylonitrile butadiene styrene (ABS)

Another commonly used thermoplastic material, ABS has been also selected for micromoulding experiments. The resin has been produced by Sabic (Cycolac - HMG94MD) for thin-wall medical applications with biocompatibility according to ISO 10993. ABS polymers known for their amorphous structure with no true melting point and their T_g has been known as ~105°C. The material also has a melt flow rate of 11.7 g/10 min at 230°C which is very close to the value of PP. Exact glass transition behaviour and viscosity of the material will be discussed in the following sub-sections. Main physical properties of ABS used for this work is given in Table 3.

Table 3. Physical properties of Sabic Cycolac HMG94MD.

Properties	Value & units
Melt flow rate at 220°C/5 kg	12 g/10 min
Tensile strength at yield	40 MPa
Heat deflection temperature at 0.45 MPa	93°C
Shrinkage (Fischer 2003)	0.5 - 0.8% (Sabic method)

3.9.3 Disc preforms for ultrasonic micromoulding

Intuitively, it can be predicted that usage of industry standard pellets in ultrasonic micromoulding may cause issues regarding dosage amount, centring of the sonotrode and interfacial friction inconsistencies from cycle to cycle. These effects add additional complexity to the process fingerprint and monitoring approaches and hinders the repeatability of the ultrasonic micromoulding process. For overcoming these problems, usage of disc shape preforms have been considered for ultrasonic micromoulding. By doing this, the deviations in shot sizes have been eliminated. Moreover, flat-disc-shaped preforms provide a proper, flat surface for the sonotrode to transmit the ultrasonic waves better for melting. Using discs also allows to have control over the interfacial heating, where thick or thinner discs could be moulded and experimented. A new mould tool has been designed for this purpose as shown in Figure 3-16a. ABS disc preforms can also be seen in Figure 3-16b.

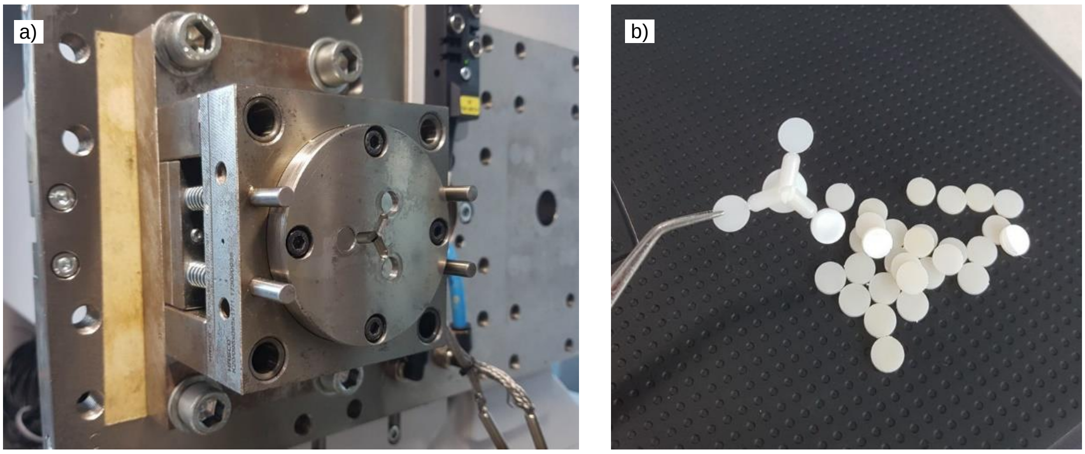

Figure 3-16. a) Mould tool for disc preforms, b) ABS disc preforms.

Disc preforms of PP and ABS have been moulded using the conventional microinjection moulding machine (Micropower 15). 1.5 mm thick discs have been used for this thesis. Our work on disc shaped preforms for ultrasonic moulding reports that higher melt temperatures have been observed when having more interfaces in the feedstock (Gulcur et al. 2018). Disc preforms have been manufactured using the settings given in Table 4.

Table 4. Parameters used for manufacturing disc preforms for ultrasonic micromoulding.

Process settings - units	Value & units (PP)	Value & units (ABS)
Melt temperature (°C)	230 (nozzle), 220, 210, 200 (hopper)	260 (nozzle), 250, 250, 240 (hopper)
Mould temperature (°C)	60	60
Injection speed (mm/s)	200	200
Switch-over pressure (bar)	400	500
Holding pressure (bar)	450	550
Holding pressure duration (s)	5	5

Moulding of preforms adds an additional processing step to the thermal history of the polymer feedstock for ultrasonic micromoulding which could affect the flow behaviour of the polymer melts (Zhang and Gilchrist 2012). In order to confirm that the disc preforms have the same or very similar properties to the virgin material, differential scanning calorimetry (DSC) tests were carried out. The technique has been widely-used for detecting the phase transition temperatures for a variety of materials. A heat-cool-heat experiment have been set with following steps for PP. First the ambient temperature of the measurement unit have been cooled down to 0°C. Then, the temperature have been ramped to 200°C with 10°C/min. This step was sufficient to capture the melting point (T_m) of PP. A similar procedure have been carried out for ABS where the temperature range of 0 – 240°C was used. T_m and T_g (glass transition temperature) values have been extracted for all measurements using Trios software which controls the DSC unit and also allows the analysis of the experimental data. Example DSC curves for both materials are given in Figure 3-17.

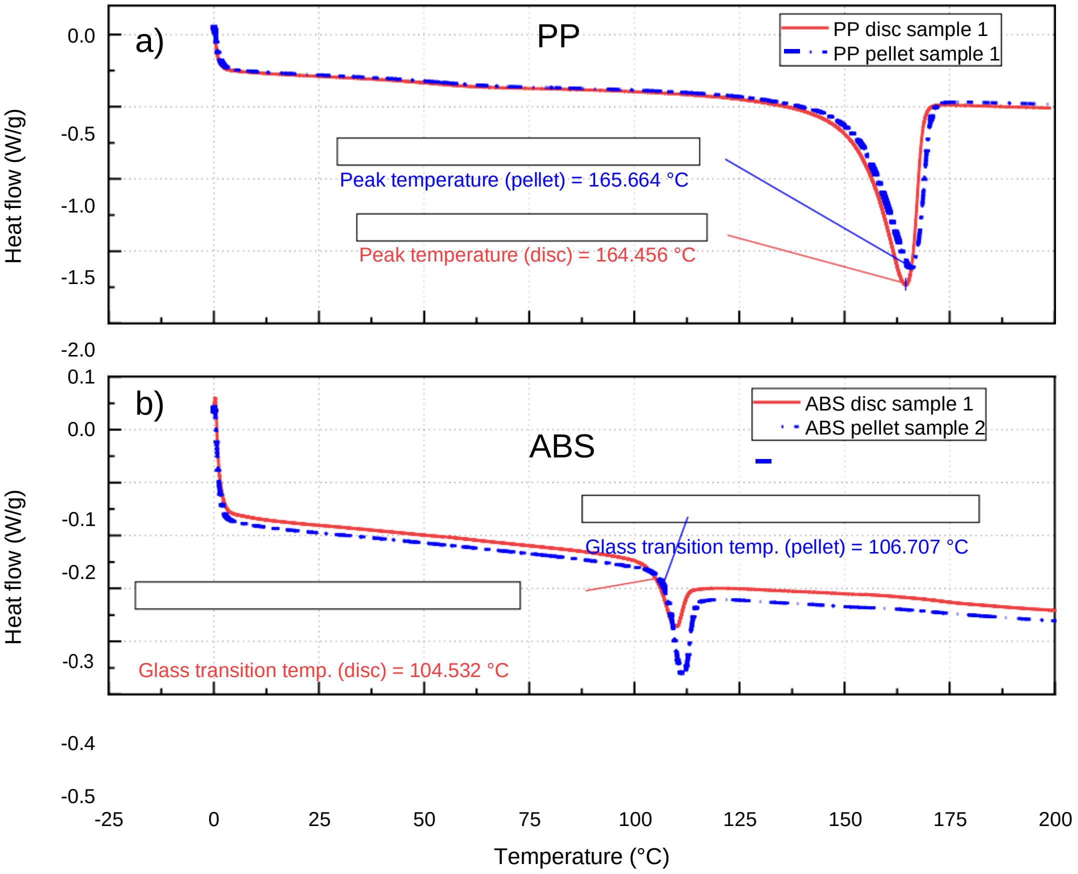

Figure 3-17. DSC tests for PP (a) and ABS (b). Temperatures of interest for both materials are indicated.

Randomly selected heat flow vs temperature plots have been presented in the above graph for showing the difference between discs and pellets for both materials. The phase transitions can be spotted by the dramatic changes in the heat flow. If semi-crystalline polymers are considered, this appears as a well-defined peak temperature, whereas for amorphous materials the decrease in heat flow could be slightly less for given amount of material. Three samples for each feedstock shape of two different materials have been prepared for DSC experiments and temperatures have been calculated from the plots. Between 7 – 10 mg of material have been used for DSC analysis. Table 5 summarises the melting and glass transition points for PP and ABS.

Table 5. Melting and glass transition temperatures given for PP and ABS, respectively. 3 measurements have been averaged for each temperature.

Material	T_m / T_g (°C)
PP pellets (semi-crystalline)	165.30
PP discs (semi-crystalline)	164.50
ABS pellets (amorphous)	106.88
ABS discs (amorphous)	104.59

A slight decrease of 0.8°C has been seen in the melting point disc shaped samples for PP. T_g has shifted by 2.29°C for disc shaped ABS feedstock. These slight changes suggest that the additional processing step of injection moulding had minimal impact on the thermal characteristics of both PP and ABS disc preforms for ultrasonic micromoulding. Further investigations on rheological characteristics of virgin material and disc preforms have been also carried out in the next section to confirm these findings.

3.9.4 Rheology measurements

Rheological behaviour of polymers is associated with their viscosity which is a measure of resistance to flow. Although simplistic flow rate analysis techniques such as melt flow index could give information regarding the flow behaviour of the polymers, viscosity is a spectrum of different values due to their molecular architecture and temperatures. More sophisticated techniques should be used for understanding the flow behaviour of polymers as the injection moulding processes could be rather complex at times due to extreme shear rates and viscoelastic behaviour of the materials. For that reason, an Anton Paar Physica MCR 301 shear rheometer has been used for characterising the flow behaviours of PP and ABS. The technique gives detailed information on lower shear regimes for polymeric materials.

Parallel plate technique has been used for rheology experiments. The upper plate is circular and attached to a sensitive force sensor where the shear rates are monitored throughout the measurement. The lower plate is basically a flat plate with temperature control where the samples are put on for the measurement. A distance of 1 mm has been set between the parallel plates for measurements.

Temperatures for rheology experiments have been set according to the conventional and ultrasonic micromoulding process conditions. A temperature range of 180 – 240°C with 20°C intervals have been set for PP. 220, 240 and 260°C have been chosen for ABS. A strain amplitude of 1% has been used for frequency sweeps which correspond to shear rates. The measurements starts from 100 rad/s of angular frequency and takes 16 points of data down to 0.1 rad/s. For each temperature and material combination, complex viscosity, G' and G'' have also been calculated and plotted by the software. Frequency sweeps carried out at 180°C and 240°C for polypropylene pellets are given in Figure 3-18 as an example.

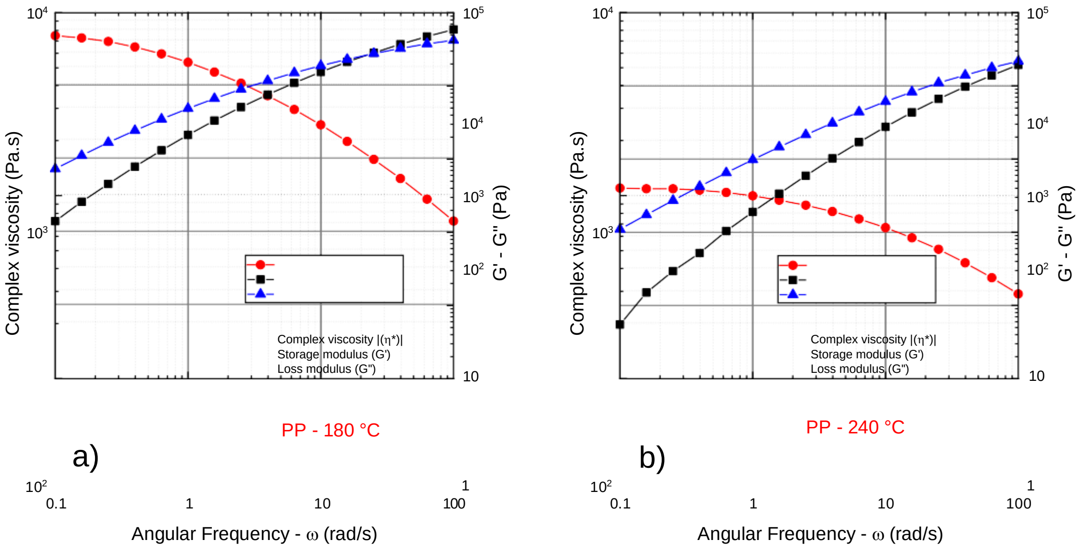

Figure 3-18. Frequency sweeps for PP pellets at 180 (a) and 240°C (b). The red curve depicts the shear thinning behaviour of the material.

Significant differences in viscosity (red curves) at different temperatures can be seen for PP from Figure 3-18. Viscosity decrease with increasing shear rates (angular frequencies) show a typical shear-thinning material behaviour.

G' and G'' decrease with lower angular frequencies where G' is associated with materials deformation storing capability and G'' is related to the viscoelastic heat dissipation of the material. One of the interesting features of these plots is that the points where G' and G'' coincide and the time scales corresponding to these times have been termed as reptation time. Reptation theory is based on the molecular entanglements of polymers and it considers them being in a tube and studies relationship between the relaxation times and molecular mass. Although this discussion might be of interest for future work in terms of studying the viscoelastic behaviour of polymers under sonication, the rheology data taken from the whole range of test temperatures are included in the Appendix A, B, C and D since the topic is not the main point of discussion for this work. Viscosity data taken from different temperatures for both PP and ABS and have been compared in the same plots. Figure 3-19 and Figure 3-20 shows the comparison between PP pellets and discs.

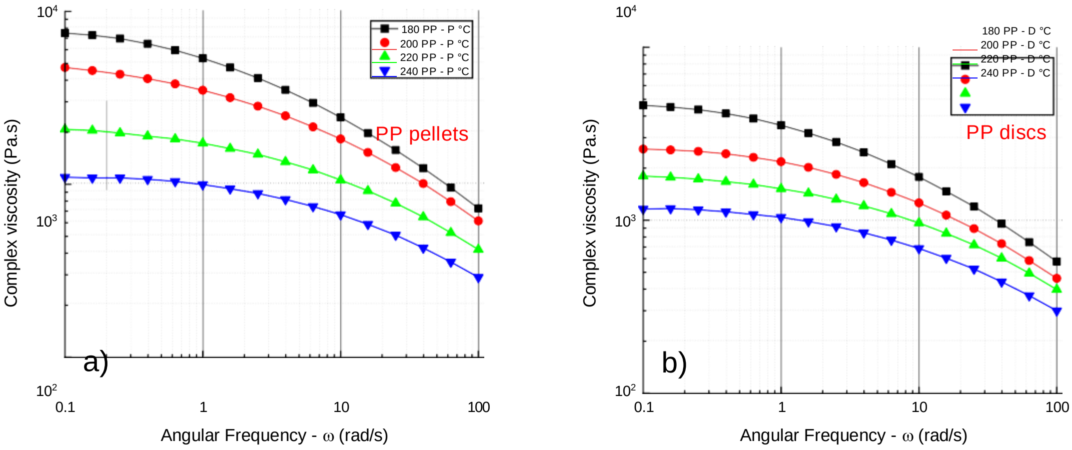

Figure 3-19. Viscosity comparison for PP pellets and discs at different temperatures.

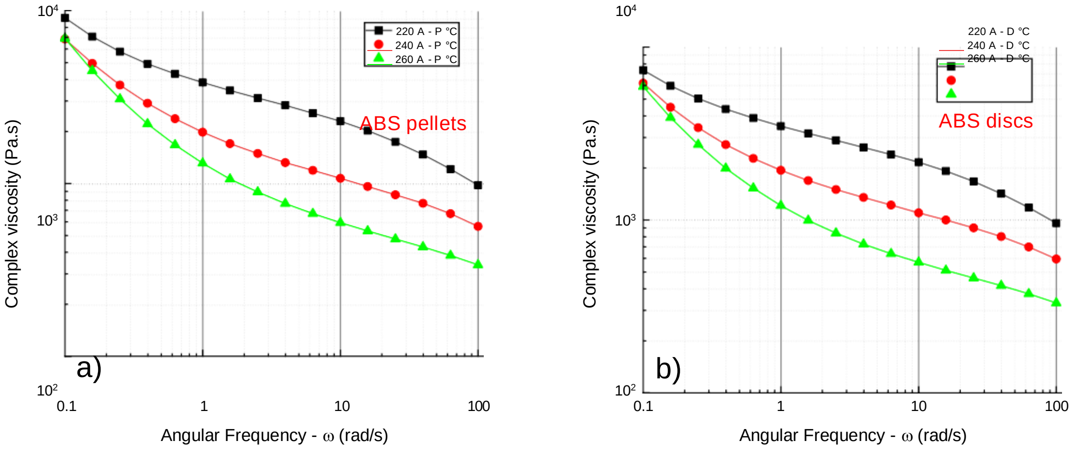

Figure 3-20. Viscosity comparison for ABS pellets and discs at different temperatures.

Slightly decreased viscosities have been seen from the rheology data for both PP and ABS discs. From PP data presented in Figure 3-19, it can be seen that viscosity difference is less for higher temperatures (220 - 240°C) which is a positive indication towards the similarities between the flow behaviour of pellets and discs. ABS rheology data have been taken from both undried and dried samples and no significant changes seen. The data presented in Figure 3-20 for ABS is from dried samples, and similar to PP no significant changes in viscosity have been spotted.

In overall, insignificant decreases in viscosities alongside with lower T_m and T_g from DSC data for discs against pellets have been found. These differences unlikely to have any effect for ultrasonic moulding experiments, as the viscosity differences are even less significant at temperatures above 220°C. The main reasons for viscosity reduction and lower transition temperatures is the additional processing step of micromoulding of discs where the polymer chains undergo cutting off some fraction of the long polymer chains which provide slightly better flow capability as suggested from rheology data.

3.10 Summary

This chapter has covered all the essential tools, techniques, and materials for pursuing an extensive process fingerprinting work for micromoulding technologies.

Principles and characteristics of state-of-the-art machining technologies have been briefly discussed by having a glance at the attempts made during the secondments and collaborative work done with external partners. Detailed technical drawings and schematics have also been provided for mould assemblies and microneedle inserts.

Thermal imaging has comprised a substantial amount of the chapter. As the technique is quite advanced and intricate, the difficulties and challenges has been discussed and detailed explanations have been given regarding the optical train and thermal images of the mould surface.

Another integral part of the chapter has been the process monitoring related sensor technologies and devices used for DAQ. This forms the cornerstones of the next chapters, as the actual data from the sensors will be used for extracting fingerprint information.

Finally the chapter concludes with rheological and thermal characterisation of two widely known materials for injection moulding applications. Parallel plate rheometry and differential thermal analysis of the materials also provide information on the main characteristics of the materials used in different forms, namely pellets and discs. No significant differences in thermal and rheological behaviour between pellets and discs have been found.

CHAPTER 4: Process and Product Fingerprints: Definitions and Methods for Extracting Information from Conventional and Ultrasonic Micromoulding

4.1 Introduction and scope of this chapter

The DAQ devices and process monitoring tools that have been discussed in the last chapter generate enormous amount of data in a manufacturing cycle of microneedle arrays. The interpretation of the process data can be somewhat challenging, because of the complex nature of highly-dynamic micromoulding processes and number of channels that produce data every cycle. However, for each sensor and process monitoring technology, the main characteristics of the plots can be studied in advance of the manufacturing of microneedles and these features can be extracted for each cycle (process fingerprint) alongside with the quality criterion obtained from metrology tools (product fingerprint).

Here, exemplar process data from each sensor and process monitoring technology or machine controller data will be provided for conventional and ultrasonic micromoulding technologies. To make best use of the large amount of process data generated from different sensors, characteristic features of the plots will be defined as specific process fingerprints. The reasons and physical importance of selected fingerprints have also been discussed and justified. Subsequently, structural features of the microneedles will be discussed and product fingerprints defined. Specifications and assembly of a bespoke, machine vision based optical measurement apparatus that is developed for microneedle inspection have been introduced and presented

4.2 Process fingerprints extracted from conventional micromoulding

The process measurement data for conventional micromoulding of microneedles can be classified and summarised source-wise as following:

1. Built-in machine sensors. These include the injection pressure and the position data from the encoder of the injection drive unit.
2. Laser displacement sensor. The position of the injection piston has been recorded with an external layer of instrumentation where it

provides better acquisition rates for capturing highly dynamic data. The increased acquisition rates allow better precision for data capture in temporal domain.

3. Cavity pressure sensor. The output of this sensor has been connected to a charge amplifier and then to the NI ethernet chassis for DAQ.

The acquisition of the data generated from the sensors described above has been initiated and synchronised using a 24 V trigger signal taken from the Micropower 15 directly. The signal is converted to 5 V and then fed to the PFI (programmable function input) port of the NI ethernet chassis.

Before introducing the characteristics of several channels of machine data and process fingerprints for conventional micromoulding, it is useful to characterise different stages of a conventional microinjection moulding process. Figure 4-1 provides important process data taken from micromoulding of PP for understanding different stages.

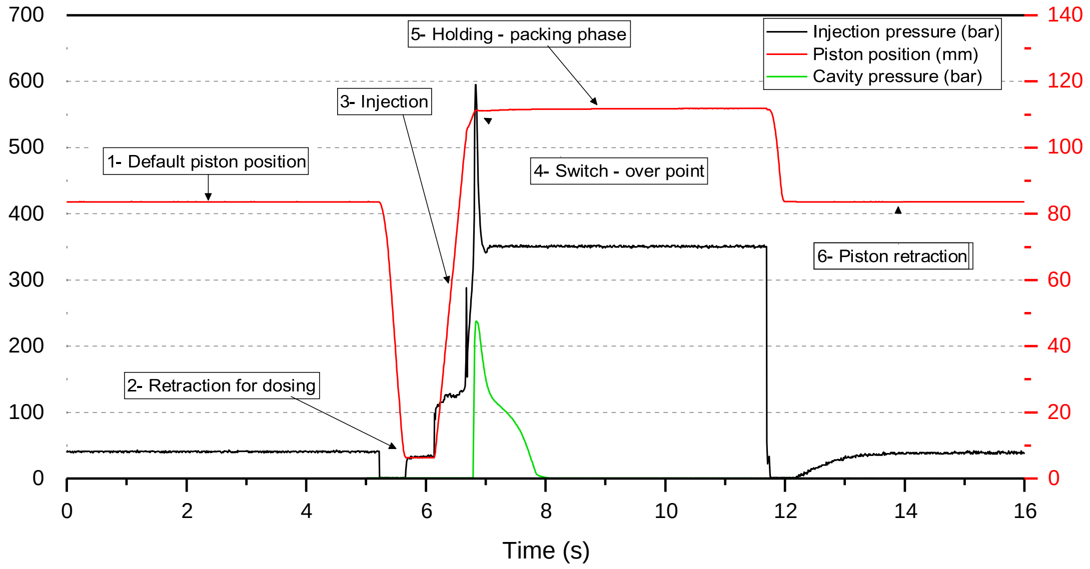

Figure 4-1. Conventional micromoulding process data taken from micromoulding of PP.

The injection piston position recorded from the encoder can be tracked in order to identify different stages of a micromoulding cycle. Acquisition of micromoulding process data has been triggered with the closing of the mould at t = 0. The injection piston stays at its default position until it has been retracted to the rearmost position for dosing of the material. There is a time interval of ~0.4 s for transferring the melt from the dosing unit to the injection channel. This stage can also be identified by the pressure values from the injection piston transducer which goes down to 0, where the preload on the transducer had been taken away by the backward movement. Injection of the molten polymer to the cavity is carried out at the stage numbered by 3 in Figure 4-1. Here, a slight increase in cavity pressure between t = 6 – 7 s indicates that the dosed material is being conveyed along the channel. An initial spike in injection pressure data can be seen in some cases and this is due to the friction and can be prevented by running the machine in full-automatic mode where the temperature gradients are stabilised. The fourth important stage is the switch-over point, where the machine switches from a velocity controlled behaviour to pressure controlled regime. For this particular moulding event, the switch over pressure has been selected as 350 bar, however, pressure increases up to 600 bar can be seen from the data. The machine quickly responds and decreases the pressure for avoiding any damage that could happen to the injection unit or the micromoulding cavity itself. A sharp increase in injection pressure signifies that the cavity is being filled, and machine control passes to the packing and holding phase to compensate the shrinkage that is happening during cooling of the material. This holding and shrinkage compensation can be seen from the slight displacements in piston position where more material is being packed to the micromoulding cavity. Holding pressure time was set for 5 s for this experiment and following that piston retraction feature of the machine has been used to prevent injection piston being stuck near the nozzle. However, this feature is particularly useful when using materials with higher melt temperatures. Alongside with the injection pressure and piston position data, cavity pressure also been included in the graph for comparison with injection pressure.

Figure 4-1 is very important in order to understand the dynamics and other physical phenomena that is going on during the process and essential to have a good understanding on process fingerprinting for conventional micromoulding process. In the following, the process data taken from different channels and sensors will be covered individually in detail for conventional micromoulding and process fingerprint extractions from the data will follow.

4.2.1 Injection pressure fingerprints

Injection pressure measurements are of crucial importance for both machine control and characterisation of the micromoulding process. In the Micropower 15, the whole switch-over and holding processes are controlled by the injection pressure data that comes from the force transducer attached at the back of the injection piston.

Similar to injection moulding, the micromoulding process is also carried out using a switch-over phase as signified previously in Figure 4-1, where the cavity is part-filled initially by a velocity controlled regime, then the machine switches to a pressure controlled regime where the filling process is controlled precisely by the measurements from the pressure transducer. This is of great importance in micromoulding since, if injection velocity is sustained there will be a sudden overshoot in the injection pressure. High injection pressures could cause damage the delicate features in the mould cavities and also the injection piston. However, microinjection mould cavities are extremely small and they are filled usually in fractions of a second and pressure peaks are usually unavoidable. Thus, Micropower 15 has been designed to switch-over to the pressure controlled regime extremely quickly and in a well-controlled manner. The machine can respond to the switch-over features on the order of μs, however due to the inertia effects and deceleration of the injection unit the actual response is usually on the order or ms.

Injection pressure measurements have been recorded for each cycle for extracting fingerprint information. The voltage output from the pressure sensor has been amplified by a Kistler 5039A type amplifier and recorded by a LabVIEW code written for micromoulding experiments.

Two process fingerprints have been extracted from the injection pressure data. The first feature to be analysed has been selected as the peak injection pressure ($\mathrm{P}_{\mathrm{inj}}^{\mathrm{p}}$) and has been extracted from each of the cycles. The second feature to be analysed from injection pressure data is the injection pressure integral ($\int \mathrm{P}_{\mathrm{inj}}^{\mathrm{p}}$) which is the numerical integration of the pressure curve in the peak region. This fingerprint has also been termed as the pressure work being carried out during injection and filling in the literature (Griffiths et al. 2011).

The features introduced above have been monitored and analysed in the literature by different authors for micromoulding applications (Whiteside et al. 2005b; Baruffi et al. 2018). However, no work has been found in the literature that uses these process measurements for microneedle feature replication in particular. Figure 4-2 depicts the calculation and detection of process fingerprints taken from a micromoulding cycle for PP using the mould cavity and microneedle features presented previously. A 100 Hz data acquisition rate has been set for this particular experiment.

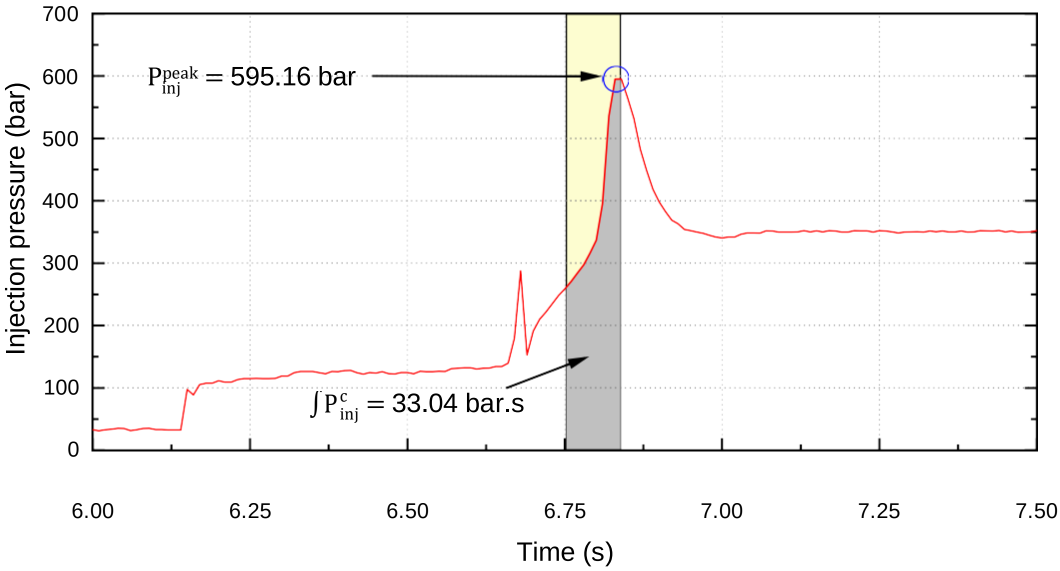

Figure 4-2. Injection pressure data for a micromoulding cycle and associated fingerprints extracted from the data.

LabVIEW scripts have been used for extracting the process fingerprints from injection pressure data. The max & Min VI from the LabVIEW library has been used for detecting the peak value and the peak value has also been selected as the datum for the integration. The integration range has been optimised by trialling different ranges and it is also dependant on the material as will be indicated in later chapters for PP and ABS. Moreover, the range has been determined in the way that it includes minimal noise and randomly occurring peaks. Integration areas have been calculated for each cycle using 1D Numeric Integration VI and the trapezoid rule. In the example, only the left side of the peak curve has been taken into account for the integration because of its better correlation as suggested by other authors in the literature (Griffiths et al. 2011). However, experience showed that the whole peak could contain useful information regarding microneedle quality, hence the integration windows are chosen according to the general behaviour of the pressure profiles.

4.2.2 Cavity pressure fingerprints

Cavity pressure measurements for each cycle have been carried out using a Kistler 9210AA indirect cavity pressure sensor which was attached to the mould in the configurations presented in Section 3.8.4 and Figure 3-15. Raw voltage signals have been converted to pressure values in bar units using the sensitivity values provided by the manufacturer of the cavity pressure transducer.

For converting voltage values to pressure, a number of simple calculations have been used. The force sensitivity (S_f) of Kistler 9210AA has been given as -10.03 pC/N. To calculate the pressure sensitivity (S_f), Equation 2.18 has been used.

$$\mathrm{S_p} = \mathrm{A} \cdot \mathrm{S_f} \cdot 0.1 \tag{2.18}$$

“A” is the area of the ejector pin in mm^2 and the formula can be written for the 1 mm ejector pin which has been used for indirect measurements. The pressure sensitivity can be calculated as:

$$\mathrm{S_p} = 3.14 \cdot 1^2 \cdot (-10.03) \cdot 0.1 = -3.14942 \text{ pC / bar} \tag{2.19}$$

A range of 5000 pC has been set for acquisitions which was available in the Dynisco CHA 4020 amplifier used for cavity pressure measurements. That range corresponds to the measurement range of 10 V, and measured voltages can be converted from pC to V by dividing the pC value to $\mathrm{S_p}$. This calculation yields a multiplication factor of 150.759 which can convert the raw data in volts directly to bar. Figure 4-3 shows the cavity pressure profile taken from the same cycle mentioned previously.

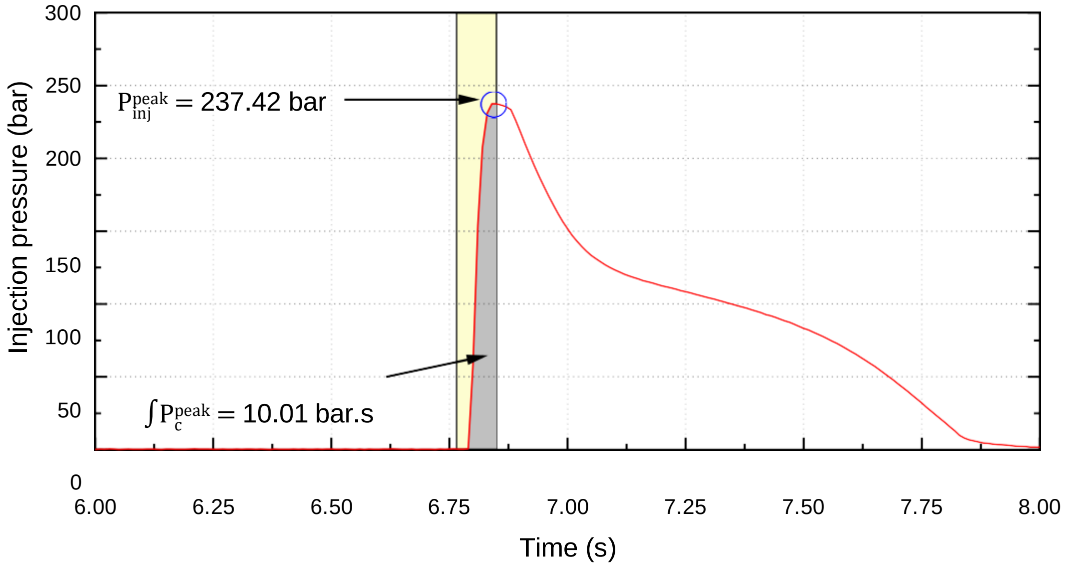

Figure 4-3. Cavity pressure profile for a micromoulding cycle and associated fingerprints extracted from the data.

Peak cavity pressure P_c^p and cavity pressure integrals have been extracted using a similar method to that used for the injection pressure fingerprints. Similar calculation procedures have been standardised and applied using LabVIEW code that extracts P_c^p and $\int P_c^p$ in array forms for every cycle. The integration range has been defined by using the pressure peak as a datum and defining a time interval that starts just before the peak, typically ~20 ms. Although the first half of the peaks during filling have been given as an examples for integration and fingerprints, depending on the experiment it was occasionally seen that pressure decays could contain some information regarding the process as well.

4.2.3 Position data from the encoder and laser displacement sensor

Displacement measurements from the injection unit provided by the encoder is not only useful for identifying different stages of the process as given in Figure 4-1 but also could contain useful information regarding the dynamics and repeatability of the micromoulding process.

Although measurements from the laser displacement sensor provide ideal measurements for characterising the position of the injection unit since it is an external measurement, encoder data available from the machine have been used in the experiments where laser displacement sensor could not be implemented at the time. In some of the experiments, the laser sensor was out of range for the measurement distance, hence, only the encoder information has been used instead. This raised questions on the information provided on the machine screen and further investigations have been carried out. The laser displacement measurements in fact showed that the machine control was moving the injection unit to a position greater towards the back where it was not supposed to be. This finding does not influence of the results; however, it signifies the importance of laser displacement measurements and proper calibrations will be carried out to correct the data on the machine screen and the encoder.

Figure 4-4 shows position data from the encoder taken during 3 different cycles belonging to the same batch of experiments.

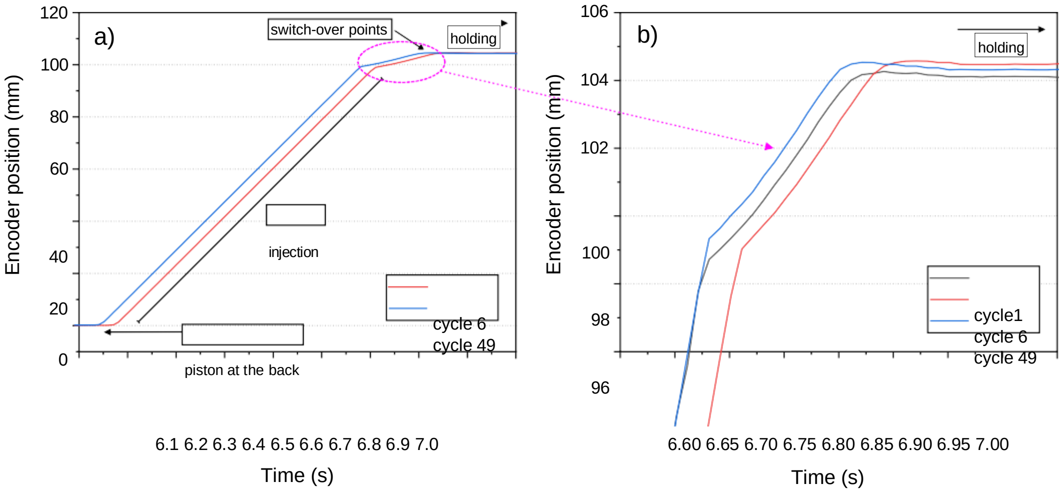

Figure 4-4. a) Position data from the encoder for 3 different cycles, b) detail of the plot in (a).

Figure 4-4a shows how the position of the injection piston or unit can change from cycle to cycle and depicts the variations that are taking place during holding. A more zoomed-in version of the curves is in Figure 4-4b, and it shows that the switch-over point for different cycles can vary from cycle to cycle. These variations can be quantified by integrating the curves after an alignment procedure in LabVIEW. Data for different cycles have been aligned and synchronised using the point where the injection starts from the very back position. The pressure peak from the injection pressure data has been used as a datum for integration window. After the alignment, the curves given in the detail in Figure 4-4b can be integrated within typically 20 ms range and compared.

Another point of interest in the plots in Figure 4-4 is that the plateau region while the polymer is being packed and shrinkages are compensated using holding pressure. The position read from the plateau corresponds to the melt cushion position, in which bigger values suggest a smaller melt cushion. Moreover, the displacement during shrinkage compensation can also be analysed as a fingerprint and these also will give useful information regarding the repeatability of the micromoulding process. Characteristics of these process fingerprints differ at times and their extraction methods will be presented in detail in Chapter 5 for conventional micromoulding experiments.

4.3 Process fingerprints extracted from ultrasonic micromoulding

The process data that is generated from the ultrasonic micromoulding process can be classified in terms of their source as following:

1. Thermal imaging data. The filling and temperature distributions of the ultrasonically plasticised polymer is quite complex and contains important information.
2. Machine data. Sonotrode frequency, power output, injection force and piston position can be extracted by built-in sensors or measurement interfaces that comes from the machine directly. They have been recorded using a network connection with the machine computer.
3. Cavity pressure. The output of this sensor has been connected to the ethernet chassis and captured using a LabVIEW based code.

All three of the measurement types given above have been synchronised with the start of sonication. A 24 V signal has been tapped to a 5 V converter, and this signal has been fed to the trigger port of the thermal camera and PFI (programmable functional input) port of the DAQ chassis.

4.3.1 Thermal imaging process fingerprint(s)

Plastication of polymers using ultrasounds under applied force is complex in nature due to simultaneous flow and melting of the feedstock. Often times, flow front of the melt often progresses asymmetrically into the circular cavity and towards the end in ultrasonic micromoulding. Subsections given in the following present examples on thermal imaging characteristics of PP and ABS as they are significantly different.

It is worth pointing out that the absorption of the IR photons within the sapphire window have not been taken into account for thermal imaging acquisitions, and actual temperatures are expected to be higher than the measured values. However, since the purpose here is to do a comparative study on temperature curves and fingerprints, the calibration procedures have not been carried out and the acquisitions were done with common settings.

4.3.1.1 Thermal imaging of PP

The asymmetric emergence and progression of the flow front in the mould cavity during ultrasonic micromoulding experienced to be a more severe effect during moulding of PP. The reasons could be attributed to the semi-crystalline nature of PP as they have a sharp melting point and they require more energy to be plasticised. The sharp melting point makes the melting stage difficult to control and the material locally melts at random points. Moreover, once the material reaches to a certain viscosity the discs in the sonication chamber which are closer to the injection plunger will be colder. Combined with the latent heat feature of semi-crystalline PP, these effects thought to be causing the very unequal distributions in temperature during ultrasonic moulding as can be seen from Figure 4-5 (Gulcur et al. 2018).

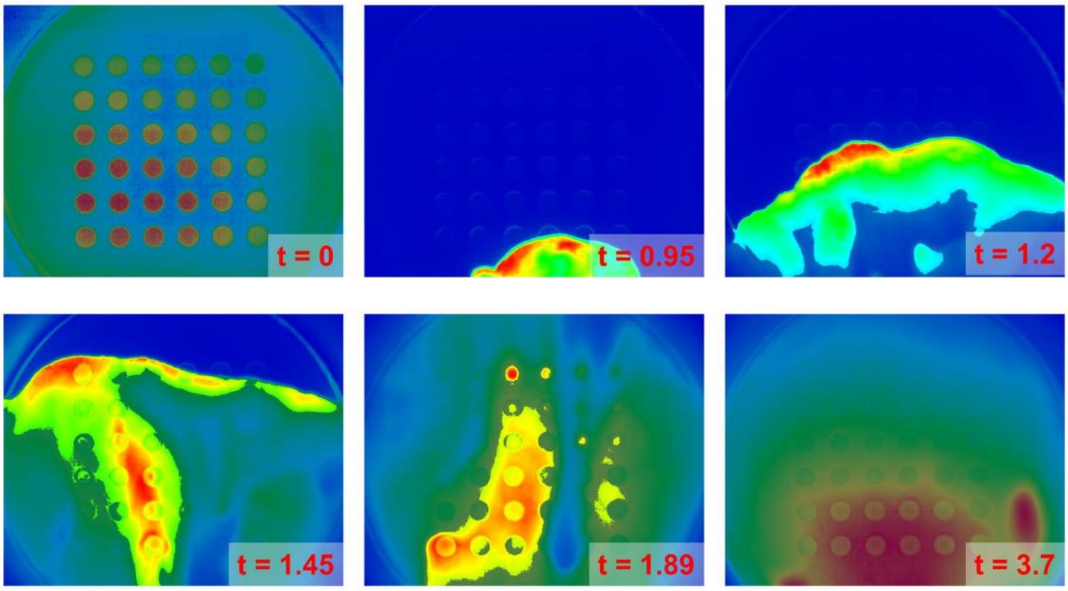

Figure 4-5. Thermal images taken during ultrasonic micromoulding of PP.

A variable scale used for the thermal images shown in Figure 4-5 for each scene. The presence of unequal temperature distributions have been proved during ultrasonic moulding of PP according to thermal images. After the cavity filled at approximately t = 2 s, the sonication is sustained and a significant heating effect can be seen near the gate. Thermal imaging acquisitions for ultrasonic moulding events have been carried out at 100 frames/s at the maximum imaging area of 640x512 pixels that corresponds to approximately 9 x 7 mm area where the microneedle array is centred in the middle. An emissivity value of 1 have been used for all thermal imaging acquisitions since polymers usually have high emissivity values and to make a comparative analysis.

4.3.1.2 Thermal imaging of ABS

Being an amorphous material, ABS has a more favourable melting behaviour compared with PP and glass transition behaviour results in relatively homogenous micromoulding flows. Thermal imaging acquisitions have been taken for ultrasonic micromoulding of ABS (Figure 4-6) with the same camera settings used for PP experiments.

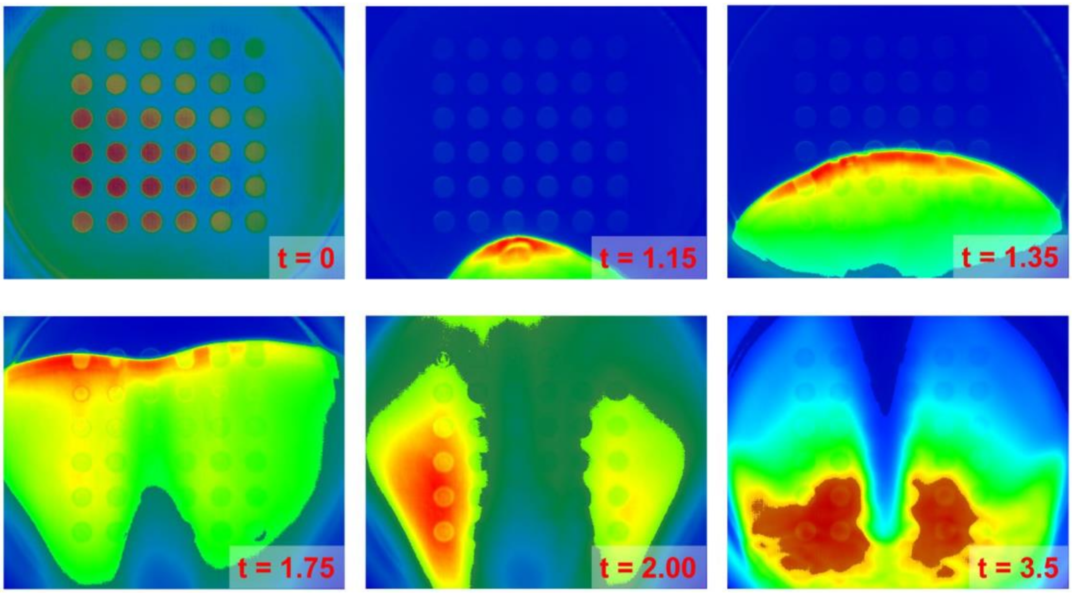

Figure 4-6. Thermal images taken during an ultrasonic micromoulding process of ABS.

4.3.1.3 Extraction of thermal imaging fingerprints

The temperature values read from the thermal camera can be recorded from certain regions of interest (ROI) for extracting process fingerprints. As the temperature distributions in ultrasonic micromoulding can be quite complex, a rectangular region of interest has been drawn which covers the whole area of 6x6 microneedle cavities to simplify the analysis. Similarly, ROIs can also be drawn near the gate and towards the end of the cavity for extracting additional process fingerprints from thermal imaging. Having different temperature values from particular ROI allow comparison of heating effects within the cavity. Temperature information from the gate has been occasionally omitted for process fingerprinting because of its similarity to 6x6 ROI data. An example temperature profile and ROI for extracting thermal imaging process fingerprints from ultrasonic moulding of PP is given in Figure 4-7.

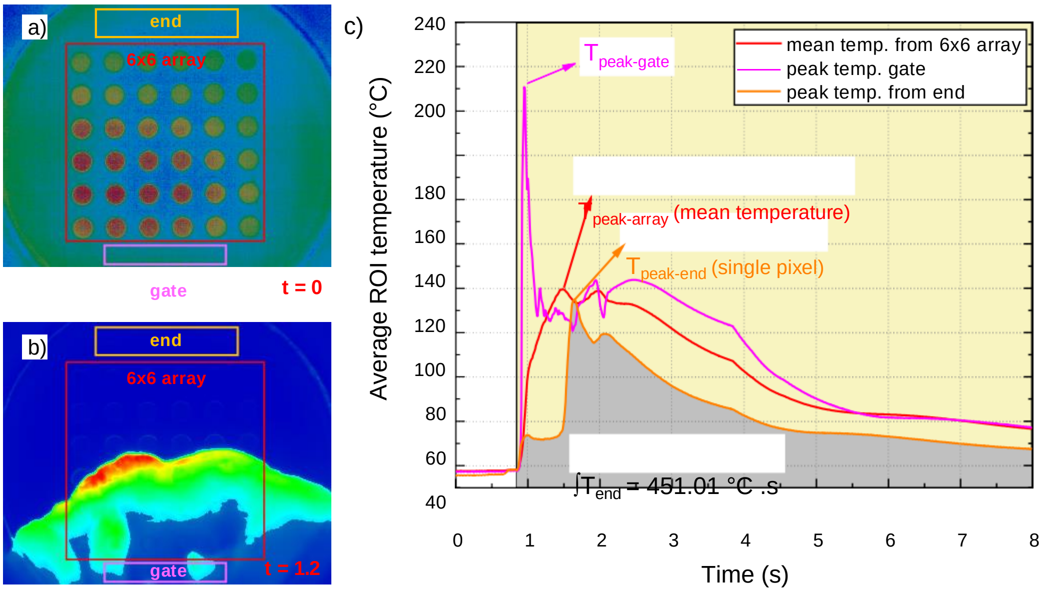

Figure 4-7. a) Regions of interest examples for thermal imaging, b) Polymer melt progression towards the end of the cavity, c) Temperature profiles obtained from three different regions of interests of 6x6 microneedle area, the gate, and the end of the cavity. Peak temperatures and an example integration are indicated for fingerprints.

The temperature profiles in Figure 4-7c shows the average temperatures coming from the particular region of interest at a given time. The measured temperatures show dramatic changes and peaks depending on the region of interest. For instance, temperatures can be as high as 210°C measured when the melt enters the mould cavity from the gate region. Whereas average temperatures of only 120°C has been recorded from the ROI which covers the 6x6 array area. It should also be noted that the gate region is the closest to the sprue and hence sonication results in higher temperature values from 6x6 array and end of the cavity. Moreover, the gate ROI is significantly smaller in area than 6x6 microneedle ROI which could result in a higher temperature when averaged.

Peak temperatures and integration areas from temperature curves have been selected as fingerprints from the thermal imaging acquisitions as indicated in Figure 4-7c. In the initial work carried out, it has been seen that peak cavity temperatures are proportional to the interfacial heating (Gulcur et al. 2018). Likewise, the integration of the temperature curve obtained from the ROIs yields values that are proportional to the total heat energy given to the system, which could be useful for obtaining indicators for replication. Process fingerprints to be used this thesis from thermal imaging are summarised in Table 6.

Table 6. Process fingerprint descriptions that are extracted from thermal imaging acquisitions.

Process fingerprint	Units	Characteristic
$\mathrm{T}_{\mathrm{p-array}}$	°C	Peak temperature from 6x6 array
$\mathrm{T}_{\mathrm{p-end}}$	°C	Peak temperature from end
� $\mathrm{T}_{\mathrm{array}}$	°C. s	Integration of T information from 6x6 array ROI
� $\mathrm{T}_{\mathrm{end}}$	°C. s	Integration of T information from end ROI

4.3.2 Process fingerprints from machine data

Machine data have been captured for each cycle including sonication frequency, power consumption and piston position for ultrasonic micromoulding experiments. The interactions between these three physical measurements are complex during an ultrasonic micromoulding process. The plots for these parameters also shown on the machine screen as they give information regarding how the process is carried out, although the software and the machine lacks a feedback system to adjust itself and carry out in-line quality checks for the micromoulded parts. An example of process data taken from the ultrasonic micromoulding cycle of a microneedle array, with the dimensions indicated in Figure 3-8, is given in Figure 4-8.

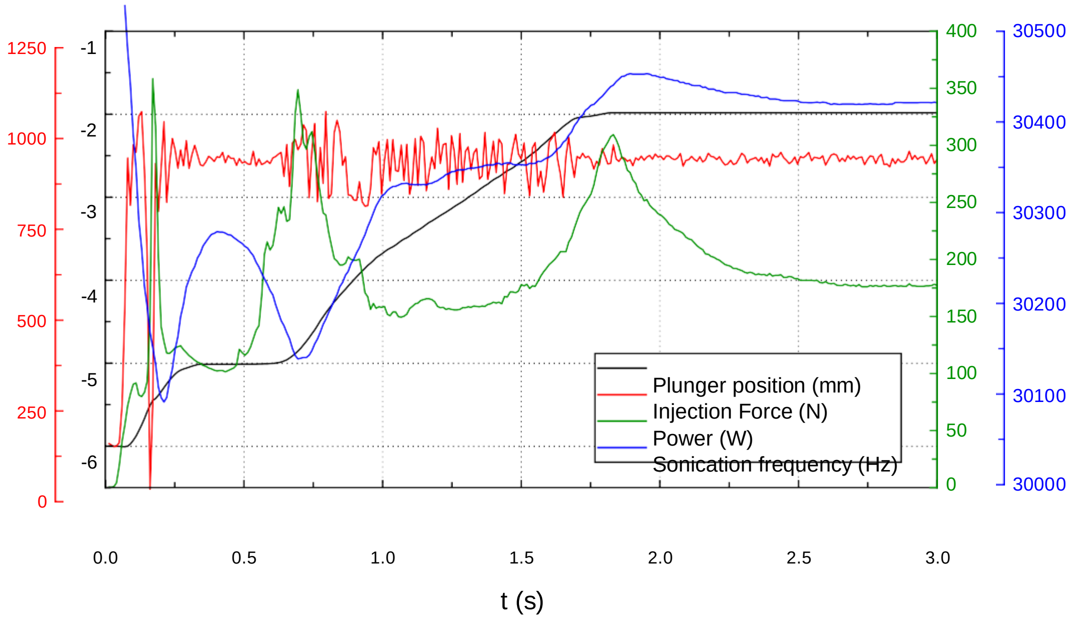

Figure 4-8. Process data taken from ultrasonic micromoulding machine. The sonication duration was 3 s.

The process data that are measured during an ultrasonic moulding process change drastically depending on each other as can be seen from Figure 4-8. Ultrasonic frequency and hence power consumption, are dependent on each other and undergo increase and decreases in different stages of the process. The main reason for this is that the feedstock undergoes elastic compression, melting and solidification stages. In each of these stages the stiffness of the material is different and hence, the sonication related outputs are affected as a result.

In the following, the channels that have been used for process fingerprinting from ultrasonic micromoulding machine data will be covered in detail in order to explain these physical phenomena alongside with the process fingerprints selected. It will be shown that some process fingerprints have been eliminated and replaced with better candidates.

4.3.2.1 Process fingerprints extracted from piston position data

Different stages of an ultrasonic moulding process can be identified by interrogating the piston position data. Disc shaped preforms provide a convenient flat surface for the first contact to be made by the sonotrode so that the compression, melting (also injection) and packing phases can be identified easily. The position information that is taken from ultrasonic moulding of a PP microneedle component is plotted against time in Figure 4-9.

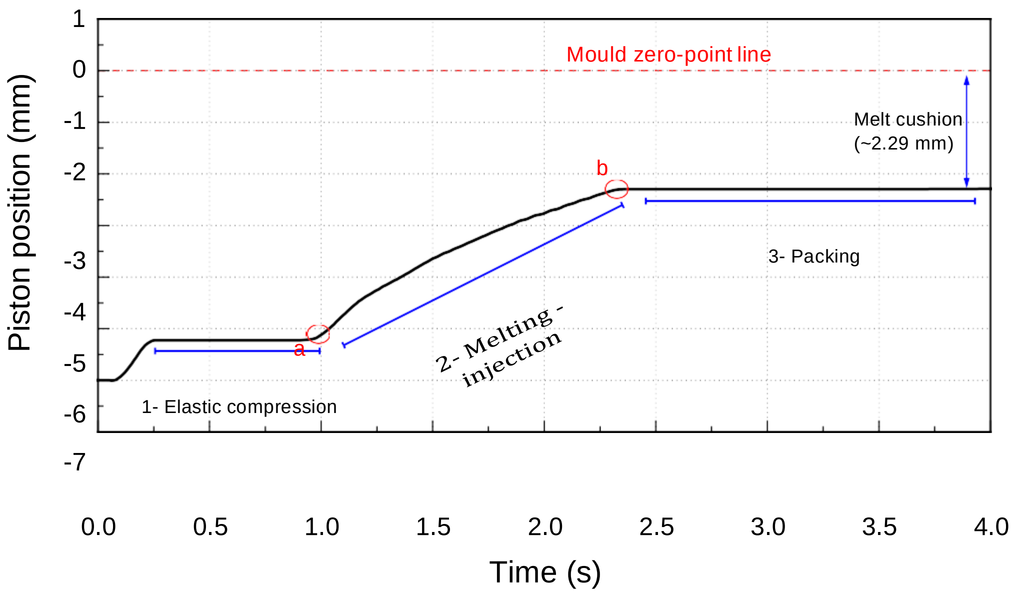

Figure 4-9. Piston position vs time for ultrasonic micromoulding process of a PP microneedle part. Sonication time is 4 s.

Characteristic regions of the piston position are indicated in Figure 4-9. Before the micromoulding process start, the piston stays at its default position, -6 mm. This is because the amount of feedstock equals four 1.5 mm thick PP or ABS discs and after the dosing, the surface is flush with the bottom mould surface. The moulding process starts with initiation of the sonication from t = 0 until t = 4 s. The piston starts to move upwards towards the sonotrode, compressing the polymer feedstock against the vibrating horn. The reason of the initial movement of the piston from -6 until ~ -5.22 mm is that the ultrasonic horn stays approximately 1 mm above the zero-point line where the two mould halves coincide. As indicated, discs in solid state undergo elastic compression against sonication for approximately 0.75 s. At around t = 1 s, sufficient energy has been given to the feedstock and the material starts to flow as can be inferred from the position of the piston. That stage is termed as the melting - injection phase the flow of the material continues until the position reaches x = -2.29 mm. After the melting - injection phase is complete the piston no longer moves, however, it continues to apply force against the vibrating sonotrode which facilitates the packing of the part. In this stage, the sonication energy is sustained and ultrasonic energy is transmitted from sprue towards the runner and then the gate of the part providing additional heating for better replication of the micro-nano features. It should be noted that this packing is more effective for obtaining better replication near the gate rather than towards the end of the cavity. This is because of the attenuation of the ultrasonic waves resulting in lower melt temperatures.

Two process fingerprint candidates have been selected and extracted from piston position data. V_{piston} is the average injection speed calculated from the slope of the curve from point a to b as indicated in Figure 4-9. All of the ultrasonic micromoulding experiments performed using disc shaped preforms, and hence main features in overall and point a and b are detectable for each cycle. In this particular micromoulding case for Figure 4-9, V_{piston} is equal to 2.03 mm/s. Regardless, it will be seen in Chapter 6 that the detection mechanism for obtaining V_{piston} is not always reliable, hence different solutions and attempts must be made to make good use of piston position information.

The second fingerprint is the deviation of the piston from the best sample ($\int \Delta x$) which has been extracted after a number of operations that based on comparison of the samples within one batch to the best sample as given in the following:

1. Since the main quality criterion of the parts is the microneedle height, the best sample with highest average microneedle height has been selected.
2. Piston position data of the other samples within the same batch have been subtracted from the best sample.
3. The differences (Δx) have been plotted against time and have been integrated. Area of the integration is the deviation of the piston ($\int \Delta x$) and it quantifies how far the inferior sample deviates from the ideal curve.

Figure 4-10 shows an example on how the analysis is carried out. The plot in Figure 4-10a indicates the best or ideal filling profile (black curve) for the position of the piston where the steepness of the filling and injection phase is quite distinguishable. These differences are quantified in the plot given in Figure 4-10b, where the reference or ideal sample is represented with a flat, dashed line. During integration of Δx values, the absolute value of the integration is calculated and taken into account where both positive and negative deviations are present from the best curve. The correlation plot in Figure 4-10c shows that by looking at the ∫ Δx values the average needle height for the microneedle arrays can be predicted. The semi-crystalline structure of the polymer manifests itself as a sharp melting point, resulting in a lack of homogeneity of the polymer melt during sonication. This was confirmed with unequal temperature distributions from the thermal imaging experiments. The flashing effect has also been encountered during ultrasonic moulding of the parts. Because of the wear on the piston and sonotrode sleeves, the plasticised material tends to fill the voids on the sides of the piston and the sonotrode, resulting in different filling profiles. The effect seemed to be less detrimental when using amorphous polymers, e.g. ABS.

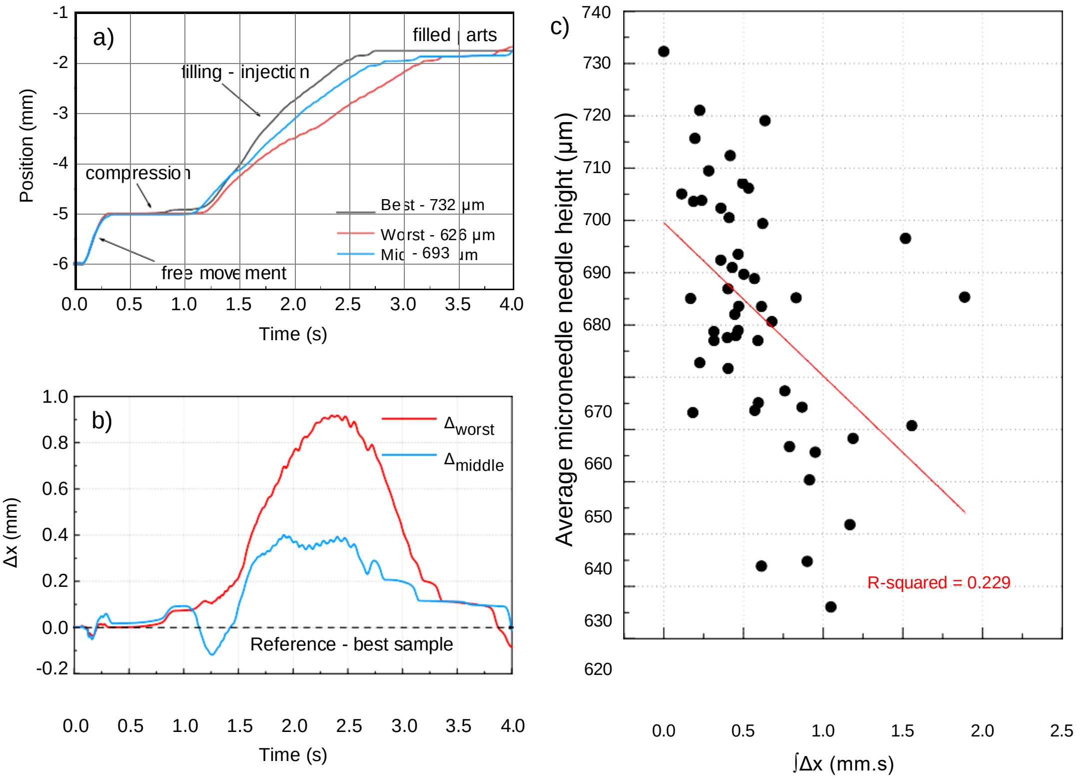

Figure 4-10. a) Example curves for obtaining the deviation of the piston from the best sample ∫ Δx. The plot shows the differences in piston position between the best, worst and medium-quality parts. b) Graph plotted by subtracting the inferior samples' data from the best sample. The graph on the right shows a correlation plot between the average needle height and ∫ Δx process fingerprint.

Each stage of this analysis in the figure has been carried out using a LabVIEW code which makes use of manipulation of multiple columns of data and extracting the fingerprint information directly. From Δx data which can be seen from Figure 4-10b, there are irrelevant parts of data which belong to the elastic compression or packing phase. It is possible to set cut-offs on each side for time information and best-sample comparison can be done only for the filling-injection phase to have better correlations.

4.3.2.2 Sonication energy and average sonication frequency

Presented in Figure 4-8 was also an indicator of how the sonication frequency could change in an USM process during different stages. In each of the three stages, the feedstock has different stiffness and capability to transmit the ultrasonic waves affecting the sonication frequency.

The ultrasonic stack has been tuned to 30 kHz with the current sonotrode design by the manufacturer. Any change in the length of the sonotrode or external load (force) will change this resonant frequency. For interpretation of the changes in sonication frequency, a frequency plot is given alongside the piston position and power consumption in Figure 4-11. Two fingerprints have been extracted from the data accordingly.

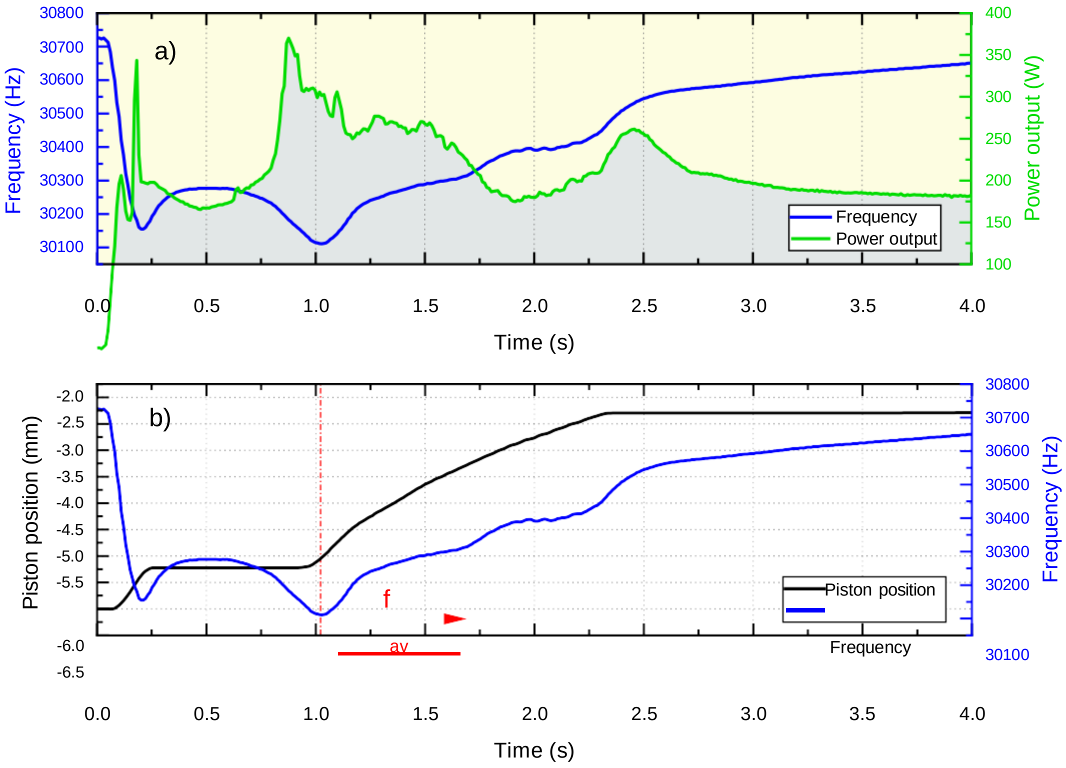

Figure 4-11. a) Sonication frequency and power output curves for an ultrasonic micromoulding event. Grey area under the curve yields the sonication energy given to the system in joules. b) Plot showing the sonication frequency and position of the piston for an ultrasonic micromoulding cycle.

A resonant frequency of the ultrasonic horn is the frequency where the transducer draws the maximum current which is in phase with the applied voltage. The resonant frequency of the ultrasonic stack changes with the length of the horn. When the ultrasonic moulding process is considered, effects including thermal expansion, the force applied by the injection plunger and stiffness of the material will alter the sonication frequency throughout the process.

In Figure 4-11a, sonication frequency and power consumption of the ultrasonic generator is presented. In Figure 4-11b, the piston position is given alongside with sonication frequency for the same ultrasonic micromoulding event. Power consumption is proportional to the current drawn by the generator and this is the main reason that power peaks or dramatic increases are seen when the sonication frequency goes towards 30 kHz as can be seen from Figure 4-11a. The sonication starts approximately at 30700 Hz, and as a result of the free upward movement of the piston it falls dramatically towards 30 kHz until the first contact with the feedstock and the sonotrode made. The first contact with the sonotrode and the feedstock has been made at approximately t = 0.25 s. This is where a slight increase and a plateau in sonication frequency are seen until the elastic compression ends. At t = 1 s, the polymer starts to flow and as a result of the decreased stiffness of the material the external load on the sonotrode is also decreased and sonication frequency tends to fall towards 30 kHz again. At this stage the molten polymer is pushed towards the runner and mould cavity where the plasticised material already tends to transfer the heat energy to the mould and could solidify. Because of this resistance to flow the sonotrode is under force load once again and sonication frequency tends to increase. The cavity is filled at t ~ 2.3 s since the piston stays fixed at approximately x = -2.5 mm. Since it is filled completely, the effect of the force load on the ultrasonic stack is more prominent where a steep increase in sonication frequency is seen. In the packing phase frequency tends to increase linearly as the injection for is sustained for better packing. The packing phase is the stage the force is likely to cause overloading of the ultrasonic stack because of this linear increase. Moreover, sonication should cease at a certain time to prevent overloads and degradation of the micromoulded part.

Two process fingerprints have been extracted from power consumption and sonication frequency data. $\mathrm{E}_{\mathrm{sonic}}$ is the area under the curve for power consumption plot and gives a number in joules signifying the amount of sonication energy given to the system for one part. f_{av} is the average sonication frequency after the feedstock starts to plasticise. As can be seen from Figure 4-11b the decrease in frequency is quite distinct (indicated by a red, dashed line) after the material starts to flow and it has been detected using a LabVIEW based script for each cycle. Starting from this point until the end of sonication, the frequency has been averaged to observe at what frequencies the micromoulding process was being carried out.

4.3.3 Cavity pressure fingerprints(s) for USM

Cavity pressures for ultrasonic micromoulding have been measured using the same amplifier and measurement combination as was used for conventional micromoulding allowing the comparison of moulding pressures for two different micromoulding techniques. An example cavity pressure measurement for ultrasonic micromoulding process is given in Figure 4-12. Sonication frequency and piston position are also plotted for better understanding of different stages and features of the process.

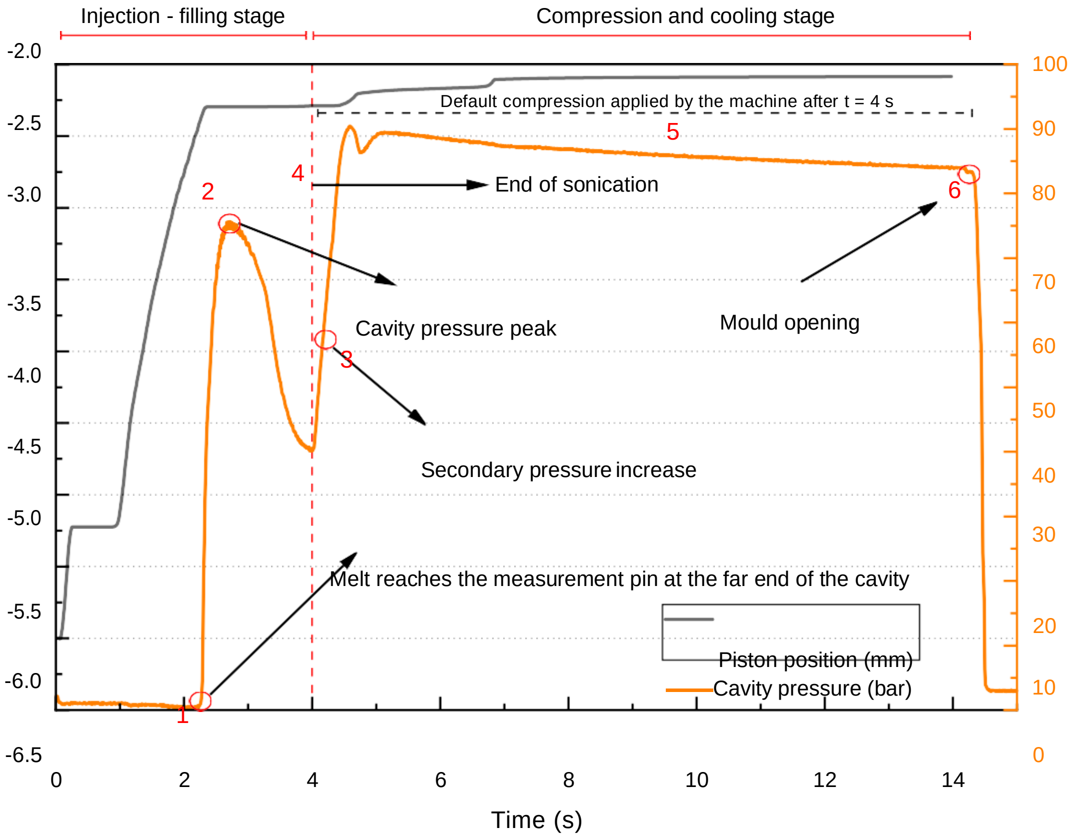

Figure 4-12. Cavity pressure, piston position and sonication frequency data recorded from an ultrasonic micromoulding cycle of PP.

Cavity pressure is seen to change drastically throughout an ultrasonic micromoulding process. In the figure, important features are numbered and indicated. At point 1, the polymer melt reaches the farthest end of the cavity and the ejector pin surface at the back of which the pressure sensor is attached. A sudden increase in cavity pressure occurs while the molten material is being packed and the cavity is completely filled. This can also be seen from the constant piston position. Sonication is sustained until t = 4 s, where more heat energy is provided towards the sprue, runner and gate. However, this does not affect the end of the cavity as the polymer on the ejector pin is now solidified and a decrease of pressure is observed. After the sonication, the machine applies 500 N force with the injection plunger by default and additional packing is provided (point 3). Slight movements have been seen in the piston position as this force is active. However, this movement does not have an impact on neither the packing of the main circular cavity or the microneedle features as the sprue region might be still slightly molten. Rather than replication of the micro features, this compression contributes to the flashing effects around the sonotrode and injection plunger.

The melting and thus injection behaviour could change in ultrasonic micromoulding due to the uneven distributions of temperatures and viscosities of the polymers. These effects also result in a change of cavity pressure profiles from cycle to cycle and hence micro-nano features replication. Therefore, process fingerprints have been defined and extracted from cavity pressure curves. The point of interest in cavity pressures is the data where the sonication is present.

The peak cavity pressure (P_c^{peak}) and peak cavity pressure integral ($\int P_c^{peak}$) have been selected as the process fingerprints. LabVIEW scripts have been written for extracting these values from each cycle. Peak cavity pressures have been detected using maximum - minimum and index array functions. For calculating pressure integrals, once again peak values were considered as a datum and width of the integration has been set according to the increase in the first derivative of the pressure value. The integrations have been calculated using the numeric integration function available in LabVIEW library with trapezoid rule. Figure 4-13 shows an example for extracting cavity pressure fingerprints.

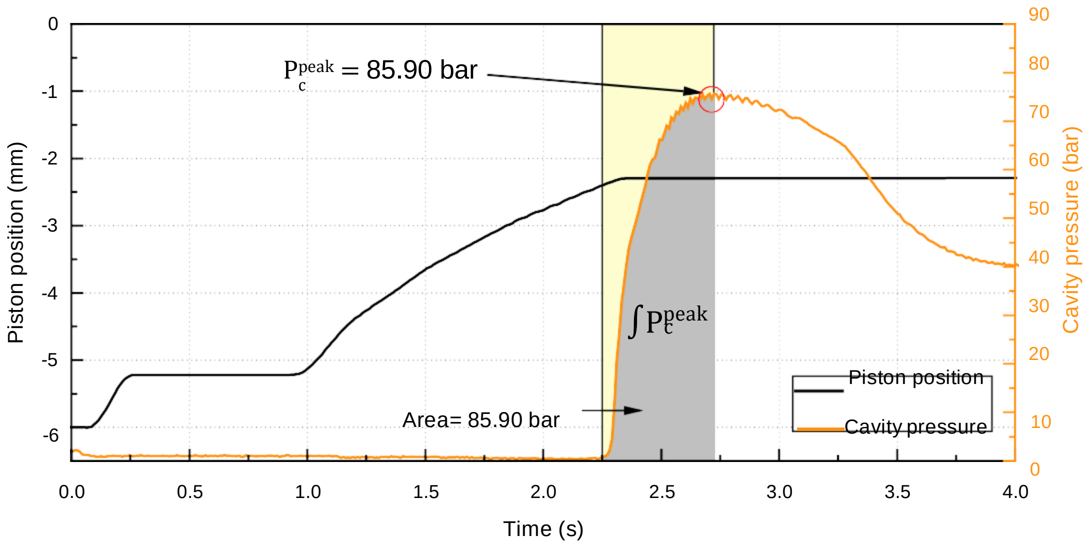

Figure 4-13 Cavity pressure profile and process fingerprints extracted.

4.4 Product fingerprints for microneedle arrays

Process fingerprinting for zero-defect micromanufacturing of miniature parts also has to include quality criteria for evaluating the correlations and success of the process. Micromanufactured parts are usually extremely small products with dimensions or tolerances on the order of a few microns in some cases. Surfaces with periodic micro and nano features also fall into this category where the product's main dimensions could be tens of millimetres. In the light of this information, the product fingerprints can be defined as geometric entities or functional properties that could be quantifiable with a measurement technique.

Baruffi et. Al. studied microinjection moulding and attempted to provide a framework for in-line quality assurance using process fingerprints for an extremely small part with dimensions on the order of hundreds of microns (Baruffi et al. 2018). The micromoulded product included a tapered through hole with 1 mm in length and the hole progressed to a diameter from 100 to 420 µm. The diameter of the part on both sides, the wider hole and amount of flash occurring on the smaller on the smaller hole were selected as the product fingerprints. The authors report correlations between the pressure integrals and particular product fingerprints such as the amount of flash on the top of the part.

Surface roughness parameters have been correlated with super hydrophobicity and reported as product fingerprints for ns-laser textured steel surfaces in the literature (Cai et al. 2019). The authors present a dimensionless surface feature obtained from confocal microscope measurements where a ratio between maximum height of profile (Rz) and mean width of the profile elements was calculated and found to have correlations with the hydrophobicity of the surfaces.

In the following, product fingerprints for microneedle arrays have been given and detailed information regarding the measurements are provided. An additional nano-fingerprint method have also been proposed.

4.4.1 Average microneedle height

The selected product fingerprints should be sensitive to the process conditions and machine dynamics in order to be detected alongside with the variations from other process measurements. When microneedles are considered, mould cavities with high aspect ratios are ideal for this purpose. The second important thing to consider is that the product fingerprint should represent the functionality of the part. In that sense, height of the microneedles will represent the success of a micromoulding cycle in terms of its functionality. Therefore, the average microneedle height ($\mathrm{h_{avg}}$) from one microneedle patch of 5x5 or 6x6 configuration has been selected as the main product fingerprint for this work.

Initial tests for process fingerprinting attempts in ultrasonic micromoulding have been carried out using the microneedle insert with the 5x5 configuration. For the assessment of the microneedle cavity depths a PDMS casting method have been used as mentioned previously. Detailed images of the PDMS replica of 5x5 microneedle mould insert is given in Figure 4-14.

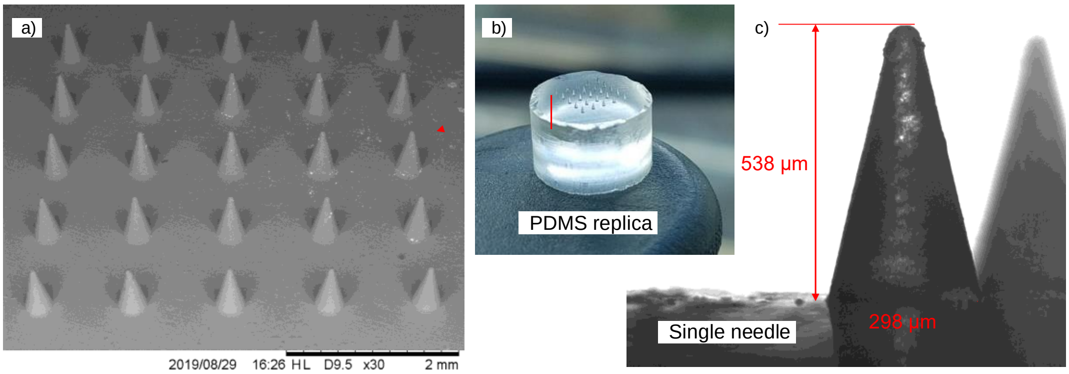

Figure 4-14 a) SEM image of the 5x5 PDMS replica (Hitachi TM-3000), b) PDMS replica of 5x5 mould insert, c) Telecentric optical image of a single needle from the same replica.

The blunt tips of the EDM-machined microneedle cavities can be seen from the optical image given in Figure 4-14c. Each of the 25 needles have been measured manually using the optical imaging technique which will be introduced in the following subsection. The average needle height from the PDMS replica has been found to be 535.9 µm. Assessment of the tip radii using the optical apparatus was not possible even in the manual mode due to the challenges in edge detection mechanisms. However, the tip radius has been measured to be approximately 33 µm for the particular needle given in Figure 4-14 and observed to be consistent for all needles.

Likewise, the same PDMS casting method has been done for the 6x6 - laser machined microneedle insert to assess the depth of the microneedle cavities. SEM images of the PDMS replica has been given in Figure 3-3 previously. Demoulding of PDMS replica from the insert was challenging and evaluation of the average height have been done out of 35 needles as one of them found to be broken after demoulding. The average cavity depth for 6x6 laser machined microneedle cavities found to be 928.9 µm. Figure 4-15 shows example optical images taken from the PDMS replica.

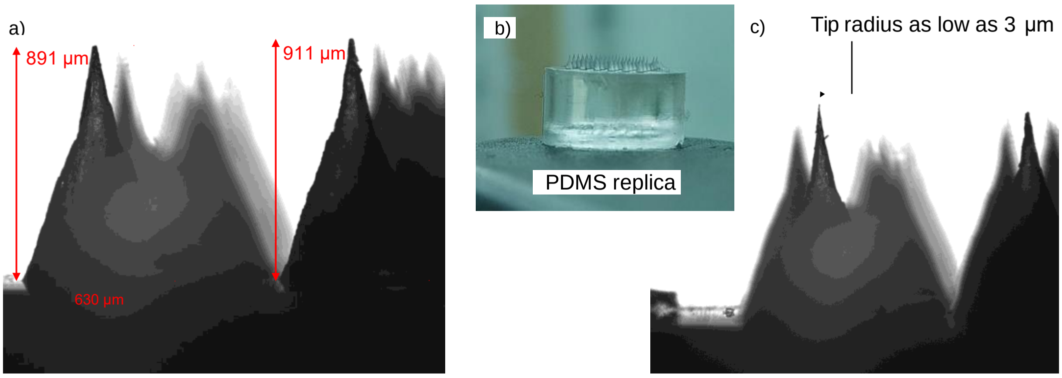

Figure 4-15 a) Telecentric optical image of some of the microneedles from 6x6 laser-machined mould insert, b) PDMS replica of the mould insert, c) Image showing some of the lowest tip radii achieved by the laser machining technique.

Slight inconsistencies observed in the height measurements of the microneedles. The height of the 35 needles changed between ~900 – 970 µm with a standard deviation of 23.73. One of the reasons for this is that some of the tips seemed to have broken during demoulding as they are extremely sharp. In overall, the shape of the tips and taper at approximately 600 µm were consistent for all microneedle cavities.

4.4.2 Telecentric optical measurement apparatus

Quality assessment of microneedles have been carried out using optical and electron microscopy techniques in the literature as the dimensions do not pose big challenges in terms of imaging the features of the microneedles (Demir et al. 2013; Larrañeta et al. 2016). However, aforementioned procedures are only viable for assessment of individual needles and are not applicable for measuring arrays of needles and automation of the measurement process must be implemented. When micromoulding process is considered, each microneedle height could be significant for assessment of the process. Therefore bespoke measurement apparatuses are needed for quantifying the replication quality of the microneedles.

Since process fingerprinting requires cycle by cycle analysis of both process features and product quality outcome, a bespoke telecentric-optical apparatus has been built for measuring each individual microneedle. The main principles of telecentric imaging is given in Figure 4-16.

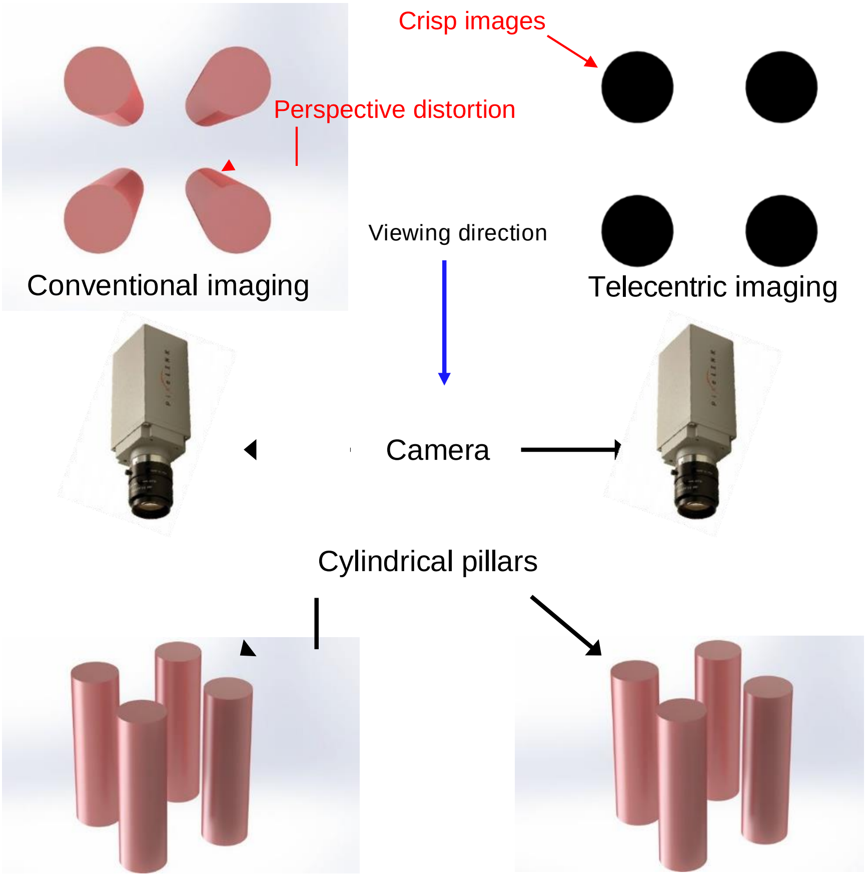

Figure 4-16. Schematic showing the principles of telecentric imaging.

As can be seen from Figure 4-16, telecentric way of imaging can be considered as a technique where a backlighting is used and shadow of the objects are captured by a camera. This can be achieved by using a backlighting source where parallel beam is generated. The objective lens also has to be telecentric for obtaining crisp images for metrology purposes.

The components of the microneedle measurement apparatus have been selected for ensuring aforementioned telecentric imaging requirements. On the illumination side, an ultra-white LED (light emitting diode) source (SugarCUBE) has been used. The illumination source has been connected with a fibre optic to the telecentric backlight illuminator (Edmund Optics). On the imaging side of the apparatus a 5x telecentric objective lens (Mitutoyo) connected to a Pixelink machine vision camera (PL-D725CU) using a C-type mount. The camera has a 2592 x 2048 resolution (5.3 megapixels) with a frame rate of 75 Hz. In the middle of the imaging and illumination sources two translational stages (Zaber Technologies) that can move in x and y directions has been used for mounting the samples. Microneedles have been aligned at a 5° inclination with respect to the viewing plane in order to be able to image the tips and the base of the microneedles. An image of the apparatus is given in Figure 4-17.

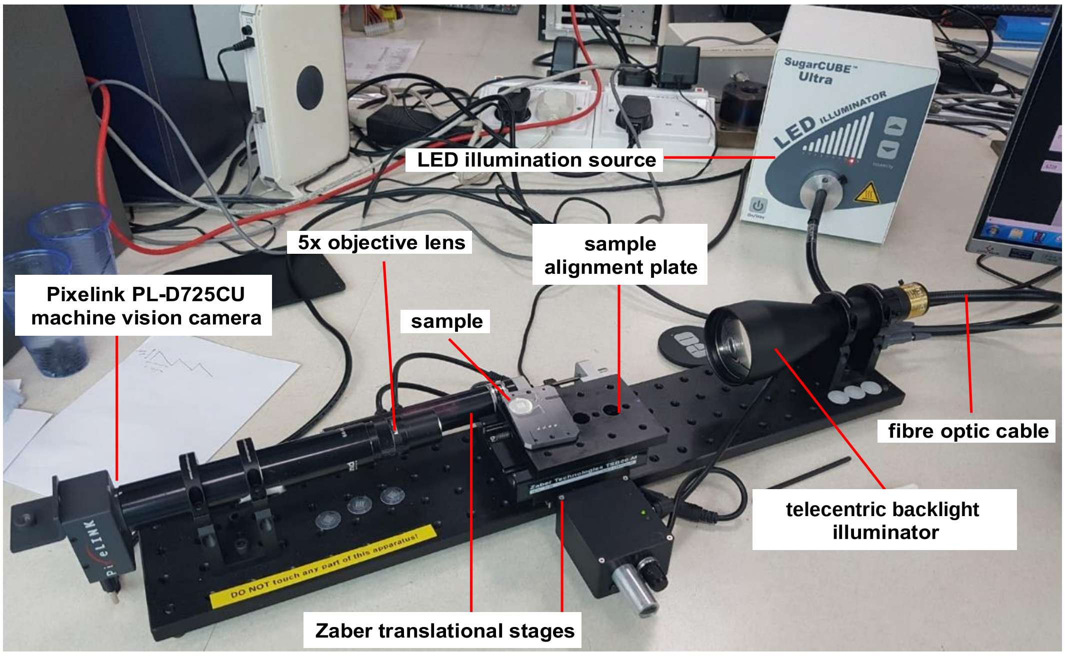

Figure 4-17. Telecentric optical microneedle measurement apparatus. All of the components have been levelled and mounted on an optical breadboard.

An in-house written LabVIEW script which was developed within the research group for a previous research project has been modified for operating the apparatus. The apparatus is capable of measuring 36 microneedles in approximately 2 minutes in automatic mode. After mounting the sample manually, the alignment has been done using the guide points calculated on the metal plate and the measurement is initiated. An overview of the software interface is presented in Figure 4-18.

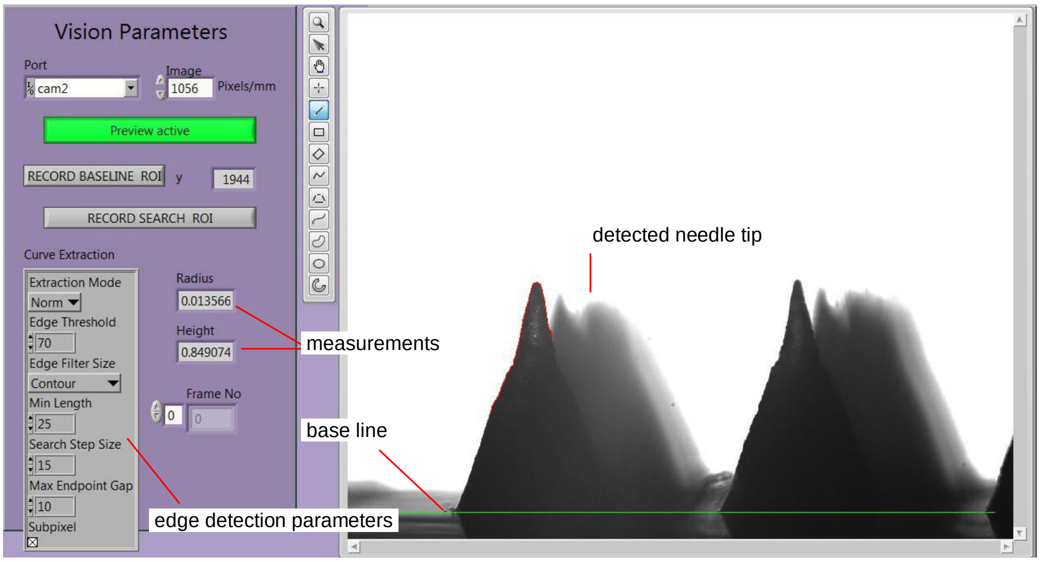

Port: cam2

Image: 1056 Pixels/mm

y: 1944

Extraction Mode: Norm

Edge Threshold: 70

Edge Filter Size: Contour

Min Length: 25

Search Step Size: 15

Max Endpoint Gap: 10

Subpixel: ☒

Radius: 0.013566

Height: 0.849074

Frame No: 0 0

Figure 4-18. LabVIEW software interface for microneedle measurement apparatus.

The system works on the principle of imaging the needles within a small depth of field where only one needle will be in focus and satisfies the prerequisite for edge detection algorithm. After the acquisition is complete for a needle in focus, the translational stages move the sample with calculated dx and dy values for focussing the next needle.

For each needle, an image in focus is captured and analysed by the edge detection mechanism. The algorithm scans the image from top to the bottom to detect the best edge based on the greyscale intensity of the pixels. After the coordinates of the edges have been found, y-axis values have been subtracted from the baseline coordinates which is set by the user in the beginning of the measurement. The distance in pixels is then converted to mm or µm by a calibration factor that is set by the user after calibrating the system with a micron-scaled calibration piece. Using the greyscale thresholds which are set for edge detection in the beginning of acquisition, only the needle which is in full focus satisfies the edge detection criteria.

4.4.3 Quantification of correlations between process and product fingerprints

It is one of the goals of this PhD project to present meaningful relationships between process fingerprints and dimensional outcome of the microneedles if there are any. This is done by plotting process fingerprints against average needle height ($\mathrm{h}_{\mathrm{avg}}$) for each cycle as x-y graphs. The relationships are usually expected to be linear, however, they can also be asymptotic depending on the physical quantity that is measured. Linear and asymptotic fitting procedures have been used for the data presented in Chapter 5 and Chapter 6 using Origin software.

It is of vital importance to show how good the fitted data represents the real phenomena happening in a production scenario. To quantify the correlations between process and product fingerprints, R-squared (R^2) values have been calculated for fitted curves where possible. This parameter is also called the coefficient of determination and is a measure of how close the actual data is to the fitted curve. R^2 changes between 0 - 1 and values closer to 1 show that the fitted curve represents the data better. Scattered data usually yield R^2 close to 0. It is worth noting that the curve fits between process and product fingerprints are valid for a microneedle height range of 0 - 930 µm in the y-axis as confirmed by the PDMS replicas for the insert.

For assessment of different process conditions and the process, two statistical terms have been calculated for product fingerprints. The first one is the standard deviation (SD) which quantifies the degree of dispersion or variation within a measurement group. While, SD quantifies the dispersion of values, the coefficient of variance (CoV) is the ratio of SD to the mean of the measurement from that group and it gives information regarding the repeatability of the process as it is standardised according to the mean.

4.5 Summary

Example process data have been given in this chapter to introduce the process fingerprinting methods for conventional and ultrasonic microinjection moulding. It should be emphasised that injection pressure, cavity pressure and laser displacement sensor data also depends on the material characteristics and can show significantly different behaviours for different materials and process conditions. Having introduced some of the process fingerprints above, the need for additional methods and calculations for extracting more relevant fingerprints could be always the case while carrying out experiments with such sophisticated machinery and micro-tooling as will be introduced in Chapter 5.

The same situation is also valid for ultrasonic micromoulding. Although main features for process fingerprints are given in the chapter for ultrasonic micromoulding, because of being a recently commercialised technology and limited availability of the literature additional process features will always be considered and covered in Chapter 6.

CHAPTER 5: Conventional Micromoulding and Process Fingerprinting for Polymeric Microneedle Arrays

5.1 Introduction

This chapter presents experiments performed for process fingerprinting and characterisation of a conventional micro-injection moulding process for manufacture of thermoplastic microneedle arrays. The experimental plan for each experimental batch is a follows:

- Setting the suitable process parameters for the circular part cavity
- Micromoulding of the parts and data collection
- Characterisation of microneedles using telecentric optical measurement system and SEM
- Process fingerprint extraction and data analysis using LabVIEW

Process data and fingerprints have been extracted and analysed based on the strategies discussed in Chapter 4 - 4.2. However, some of the work performed during the conventional micromoulding experiments made it necessary to extract and analyse additional fingerprints and process features with appropriate explanations in addition to the ones given in Chapter 4. All conventional micromoulding experiments have been carried out using the 6x6 laser machined microneedle insert since there has been an detailed study carried out in the group previously for 5x5 configuration (Nair 2014).

The work has been divided into four experimental batches, namely; m1, m2, m3 and m4. First two batches have been done in semi-automatic mode whereas m3 and m4 in full-automatic mode. Because of the availability of the technology laser displacement sensor measurements have been included only in full-automatic experiments. Details of the batches can be seen in Table 7.

Table 7. Experimental batches and main features.

Experimental batch	Mode	Material	Injection position measurements
Batch-m1	Semi-auto	PP	Encoder data only
Batch-m2	Sem-auto	ABS	Encoder data only
Batch-m3	Full-auto	PP	Laser sensor and encoder data
Batch-m4	Full-auto	ABS	Laser sensor and encoder data

Discussions in this chapter include process characteristics, microneedle replication quality assessment and process fingerprint analysis and their relevance to an in-line quality assurance scenario for conventional micro-injection moulding of microneedle drug delivery devices.

5.2 Process fingerprinting for conventional microinjection moulding in semi-automatic mode

Conventional micromoulding experiments have been carried out on the Wittmann-Battenfeld Micropower 15 micromoulding machine, together with additional DAQ hardware and sensors. In this section, initial experiments which have been carried out for identifying the main characteristics of the process and determining the process parameters correctly to produce a part with reasonable quality using PP and ABS will be discussed.

5.2.1 PP experiments (Batch-m1)

Experiments were carried out with PP (Ineos – GA12) has been presented in this sub-section providing experimental details, interpretation of the process data and process characteristics.

5.2.1.1 Selection of process parameters and preparation

In order to see how the process fingerprints behave and if they could be of relevance to the microfeature replication, reasonable parameters that will yield an average replication performance have been chosen for the initial batches as a well-defined starting point. Similar parameters that were used for making disc preforms for ultrasonic moulding have been slightly modified and used for PP microneedle experiments as given in Table 8.

Table 8. Process parameters used for moulding PP microneedles for Batch-m1.

Process parameter	Value - unit
Melt temperature	225 (nozzle), 220, 220, 210°C (hopper)
Mould temperature (T_{mould})	40, 60 and 80°C
Injection speed	150 mm/s
Switch - over pressure	300 bar
Holding pressure	350 bar
Holding pressure duration	5 s
Cooling time	5 s

The effect of process parameters on micro and nano replication during micromoulding has been long known and there are many reports in the literature (Nair 2014; Baruffi et al. 2018). Mould temperature (T_{mould}) has been reported to be a very important process variable as it affects the abrupt cooling behaviour and corresponding increase in viscosity of the material during its injection into the mould tool. Hence, T_{mould} was selected as the only parameter for experimentation of process fingerprinting for the first set of experiments. It has been known that most commonly used mould temperature values for PP is in the vicinity of 50°C. Temperatures of 40, 60 and 80°C will allow to see how the microfeature replication changes for both towards lower and higher end of usable mould temperatures.

The main criteria for making an acceptable part for experimentation has been considered as the completely filling of the circular cavity around the microneedle features. Parameters selected in Table 8 made sure that every part is of good quality in terms of completeness of the part. For instance, at switch - over pressures above 500 bar, flashing effects have been seen around the parts and hence the switch-over pressure decreased considerably to 300 bar for avoiding these effects. Injection speed has also been kept minimum for obtaining parts with reasonable quality alongside with other parameters.

Great care must be taken before micromoulding and collecting the parts regarding cleanliness of the dosing system and the injection unit. A purging material (Ambersil - Polyklene R-RTU) has been used for purging the remnants of previous materials from the dosing unit. The cleaning has been carried out first by conveying some purge material by the movement of the screw without using the injection system. After conveying ~200 g of material, the same amount has been loaded and automatic purging carried out using the movement of the piston. This step involves the dosing of the material using the screw system and pushing it out from the nozzle using an injection speed of 200 mm/s. Hence, degraded materials from previous experiments are encapsulated and pushed out from the injection channel. After this step, GA12 PP resin has been put into the hopper and the material has been conveyed using the movement of the screw. The process has been repeated more than 100 dosing and injection cycles until the material looked transparent and clear without any contaminants.

5.2.1.2 Experimental details and microneedle measurements

After setting the process parameters carefully by inspecting the visual quality of the samples and purging steps, the DAQ system has been configured for collection of the process data. 100 Hz acquisition rate has been used for acquiring process data. This batch of experiments have been run on the semi-automatic mode of Micropower 15, as the in-house written DAQ software did not have the capability to record the process data automatically at the time. This also allowed comparison of semi and full-automatic modes of the machine for later experiments.

20 samples have been discarded before collecting the actual samples for allowing settling down of the thermal gradients and other friction related effects that could arise. After stabilising the process, 20 samples have been collected for each mould temperature. The machine was kept idle for 5 minutes when increasing the mould temperatures in order to eliminate temperature gradients that could affect the injection process. Then, 20 samples have been collected as usual for each mould temperature. All 60 samples have been cut carefully from the gate and inspected under telecentric optical measurement system for the assessment of the microneedle heights. An image of a part and an SEM image taken from one of the better replicated needles (cycle 14 - T_{mould}= 40°C) can be seen in Figure 5-1. The SEM image in b) show that the machining marks on the microneedle cavity walls have been replicated completely, however the smooth surface texture towards the tip indicate that the cavity is not completely filled.

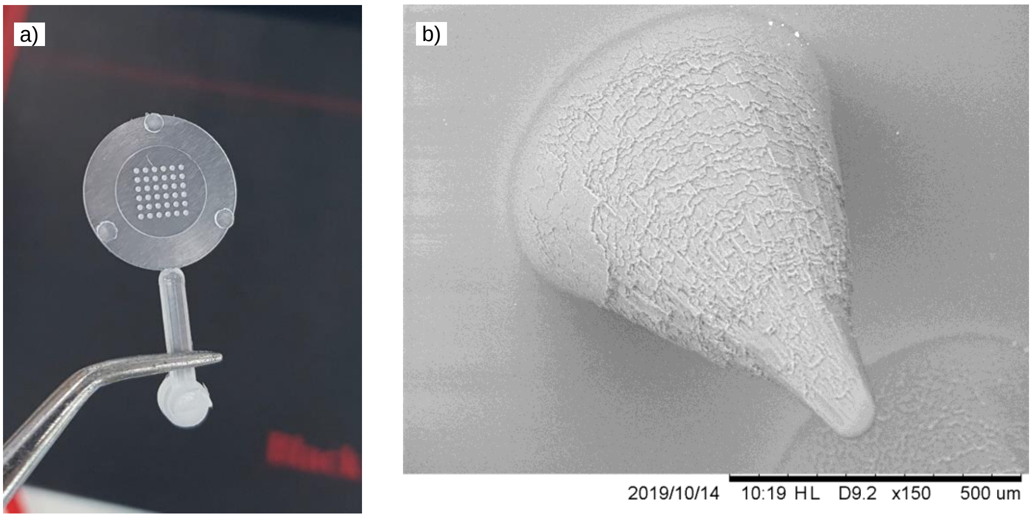

Figure 5-1. a) Micromoulded PP microneedle patch containing 36 microneedles, b) SEM image of one of the better replicated needles.

For comparing replication capabilities at different mould temperatures, standard deviation (SD) and coefficient of variation (CoV) have been calculated. Each part has 36 needles and average needle height has been selected as the quality criterion of one single moulding part or moulding cycle.

Microneedle arrays have been inspected on the telecentric optical measurement apparatus for assessment of average needle height ($\mathrm{h}_{\mathrm{avg}}$) for each cycle or microneedle patch. It can be recalled that $\mathrm{h}_{\mathrm{avg}}$ is defined as the key product fingerprint within this thesis. Figure 5-2 shows the average needle heights, SD and CoV values for each mould temperature used for PP experiments. Each set of data for mould temperatures contain 20 samples/patches, meaning 20 x 36 = 720 individual microneedles.

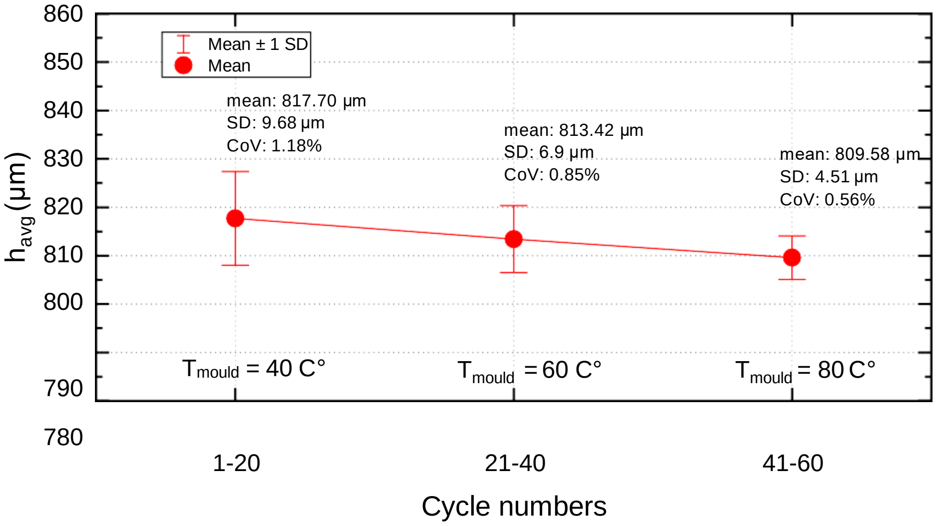

Figure 5-2. Interval plots showing the standard deviation and means of average needle height from one microneedle part (h_{avg}) for cycles 1-50 and 51-100 with different mould temperatures of 50 and 60 C° respectively. SD, CoV and mean have also been given.

It can be seen from Figure 5-2 that, there is a clear decreasing trend in average needle height from one patch (h_{avg}) with increasing mould temperature whilst the repeatability of the process increases. This is something that is completely opposite to what is expected when micro-nanofeature replication capability of the moulding and embossing processes are considered, both of which have been known for years to improve with increasing mould or tool temperature (Whiteside et al. 2003; Worgull 2009; Tosello et al. 2010; Baruffi et al. 2019). The following points can be considered for the cause of this peculiar effect:

1. Higher mould temperatures will give more time for crystallisation of polypropylene and will result in more crystallites in the parts. The amount of crystallites formed during cooling will have effect on the shrinkage, which is substantial for polypropylene up to 2.5% (Fischer 2003). Because of higher amounts of crystals that might be formed for higher mould temperatures, shrinkage could be seen more prominently causing smaller average heights in microneedles.
2. Elastic recovery of the material after cooling and packing of the part can also contribute to the differences in the height of the replicated micro features. Results in the following suggest that cavity pressure integrals taken from the whole profiles are significantly bigger for higher mould temperatures which might escalate elastic recovery effect to be seen more dominantly for higher mould temperatures.

DSC tests have been carried out to assess if there are any differences in melting enthalpies for PP which is an indicator of crystallite amount for the PP samples. Microneedles have been carefully cut and scraped off from the parts using a scalpel. Figure 5-3 shows the curves for DSC experiments carried out for PP microneedles.

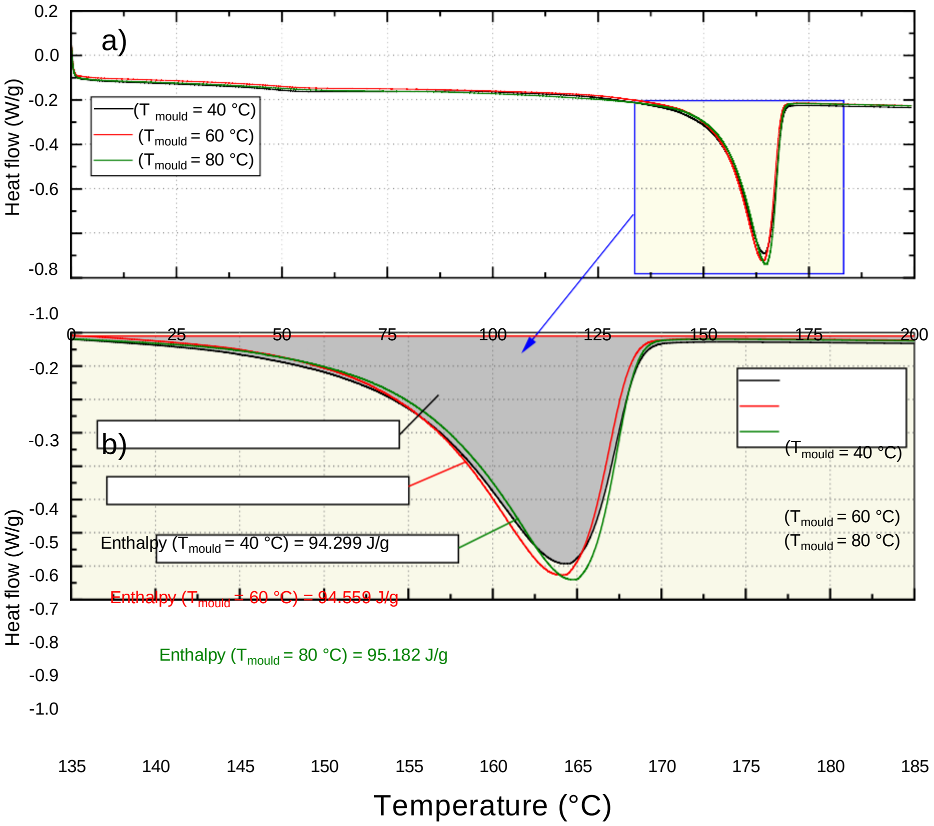

Figure 5-3. a) DSC heating curves for microneedles for assessing the melting enthalpies, b) Zoomed region of interest in the peak region for heat flow.

Three DSC measurements have been done for mould temperatures of 40, 60 and 80°C. For each measurement ~8 mg of microneedles have been used in the standard DSC pans. The heating tests have been run from 0 to 200°C with 5°C/min of heating rate. The DSC curves in Figure 5-3b may seem to be similar for three different mould temperatures, however, they show slight differences in normalised enthalpies calculated by the TA Trios software when evaluated carefully. The integrated enthalpies have been calculated as 94.299, 94.559 and 95.182 J/g for 40, 60 and 80°C respectively. The difference between the latter two values have been 0.623 J/g which suggests the microneedles moulded with 80°C have more crystallites resulting in more shrinkage in the samples and microfeatures. It should also be considered that the shrinkage will be particularly more dominant in the main axis of the conical structure which could affect microneedle measurements.

It should also be noted that the standard deviation in $\mathrm{h}_{\mathrm{avg}}$ for lower $\mathrm{T}_{\mathrm{mould}}$ given in Figure 5-2 is considerably higher than the samples moulded with higher mould temperatures. Apart from the effect of crystallites and recovery, this variability can also be attributed to the surface finish of the microneedle cavities, which could be different from one another. Figure 3-3 showed that although the surface finish and quality of the microneedle cavities from laser machining are quite acceptable, the difference in surface roughness from cavity to cavity could exhibit variable cooling rates during moulding. Combined with the abrupt solidification of PP and also shrinkage alongside with recovery effects, the high CoV in average microneedle height is reasonable for lower mould temperatures of 40°C.

Figure 5-4 shows a telecentric image of the microneedles from the first column of array with respect to camera position. The purpose to present this is to have an impression to what extent the needle cavities have been filled for this particular batch so that comparisons can be carried out with other combination of experiments. The image once again has been taken from the best sample from the batch in terms of average microneedle height (cycle 14 - $\mathrm{T}_{\mathrm{mould}}$= 40°C).

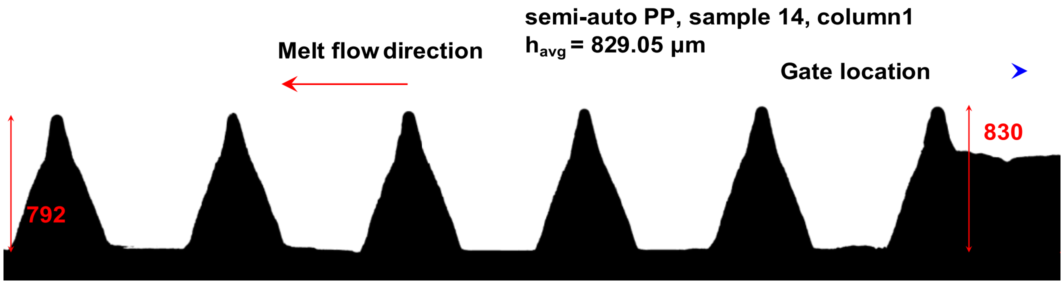

Figure 5-4. Telecentric optical image taken from the first column with respect to the camera position from the best sample (cycle 14). The image gives an impression how the better replicated needles look like from the batch.

The image above show that it is likely to have issues while selecting the base line before starting the automatic measurement due to flashing effects which affects the flatness of the sample. The unevenness of the sample is obvious if the baseline given in Figure 5-4 inspected carefully. To be able to carry out reliable measurements with the hardware available, a convention of measurement has been set for all samples where the left-uppermost needle was taken as the first needle to be measured and the baseline have been set according to this particular needle for all measurements. In this case it has been experienced that there may have been an approximately 15 - 20 μm of difference for the average height of microneedles in the last row (rightmost needle's row in Figure 5-4). However, as the flatness and measurement stage is the same for all samples, this has been expected to have a less significant effect on the results presented in Figure 5-2.

5.2.1.3 Process characteristics

It has been witnessed that there have been some physical phenomena occurring during the injection phase that alter the pressure profiles during moulding that affect the reliability of the fingerprint data. Although the main characteristics and different stages of piston movement have been explained previously in Figure 4-1, example pressure curves in the following will be given for discussing some of the inconsistencies in pressure information from this batch of experiments.

Figure 5-5 depicts two injection pressure profiles from cycle 6 and 12 to compare the pressure profiles which the latter (b) shows a significantly different behaviour than the majority of the cycles with an additional dominant pressure peak in the beginning of the injection phase. The plunger position data recorded from the injection servo encoder is also given for showing the stages of injection.

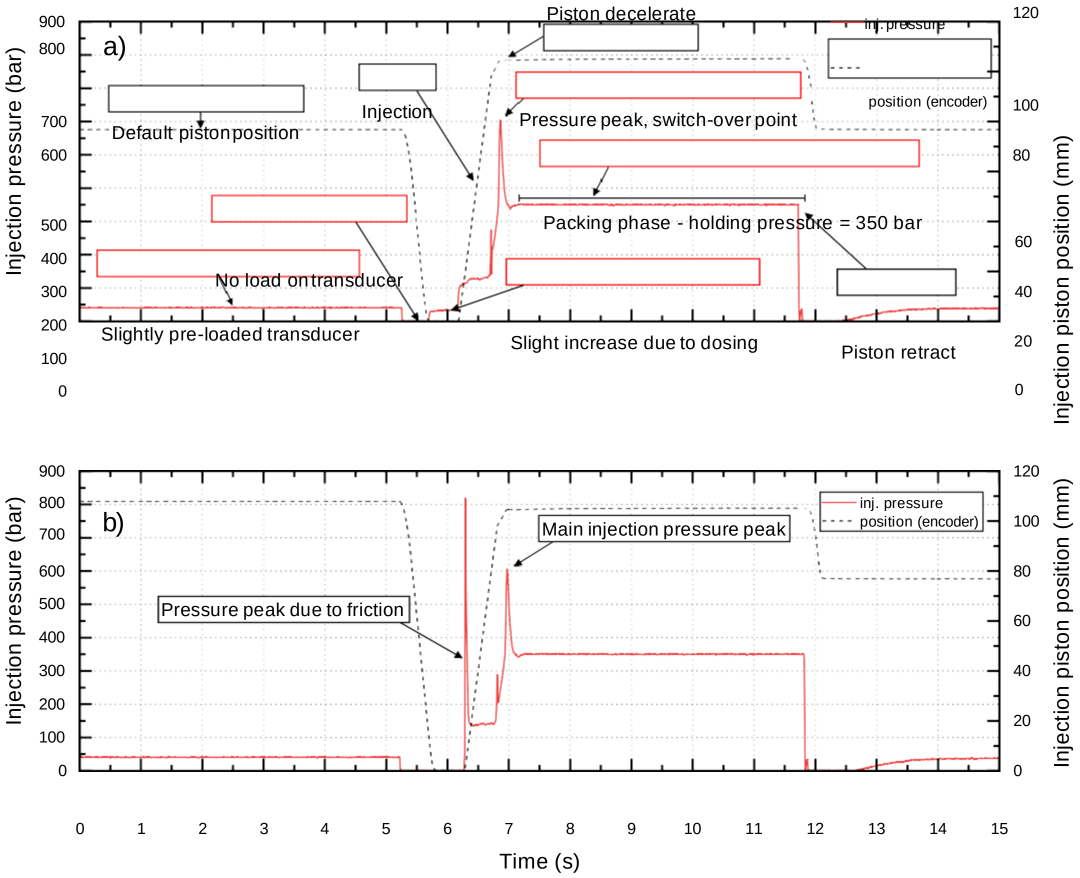

Figure 5-5. Injection pressure profiles and process characteristics for cycle 6 (a) and 12 (b).

It can be seen from the injection pressure profile of cycle 6 (Figure 5-5a) that ideal injection pressure curve starts off with a slight pre-load on the transducer and when the injection piston is retracted to very back this pre-load has been seen to decrease to zero suggesting no force or pressure acting on the injection piston - pressure transducer. Then, a slight increase in pressure is observed because of the dosing of the molten polymer in front of the injection piston followed by a step-like increase in pressure due to conveying of the material towards the mould cavity. A more prominent pressure peak is then seen, and afterwards the machine switches over to the pressure controlled regime at a holding pressure of 350 bar.

The pressure curve at the bottom shows a significant pressure overshoot before the main injection pressure peak caused by frictional effects. Since the cycles were run on semi-auto mode, the default piston positions changed for some cycles causing the piston or the piston channel to cool down causing frictional effects to manifest themselves on the pressure transducer data. 6 cycles out of 60 have been found to have such pressure peaks which caused problems during process fingerprint extraction. Moreover, it is worth emphasising that process data and fingerprints will be most reliable when the temperature gradients are in completely steady-state conditions and this approach will be adopted for the later experimental batches.

In the following, process fingerprints from injection and cavity pressure data have been extracted with the methods presented in 4.2.1 and 4.2.2. Scatter plots have been plotted and analysed for each fingerprint which represents the correlations between the microneedle replication and process fingerprints.

5.2.1.4 Process fingerprints obtained from position encoder data

The position information of the injection unit from the encoder has been recorded for each cycle. Certain points of data that could be relevant to the final quality of the microneedles or the repeatability of the process have been selected from the data as process fingerprints.

The features of interest are mainly two aspects of the encoder data. The first one is the position data where the injection unit decelerates and switches to a pressure controlled behaviour for filling. Secondly, the packing and shrinkage compensation during the holding pressure could provide useful information regarding the final quality of the part and process characteristics. Moreover, the final position of the piston which corresponds to the melt cushion could also be extracted and analysed, which provides information regarding the repeatability of the process. The main features of encoder data for this PP batch have been illustrated in Figure 5-6 including the aforementioned process fingerprints to be analysed.

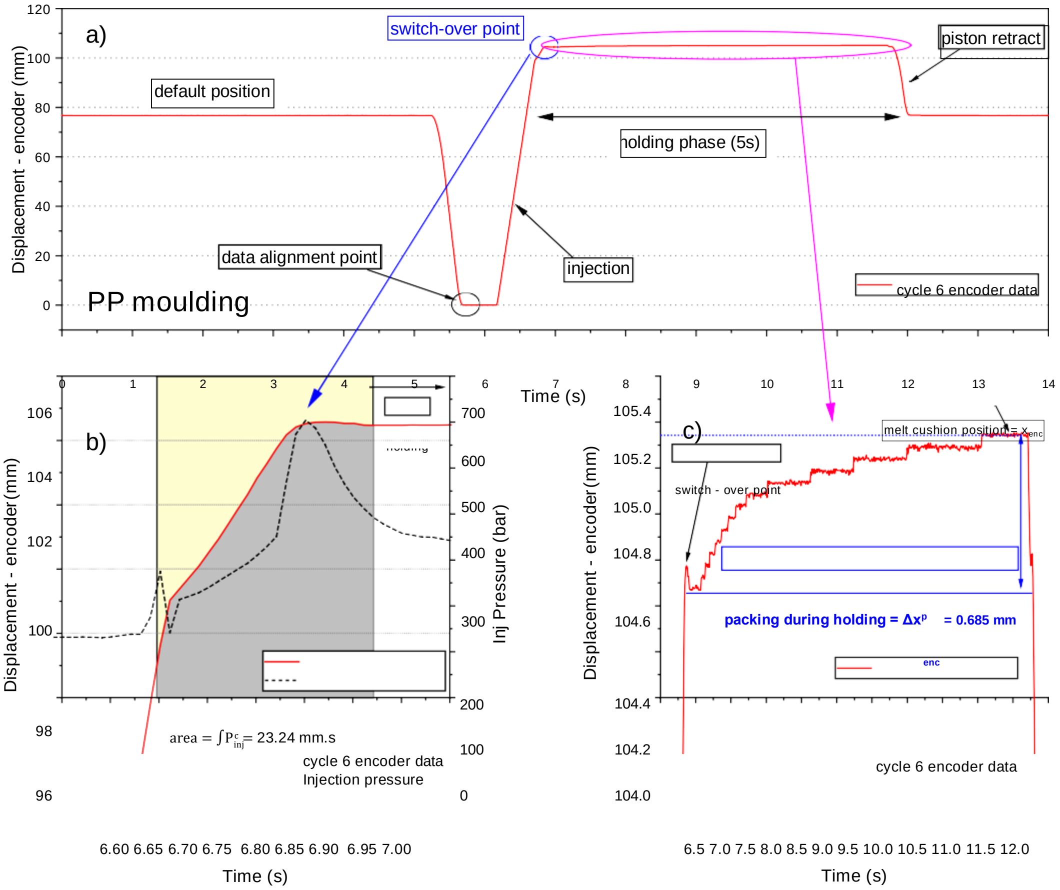

Figure 5-6. a) Encoder position taken from PP - moulding cycle 6 and details, b) an example for integration of the position data near the switch-over point, c) detail of the encoder data within the holding pressure interval.

In order to be able to capture important features of the plots in an orderly and consistent manner, the position data for all 60 cycles have been aligned according to the start of the injection, indicated by the black circle in Figure 5-6 a.

Position information from the encoder has been integrated near the switch - over point within a ~250 ms time window for comparison (Figure 5-6b). The position of injection pressure peak has been selected as a datum for determining integration time interval. As can be seen from the figure, the injection unit stops moving at around t = 6.85 s and is followed by a slight retraction. The time interval has been set to capture this behaviour and also a portion of the movement before the unit stops. The integral has been indicated with the term $\int x_{enc}$, and has been calculated for every cycle. An integration function in the LabVIEW library which use trapezoidal rule has been used for calculation with a time interval set as 0.01 s, corresponding with the data acquisition rate for this batch.

Displacement associated with the shrinkage compensation during holding is also analysed in detail in the following (Figure 5-6c). $\mathrm{x}_{\mathrm{enc}}$ has been extracted as the final position of the injection piston which corresponds to the melt cushion at the sprue of the part. It is worth noting that higher $\mathrm{x}_{\mathrm{enc}}$ values indicate a shorter slug or melt cushion of the material since it is the absolute position of the unit where higher values mean that the piston is closer to the nozzle.

The amount of shrinkage compensation has also been quantified by subtracting the peak position just after the switch over from $\mathrm{x}_{\mathrm{enc}}$. This term gives information on the scale of shrinkage compensation during packing have been indicated with $\Delta\mathrm{x}_{\mathrm{enc}}^{\mathrm{p}}$Step-like behaviour of position information in Figure 5-6c is the resolution of the encoder in y-axis where the data is seen to be slightly digitised within this small displacement window. According to the steps in the encoder data, the positional accuracy or resolution of the unit is measured at approximately 60 μm. Moreover, the retraction movement that have been carried out by the injection unit can also be clearly seen near t = 7 s.

Scatter plots given in the following (Figure 5-7) have been formed using the average microneedle height ($\mathrm{h}_{\mathrm{avg}}$) in the y-axis and process fingerprints for each of the cycles in the x-axis. Linear fits applied wherever possible for interpretation of the correlations.

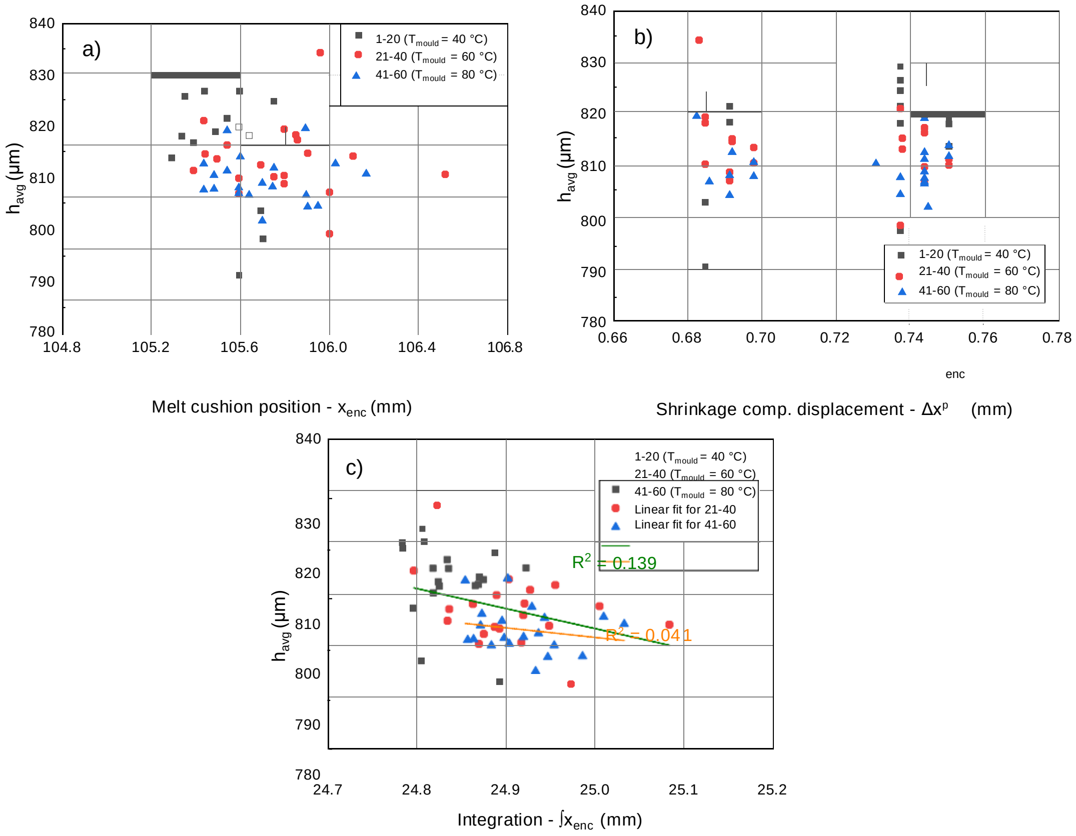

Figure 5-7. Scatter plots for x_{enc} (a), Δx^{p}_{enc} (b) and $\int x_{enc}$ (c) vs average needle height (h_{avg}).

According to the scatter plot above (Figure 5-7a), no clear trends are seen for the melt cushion (x_{enc}) information which is an expected behaviour. Micropower 15 has been designed to have a pressure controlled switch-over feature where the injection pressure is controlled in a feedback loop. For avoiding extreme pressure overshoots, after the pressure value from the transducer reaches a certain value which is set by the user, machine quickly responds and completes the filling process in a pressure controlled manner. In that sense, variations in the dosing and hence in the melt cushion are expected to be irrelevant in terms of the filling behaviour of the melt since the filling is entirely handled by the pressure monitoring. Hence, since the data is all scattered it can be said that the injection unit and this closed - loop mechanism for injection pressure is working properly throughout the process. However, these particular process fingerprints can be used as an indicator that the process is being carried out as it should be.

Δx^{p}_{enc} is a considerably different feature from the melt cushion and represented some certain patterns in the distribution of the data (Figure 5-7 b). Accumulations of data are because of the encoder resolution which is not high enough to provide a better distribution for understanding the behaviour. Laser displacement sensor measurements can provide much better information regarding this shrinkage process fingerprint.

The scatter plot given for $\int x_{\mathrm{enc}}$ (Figure 5-7c) presented a slight linear correlation for the highest mould temperature of 60°C. The linear fit has an R^2 value of 0.139 which showed a negative trend for h_{avg} with increasing integral values. One of the reasons that cause these integrals to be small or bigger could be the time where the injection unit switches over to the pressure controlled regime. Early triggers for switch - over likely to cause smaller integrals where later triggers will result in bigger integral values. Moreover, lower integration values could show that switch-over and hence packing were triggered earlier which resulted in less replicated needles combined with shrinkage effects for higher mould temperatures.

To summarise, injection piston position taken from the drive encoder is very useful for identifying different stages and features of injection and packing. The data can also be used as an indicator of repeatability of the process according to the melt cushion information given above. Better interpretation of the data can be made by using a device with faster acquisition capability such as the high-speed laser displacement sensor introduced in Chapter 3.

5.2.1.5 Process fingerprints from injection and cavity pressure data

Following scatter plots represent average microneedle height measured from each microneedle patch vs the process fingerprints extracted from injection pressure data. Peak injection pressure ($\mathrm{P}_{\mathrm{inj}}^{\mathrm{p}}$) and pressure integral ($\int \mathrm{P}_{\mathrm{inj}}^{\mathrm{p}}$) have been given in different colours indicating the mould temperatures. $\int \mathrm{P}_{\mathrm{inj}}^{\mathrm{p}}$ has been extracted by integrating the peak within an approximately 250 ms integration range unlike the integration shown as an example in Figure 4-2 where only the first half of the peak was integrated. Figure 5-8 shows scatter plots of injection pressure fingerprints against h_{avg}.

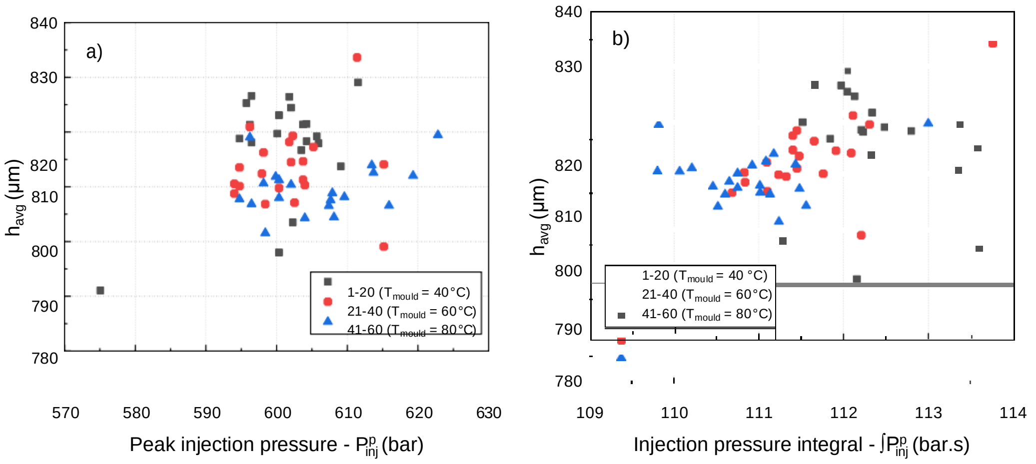

Figure 5-8. Scatter plots for P^p_{inj} (a) and $\int P^p_{inj}$ (b) against average needle height from microneedle arrays.

It can be seen that no clear trends have been observed for both P^p_{inj} and $\int P^p_{inj}$ in terms of their relevance to the h_{avg} which was measured for each cycle using the telecentric optical measurement system. There is an apparent decrease in the injection pressure integrals which can be seen from the scatter plot on the right when higher mould temperatures are considered. The reason for this could be attributed to the lower viscosity of the polymer for higher mould temperatures which would decrease the polymer melt's resistance to flow causing a narrower pressure peak which results in smaller integral values. However, the scattered nature of the data make it difficult to present any sort of correlation between the process and product fingerprints. The rapid cooling of the polymer alongside with semi-crystalline structure and shrinkage behaviour of PP also contribute to this scattered behaviour of results making it difficult for the injection pressure information to have a clear impact on the dimensional outcome of the needles.

Cavity pressures, however, have been more representative of the dimensional features of the micromoulded parts. Figure 5-9 shows scatter plots for peak cavity pressure (P^p_c) in (a) and cavity pressure integral ($\int P^p_c$) in (b) against average needle height from each cycle. Cavity pressure integrals given in Figure 5-9 have been calculated within an approximately 15 ms window as depicted previously in Figure 4-3.

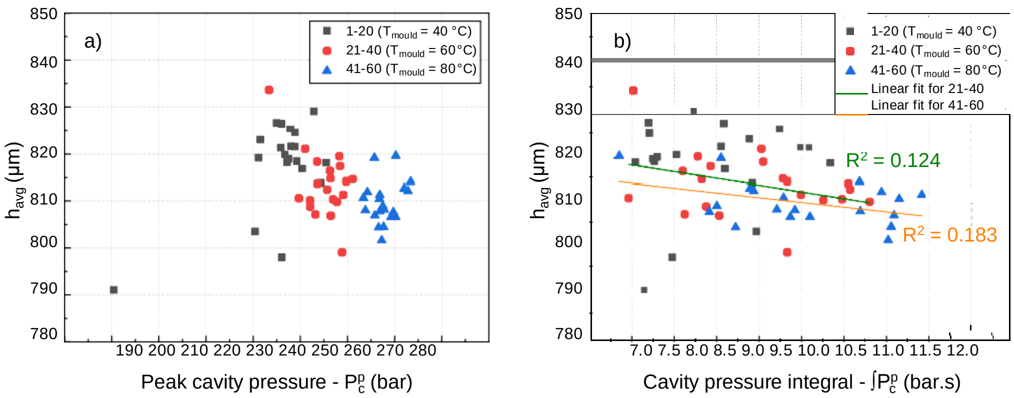

Figure 5-9. Scatter plots for P_c^p (a) and $\int P_c^p$ (b) against average needle height from microneedle arrays.

Figure 5-9 depict that cavity pressure data is more relevant in terms of its relations to quality criterion as a fingerprint since some distinct trends can be seen. Although there seems to be an inverse relationship between the peak cavity pressures and average microneedle height it is difficult to present a linear relationship because of the outliers in the data. However, the negative trend is unexpected which is in correspondence with the results given in Figure 5-2 and Figure 5-3. Although higher cavity pressures could be achieved by being able to sustain and pack the molten polymer into the cavity better, recovery and shrinkage effects could become dominant.

Cavity pressure integrals given in Figure 5-9b presented a moderate, linear - inverse relationship where lesser replication of microneedle features obtained when higher cavity pressure integrals were present when using mould temperatures of 60 and 80°C with R^2 values of 0.124 and 0.183 respectively.

During data evaluation in LabVIEW, it was seen that the cavity pressure profiles changed considerably with increasing mould temperatures. The cavity pressure profiles tend to get wider and cavity pressure has been sustained for longer when higher mould temperatures were used. For assessing this behaviour, the pressure integrals have been integrated from a wider integration window of 1.5 s and $\int P_c^p$ have been analysed accordingly. The plots depicting this behaviour is given in Figure 5-10. Presented in (a) is the individual cavity pressure profiles from 3 cycles taken from different mould temperatures. Scatter plot is given in (b) for h_{avg} and $\int P_c^p$ correlations.

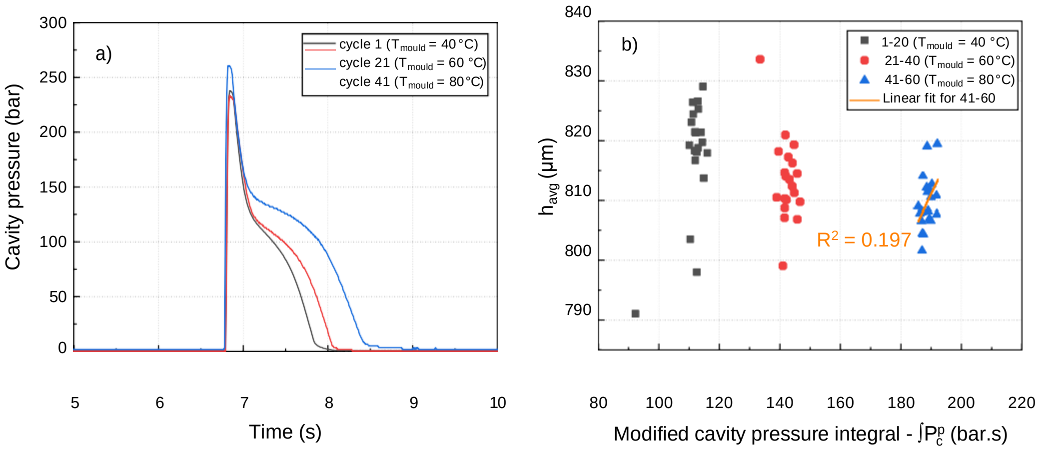

Figure 5-10. a) Cavity pressure profiles for different mould temperatures, b) scatter plots for cavity pressure integrals taken from the whole area of the cavity pressure curves.

Cavity pressure curves in Figure 5-10a depict a typical behaviour of widened cavity pressure profiles while using higher mould temperatures (Whiteside et al. 2004). Increased mould temperatures keep the polymer molten at the gate of the cavity for longer (Zhang et al. 2019). Hence, the cavity pressure is sustained for elongated times. Figure 5-10b is the scatter plot for modified cavity pressure integrals where each of these measurements have been taken from the whole area under the curve of cavity pressure profiles. These integrals show the clear differences between mould temperatures and quantify the widening for higher mould temperatures. Although few outliers in the data presented in the scatter plot on the right is present, clear linear trends can be seen. Once again, the frictional forces that arise from cooling of the injection piston due to the semi-automatic mode have an impact on the data which results in these outliers. An R^2 value of 0.197 for a linear fit has been found for higher mould temperature of 80°C.

5.2.1.6 Summary of the results for PP microneedles moulded in semi-automatic mode

In this experiment, PP microneedle patches have been manufactured using conventional micromoulding technology in semi-automatic mode. Retracted process parameters have been chosen and experimented for better assessment of the process in the first place. Replication of the deep microneedle cavities has been a challenge, where a maximum average needle height between 810 - 820 µm has been achieved.

A significant outcome of the experiments has been the effect of crystallinity for PP material, where higher mould temperatures yielded a slight increase in the crystallinity of the polymer which filled the laser machined microneedle cavities. Higher crystallinity at elevated mould temperatures resulted in more shrinkage which in turn yielded lower $\mathrm{h_{avg}}$ values. Moreover, the likelihood of elastic recovery of the polymer material which might escalate this effect has also been discussed.

Process characteristics for manufacturing PP microneedles in semi-automatic mode have been studied in detail. Position encoder data have been analysed for characterising the injection and packing behaviour during switch - over and holding phases. General trends have been identified with the help of the process fingerprints extracted from the process data and have been correlated to the microfeature replication where possible. Obscurities and limitations of encoder data have been discussed and significance of using high-speed laser displacement sensors has been emphasised.

Finally, injection and cavity pressure characteristics have been discussed in detail. Process fingerprints for both data channels have been presented and relationships between these measurements and microneedle replication are discussed.

5.2.2 ABS experiments (Batch-m2)

PP experiments have been followed by ABS (Cycolac - HMG94MD), which will provide insight on process fingerprint response of an amorphous polymer in semi - automatic mode. The section will be finalised with a comparison of first two-batches and considerations for further experiments.

5.2.2.1 Selection of process parameters and preparation

Similar to the previous PP experimental batch, slightly reduced parameters which would result in reasonable microfeature replication has been used for the first ABS experiment. The process parameters that have been set for this particular batch are given in Table 9.

Table 9. Process parameters used for moulding PP microneedles for Batch-m2.

Process parameter	Value - unit
Melt temperature	240 (nozzle), 235, 235, 225°C (hopper)
Mould temperature	50, 60 and 70°C
Injection speed	400 mm/s
Switch - over pressure	700 bar
Holding pressure	750 bar
Holding pressure duration	7.5 s
Cooling time	10 s

Once again, mould temperatures have been varied to see how the process measurements behave and their correlation to the product fingerprints. Mould temperatures below 50°C resulted in significantly lower needle heights and hence 50, 60 and 70°C have been selected as the mould temperatures to have both reasonable microfeature replication and a well-defined starting point in terms of process fingerprinting.

Similar procedures have been carried out in terms of moulding parts with acceptable visual quality where the circular base of the cavity is completely filled and packed. Most of the chosen parameters in Table 9 were kept as minimum as possible in order to assess the process data and microneedle features better. Similar purging procedures have been performed ensuring that no contamination was present in the barrel and injection unit.

5.2.3 Experimental details and microneedle measurements

The same DAQ hardware and software have been used previously for collection of process data at the same rate of 100 Hz. Once again, the experiments carried out in semi-automatic mode where, the part is collected manually by the operator at the end of the moulding cycle. Similar sample collection procedures have been applied, where 20 parts were discarded in the beginning then 20 collected for each mould temperature.

Micromoulded parts have been cut from the gate carefully and needle heights have been measured using telecentric optical measurement apparatus. Figure 5-11 shows an image of one of the moulded ABS parts (a), and an SEM image (b) taken from a single needle from one of the better replicated needles. As expected, the microfeature replication has not been at its maximum with parameters selected which are significantly lower than what can be set to maximise replication. The smooth tip of the microneedle indicate that the microneedle cavities have not been replicated completely and it can also be seen from the SEM image.

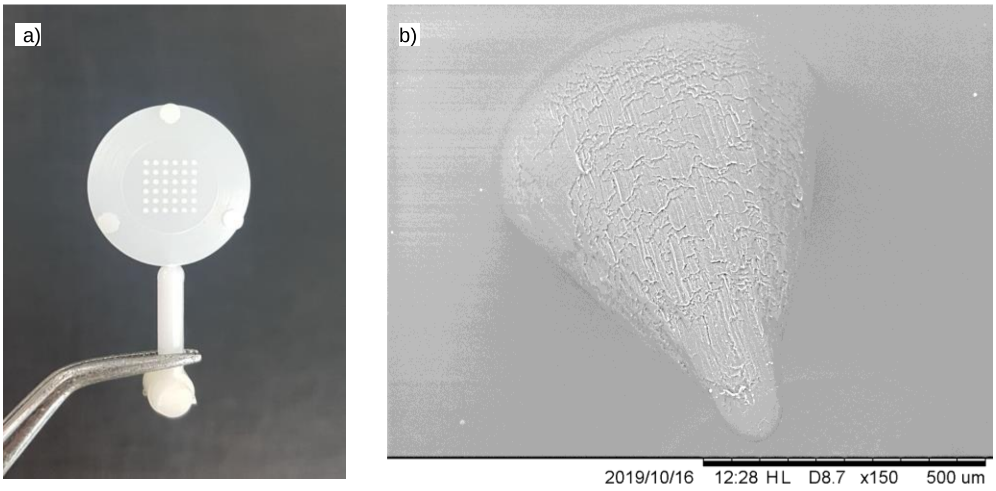

Figure 5-11. a) Micromoulded ABS microneedle patch, b) SEM image of one of the better replicated needles.

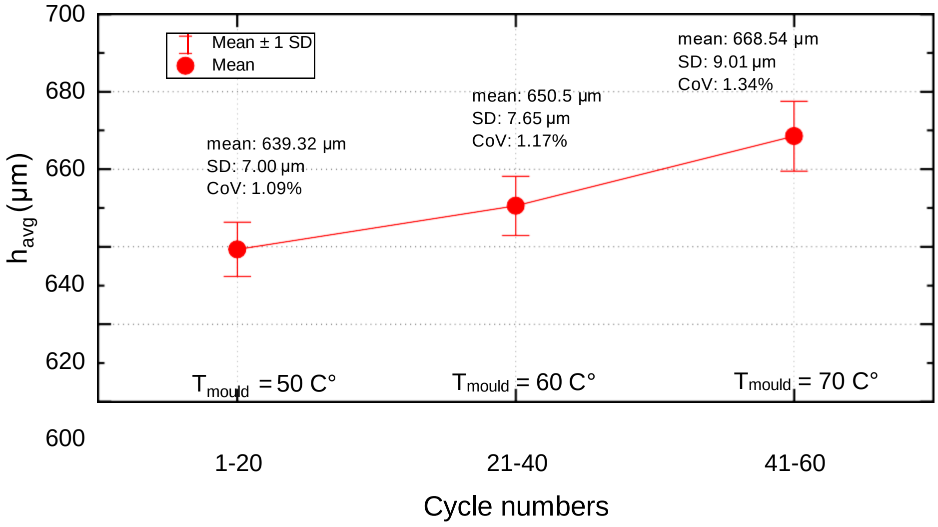

Figure 5-12. Interval plots showing the standard deviation and means of average needle height for cycles 1-60. Different mould temperatures are indicated.

Microneedle height measurement results presented in Figure 5-2 clearly indicate the effect of having different mould temperatures. As expected, a considerable difference is present between results for lower and higher mould temperatures. SD and CoV values seemed to increase, however, for experiments where better microfeature replication was present. It should be noted that all the needles have nearly surpassed the narrower taper in the conical shape of the needle which is present at around ~650 µm. Above this height, feature replication is obviously more difficult, which manifests itself as increased SD and CoV values although h_{avg} is improved when means are considered for higher mould temperatures.

A representative telecentric optical image is given in Figure 5-13 to give an impression on shape of the microneedles.

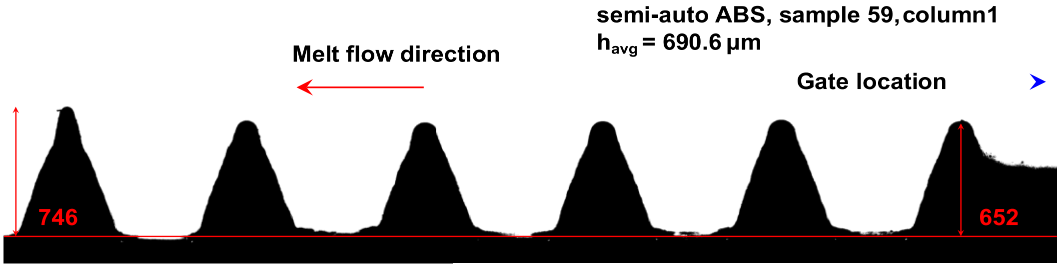

Figure 5-13 Telecentric optical image taken from the first column with respect to the camera position from the best sample (cycle number 59 - out of 60). The image gives an impression how the better replicated needles look like from the batch.

The narrower taper of the needles can be seen clearly from Figure 5-13. Another important observation from the telecentric images were the difference in degree of replication of microneedles for different rows for ABS. Flow direction has been indicated to the left in Figure 5-13 which is towards the end of the part, away from the gate, hence the right side of the image is closer to the gate. The leftmost needle in the image that belong to the row that is farthest from the gate measures ~746 µm, which is significantly better replicated than the other rows. This can be explained by the fact that the flow of molten polymer heats up the air by shear and compression inside the mould cavity, resulting in a local increase of surface temperature of the mould surface making the filling of the microneedle cavities easier towards the end of the cavity. The amorphous nature of ABS also contributes to this, as the material does not have a sharp solidification point where its viscosity does not increase abruptly and the pressure is sustained for longer. This affect also have not been seen to be present in the previous batch for PP, where slightly shorter or microneedles with similar heights have been measured from the row located towards the end of the cavity.

5.2.3.1 Process characteristics and fingerprints obtained from position encoder data

Process characteristics of micromoulding ABS may seem very similar to the PP, however there are significant differences in the encoder data which will be discussed in the following. Figure 5-14, shows the main features of the encoder data for ABS experiments. One of the main differences from the PP example given in Figure 5-6 is that ABS cycles have a longer holding phase which lasts 7.5 s for packing.

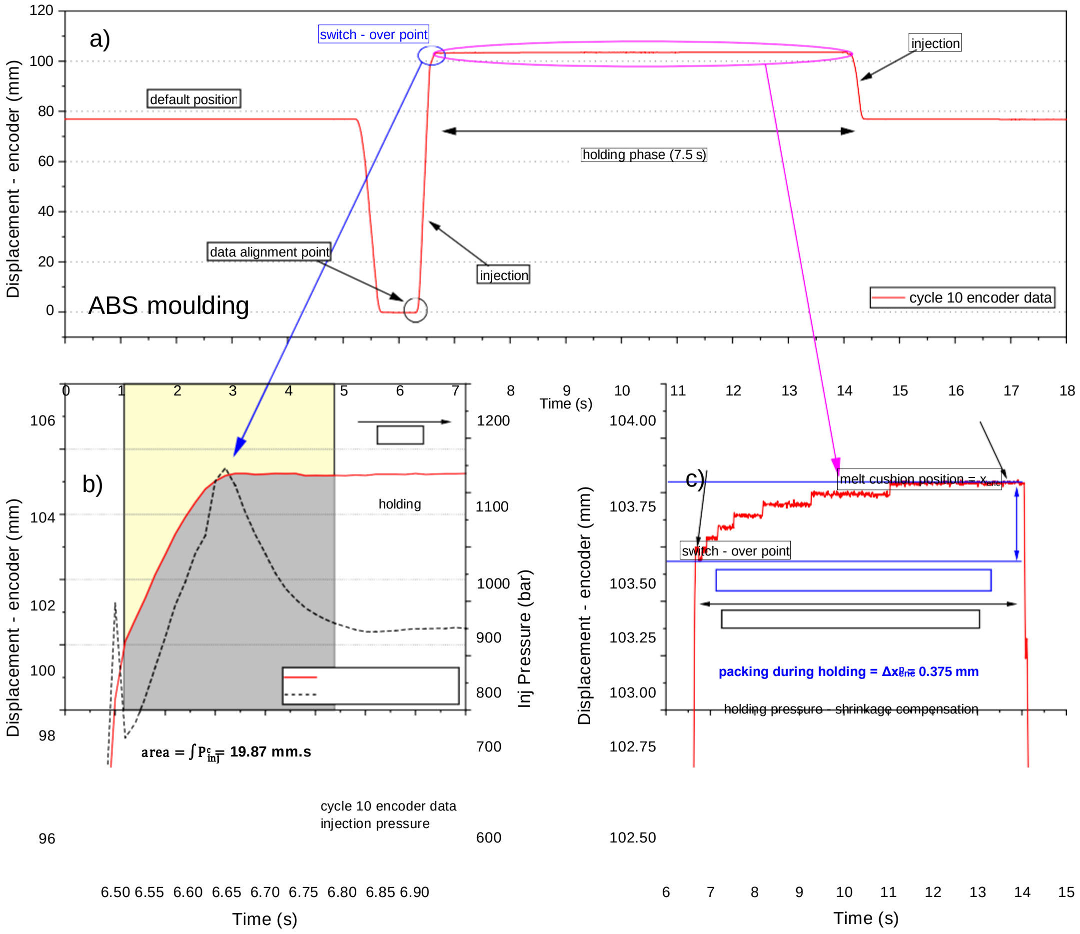

Figure 5-14. a) Encoder position taken from ABS - moulding cycle 10 and details, b) an example for integration of the position data near the switch-over point, c) detail for encoder data within the holding pressure interval.

From Figure 5-14b it can be seen that the transition to the holding phase is more abrupt when it is compared with polypropylene. This is because the significantly higher injection velocity used for ABS which is 400 mm/s, whereas it was set as 150 mm/s for PP. Hence, a narrower range of ~200 ms has been used for integration of the encoder displacement. Other important feature to see is that the displacement during packing (Δx^{p}_{enc}) is also significantly smaller with a value of 0.375 mm which was on the order or 0.7 mm for polypropylene experiments. This behaviour could be attributed to the shrinkage of ABS (~0.5 – 0.8%) which is significantly lower than PP (1 – 2.5%).

Given in the following are the scatter plots for process fingerprints extracted from the position encoder data for ABS experiments.

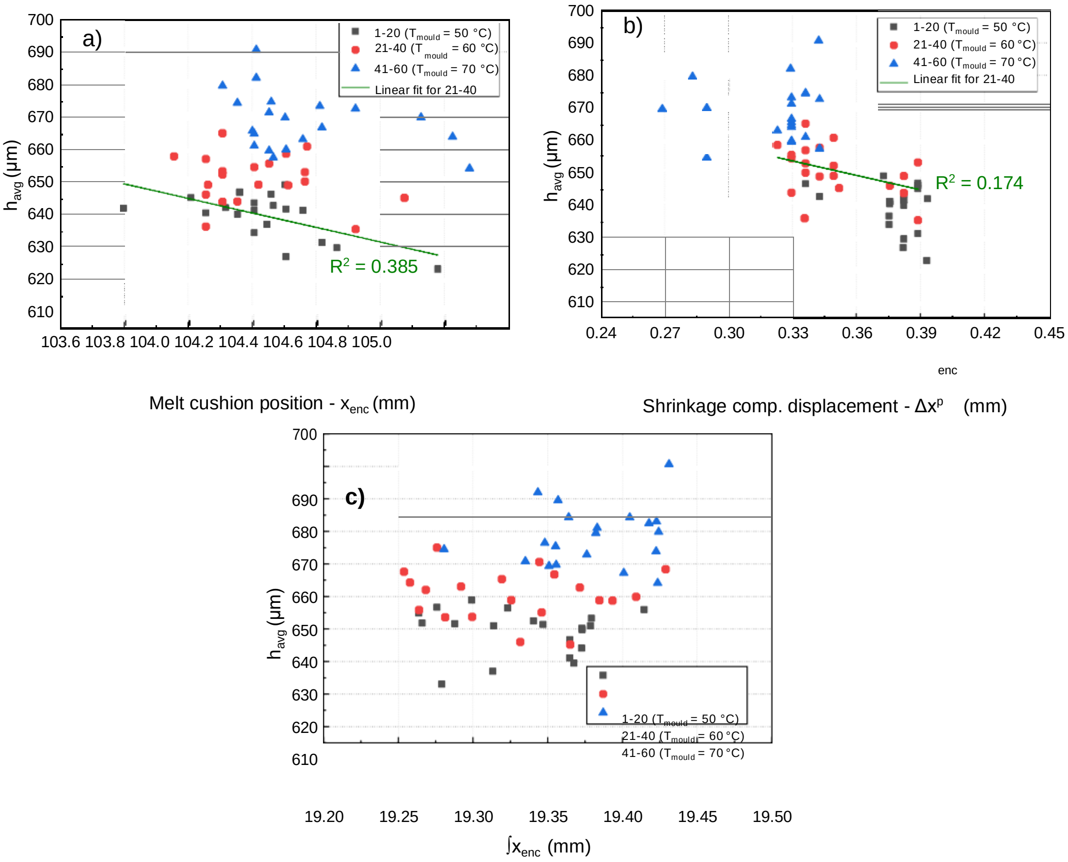

Figure 5-15. Scatter plots for x_{enc} (a) , Δx^{p}_{enc} (b) and $\int x_{enc}$ (c) vs average needle height (h_{avg}).

Similar to the data taken from previous PP batch, no clear trends have been seen for the process fingerprints as can be seen from the above figure. The data in Figure 5-15a for h_{avg} vs x_{enc} show scattered behaviour, however, the data for cycles 1-20 show a reasonable linear correlation with $R^2 = 0.385$. For this linear fit, given data suggest that increased melt cushion position would yield in lesser microfeature replication. As far as this linear fit is concerned, ~ 1 mm of displacement corresponds to a drop of ~30 µm in average needle from one patch. Increased values of x_{enc} suggest that the final position of the piston is further towards the nozzle meaning a smaller melt cushion. The height or the length of the melt cushion is associated with the dosing and the variability in the amount of the material conveyed to the injection channel could contribute to the behaviour shown by x_{enc}. Moreover, higher mould temperatures tend to show slightly higher x_{enc} values and better replication which might suggest that more ABS can be packed towards the cavity.

Data from ABS experiments for Δx^{p}_{enc} showed slightly more reasonable distributions (Figure 5-15b). Although no strong linear correlations are present and h_{avg} has a negative relationship with Δx^{p}_{enc}. This was also shown with the linear fit provided in the graph which showed an R^2 value of 0.174. One could expect that increased shrinkage compensation or packing would yield increased average needle heights and better microfeature replication. However, the following points should be considered in order to understand the packing dynamics and filling behaviour of the microneedle features:

1. Increased amounts of shrinkage compensation displacement (Δx_{enc}^{p}) can sometimes be misleading when expecting better microfeature replication, as the packing is facilitated by the injection piston which compresses the melt cushion (or the sprue) towards the cavity. This will not have an impact on the microfeature replication areas at which the molten polymer has already been rapidly solidified.
2. It can be seen that for lower mould temperatures of 50°C the highest shrinkage compensation values have been reported (Figure 5-15b). Lower mould temperatures will cause amorphous ABS to solidify much earlier leading to significantly lower h_{avg} values. However, the piston near the sprue will still be able to pack the material towards the cavity leading to an increased Δx_{enc}^{p} This usually results in slight flashing effects near the sprue, especially for PP where significantly higher Δx_{enc}^{p} values have been observed.

The data regarding the integrations in the vicinity of switch - over points showed a scattered and random behaviour (Figure 5-15c). Although no clear trends and correlations could be presented from the data, the overall trend in the distribution of the data show that cycles with high $\int x_{enc}$ calculated (blue and some of the red data points) show better replication of microfeatures. It can be also said that for higher mould temperatures when $\int x_{enc}$ is considered, the pressure to fill the mould is reduced because of the viscosity reduction and switch-over triggers later causing the position curve to go upward resulting in higher integral values.

5.2.3.2 Process fingerprints from injection and cavity pressure data

Similar issues of having unexpected pressure overshoots have also been seen during ABS experiments likewise in PP batch. These steep pressure increases before the main injection peaks have been seen more frequently with 8 times out of 60 semi-automatic cycles whereas they were seen 6 times for PP experiment. The reason for this is the higher viscosity of ABS in overall as compared with PP where it tends to cause more friction during movement of the injection piston. These pressure profiles look similar to that of PP batch and for preventing redundancy the pressure profiles are not presented.

The graphs given in Figure 5-16 illustrate the correlations between maximum cavity pressure and microneedle height for different mould temperatures.

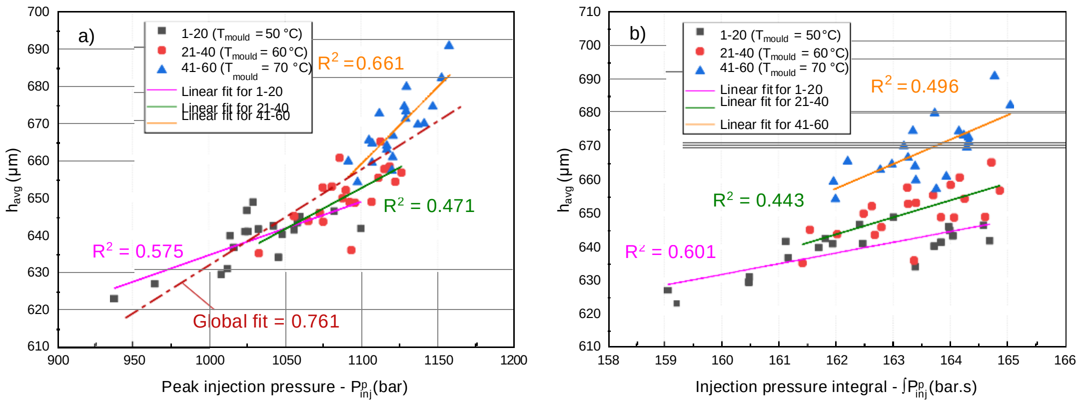

Figure 5-16. Scatter plots for P^{p}_{inj} (a) and $\int P^{p}_{inj}$ (b) against average needle height measured from microneedle arrays.

The first important feature one could notice from P^{p}_{inj} data shown (Figure 5-16a) is that there is a definite positive relationship between the peak injection pressure and microfeature replication. The global fit for P^{p}_{inj} showed correlations with an R^2 value of 0.761. Moreover, correlations have also been found when applying linear fits for the data with different mould temperatures. Injection pressure has been known to be directly relevant to the filling behaviour of miniature products and the correlations presented here have been significant compared with previous work (Whiteside et al. 2005b; Baruffi et al. 2018).

The scatter plot in Figure 5-16a show that the R^2 value reached 0.661 when using T_{mould} = 70°C, where the microneedle heights measured within the range 650 - 690 µm. These average heights suggest that the tip of the needle is well above the height where the taper of the conical gets narrower which could explain the fact that higher R^2 values have been found. Process fingerprints could manifest themselves better in this narrower taper up to a certain point, and better correlations might have been seen because of that reason.

Injection pressure integrals presented (Figure 5-16b) similar linear correlations compared with peak pressure values. Slightly decreased R^2 values have been seen when the mould temperature increased. It should be bared in mind that mould temperatures affect the pressure profiles significantly and hence the width of the peaks, which are integrated. This effect can be seen from the narrow distribution of the integral values presented for T_{mould} = 70°C.

Cavity pressure behaviour has been investigated in detail using LabVIEW scripts which are included in the Appendices section. It was seen that even within the cycles with same mould temperatures the cavity pressure profiles differed considerably. Figure 5-17 shows this effect by showing representative cavity pressure data taken from 3 different cycles for 3 different mould temperatures.

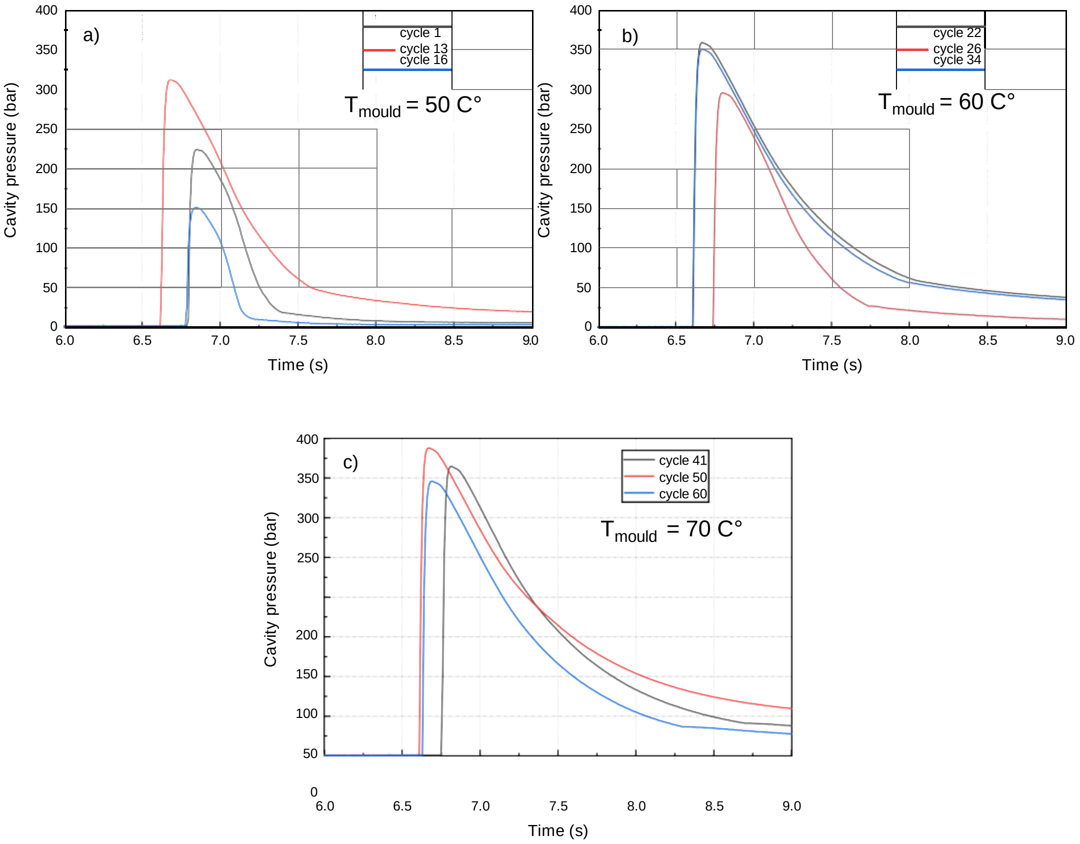

Figure 5-17. Cavity pressure profiles for 3 mould temperatures, 50 (a), 60 (b) and 70°C (c) including 3 representative cycles for each group.

The graphs in Figure 5-17 are given with the same y-axis scale so that one is able to see the differences easier. The first obvious feature to be spotted is the difference between cycles that have been carried out with exactly the same process parameters. Peak values and areas associated with the integration of the whole pressure profiles have also increased as expected because of the same reasons given for PP. The pressure decrease for ABS has been gradual and with the same rate, whereas due to semi-crystalline nature of PP a difference in the decay rate of the cavity pressure was seen previously.

Scatter plots in Figure 5-18 represent the correlations between the cavity pressure fingerprints and dimensional outcome of the replicated microneedles.

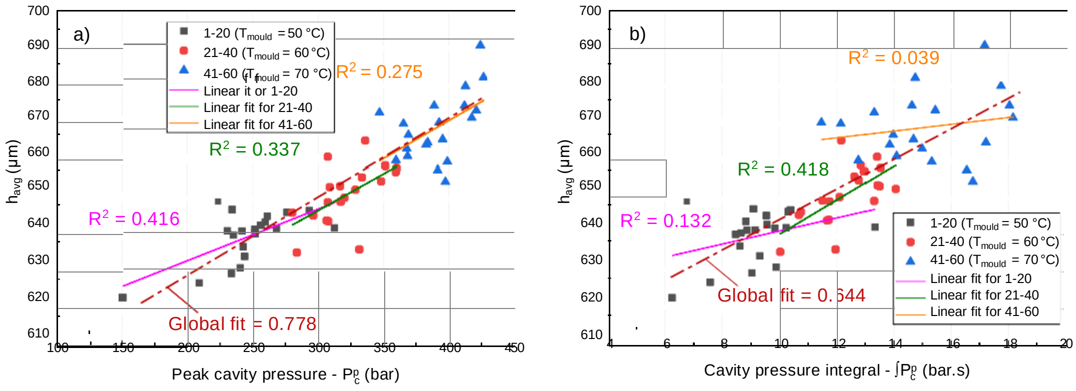

Figure 5-18. Scatter plots for P^{p}_{cc} and $\int P^{p}_{cc}$ against average needle height measured from microneedle arrays.

Similar to injection pressure fingerprints, a positive trend is observed from the scatter plots given in Figure 5-18 between cavity pressure fingerprints and average needle height. R^2 value of 0.778 for the global fit given in Figure 5-18a have been found which shows that there is a significant correlation between the peak cavity pressures vs average needle heights. This is an expected result as cavity pressure measurements are proved to be relevant to the quality of the small micromoulded parts or features compared with injection pressure data (Whiteside et al. 2004; Kurt et al. 2009).

Cavity pressure integrals also exhibit good correlations with R^2 values of 0.644. Although peak values and integrals usually correlate, integration method and time interval selection for the integration could explain the lesser relevance of cavity pressure integrals to the replication quality. The effect could also be amplified with high mould temperatures. Notably, for higher mould temperatures $\int P_c^p$ became less relevant and become completely scattered when its relationship with h_{avg} is considered.

5.2.3.3 Summary of the results for ABS microneedles moulded in semi-automatic mode

The experiments carried out with ABS in semi-automatic mode provided a good starting point for process fingerprinting of microneedle arrays for amorphous polymers. Lower process parameters resulted in above average microfeature replication results with ~670 µm average needle height for higher mould temperatures. As expected, the blunt needle tips have been spotted.

Process characteristics have been evaluated using the position data from the machine encoder and pressure transducers. ABS with slightly higher viscosity than PP resulted in smaller piston displacements during holding. Possible explanations for packing dynamics and filling behaviour has been introduced by evaluation of process fingerprints extracted from the position encoder data. Reasonable linear correlations have been found for lower mould temperatures for melt cushion position.

Correlations have been found while evaluating process fingerprints extracted from injection and cavity pressure. Linear correlations with R^2 values of ~0.8 have been found in h_{avg} vs peak pressure plots. Cavity pressure data was also seen to be variable throughout the cycles. To summarise, relationships and correlations have been found between process fingerprints and average microneedle heights that could be used for an in-line quality assessment procedure of microneedle manufacture.

5.2.4 Comments on semi-automatic experiments and further strategies for improvement

Experiments carried out for PP and ABS in semi-automatic mode have been extremely useful for characterising main process features and assessment of microfeature replication capabilities and potentials of conventional micro-injection moulding. In order to improve the replication of microneedle cavities and to know more about the process and run the cycles in a more of a pilot production scenario following points will be considered for further experiments:

1. Running the micromoulding machine in semi-auto mode with approximately a minute time interval between every cycle causes cooling down of the injection piston which escalates the frictional effects as indicated in Figure 5-5. There is occasionally a thin film of polymer around the injection piston due to its movement and low viscosity of the molten polymer and this film tends to solidify while the user collects the moulded part and records the process data. This effect is thought to be the reason for the friction. For the sake of stabilisation of all thermal gradients and reducing these frictional effects, the cycles have to be run in the fully automated mode where the machine produces parts back to back without waiting idle.
2. Process parameters such as injection speed, injection and holding pressures have to be increased for better filling behaviour for producing functional microneedles with pointy tips, which will be able to penetrate through the skin for functionality.
3. Injection position data taken from the encoder have been often insufficient to capture smallest displacements that occur during holding phases. Using a high-speed laser displacement sensor will definitely improve capturing this important stage of the process.

5.3 Process fingerprinting for conventional microinjection moulding in full-automatic mode

In this section, experiments carried out in full-auto mode in Micropower 15 for PP and ABS. For each experiment, experimental details, process measurements and results have been given.

5.3.1 PP experiments (Batch-m3)

PP microneedles have been produced in full-auto mode using conventional micromoulding for this section and details are as following.

5.3.1.1 Selection of process parameters and preparation

Micromoulding process parameters have been used at their maximum where possible for this set of experiments to have fully replicated microneedles with the best quality. The parameters in Table 10 have been used for PP experiments in full-automatic mode.

Table 10. Process parameters used for moulding PP microneedles for Batch-m3.

Process parameter	Value - unit
Melt temperature	225 (nozzle), 220, 220, 210 (hopper)
Mould temperature	60°C
Injection speed	250 mm/s
Switch - over pressure	550 bar
Holding pressure	600 bar
Holding pressure duration	5 s
Cooling time	5 s

Different process parameter values have not been experimented for this batch. The main purpose is to maximise the replication capability and characterisation the manufacturing cycles using process measurements and fingerprints. As indicated in the table, melt temperature, hold pressure duration and cooling time kept at the same values as used previously for Batch-2m. Injection speed has been increased to 250 mm/s from 150 mm/s which is thought to be an effective parameter. Holding pressure has been set at 600 bar which was 350 previously. Mould temperature of 60°C was selected, as higher mould temperatures showed severe flashing effects due to increased parameters. Obviously, the main criteria in selecting the maximum conditions was the visual quality of the circular cavity and minimised flashing effects. While collecting the samples the process has not been interrupted and parts have been taken from the opening below the mould and moving platen.

5.3.1.2 Experimental details and microneedle measurements

DAQ software have been modified in order to be able to capture process data automatically for each micromoulding cycle. Four channels of data have been used. In addition to previous experiments, laser displacement sensor output has also been connected to the BNC ports and recorded in addition to the injection pressure, position information from the encoder and cavity pressure. Instead of using 100 Hz of data acquisition rate, 1000 Hz has been set in order to capture the process features in more detail. Higher acquisition rates are also more appropriate while using more extreme process conditions such as high injection velocities and pressures.

After starting the production of microneedle arrays in full-auto mode, 50 samples have been discarded in order to have the temperature gradients settled and minimising frictional effects. Process has been considered as stabilised after 50 cycles and 50 samples have been collected. The samples have been cut from the gate as done before and inspected under telecentric optical measurement system.

One of the significant features of the PP microneedles from this batch at the first glance was their flattened or dimpled tips. The effect was present for almost all of the microneedles. SEM images shown in Figure 5-19 illustrates the dimpled tips of the microneedles in detail.

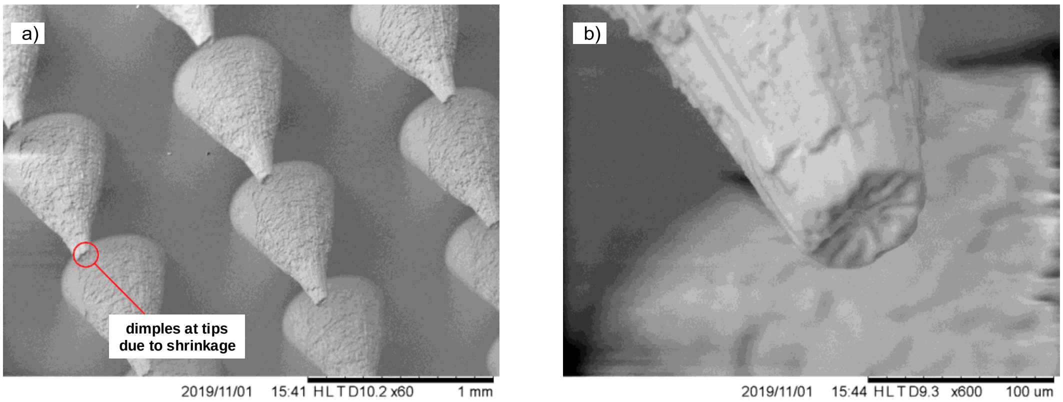

Figure 5-19. PP microneedles with dimpled tips (a) and detail of the dimpled tips (b).

The effect shown in the previous figure is thought to be caused by the considerable amount of shrinkage during solidification for PP which is reportedly on the order of 2% (Fischer 2003). Figure 5-20 shows a telecentric image of the left-most needles from sample 49.

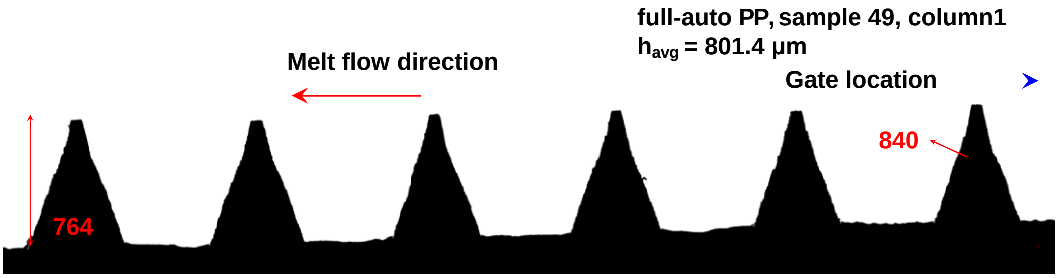

Figure 5-20. Figure showing a telecentric image of the leftmost column from cycle 49.

In the above figure, flat or dimpled tips of the microneedles can be seen. Another feature to note is that the baseline selection has been severely problematic for this particular sample where a slight inclination in the image towards the right edge can be spotted. Averaged microneedle height from 50 samples and other statistical data have been given in Table 11.

Table 11. Measurement results taken from telecentric microneedle inspection system for Batch-m3.

Average needle height ($\mathrm{h_{avg}}$)	Standard deviation for $\mathrm{h_{avg}}$ (SD)	Coefficient of Variance for $\mathrm{h_{avg}}$ (CoV)
801.4 μm	3.636 μm	0.45 %

It has been seen that significantly increased injection velocity and pressures selected for this batch have not improved microneedle replication quality according to the average needle height of 801.4 μm. In the previous experimental set where semi-automatic mode has been used for PP, an $\mathrm{h_{avg}}$ of 813.42 μm have been achieved.

5.3.1.3 Process fingerprints extracted from encoder and laser sensor data

Process characteristics of this batch have been very similar to the previous semi-automatic experiments with PP. Hence, graphs regarding injection pressures and position data from the encoder will not be discussed here for avoiding data redundancy. However, laser displacement measurements have been a new feature that were added to the experiments and characteristics of this technique will be discussed in the following.

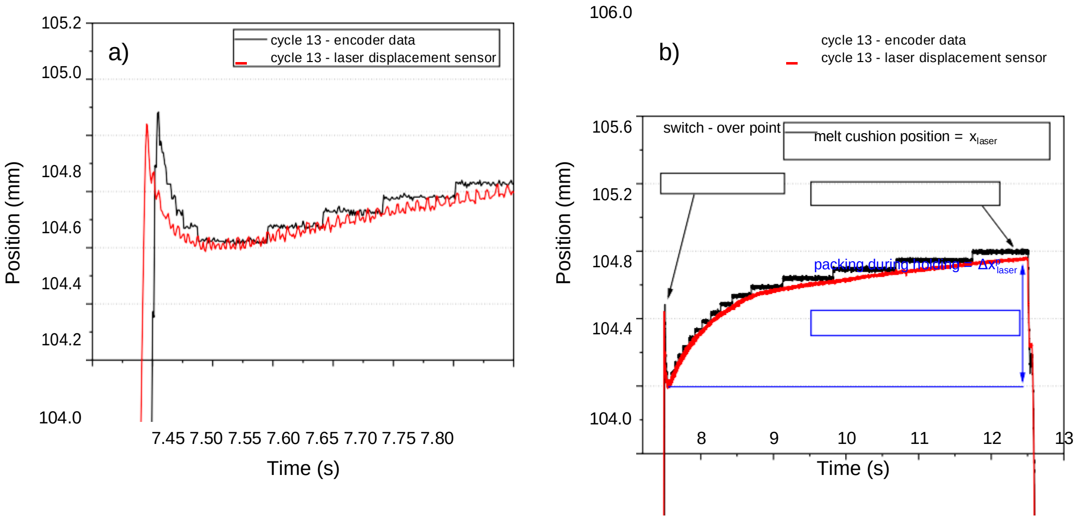

Figure 5-21. Comparison of position data taken from the encoder and laser displacement sensor. (a) shows a comparison of two measurements. Detail for packing phase is given by the plot given in (b).

Overall, it can be observed from the figures that the laser displacement sensor provides much more accurate measurements for the position of the injection unit. The limitations in encoder data can also clearly be seen, where stepped values in the data suggest that the measurement interval or resolution of the encoder is ~60 µm. Displacement data given in the graph on in Figure 5-21a proves that the laser sensor would provide much better measurements over the encoder. Similar to the previous batches where three process fingerprints have been extracted from the encoder data, similar fingerprints have been extracted from the laser sensor data, namely x_{laser} Δx^{p}_{laser}, $\int x_{laser}$. The integration of the curves for $\int x_{enc}$ have been carried out from a ~25 ms window which is circa an order of magnitude lower than the previous batches.

Data presented in Figure 5-22 are the scatter plots for h_{avg} vs the process fingerprints extracted from the encoder and laser displacement sensor according to procedures mentioned previously. For comparison, encoder fingerprints have been given on the left column and laser displacement on the right.

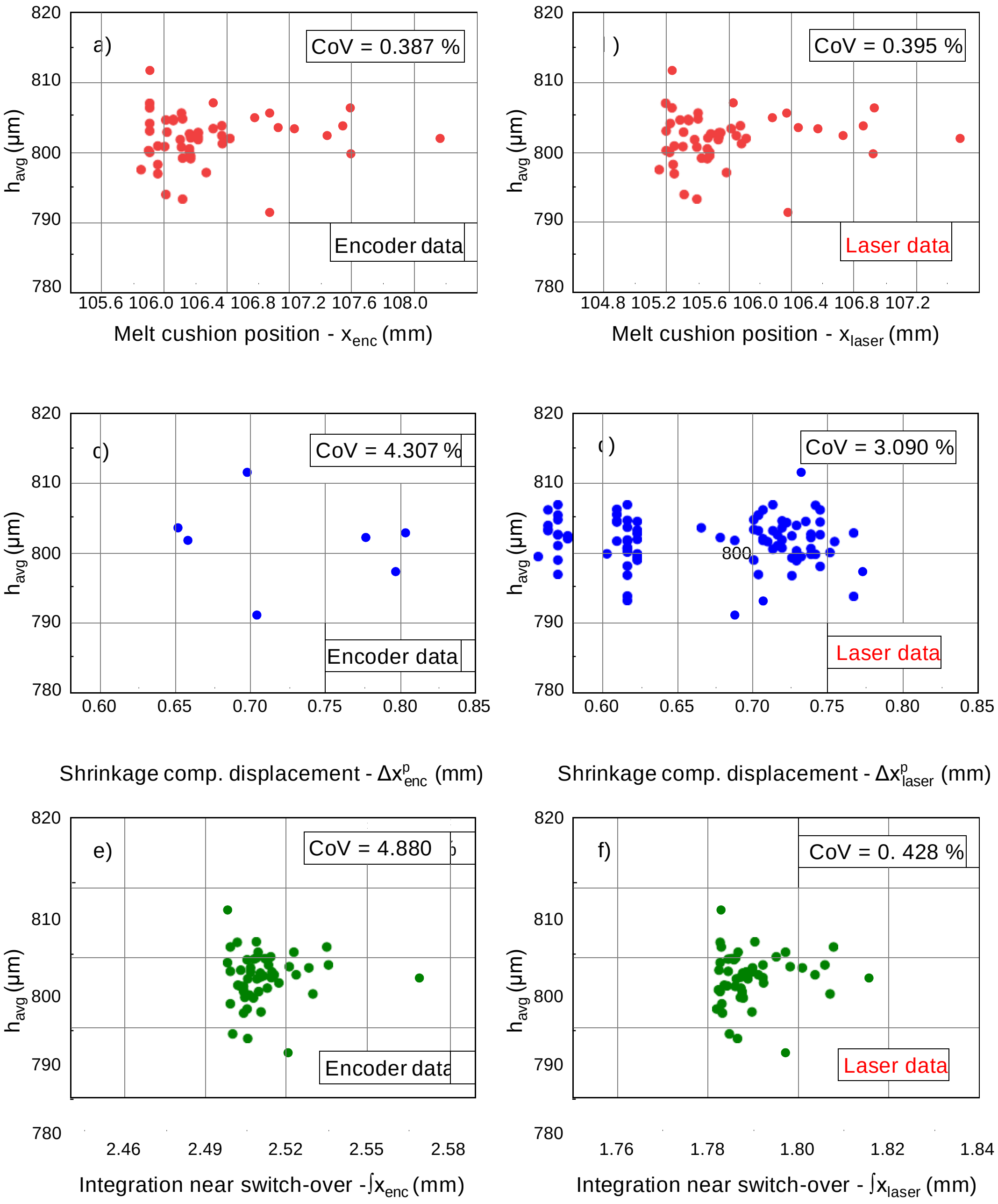

Figure 5-22. Scatter plots for average needle height and process fingerprints extracted from piston displacement information obtained from the encoder (left column) and laser displacement sensor (right column).

The graphs given above exhibit a scattered behaviour for process fingerprints extracted from the encoder and laser displacement sensor. Graphs given in the first row for x_{enc} show a great deal of similarity where the data points from encoder are very similar with the laser displacement data. In this particular case, laser displacement data verifies that encoder data can be sufficient in terms of its resolution and accuracy for analysing melt cushion of the micromoulded parts to some extent. However, it is likely that if data acquisition rate increased above 1000 Hz, encoder data could become obsolete due to its low accuracy because of its resolution in both position axis and time domain. The resolution in time domain for machine data is defined by the machine controller, which is also affected by the inertia effects.

According to the second row of scatter plots given in Figure 5-22, the encoder's resolution limitation is repeatedly obvious where the laser triangulation sensor provide better measurements for $\Delta x^{p}_{\mathrm{laser}}$.

Integration values extracted from near the switch-over region ($\int x_{\mathrm{laser}}$) showed a similar behaviour to the other fingerprints, where no trends have been detected in the data. It should be noted once again that the width of the data in time axis during the switch-over decreased to ~25 ms from 250 ms which makes it more difficult to assess since the data acquisition rate of 1000 Hz might not be sufficient. As the time intervals for integration become smaller, high acquisition speeds are definitely needed to record more data points.

To summarise, it has been seen and experimented that the injection plunger position data recorded from encoder and laser displacement sensor showed a scattered behaviour and do not show any correlation to the final product quality of microneedles. The reasons could be summarised and discussed as following:

1. Increased injection velocities for this batch (250 mm/s) which was set makes it more challenging and difficult to detect the dynamics of the process although a high-spec laser displacement sensor has been used. Laser sensor data have been found to be very accurate and reliable, however, software-wise improvements must be carried out in when detecting or calculating the actual process fingerprints. For instance, integration of the position data have been a challenge because of the varying dosage and hence the switch-over point.
2. Another main reason that could lead to scattered behaviour of the data is the material (PP) itself, which may not be very ideal for high-precision micro replication processes. The shrinkage values of the material are reportedly very high as compared with other materials available. The shrinkage effects were very obvious at the tip of the microneedles which could totally eliminate any correlation present between the height of the needles and process fingerprints. Dimpled

tips also makes edge detection algorithms difficult when it comes to measuring the exact height of the microneedles.

3. Slight inclinations in the circular base of the parts have also been noticed which might have affected the microneedle measurements, leading inaccurate needle heights. However, the effect is there for almost all the samples within the batch, hence decreasing its likelihood.

5.3.1.4 Process fingerprints extracted from injection and cavity pressure data

Injection and cavity pressure profiles showed slightly different characteristics from previous PP experiments with semi-automatic mode. For investigation of switch-over behaviour of the process pressure data graphs have been plotted alongside with laser displacement sensor data. Given in Figure 5-23 is a graph that belongs to cycle 21 where relevant process data have been given.

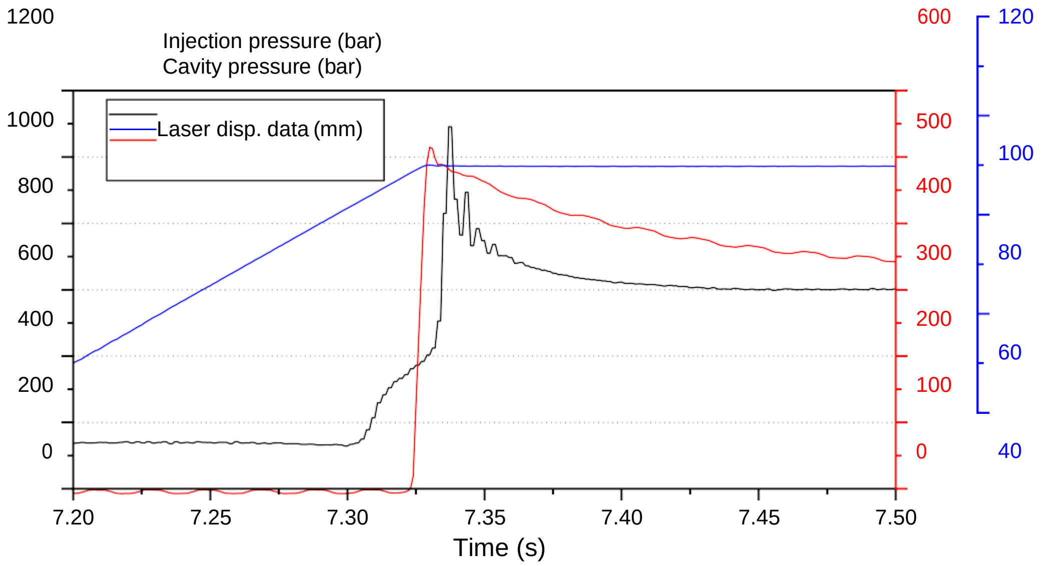

Figure 5-23. Injection pressure, cavity pressure and laser displacement sensor information for cycle 21 near switch-over point of the cycle.

One of the interesting features of the pressure curves is that the injection pressure has an oscillatory decay after it reaches its maximum. The effect could be present due to the closed loop feedback control of the injection unit. Cavity pressure peak also has been detected before the injection pressure peak which is unexpected.

Peak injection pressure (P^{P}_{inj}) and injection pressure integral ($\int P^{p}_{inj}$) have been extracted from the data with similar procedures used in previous experiments. Time interval for the integration have been chosen as 10 ms and wider time interval that extend towards the hold pressure seemed to be irrelevant to the results. Cavity pressure fingerprints, P_c^p and $\int P_c^p$ have been extracted using same procedures, except for using 15 ms of integration time. Scatter graphs have been plotted accordingly as given in Figure 5-24 with h_{avg} in y-axis.

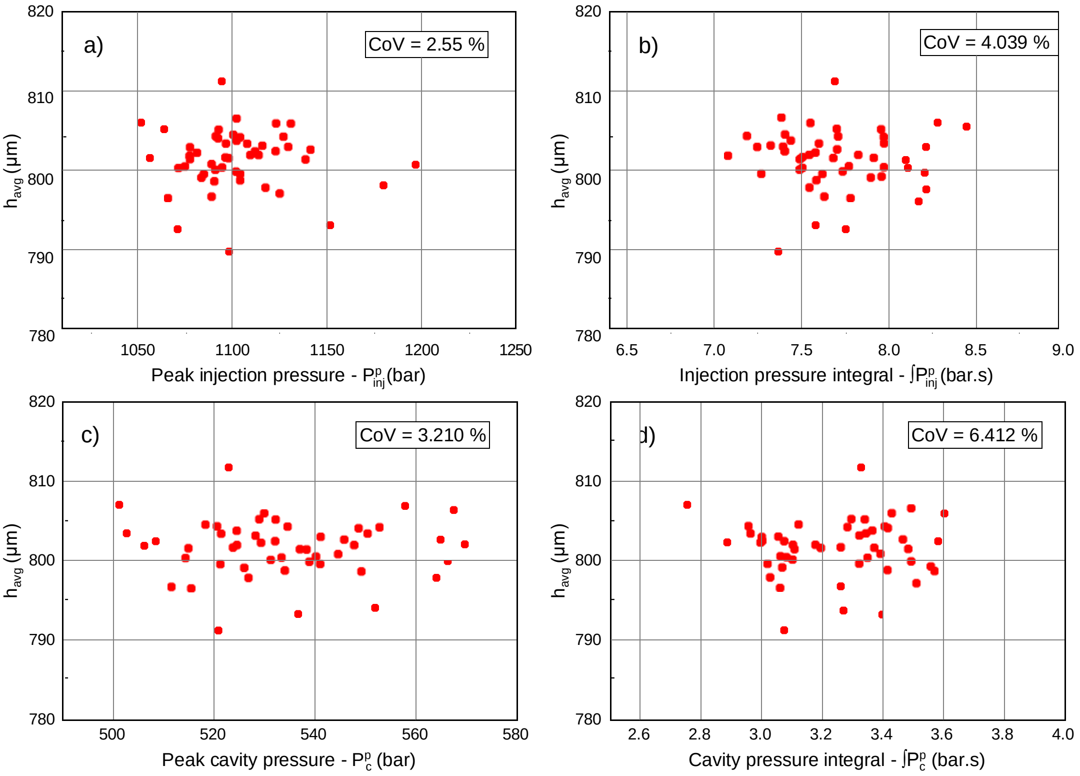

Figure 5-24. Scatter plots for process fingerprints extracted from injection (a and b) and cavity pressure data (c and d).

No trends have been seen for process fingerprints extracted from injection and cavity pressure data as given in above figure. Similar reasons given for the encoder and laser displacement sensor fingerprints can be considered for the scattered behaviour of pressure fingerprints. Moreover, it should be noted that the increased injection velocities and pressures used for this batch did not improve the filling of microneedle cavities as far as the average microneedle heights are concerned.

5.3.1.5 Summary of the results for PP microneedles moulded in full-automatic mode

PP microneedles have been produced in full-automatic mode based on the insights gained from the previous batches. For maximising replication, injection velocity and injection pressures have been increased significantly as compared with previous batches.

One of the interesting results has been that although injection pressure and velocity has been increased significantly, for the same mould temperature of 60°C, semi-automatic experiments resulted in 813.4 μm average microneedle height whereas full-automatic experiments with more extreme conditions resulted in 801.4 μm. The unusual dimpled tips of the microneedles were present only for the latter and seemed to affect this result.

Regarding the correlations between the process fingerprints and dimensional outcome of the PP microneedles no trends have been seen. The process data found to be scattered for both process fingerprints extracted from encoder, laser displacement sensor and pressure transducers. It should be pointed out that the dimpled tips of the microneedles might have affected the measuring the heights correctly and have an impact on the correlations. Moreover, the variability in the microneedle measurements has been very low, where the values seem to change between 790 – 810 μm range. Another possibility for not seeing correlations could be due to the telecentric optical inspection system. Ideally, the measurement method for microneedles should be able to detect even smallest changes, however, the mounting of the sample and baseline determination definitely will affect the outcome of the measurements. Alignment of the sample on the optical axis is carried out manually and slight human error will be present although the positioning of the holder plate and the sample is being done using geometrical calculations.

5.3.2 ABS experiments (Batch-m4)

ABS microneedles have been produced in full-automatic mode using conventional micromoulding. Experimental details and results have been discussed in the following.

5.3.2.1 Selection of process parameters and preparation

Process parameters have been maximised where possible in order to be able to fill the microneedle cavities completely. Following parameters given in Table 12 have been used for ABS experiments in full-automatic mode.

Table 12. Process parameters used for moulding ABS microneedles for Batch-m4.

Process parameter	Value - unit
Melt temperature	240 (nozzle), 235, 235, 225 (hopper)
Mould temperature	60°C
Injection velocity	400 mm/s
Switch-over pressure	1050 bar
Holding pressure	1100 bar
Holding pressure duration	7.5 s
Cooling time	10 s

Once again, different process parameters have not been experimented since the purpose is to increase the parameters where possible for better replication. 60°C mould temperature has been used which was the middle setting for semi-automatic ABS experiments discussed in 5.2.2. Switch – over pressure has been significantly increased as compared with the semi-automatic ABS experiment, from 700 to 1050 bar. Since this increase was very effective in obtaining very good replication in the initial observations, other parameters have not been changed. The main reason for this was the flashing defects around the circular base of the patch and this affects setting the baseline during microneedle measurements and visual quality of the part.

5.3.3 Experimental details and microneedle measurements

Process data have been captured automatically for each cycle as done previously. Four channels of data, namely injection pressure, position data from the encoder, position data from laser displacement sensor and cavity pressure have been recorded using 1000 Hz of acquisition rate.

The previous procedure used for stabilising the thermal gradients within the machine, where 50 parts have been discarded first in full-auto mode and 50 collected afterwards. Microneedle measurements have been carried out using the telecentric optical measurement system. Figure 5-25 shows an SEM image of one of the better replicated needles from the batch. The pointy tip of an ABS needle can be clearly seen which suggests very good replication of microneedle cavities.

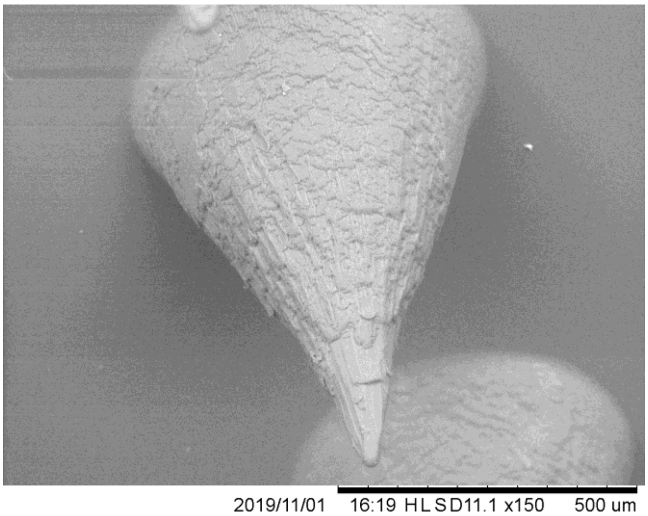

Figure 5-25. SEM image one of the better replicated needles taken from Batch-4m

Statistical terms extracted from the microneedle measurements for this batch are given in Table 13.

Table 13. Microneedle measurement results from telecentric inspection system for Batch-4m.

Average needle height ($\mathrm{h}_{\mathrm{avg}}$)	Standard deviation for $\mathrm{h}_{\mathrm{avg}}$ (SD)	Coefficient of Variance for $\mathrm{h}_{\mathrm{avg}}$ (CoV)
886.7 μm	4.282 μm	0.48 %

The measurement result suggest that increased packing and switch-over pressures had significant impact on microneedle replication as compared with previous ABS batch which was carried out in semi-automatic mode. Average needle height of 886.7 μm is the best value have been achieved so far, which also signifies importance of using an amorphous polymer (ABS) over semi-crystalline (PP). SD and CoV for $\mathrm{h}_{\mathrm{avg}}$ also decreased significantly when it is compared with Batch-2m. The better filling behaviour is evident from the telecentric image given below in Figure 5-26.

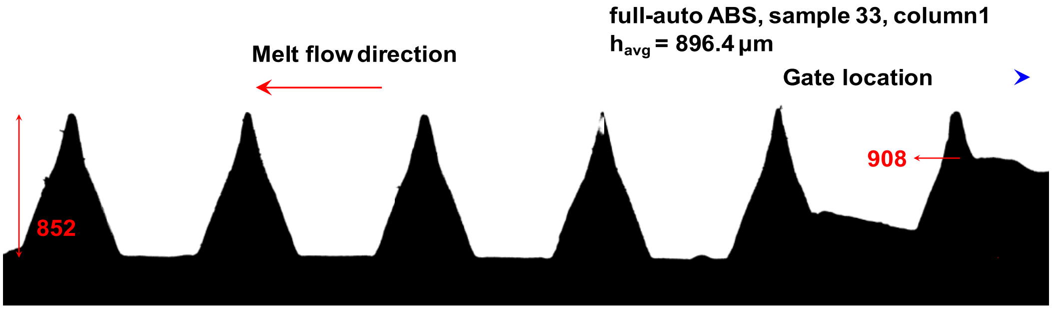

Figure 5-26. Figure showing a telecentric image of the leftmost column from cycle 33.

Telecentric image above show a reasonably flat base for telecentric measurements where it had been an issue in the previous batch with PP. However, the round tips and relatively longer needles according to the measurements raise concerns regarding bent or tilted samples during ejection. It could be expected that the needle on the right-end with 908 µm should have had a smaller tip radius.

5.3.3.1 Process fingerprints extracted from encoder and laser sensor data

Process fingerprints have been extracted using displacement data from the encoder and laser displacement sensor as done previously for Batch-3m. $\int x_{encoder}$ and $\int x_{laser}$ has been integrated from ~25 ms window near the switch-over point. $x_{encoder}$, x_{laser} $\Delta x^{p}_{encoder}$ and Δx^{p}_{laser} have been extracted using previous methods. Scatter plots given below depict the relationships between the mentioned process fingerprints and average needle height (h_{avg}).

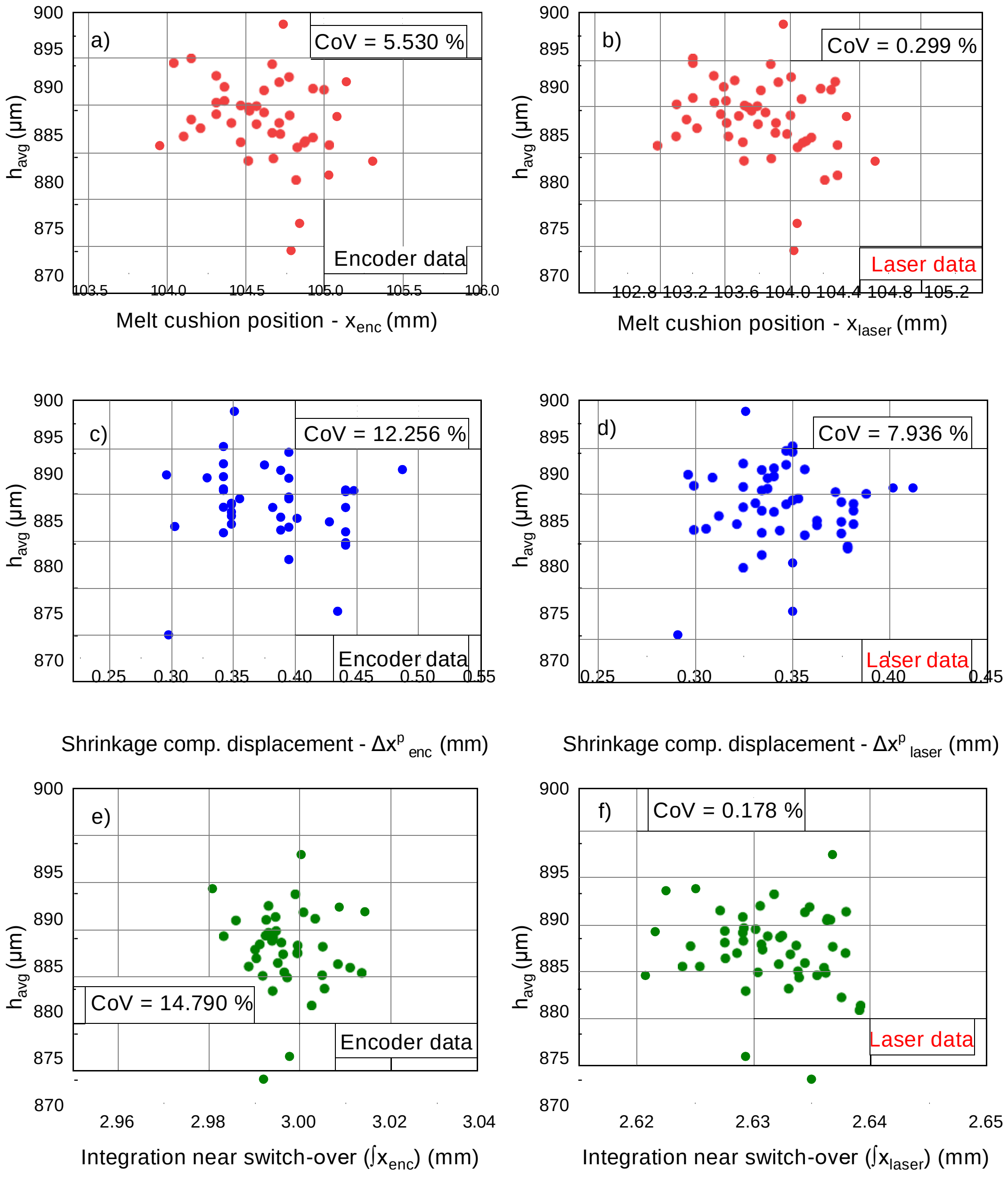

Figure 5-27. Scatter plots for average needle height and process fingerprints extracted from displacement information obtained from the encoder (left column) and laser displacement sensor (right column). The CoVs above 10% are due to some outliers which are not visible in the graphs.

Data in the above graphs depict a scattered behaviour for six different process fingerprints extracted from the position information of the injection unit. The reasons could be discussed as following:

1. It can be recalled from previous experiment where PP microneedles produced in full-automatic mode, shrinkage could have been an issue in accurately measuring the needle heights. For this batch where ABS was used however, the shrinkage effects that could impact the scattered behaviour can be discarded. Instead, the good performance

of filling the deep microneedle cavities could also contribute to this scattered behaviour where it is almost moulding too well that the fingerprint information or impact cannot be detected.

2. Molecular ordering of the polymer used for micromoulding is of great importance. Due to the shrinkage effects that could affect the final dimensions and functionality of the part, it can be said that using amorphous polymer will be more suitable. Hence, it can be stated that process characteristics and product measurement outputs will be close to an ideal micromoulding process. As Micropower 15 uses pressure-controlled switchover for making sure that the moulded product is of good quality and dosing variations are very common in the process, the scattered behaviour of process fingerprints show to some extent that the process is behaving according to its design.

5.3.3.2 Process fingerprints extracted from injection and cavity pressure data

Switch-over behaviour of this batch seemed to be on the same par with full-automatic PP experiments as given in Figure 5-23. These plots have been omitted for the sake of not being redundant. The difference between this batch and previous batches was rather in cavity pressure profiles, where it was seen that the cavity pressure decays reaches a plateau and stays at a constant value until the ejection of the part. An example cavity pressure profile for cycle 44 can be seen in Figure 5-28.

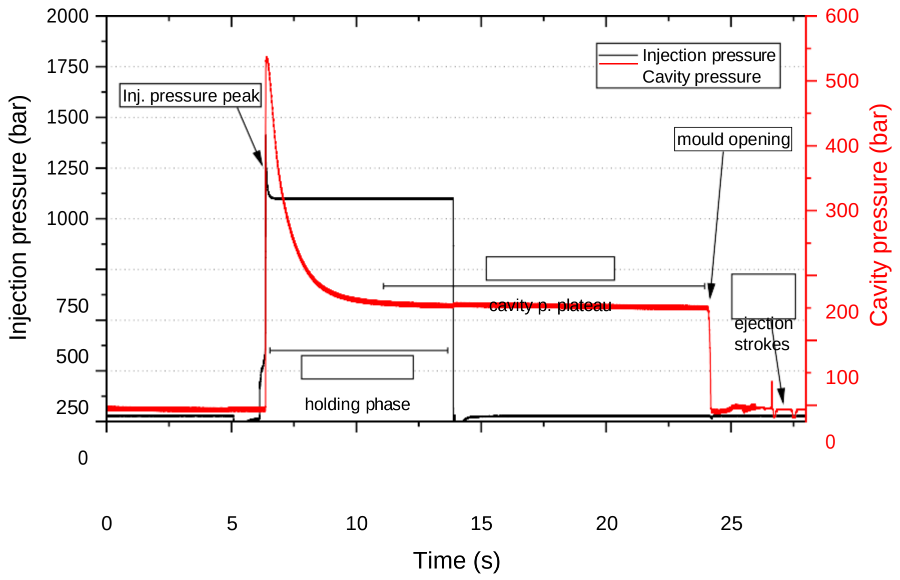

Figure 5-28. Cavity pressure profile for cycle 44 (red). Injection pressure is also included in black.

The cavity pressure behaviour shown in Figure 5-28 is likely to be caused by the frictional effects, where the load on the indirect pressure sensor could not be released due to high pressures applied during injection. Rather than exhibiting a decay towards zero pressure, the curve shows a plateau from t=14 s which clearly shows the load on the transducer even though the holding pressures is taken off.

Process fingerprints from injection and cavity pressures have been extracted using the same procedures given in 5.2.1.4. Given in the following are the scatter plots for h_{avg} vs pressure fingerprints.

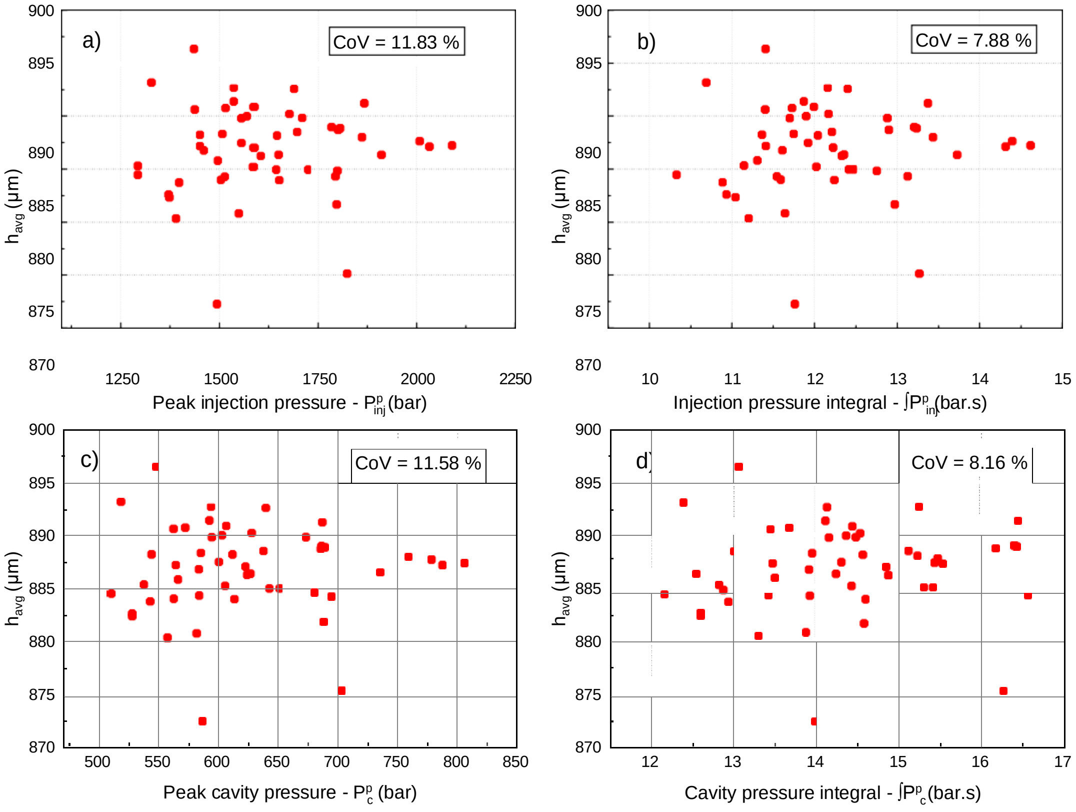

Figure 5-29. Scatter plots for process fingerprints extracted from injection (a and b) and cavity pressure (c and d) data.

The data given in Figure 5-29 once again showed a scattered behaviour similar to previous PP batch. One important feature to spot from the data is from the left-bottom graph where with increasing cavity pressures above ~750 bar, h_{avg} values seem to vary between 885 and 890 µm. That might suggest removing any physical effect that causes the fluctuations in cavity pressure measurements could result in obtaining reasonably pointy-tipped microneedles with good repeatability. Similar to the encoder and laser displacement sensor results, the optical measurements also might have an impact on the scattered behaviour in correlations. This is because, as the needles get sharp towards the end of the microneedle cavities it becomes harder to handle them without damaging the tips of the needles. And deformation occurred during ejection or handling of the parts results in even more scattered results. $\mathrm{P}_{\mathrm{inj}}^{\mathrm{p}}$ and $\int \mathrm{P}_{\mathrm{inj}}^{\mathrm{p}}$ also showed a similar behaviour to peak cavity pressures where above a certain pressure or integral value the needle height accumulated within the same ranges.

5.3.4 Comments on full-automatic experiments and suggestions

Full-automatic experiments have been run at more extreme conditions (higher injection velocities and pressures) than the semi-automatic experiments presented previously in order to maximise the replication of microneedle cavities. Moreover, continuous running of the machine at full-auto mode has shown almost like a pilot production scenario where the process data have also been recorded.

One of the main results from PP experiments has been that increased injection speed and pressures did not have impact the replication capability of the process. Moreover, the process fingerprint data against the product fingerprint showed a scattered behaviour in all aspects. In essence, this particular experimental batch has shown the challenges when using semi-crystalline polymers such as PP with considerable amount of shrinkage, which might not be suitable at all for precision manufacturing of polymeric micro-nano featured components.

ABS experiments on the other hand, presented the best microneedles in terms of their average height where it reached ~900 μm in some instances. This result showed the suitability of amorphous polymers to this particular application where pointy and sharp tips are needed for microneedles in order to penetrate easily to the skin. Process data against the quality criterion have been somewhat scattered, not showing any particular correlations or relationships. Following points can be considered for having more meaningful data and getting better understanding of the process:

1. Because of the high injection velocities and pressures have been used, some of the important dynamic aspects of the process could be hidden within the data. In order to be able to capture these details,

DAQ rate can be increased further up to ~50 kHZ which is the limit for laser displacement sensor.

2. It is likely that optical inspection system also reaches its limits when the needles are replicated almost too well, as witnessed for ABS experiments. The capability of the apparatus can be improved by developing a better flat-base holder for the samples and a better edge detection mechanism in the software.
3. As the microfeatures replicated as well as they can be, the conical structure gets narrower and more challenging for filling towards the end of the cavity. Meaning that there could be a relationship between the process and product fingerprints however, the measurement system might not be able to detect it.

5.4 Summary

This chapter has demonstrated conventional micro-injection moulding and process fingerprinting attempts for thermoplastic microneedles using both semi-crystalline and amorphous polymers. Extensive process monitoring devices have been used in order to extract meaningful process fingerprint information from acquired data. These unique features of process data have been interrogated with respect to final product quality. The work introduces such a fingerprint concept for the first time involving microneedle arrays. Moreover, different stages and features of a conventional, state-of-the-art micromoulding process have been identified and discussed in detail.

The suitability of semi-crystalline and amorphous materials for manufacturing of microneedle arrays was another focal point in the chapter, where significant differences in filling behaviour of PP and ABS have been demonstrated. Best results have been achieved in terms of obtaining sharp microneedles when using ABS.

Data presented for this chapter also shows that process fingerprinting could be more effective in certain ranges of process parameters or replication degrees. Furthermore, suggestions have been made for obtaining better correlations out of process fingerprints to use this concept in an in-line quality assurance scenario.

CHAPTER 6: Ultrasonic Micromoulding and Process Fingerprinting for Polymeric Microneedle Arrays

6.1 Introduction

This chapter discusses the experiments performed for process fingerprinting and characterisation of the ultrasonic micro-injection moulding process of thermoplastic microneedles. The experimental campaign has been structured according to the tools, materials and process fingerprint extraction methods that have been given in Chapter 3 and 4. The initial experiments have been carried out on the 5x5 EDM machined microneedle insert that was available at the time, which is different from the previous chapter where only the laser machined insert with 6x6 configuration has been used. However, a majority of the experiments have been carried out using the 6x6 laser machined insert due to it having more suitable geometrical features and challenging filling behaviour. Detailed analysis and discussion regarding process measurements taken from machine data, thermal imaging and cavity pressures are presented.

The experimental campaign for ultrasonic micromoulding consists of 5 experimental batches, namely; u1, u2, u3, u4 and u5. Because of the availability and tool modification requirements, cavity pressure measurements have only been carried out for the last two batches. Details of the experiments and process measurements used for different batches can be seen in Table 14.

Table 14. Experimental batches and main features.

Experimental batch	Material	Sensor technologies
Batch-u1	PP	Thermal imaging, machine data
Batch-u2	PP	Thermal imaging, machine data
Batch-u3	ABS	Thermal imaging, machine data
Batch-u4	PP	Thermal imaging, machine data, cavity pressure sensor
Batch-u5	ABS	Thermal imaging, machine data, cavity pressure sensor

Discussions in this chapter include interrogation of process data taken from different sensors, quality and process fingerprint analysis and material specific behaviour in ultrasonic micromoulding for polymer replication.

6.2 Initial process fingerprinting attempts for 5x5 microneedle configuration (Batch-u1)

A 5x5 EDM machined microneedle array insert presented in Chapter 3 previously has been used initially because of its availability for initial experiments for ultrasonic micromoulding. The insert also provides a good starting point as it has a simple, conical design without any additional tapers or extremely sharp tips. Also, the first experiment have been carried out using PP which is a relatively easy material to start with.

6.2.1 Process settings and conditions

The first task to set an ultrasonic micromoulding process is to determine the correct shot size for the particular micromoulding cavity. Although the main features and circular cavity size for the microneedle component are the same as given in Figure 3-8, the ultrasonically moulded part has a slightly different sprue geometry and slightly wider runner by 0.5 mm. Components which were produced using conventional micromoulding had a part weight of approximately 225 mg. Hence, a shot size of ~260 mg was set for ultrasonic micromoulding experiments and it corresponds to the weight of four PP disc preforms with 1.5 mm thickness. The shot-to-shot difference in weight was not significant as the preforms have been moulded with highly repeatable Micropower 15 conventional micromoulding machine. An image of the microneedle component with 5x5 configuration and discs in the sonication chamber are given in Figure 6-1.

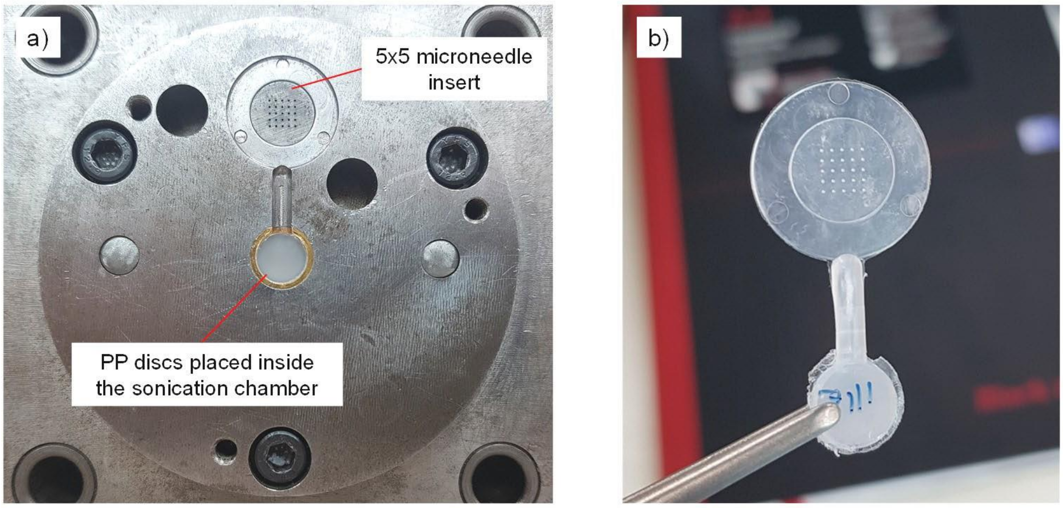

Figure 6-1. a) An image of the bottom die plate with 5x5 microneedle insert and PP discs placed inside the sonication chamber before moulding, b) an ultrasonically micromoulded 5x5 microneedle patch.

For this batch, the maximum process parameters were experimented where possible for fully replicating the micro features. A design of experiments (DoE) approach was not adopted for producing microneedle arrays due to the dependent variables of the ultrasonic micromoulding process. Instead, a set of parameters have been chosen and process and fingerprint variations from cycle-to-cycle have been studied.

Table 15. Process settings used for Batch-u1.

Process parameter	Value - unit
Sonication amplitude (A_{sonic})	~100 µm
Sonication duration - time (t_{sonic})	3 s
Mould temperature (T_{mould})	90°C
Injection force (F_{inj})	900 N

The sonication amplitude (A_{sonic}) has been selected at its maximum value of ~100 µm, as semi-crystalline polymers usually require more energy inputs initially because of their crystallites in the structure and sharp melting point. The sonication duration (t_{sonic}) could have been set for longer durations, however, since prolonged sonication durations make it more likely to overload the sonotrode it was kept as low as possible at 3 s.

T_{mould} is one of the critical parameters that affect the replication capability of an ultrasonic micromoulding process. It is usually a necessity to use as high mould temperatures as possible to overcome the overloading problems of the sonotrode. This is facilitated by not restricting the flow of the sonicated melt using high temperatures where applicable. 900 N was the maximum injection force (F_{inj}) that could be used without overloading the sonotrode and hence, it has been selected to provide better filling of the microneedle cavities alongside with other parameters.

6.2.2 Experimental details and results

100 parts were ultrasonically moulded using the parameters given in Table 15 for characterising the behaviour of the ultrasonic micromoulding process and replication assessment of 5x5 microneedle arrays. Thermal imaging and machine data have been used for process monitoring purposes due to the availability of the technologies at the time. 100 Hz frame rate and data acquisition rate has been set for thermal imaging and machine data capturing. Each sample and corresponding process monitoring data alongside with height measurements from microneedle measurement apparatus have been assigned to numbers for cycle-by-cycle analysis. Given in Table 16 are the process fingerprints extracted for this particular batch of experiments. Region of interest (ROI) for thermal imaging has been drawn in thermal imaging software for extracting temperature information 5x5 microneedle array area.

Table 16. Process fingerprints extracted machine data and thermal imaging.

Process fingerprint	Units	Characteristics
T_{peak}	°C	Peak temperature from 5x5 array
� T_{array}	°C. s	Integration of average temp. data from 5x5 or 6x6 ROI
V_{piston}	mm/s	Piston or injection velocity calculation using dx/dt
� Δx	°C. s	Integral of the piston deviation
E_{sonic}	Joule	Sonication energy
f_{av}	Hz	Average sonication frequency calculated from the start of melting until the end of sonication

Microneedles have been inspected manually using the telecentric optical measurement system. Measurements results and statistical terms regarding the height of the needles have been given in Table 17.

Table 17. Measurement results taken from telecentric inspection system for Batch-4m.

Average needle height (h_{avg})	Standard deviation for h_{avg} (SD)	Coefficient of Variance for h_{avg} (CoV)
521.1 µm	5.77 µm	1.10 %

Out of 2500 microneedles (25 on each patch) the average microneedle height and standard deviation was found to be 521.1 and 5.77 µm respectively. This average needle height suggests that ~98% of the microneedle cavity volume has been filled and relatively low standard deviations also prove the good packing of the polymer melt. A randomly selected sample has been inspected under SEM for seeing the details in the micron scale. An SEM image of a single needle at a 45° angle and telecentric optical images of some needles are given in Figure 6-2.

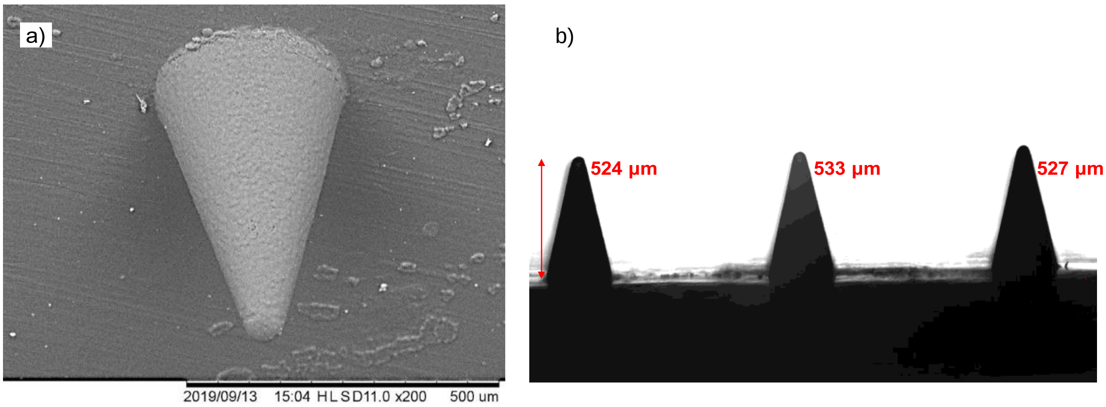

Figure 6-2. a) An SEM image of a PP single needle, b) telecentric optical images of three microneedles as an example.

The SEM image of a single needle in Figure 6-2a show that the microneedle cavities have been replicated successfully. A good indicator of replication is also the obvious roughness features on the conical structure caused by EDM machining technique for generating microneedle cavities. The telecentric optical image in Figure 6-2b does not show very detailed information other than height of the needles. However, it can be seen that the baselines of the needles are not level, and this was one of the reasons why the measurements were carried out manually.

6.2.2.1 Process and product fingerprint analysis

The graphs in Figure 6-3 depict that for each of the six different process measurements, no clear trends or correlations are seen between h_{avg} and process fingerprints. Only slight trends or accumulations of data within 100 points might suggest some relation between h_{avg} and T_{peak}, however, it is far from presenting a linear or other sorts of regression models. The results and SEM investigations suggest that the measured process fingerprints could be ineffective while using extreme process conditions.

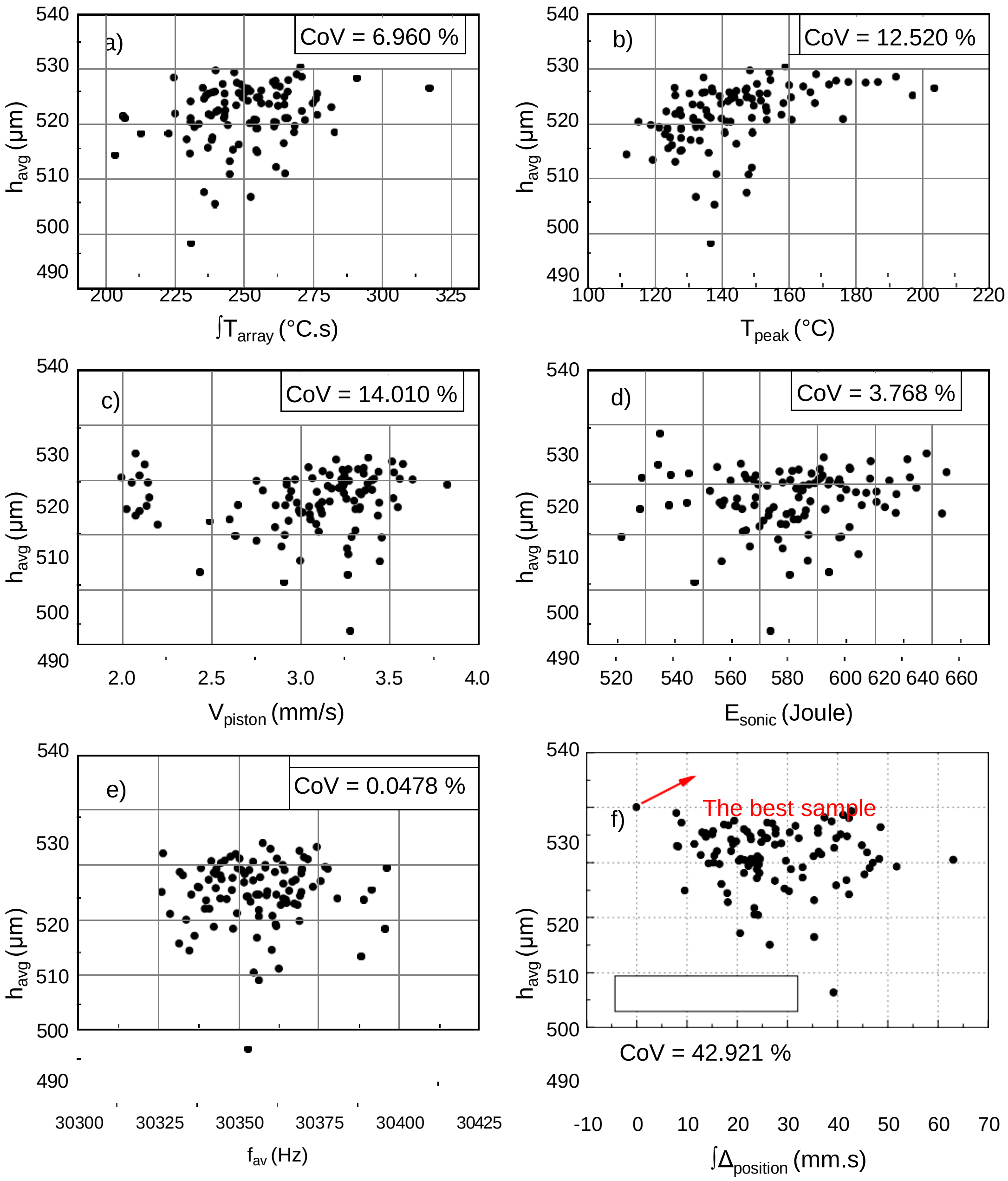

Figure 6-3 Average needle heights (h_{avg}) vs process fingerprints taken from ultrasonic micromoulding PP for 5x5 microneedle arrays. a) $\int T_{array}$: integration of average temp. data from 5x5 ROI, b) T_{peak}: peak temperature taken from 5x5 ROI, c) V_{piston}: Piston or injection velocity calculation using dx/dt, d) E_{sonic}: sonication energy, e) f_{av}: average sonication frequency, f) $\int \Delta x$: integral of the piston deviation from the best sample.

Fundamentally, one can expect that from a product fingerprint with ~530 µm deep microneedle features should yield some correlation, however, there are critical reasons and considerations behind for this particular random behaviour discussed as following:

1. The material has been used for this particular batch is PP with a semi-crystalline structure as discussed previously. Thermal imaging acquisitions for PP given in Figure 4-5 show extremely random and unpredictable temperature fields throughout the process. This effect is caused by the sharp melting point of PP where crystallites are present in the structure. Crystallites absorb some of the energy provided before the phase change, which is also called as latent heat and this leads to variations and randomness in local temperatures, hence viscosities of the material during filling of the microneedle cavities. The presence of latent heat in PP structures also has been presented in Figure 5-3. The effect can be considered as one of the major reasons for not seeing of any correlations. The highest temperatures witnessed after the filling might not be very effective for ultrasonic moulding of PP, as the material has an abrupt solidification point. Microneedles might have already been solidified in that sense, making any packing, or sustained ultrasonic heating ineffective.
2. Microneedle features on the 5x5 insert may not be particularly challenging in terms of feature replication as it is thought to be because of the blunt tips that has tip radii around 30 μm which is relatively easy to fill. Moreover, cavity depths of ~530 μm could be replicated without too much effort until 450-500 μm of needle heights achieved. The statistics out of 100 parts also suggest that the average needle height is around 520 μm although a high T_{mould} of 90°C have been used.
3. A combination of relatively high-end process parameters and less challenging micro-features result in additional randomness in the data where manifestation of dynamics of the machine is hindered. The significant randomness in machine and sonication related fingerprints such as V_{piston}, $\int \Delta x$, f_{av} and E_{sonic} that support this view.
4. The majority of the process fingerprints have been detected and extracted automatically using LabVIEW scripts. Some of the fingerprints such as V_{piston} have been calculated using a detection

method of the first derivative of the piston position. However, according to the accumulations of the results, some errors are present and there are room for improvements for detecting V_{piston}. The compaction of the discs before melting and slight inconsistencies in the sonotrode position also escalates this effect.

5. Since this is the first set of the experiments for ultrasonic moulding, the suitability or applicability of the selected process fingerprints cannot be evaluated or compared on their own only. The lesser correlations in data might suggest that the process fingerprints selected are not relevant or inadequate. However, some relations at least are expected as they have been selected quite carefully.
6. The final comment might be given on the errors of the telecentric microneedle measurement apparatus; however it is unlikely since every single needle has been measured manually with individual baselines. It is reasonable and expected that the system might introduce some errors because of the baseline selection and flatness of the samples during automatic acquisition mode. However, manual measurements signify the importance of the first five reasons above, where process-related issues are justified with the combination of randomness in melting and less-challenging micromoulding features.

6.2.3 Strategies for obtaining better correlations from process fingerprints

In order to present methods or models for an in-line quality assurance procedure based on process fingerprints for microneedles using ultrasonic micromoulding, the approach taken in the first experiment - Batch-1 must be revised and updated according to the below statements proposed in the light of the findings given in 6.2.2:

1. It is discernible that using amorphous polymers could result in better fingerprint responses due to their glass transition behaviour and not having sharp solidification points. After the main circular cavity is filled, partly-solidified material can be exerted towards the microneedle cavities to better extent which might yield better correlations particularly for piston position-related fingerprints. Moreover,

amorphous materials might show more equal distributions of temperatures which would result in consistent viscosities.

2. More challenging microneedle features could be used for allowing the manifestation of machine dynamics and sonication onto the part quality.
3. Rather than using maximum process parameters available, they can be decreased slightly for the experimentation of fingerprint responses. Furthermore, optimising a micromoulding process from part-filling the cavity towards applying more packing pressure is a more appropriate method to overcome pressure overshoots and other extreme effects.

By implementing these approaches, the suitability of the selected fingerprints and fingerprint extraction scripts in LabVIEW will be evaluated in a more realistic approach. Furthermore, it will be seen that whether the microneedle measurement apparatus have an effect on the correlation.

6.3 Initial process fingerprinting attempts for the laser machined 6x6 microneedle configuration

Based on the insight and experience gained from 5x5 EDM machined microneedle insert experiments, a more challenging task of laser machining of microneedle cavities with extremely small tip radii was undertaken and previously presented microneedle mould insert in 6x6 configuration has been machined as given in Figure 3-7. The experiments have included usage of two different materials, namely PP and ABS. 6x6 mould insert has been installed to the cavity die plate as shown previously in Figure 6-1.

6.3.1 Polypropylene experiments using the 6x6 insert (Batch-u2)

The same shot size of ~260 mg used for has been used which correspond to four PP discs with 1.5 mm thickness. Alongside with a more challenging microneedle geometry to fill, the process parameters were also decreased for having better correlations between the average needle height from one patch ($\mathrm{h}_{\mathrm{avg}}$) and process fingerprints and a well-defined starting point for process fingerprint analysis.

Relatively lower mould temperatures (50 - 60°C) have been chosen for this batch compared with the previous experiment where 90°C was used. Lower mould temperatures require more sonication energy to be able to melt and inject the polymer. Hence, sonication time has been increased from 3 to 4 s compared with previous batch for providing sufficient energy for melting and filling. The process parameters used for this batch have been summarised in Table 18.

Table 18. Process settings used for Batch-u2.

Process parameter	Value - unit
Sonication amplitude (A_{sonic})	~100 μm
Sonication duration - time (t_{sonic})	4 s
Mould temperature (T_{mould})	50 - 60°C
Injection force (F_{inj})	750 N

100 parts have been ultrasonically moulded with the process parameters shown in Table 18. Two different mould temperatures are used to disturb the process through 100 cycles and see if there are differences in process and product fingerprints. The first 50 parts have been moulded with 50°C and the remainder have been with 60°C. Once again, thermal imaging and machine data were recorded for every cycle. The mould tool was not modified for pressure sensor attachment at the time. Each of the microneedle arrays have been measured using the microneedle measurement apparatus in automatic mode.

Visual inspection of the samples showed that some of the parts were not completely filled when the 50°C mould temperature was used Figure 6-4a. 60°C yielded better filling and higher average microneedle height as expected Figure 6-4b. Telecentric images of some of the characteristic parts have also been given in Figure 6-4. It can be also seen that translucency of the parts were also negatively affected for T_{mould} = 60°C. This optical effect likely to be caused because of the amount of crystallites that are formed upon solidification which could be more abundant for T_{mould} = 60°C. Because of that reason 60°C samples seemed to be in a less transparent appearance whereas 50°C samples appeared to be more transparent. Amorphous regions have smaller refractive indices whereas crystalline regions tend to refract the light more due to their more ordered structures.

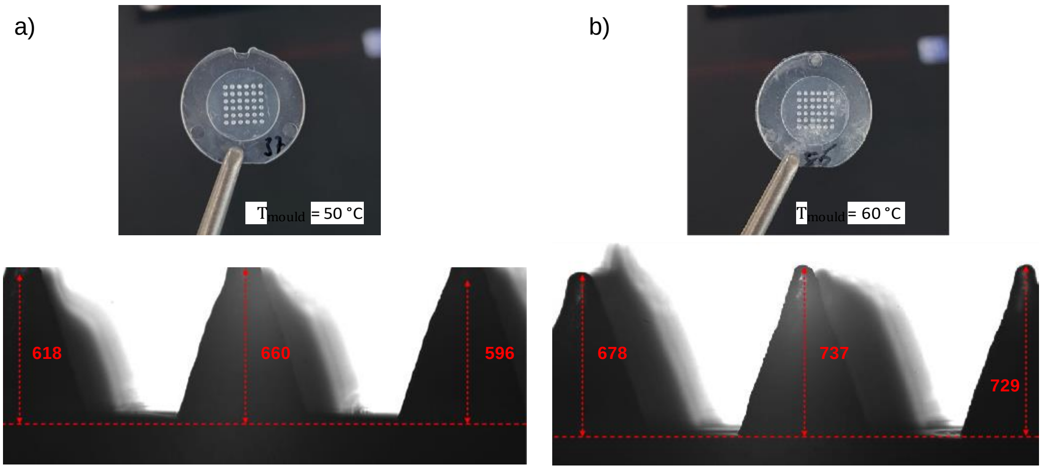

Figure 6-4. Images and characteristic microneedle measurements from parts moulded with 50 (a) and 60°C (b). Microneedle dimensions are in µm.

For assessment of different process conditions, given in the following Figure 6-5 depicts average needle heights, SD and CoV for different mould temperatures.

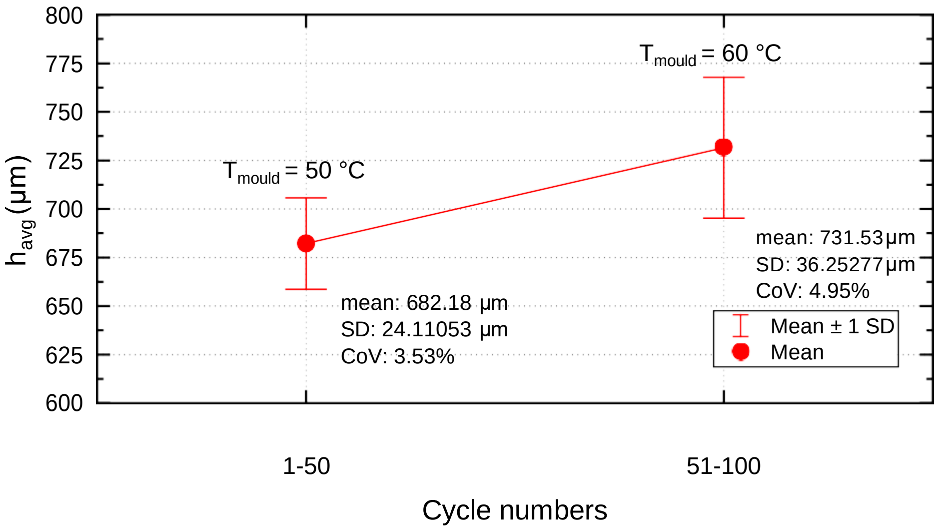

Figure 6-5. Interval plots showing the standard deviation and means of h_{avg} for cycles 1-50 and 51-100 with different mould temperatures of 50 and 60 C° respectively. SD, CoV and mean values have also been given.

Figure 6-5 shows that the average needle height is 682.18 and 731.53 µm for 50 and 60°C of mould temperature, respectively. A standard deviation of 36.25 µm for T_{mould} = 60°C can be seen which is significantly higher than that for samples moulded at 50°C. The main reason for these higher SD values is that the needle shaft gets narrower and becomes even more difficult to fill combined with the randomness of the temperature and viscosity distributions. Moreover, the CoV for the average height of the microneedles has also been increased with higher mould temperature by a factor of approximately 40%. During the inspection of microneedle patches under the optical apparatus, microneedle heights above 850 µm for $T_{mould} = 60°C$ were seen (Figure 6-6b), which contributes to the high SD and CoV of the data. These long-needles are in correspondence with the local viscosity differences and appear randomly according to the SEM and telecentric optical measurement system. An SEM and optical image of one of these needles are given in Figure 6-6.

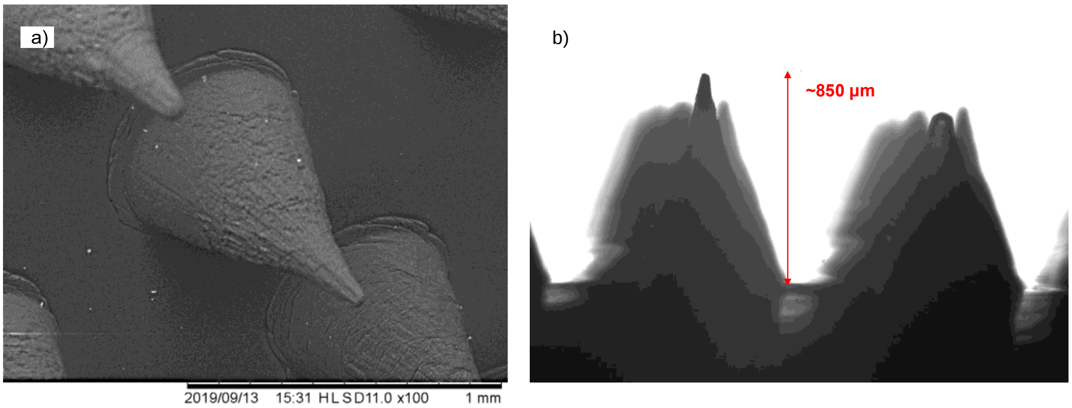

Figure 6-6 a) An SEM image of a PP single needle, b) telecentric optical images of better-replicated microneedles.

6.3.1.1 Process fingerprints from machine data

In the following, scatter plots have been given for h_{avg} vs process fingerprints. Machine data and thermal imaging fingerprints have been given separately. The scatter plots have been given for 100 samples representing both mould temperatures. The effect of mould temperature has also been discussed where possible. Scatter plots for h_{avg} vs V_{piston} (piston velocity during injection), $\int \Delta x$ (Integral of the piston deviation), E_{sonic} (Sonication energy) and f_{av} (average sonication frequency presented in Figure 6-7.

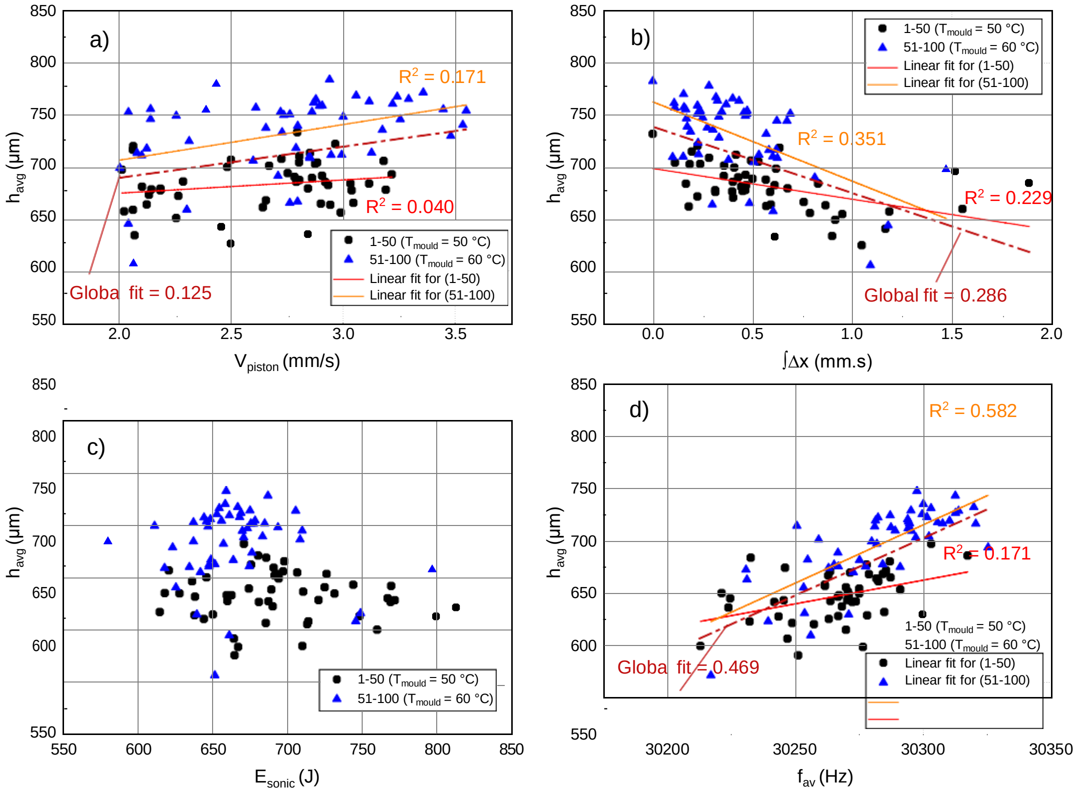

Figure 6-7 Scatter plots depicting correlations for $\mathrm{h_{avg}}$ vs $\mathrm{V_{piston}}$, $\int \Delta\mathrm{x}$, $\mathrm{E_{sonic}}$, $\mathrm{f_{av}}$.

Figure 6-7 shows the correlations between the process fingerprints extracted from machine data and quality criterion, $\mathrm{h_{avg}}$. The data includes samples from both mould temperatures of 50 and 60°C. To quantify the correlations between process and product fingerprints, linear fits are applied and R^2 values have been calculated.

Significant improvements have been seen as compared with the previous batch in $\mathrm{V_{piston}}$ although the same boundary detection method was used for setting the start and end points for calculating this particular fingerprint (Figure 6-7a). $\int \Delta\mathrm{x}$ given in Figure 6-7b showed slight correlations with an R^2 value of 0.229 and 0.351 for 50 and 60°C mould temperatures respectively. The global fit has shown some correlation with approximately R^2 = 0.3 which could be promising for further experiments. It should be noted that inhomogeneous melting also will cause differences and inconsistencies in injection and conveyance of the material which is being melted and injected simultaneously. Hence, although there is room for improvement, R^2 values from piston position information can be considered as a significant result. The inconsistencies and randomness during melting in turn affects the actual position and injection velocity applied by the piston, causing differences cycle to cycle. Higher V_{piston} and lower $\int \Delta x$ values indicate the material is somewhat being melted and injected in a more rapid way. This is most likely to be caused by the initial ordering of the disc preforms and interfaces between them where some of the discs might have better contact with the other preforms either above or below.

Sonication energy, E_{sonic}, did not present any trend or correlation and suitability of this fingerprint might be questioned for this semi-crystalline material Figure 6-7c. The latent heat needed for PP to initiate the phase change of PP from solid to viscous state amplifies the scattered behaviour of sonication energy data. E_{sonic} and f_{av} usually have positive relationship and their behaviour could be predicted by one another, however, this is more valid for amorphous polymers. f_{av} yielded the most obvious linear trend for predicting microneedle height. R^2 value of 0.469 for the global fit is significantly higher than the values obtained other fingerprints extracted from machine data. In Chapter 2, Eq. 2.28 was given and it shows that there is a linear relationship between viscoelastic heat generation and frequency of the applied strain. This is in correspondence with the data in Figure 6-7. Higher average sonication frequencies during the process yields better filling of microneedle cavities due to more energy generated during melting of the polymer. Reduced viscosities which in turn results in better filling behaviour. This is a significant result as good correlations with R^2 value of ~0.5 is significant from a process fingerprints taken from machine data without additional sensor technologies.

6.3.1.2 Process fingerprints from thermal imaging

Scatter plots regarding process fingerprints that have been extracted from thermal imaging are given in Figure 6-8. Temperature measurements from the gate region have been omitted due to their lesser correlations and randomness of the data. Linear and asymptotic exponential fits have been applied to the data sets where applicable. For the sake of clarity, T_{array} and T_{end} are the average temperature values recorded from the ROI drawn on the 6x6 array or the end of cavity for each frame acquired. $T_{p-array}$ and T_{p-end} are a single-peak temperature values extracted within the 6x6 ROI and the end ROI, and are unique for each cycle.

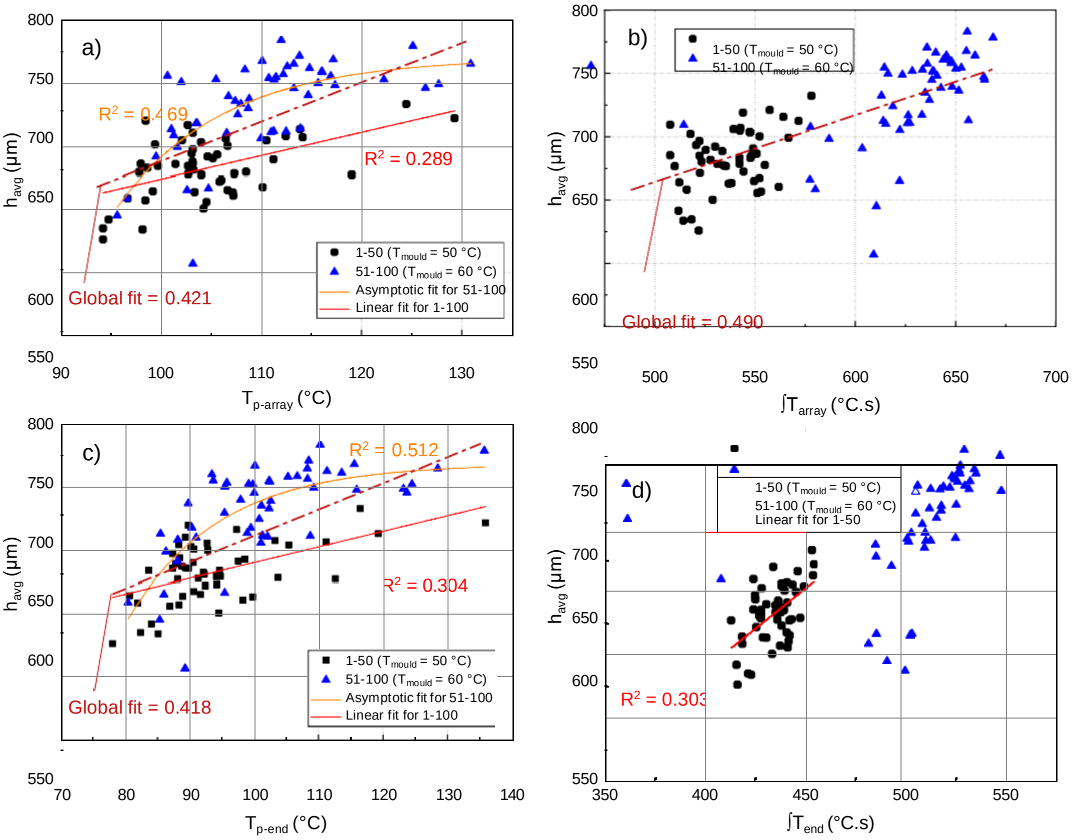

Figure 6-8. Scatter plots depicting correlations for h_{avg} vs $T_{p-array}$, T_{p-end}, $\int T_{array}$, $\int T_{end}$.

Obvious improvements in terms of correlations for process fingerprints extracted from thermal images are seen from Figure 6-8 as compared with previous Batch-u1 where the blunt 5x5 microneedle insert was used. In general, for lower mould temperatures a positive-linear relationship is present with increasing values of both peak temperatures and temperature integrals. Linear fits result in R^2 values of ~0.4 and 0.5 where good correlations are present in general.

The distribution of data for peak temperatures (Figure 6-8a and c) suggest that an asymptotic exponential fits could be more appropriate rather than having linear fits. Asymptotic fits for 60°C of mould temperature yielded ~0.5 of R^2 for peak temperatures which were read from both 6x6 array and end ROI of the thermal images. T_{p-end} in Figure 6-8c shows slightly better correlation as suggested from R^2 value of 0.512 over 0.469 from the measurement taken from the 6x6 array ROI. The data shows average needle height increases with temperature between ~90 - 100°C and then temperature does not have a significant effect on the microfeature replication. Temperature integrals generally showed scattered data (Figure

6-8 d) for higher mould temperature in particular, although a slight positive trend between $\mathrm{h}_{\mathrm{avg}}$ and process fingerprints are present.

By implementing the experimental approaches suggested in 6.2.3, significant improvements have been made in terms of predicting the trends in the quality criterion cycle by cycle using process measurements. The most meaningful data came from the average sonication frequency and peak temperature fingerprints where R^2 values of ~0.5 were present for different type of fits. It should be noted that the changes made in experimental approaches were quite radical and one might expect better correlations from the process data. However, the results still signify that usage of a semi-crystalline material such as PP in ultrasonic micromoulding for process fingerprinting methods is a challenge. As previously discussed, the randomness in melt temperatures alongside with its effect on the viscosity distribution of the material and also shrinkage effects amplify the randomness and unpredictability for PP experiments.

The mould temperature in this particular experiment can be increased and likelihood of obtaining slightly better correlations is present, since the average needle height was only 731.53 μm for 60°C of mould temperature and there is room for improvement. As the filling progresses, it becomes more difficult for the polymer melt to fill the sharp microneedle tips. This could allow stronger manifestation of sonication related fingerprints and piston movement on $\mathrm{h}_{\mathrm{avg}}$.

6.3.1.3 Summary of this experiment

Results presented for this experiment show that filling behaviour of the deeper 6x6 microneedle configuration is more sensitive to the process fingerprints. Average sonication frequency and piston position data presented for the first time yielding moderate relationships to the final part quality. Asymptotic behaviour of peak temperatures has been one of the most interesting results from the thermal imaging acquisitions, where integral values have been somewhat scattered that could be attributed to the extremely random melt temperatures reported previously. Another outcome of the experiment is that the deviation in average needle height increases as the polymer melt reaches to the second, narrower taper of the microneedle cavities.

6.3.2 ABS experiments using 6x6 insert (Batch-u3)

A similar set of experiments have been carried out using ABS instead of PP to see how the process measurements and replication of the micro-features change when using an amorphous polymer.

The same shot size of that corresponds to 4 disc preforms of ABS has been used and weighed 270 mg. Once again, slightly lower-end process parameters that would result part-filled microneedle cavities has been experimented first and set accordingly. Following process parameters given in Table 19 have been used for ABS.

Table 19. Process settings used for ABS in Batch-u3.

Process parameter	Value - unit
Sonication amplitude ($\mathrm{A_{sonic}}$)	~90 μm
Sonication duration - time ($\mathrm{t_{sonic}}$)	3.5 s
Mould temperature ($\mathrm{T_{mould}}$)	80 - 90°C
Injection force ($\mathrm{F_{inj}}$)	1500 N
Packing force and duration	2000 N for 6 s

Because of the higher viscosities of ABS compared with PP, each of the process parameters have been increased significantly for obtaining a part with adequate quality. One of the main differences between ultrasonic micromoulding of ABS and PP is the packing phase that is present for ABS. The amorphous structure of the polymer allow the flow of the melt to a longer extent as compared with PP which has an abrupt solidification point. An additional force of 2000 N for 6 s has been applied for packing ABS into the cavity. 100 parts have been ultrasonically moulded with the process parameters given in Table 19. Once again two different mould temperatures have been used here to disturb the process through 100 cycles and see if there are differences in process and product fingerprints. The first 50 parts have been moulded with 80°C and the remainder have been with 90°C. Similarly to the previous batch, thermal imaging and machine data were recorded for every cycle. The mould tool was not modified for pressure sensor attachment at the time. Each of the microneedle arrays have been measured using microneedle measurement apparatus in automatic mode. Visual inspection of the samples suggested that the main cavity was filled completely for both mould temperatures. Optical images show slightly shorter microneedle heights as compared with PP batches. Figure 6-9 shows images taken from samples

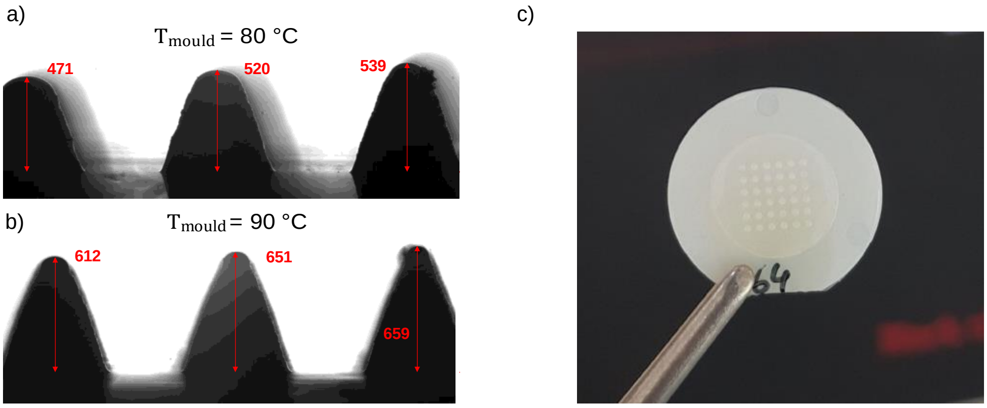

Figure 6-9. a) and b) characteristic microneedle measurements from ABS parts moulded with 80 and 90°C, c) an image of the ABS microneedle patch and the microneedle dimensions are in μm.

The best replication is achieved for needles that are the ones closest to the gate (the rightmost needles in Figure 6-9a and b. Different from the PP experiments, there is a consistent decreasing trend in microneedle height towards the end of the cavity. The reason for this effect is that the sonication source being closer to the gate and hence more energy is provided to the melt in that location decreasing its viscosity which results in better replication of microneedle cavities near the gate. Moreover, the effect of sonication towards the end of the cavity decreases because of the attenuation of the sonication waves.

The measurement results showed that the average needle height is 448.58 and 568.51 μm for 80 and 90°C of mould temperatures, respectively. Standard deviations of 35.08 and 50.29 μm have also been calculated which are significantly high, presenting a wide spread of average height of the microneedles. CoV increased about 13% for higher mould temperatures. The interval plots for the microneedle measurements is shown in Figure 6-10.

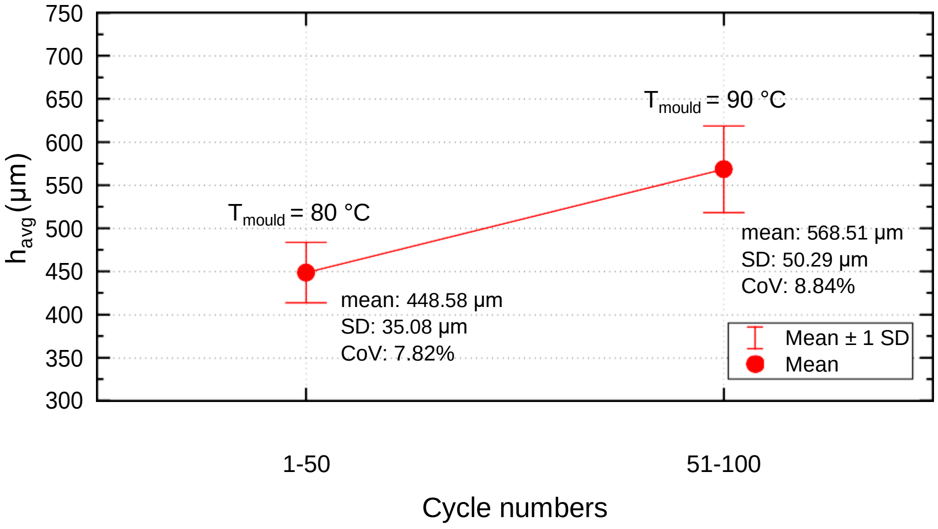

Figure 6-10. Interval plots showing the standard deviation and means of h_{avg} for cycles 1-50 and 51-100 with different mould temperatures of 80 and 90°C respectively. SD, CoV and mean have also been given.

Sporadic and extremely long needles have not been spotted for ABS experiments because of its relatively homogenous temperature distribution and lower viscosity than of PP. The longest microneedles from this batch have been measured at around 700 µm. The investigations under SEM showed that most of the needle cavities have been filled up to or slightly into the second narrower taper which starts around ~650 µm Figure 6-11.

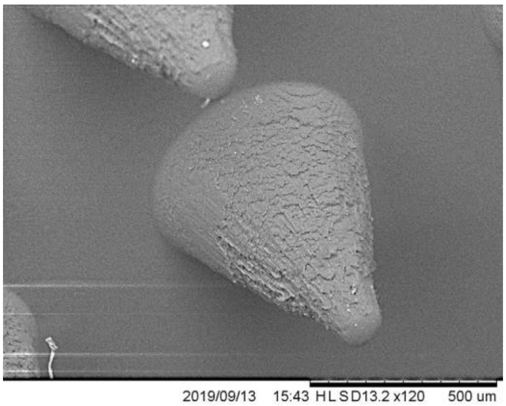

Figure 6-11. SEM image of an ABS microneedle taken from a random sample.

6.3.2.1 Process fingerprints from machine data

The analysis of the process and product fingerprints have been carried out in the similar manner with the previous batch for better comparison. Given in Figure 6-12 are the process fingerprints extracted from the machine data vs h_{avg}. Linear fits applied to the data where possible.

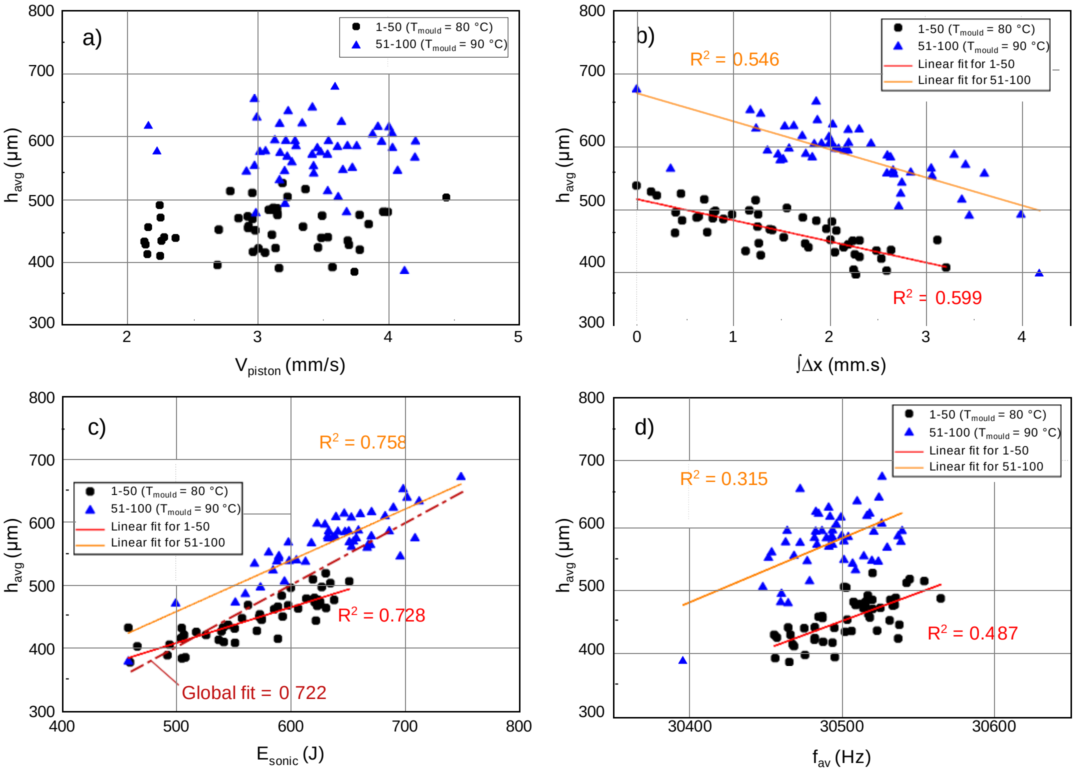

Figure 6-12. Scatter plots depicting correlations for h_{avg} vs V_{piston}, $\int \Delta x$, E_{sonic}, f_{av}.

The data in Figure 6-12 represents substantial correlations between process and product fingerprints when compared with PP experiments for all fingerprints except V_{piston}. The obscure data for the piston velocity prove that piston movement described using $\int \Delta x$ is a better candidate for process monitoring purposes as suggested with its very good R^2 values of 0.599 and 0.546 for 50 and 60°C of mould temperature respectively (Figure 6-12b). It can be suggested that the deviation of the piston position can be a measure of microfeature replication quality for ABS. E_{sonic} measurements resulted in the best correlations with R^2 values reaching 0.722 (Figure 6-12c). Apparently, the sonication characteristics of the ultrasonic stack and melting of the polymer largely dependent on the molecular structure as the E_{sonic} were scattered for previous batches. The main reason for this is that ABS does not have a latent heat during melting and most of the heat or sonication energy given to the feedstock contributes to the movement of the molecules and viscosity decrease. It can be clearly stated that E_{sonic} could be a reliable process fingerprint for amorphous materials. The result is also significant from cost and labour point of view as the data is directly taken from the ultrasonic micromoulding machine itself, without any additional sensor implementation. f_{av} also showed a positive linear trend and yielded reasonable R^2 values of 0.3 - 0.5 (Figure 6-12d). The data for average sonication frequency also present that a 10°C mould temperature increase did not have a big impact on the resonant frequency of the horn as the data accumulate around the same frequency values.

6.3.2.2 Process fingerprints from thermal imaging

Figure 6-13 represents information regarding the process fingerprints extracted from thermal imaging. Linear fits were applied to the data where appropriate.

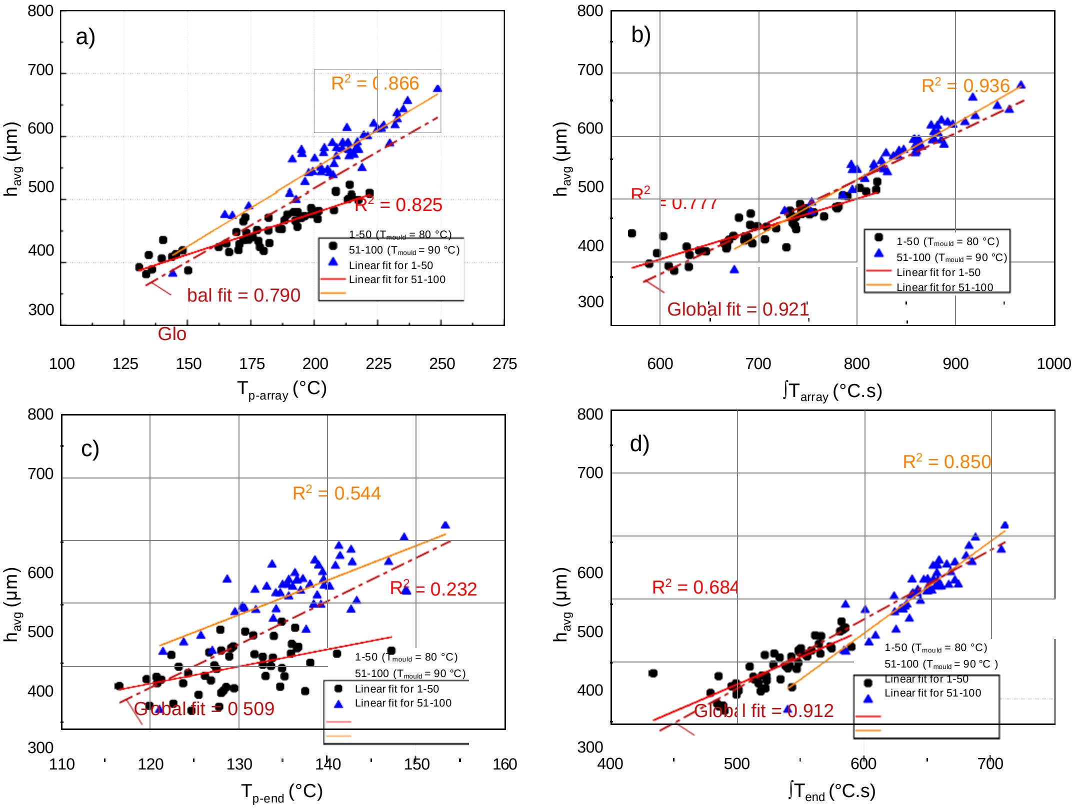

Figure 6-13. Scatter plots depicting correlations for h_{avg} vs $T_{p-array}$, T_{p-end}, $\int T_{array}$, $\int T_{end}$.

Ultrasonic plasticisation of amorphous and semi-crystalline polymers is significantly different from each other as discussed previously. Thermal imaging results presented in Figure 6-13 also support this view as there are very strong correlations between microfeature replication and process fingerprints whereas the previous batch with PP only yielded reasonable correlations.

Peak temperatures measured from the 6x6 array ROI ($T_{p-array}$) show strong correlations with the part quality with R^2 values of 0.825 and 0.866 for 80 and 90°C, respectively. T_{p-end} in Figure 6-13c towards the end of the cavity seemed to be less relevant to the microneedle heights as suggested with their significantly lower R^2 values. Temperature integrals, however, are the best process fingerprints extracted from thermal imaging in terms of their strong linear correlation with the part quality. R^2 values of up to 0.936 for higher mould temperatures reached (Figure 6-13b). It is worth pointing out that peak temperatures and associated temperature integrals are proportional to each other during cycles, however, according to the strong linear correlations, integral values stand out as significantly better fingerprints as they are proportional to the total energy provided for melting and packing since the time term is present in the calculation. Global fits presented for $\int T_{array}$ and $\int T_{end}$ resulted in R^2 of 0.921 and 0.912 respectively, showing a very strong correlation between integrals and microreplication (Figure 6-13b and d).

Strong correlations from thermal imaging process fingerprints suggest that the replication success of the microfeatures is directly linked to the amount of sonication energy given to the system. The temperature integrals are directly proportional to the heat energy provided as the measured temperatures are average values from particular regions of interests.

6.3.2.3 Summary of the experiment

In 6.2.3, the disadvantages of having less challenging microneedle features for process fingerprinting was discussed and ways of obtaining better correlations between process and product fingerprints was proposed. These strategies once again appeared to be useful for amorphous materials. The trends in correlations for this particular batch suggest that elevated mould temperatures even above 90°C could be beneficial for achieving better filling of the microneedle cavities. The crucial thing to notice and to bear in mind is that although significantly higher mould temperatures are beneficial for ultrasonic moulding, flashing and deformation during ejection could become problematic and experiments should be set carefully. Microneedle replication aspect of the experiment have been only reasonable however, where average microneedle heights reached only ~700 μm, occasionally.

6.4 Process fingerprinting for ultrasonic micromoulding including cavity pressure measurements

Based on the knowledge and experience obtained from the initial process monitoring and fingerprinting attempts, further experiments have been carried out including cavity pressure measurements for ultrasonic micromoulding of PP and ABS. This section will provide a better overview of suitability and evaluation of different layers of instrumentation for ultrasonic micromoulding.

6.4.1 Polypropylene experiments (Batch-u4)

This final batch of experiments for PP include 3 different mould temperatures to be investigated, namely 70, 80 and 90°C. Higher mould temperatures are also included to see the maximum achievable microneedle heights using PP. 15 samples for each mould temperature have been produced. Table 20 summarises the process settings used for Batch-4.

Table 20. Process settings used for Batch-u4.

Process parameter	Value - unit
Sonication amplitude ($\mathrm{A_{sonic}}$)	~100 µm
Sonication duration - time ($\mathrm{t_{sonic}}$)	4 s
Mould temperature ($\mathrm{T_{mould}}$)	70 - 80 - 90°C
Injection force ($\mathrm{F_{inj}}$)	750 N

Great care has been taken while doing experiments in order to mimic a pilot production scenario. Before collecting the samples, 10 samples have been moulded and discarded in order to stabilise all the thermal gradients present on the parts of ultrasonic micromoulding machine. All samples have been collected from back to back cycles, in order to be able to record and detect the dynamic aspects of the process. After moulding 15 samples with the lowest mould temperature, mould temperatures have been increased and waited for 5 minutes to stabilise. This made sure that samples that belong to the same mould temperatures have been moulded in stabilised conditions. Figure 6-14 shows the mean, SD and CoV for $\mathrm{h_{avg}}$ measured for different mould temperatures.

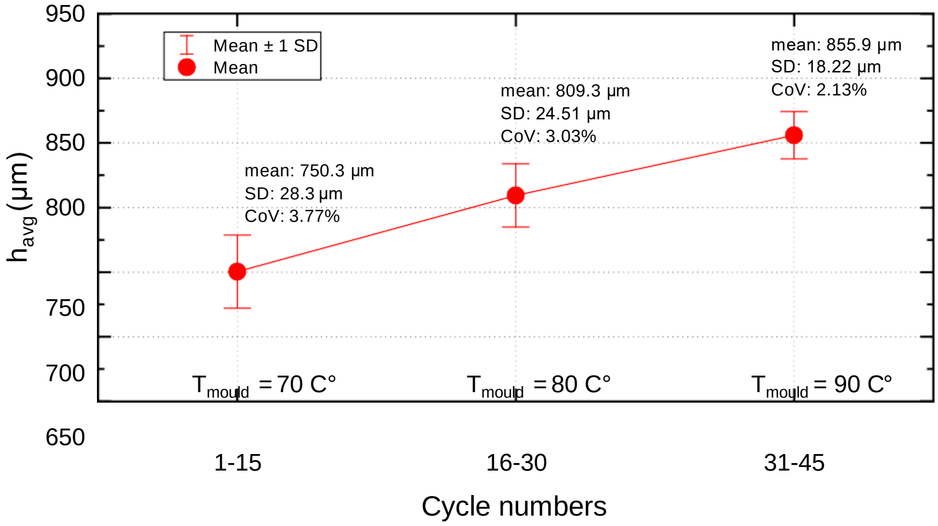

Figure 6-14. Interval plots showing the standard deviation and means of $\mathrm{h_{avg}}$ for cycles with different mould temperatures of 70, 80 and 90°C respectively. SD, CoV and mean have also been given.

Average needle height of 855.9 µm is significant as the value for conventional micromoulding has been changing between 800 - 820 µm. That might suggest that sustaining the sonication after the filling helps obtaining better microfeature replication as compared with conventional micromoulding as premature solidification is a dominant phenomenon. The CoV also decreased significantly from 3.77% to 2.13% with higher mould temperatures.

6.4.1.1 Process fingerprints from machine data

$\mathrm{V_{piston}}$ has been omitted from the process fingerprints from machine data due to its lesser relevance and correlations to the microfeature replication. It can be stated that the method for calculating $\mathrm{V_{piston}}$ was quite simplistic, and more intricate ways of detecting the points of interest are needed. Instead of this measurement, sonication energy difference (dW) has been used and included in the analysis. dW is a term calculated by first subtracting the power output curves for making one part from the curve of the best replicated part, then integrating the difference curve for quantifying the energy deviation. The method uses the same calculation procedures for $\int \Delta \mathrm{x}$ which is calculated from piston data. Graphs given in Figure 6-15 depict the correlations and fits where possible between the process fingerprints and $\mathrm{h_{avg}}$ for this batch.

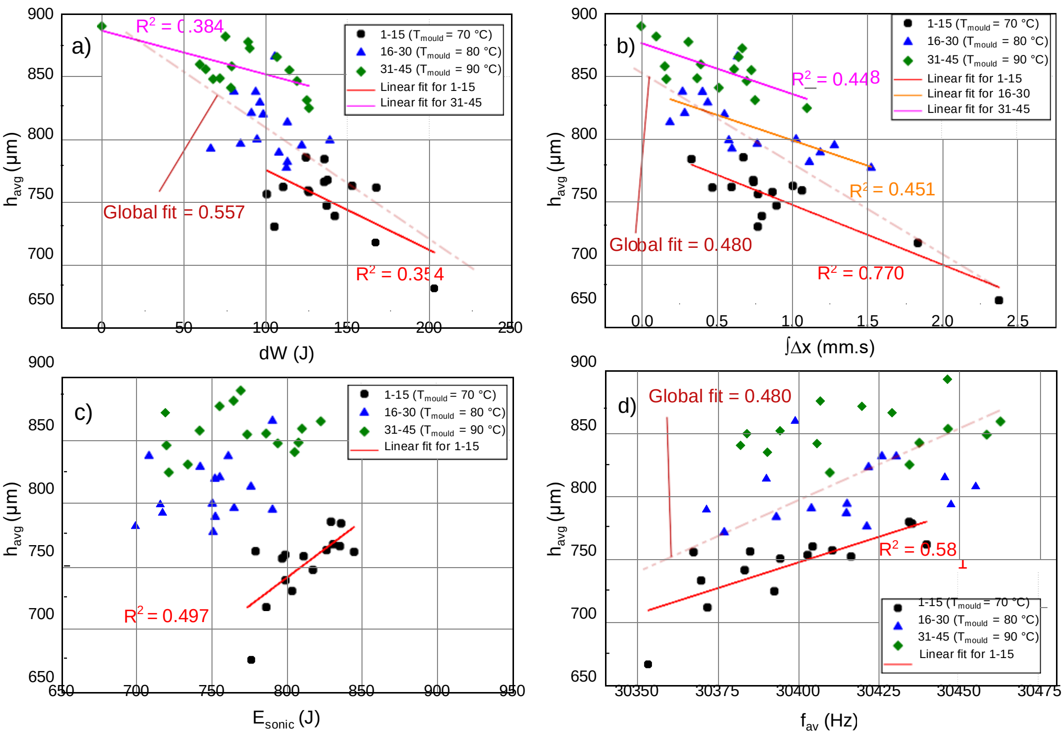

Figure 6-15. Scatter plots depicting correlations for h_{avg} vs dW, $\int \Delta x$, E_{sonic}, f_{av}.

Linear fits have been applied to the data in Figure 6-15 where possible. The results show that data points are usually accumulated for different mould temperatures. All four of the process fingerprints showed reasonable correlations for needle height range between ~650 - 800 µm. However, higher mould temperatures yielded h_{avg} of as high as 880 µm generally lesser correlations.

One could comment that dW and E_{sonic} are taken and derived from the same data which could lead to redundancy. However, the results show that dW is a significantly better process fingerprint compared with E_{sonic} at times, even for a semi-crystalline polymer which has latent heat during its melting. The semi-crystalline nature and latent heat which is present within PP does not allow E_{sonic} to be in correlation with the microfeature replication as discussed in previous experiments. However, dW is a term that quantifies the deviations in consumed energy from the best part rather than measuring the whole energy put into the system. Hence, dW is a more refined version of sonication energy and has been proved that works well with very good correlations (R^2 = 0.557) for PP as well which is a significant result (Figure 6-15 a.

$\int \Delta x$ once again showed an improvement when the R^2 values are compared with Batch-u2. The global fit drawn in Figure 6-15b resulted in an R^2 of 0.480 which was 0.286 for Batch-u2 previously. This is a significant improvement since although there is a randomness associated with the melt progression and filling, piston position is proved to be a very good indicator of the moulding quality. Average sonication frequency (f_{av}) does not seem to be affected with the mould temperatures since, an R^2 value of 0.480 has been calculated which was 0.469 for Batch-u2. When the global fits are considered, f_{av} also can be a good quality indicator of the process.

To summarise, the dataset shows that some useful information have been extracted from the machine data which is readily available from the ultrasonic micromoulding control unit. With a more controlled approach, where the machine could run in fully automated mode with a pick and place robot, $\int \Delta x$ which extracted from piston data could be a useful process fingerprint even for a semi-crystalline polymer such as PP. R^2 values of 0.770 are seen for $\int \Delta x$ while using lower mould temperatures and this can be considered as one of the most significant result from machine data. f_{av} is also another useful process fingerprint and can be used for similar purposes. Unexpectedly, sonication energy difference (dW) yielded the best result in terms of a goodness of the linear fit to the data with R^2 values of 0.557. All three of these process fingerprints are proved that it is possible to extract meaningful features from the ultrasonic micromoulding data.

6.4.1.2 Process fingerprints from thermal imaging

Thermal imaging acquisitions have been made with the same settings used for previous batches. Figure 6-16 represents data from thermal imaging vs h_{avg}.

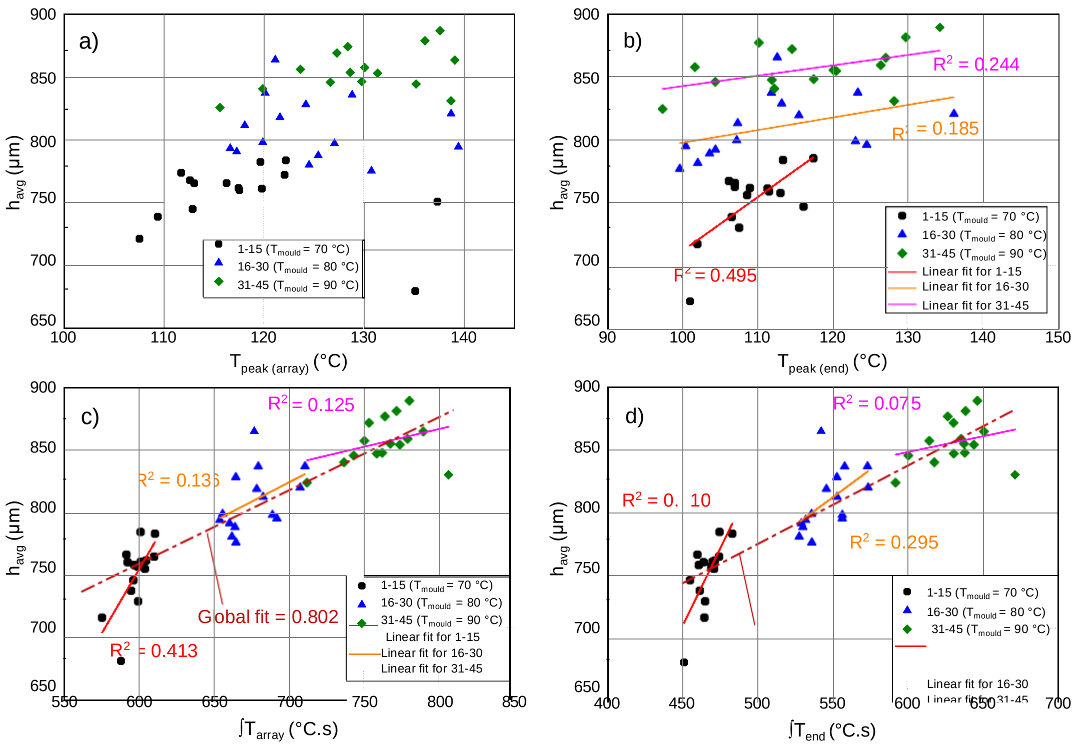

Figure 6-16. Scatter plots depicting correlations for h_{avg} vs $T_{p-array}$, $T_{peak\ (end)}$, $\int T_{array}$, $\int T_{end}$.

Thermal imaging acquisitions given in Figure 6-16 also showed similar behaviour for process fingerprints extracted from machine data as given in Figure 6-15. However, one of the significant results is that a global fit for $\int T_{array}$ and $\int T_{array}$ resulted in R^2 values of 0.802 and 0.806 respectively (Figure 6-16c and d). This is a remarkable result for polypropylene experiments because of their semi-crystallinity and relatively random filling behaviour. These values are almost as good as some of the correlations ABS exhibited. One could expect that the randomness could increase when increasing the mould temperatures in ultrasonic micromoulding. However, these integral fingerprints show the opposite and higher mould temperatures are both beneficial for microfeature replication and process monitoring point of view.

Peak temperature values usually showed more scattered behaviour compared with temperature integrals for higher mould temperatures in particular (Figure 6-16a and b). It can be said that while using higher mould temperatures, simultaneous injection and plastication of the feedstock are being carried out in a better or easier way because of the higher fingerprint values and reduced viscosities.

6.4.1.3 Process fingerprints extracted from cavity pressure data

It has been experienced that cavity pressures differ significantly from cycle to cycle even for the samples that have been ultrasonically micromoulded with the exactly the same parameters. Three graphs given with a common cavity pressure axis in Figure 6-17 that depict the data taken from 3 random cycles for each mould temperatures of 70, 80 and 90°C.

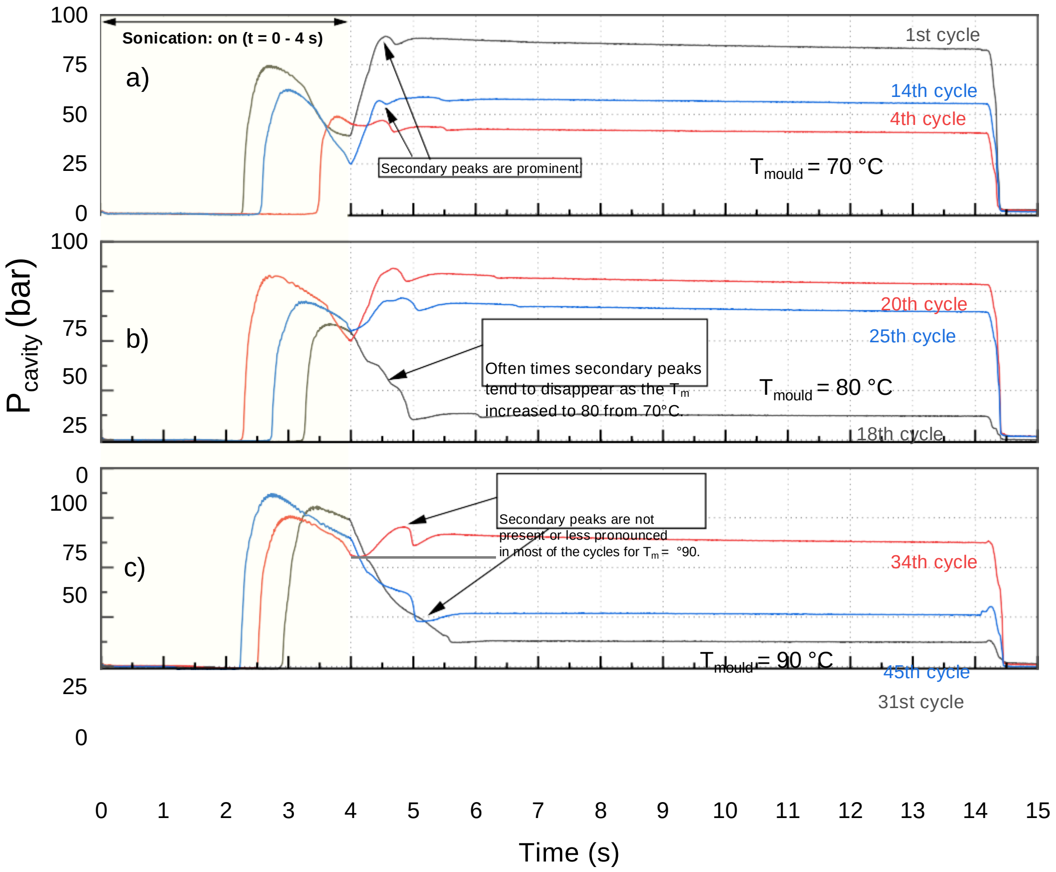

Figure 6-17. Cavity pressure profiles for different mould temperatures. a) 70°C, b) 80°C, c) 90°C.

The differences in cavity pressure profiles are very prominent even for the samples taken from the same mould temperature. According to the shifts in the time scale for pressure peaks, it is clear that the melting initiates at different times for different cycles. The reason for seeing these could be that the differences between the surface roughnesses of the preforms and their placing in the sonication chamber before the melting happens. Moreover, for the cycle that took long for initiating the melting of the feedstock (4th and 18th cycle) tend to show lower pressure values. 4th cycle has an average microneedle height of 716.6 μm whereas 1st and 14th cycles have 783.25 and 784.5 μm respectively. Although the scatter plots will be given in the following, this information shows a relationship between the replication and cavity pressures.

One of the significant features seen in Figure 6-17 is that the peak cavity pressures are way lower than those seen in conventional micromoulding processes and exhibit a gradual decrease or decay of cavity pressures in comparison to conventional micromoulding cavity pressure measurements. For this particular batch, cavity pressures changes between 45 and 100 bars whereas the typical cavity pressure peaks for conventional moulding were in the vicinity of 250 and 500 bars depending on the switch - over pressure. And yet, for the majority of instances (for T_{mould} = 80 and 90°C) the replication performance of ultrasonic micromoulding has been better, yielding average needle heights of near 800 and 850 μm for 80 and 90°C mould temperatures, respectively. As can be recalled from Chapter 5, the maximum average needle height for conventional micromoulding was reported to be ~820 μm only.

The wider peaks and gradual decays of the pressures are in correspondence with the sustained sonication energy throughout the process which causes the polymer to stay in the molten phase for longer. In turn, the gate of the main circular cavity is not solidified and cavity pressure sustained for longer.

The presence of the initial pressure peak, a significant decrease, then a secondary increase in cavity pressure is a behaviour that is drastically different from the cavity pressure seen in conventional microinjection moulding. It has also been seen from Figure 6-17 that the secondary pressure peaks tend to disappear, for higher mould temperatures. For better understanding of these secondary pressure peaks, force and piston position information also included in Figure 6-18.

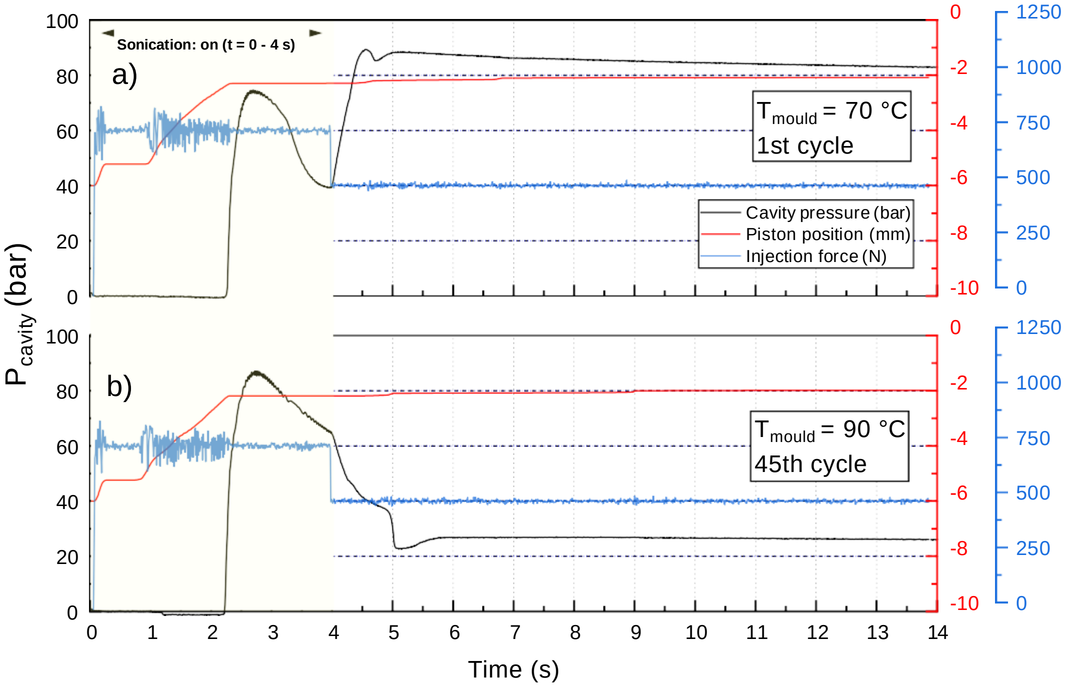

Figure 6-18. Cavity pressure, injection force and plunger position for the 1st and 45th cycles for comparison. a) 70°C, b) 90°C mould temperature.

Secondary increases in cavity pressures are unexpected, as the cavity pressure behaviour in micromoulding or injection moulding in general experiences a single increase in cavity pressure initially and then decays due to the solidification. However, in ultrasonic micromoulding the cooling of the melt in the main cavity is significantly different as the ultrasonic energy is sustained while the polymer is being injected and also during packing to some extent. The following points summarise and support the main features of data given in Figure 6-18.

1. The peaks for cavity pressure are seen near t = 2.75 s. This implies that the melt is in contact with the cavity measurement pin which is at the end of the cavity. There is a 1.25 s time interval where the sonication of the polymer feedstock is sustained. This provides additional heat energy and results in a decrease in the rate of cooling hence lower viscosities can be sustained for longer.
2. A secondary pressure peak and increase in the top graph in Figure 6-18 suggests that the shrinkage compensation in the cavity is carried out in a significantly different way in ultrasonic moulding. It could be possible that the shrinkage compensation is being carried out by the clamping force according to the increase in cavity pressure transducer

output. The piston also stays fixed according to the red curve near t = 0, which supports this view.

3. A plunger force of 2000 N correspond to a pressure value of ~398 bar during injection and packing. The whole area of the part including the circular cavity and runner are considered for calculation of the force that is imparting on the clamping unit. The total area of the part that is in contact with the upper mould is 270.05 mm^2. As a result 10748 N (~1 ton) force have been found to be acting against the clamping unit. The clamping force has been reported to be 33000 N (~3 tons) according to the manufacturer of the machine. Although ~1 ton of force is much less than the specs of the machine, it could be the case that the secondary pressure increases are due to clamping force. Moreover, some mismatch and gap has been found between the top and bottom mould which might cause and amplify this effect.
4. In Figure 6-18b, secondary pressure is not present which is seen occasionally from cycle to cycle. For these samples it has been observed that there are serious amounts of flashing that occurred near the sprue and runner of the parts. Since the melt is more conveyable towards the sprue and the runner, shrinkage is not compensated by the clamping force or any other effect anymore, in turn leading to disappearance of the secondary pressure increases.

For each cycle, $\mathrm{P}_{\mathrm{c}}^{\mathrm{peak}}$ and $\int \mathrm{P}_{\mathrm{c}}^{\mathrm{peak}}$ have been extracted from cavity pressure data which has been recorded for each cycle during the ultrasonic micromoulding process. Once again, scatter plots between $\mathrm{h}_{\mathrm{avg}}$ and the cavity pressure process fingerprints have been provided in the following and fits are applied to the data where possible. Figure 6-19 shows the scatter plots for cavity pressure fingerprints against average needle height.

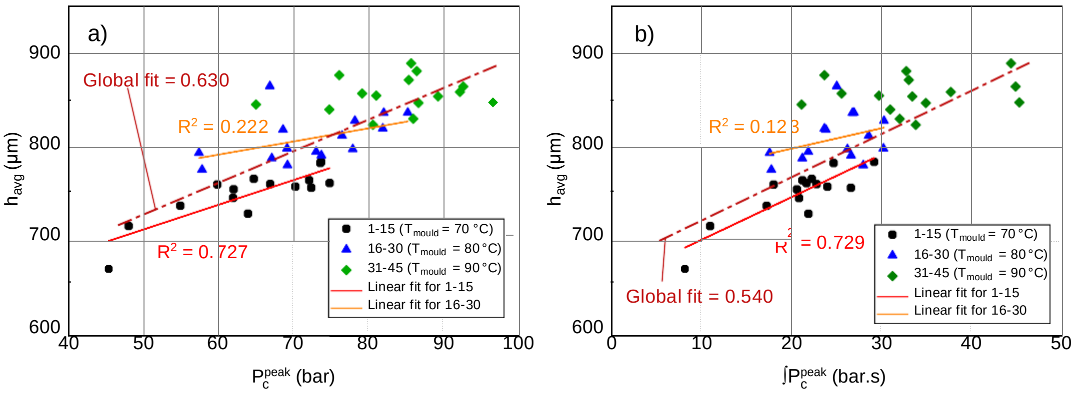

Figure 6-19 Scatter plots for cavity pressure fingerprints.

Both cavity pressure integrals of P_c^{peak} and $\int P_c^{peak}$ yielded in similar results and correlations as can be seen from Figure 6-19. Peak cavity pressure values showed a positive linear behaviour according to the data and the global fit (Figure 6-19a). An R^2 value of 0.630 has been found which can be considered as a good correlation although lower values have been seen for individual mould temperatures. Cavity pressure integrals resulted in an R^2 of 0.540 for the global linear fit, which is slightly lower than the fits for the peak values Figure 6-19b. The scatter plots are also very similar to the temperature integral fingerprints, which suggests the temperature - viscosity relationship also manifest itself for cavity pressure measurements, as expected.

6.4.2 ABS experiments (Batch-u5)

A similar experimental work has been carried out for the last batch of ABS experiments including the cavity pressure measurements. In order to maximise microfeature replication and the mould temperatures have been increased to 85, 90 and 95°C. Mould temperatures above 100°C also have been considered, however due to the deformation of the sample during the ejection the maximum mould temperature has been selected as 95°C.

The maximum mould temperature has been selected carefully as the heat deflection temperature of ABS is 95°C which is quite close to the maximum mould temperature used. After the sonication ends and while the packing of the part is carried out temperatures above 100°C were still present during the tests where deformations during ejection had been experienced during initial tests. Hence, cooling times of 25 s have been used for the experiments with

T_{mould} = 95°C, to avoid and distortions or warpages during ejection of the parts. Cooling times of 15 s have been used for lower mould temperatures.

Similar to the previous batch, 15 samples for each mould temperature have been moulded and process data recorded accordingly. Before collecting the samples 10 samples have been moulded and discarded. All samples have been collected following the procedures explained previously. Table 21summarises the process settings used for Batch-5.

Table 21. Process settings used for Batch-u5.

Process parameter	Value - unit
Sonication amplitude (A_{sonic})	~90 µm
Sonication duration - time (t_{sonic})	3.5 s
Mould temperature (T_{mould})	85 - 90 - 95°C
Injection force (F_{inj})	1600 N
Packing force and duration	2000 N for 4 s

Figure 6-20 shows the mean, SD and CoV for h_{avg} measured for different mould temperatures.

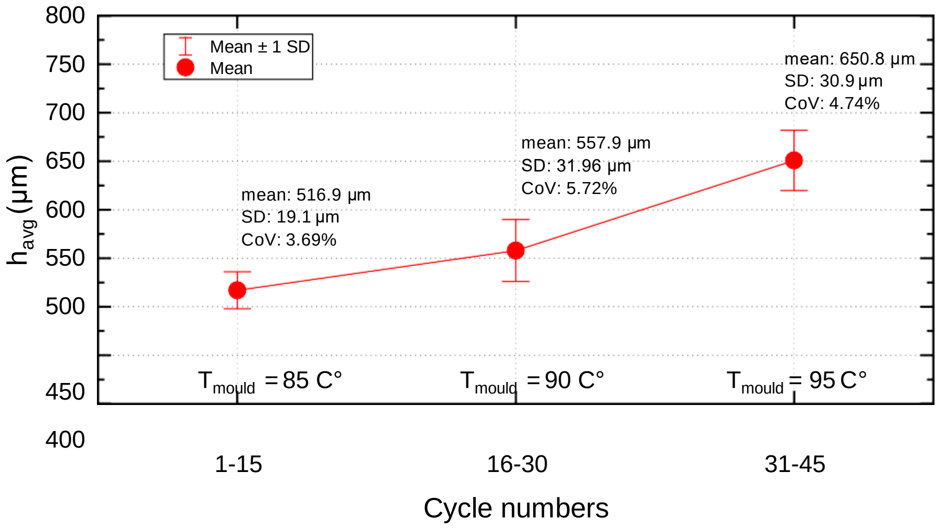

Figure 6-20. Interval plots showing the standard deviation and means of h_{avg} for cycles with different mould temperatures of 70, 80 and 90 °C, respectively. SD, CoV and mean have also been given.

The usage of slightly higher mould temperatures of 95°C has been resulted in a significant improvement in maximum mean microneedle height for ABS experiments, which was measured to be 650.8 µm according to the measurement results given in Figure 6-20. A 5 °C in mould temperature yielded an increase of ~92.9 µm, however, the standard deviations and CoV values have been reportedly high as opposed to PP experiments.

6.4.2.1 Process fingerprints from machine data

Similar analysis carried out from previous batches to see the effect of higher mould temperatures on all the datasets and correlations. Once again, $\mathrm{V_{piston}}$ has been replaced by dW for its lesser relevance. Figure 6-21 presents the fingerprints extracted from this particular batch and their correlations with average needle height ($\mathrm{h_{avg}}$).

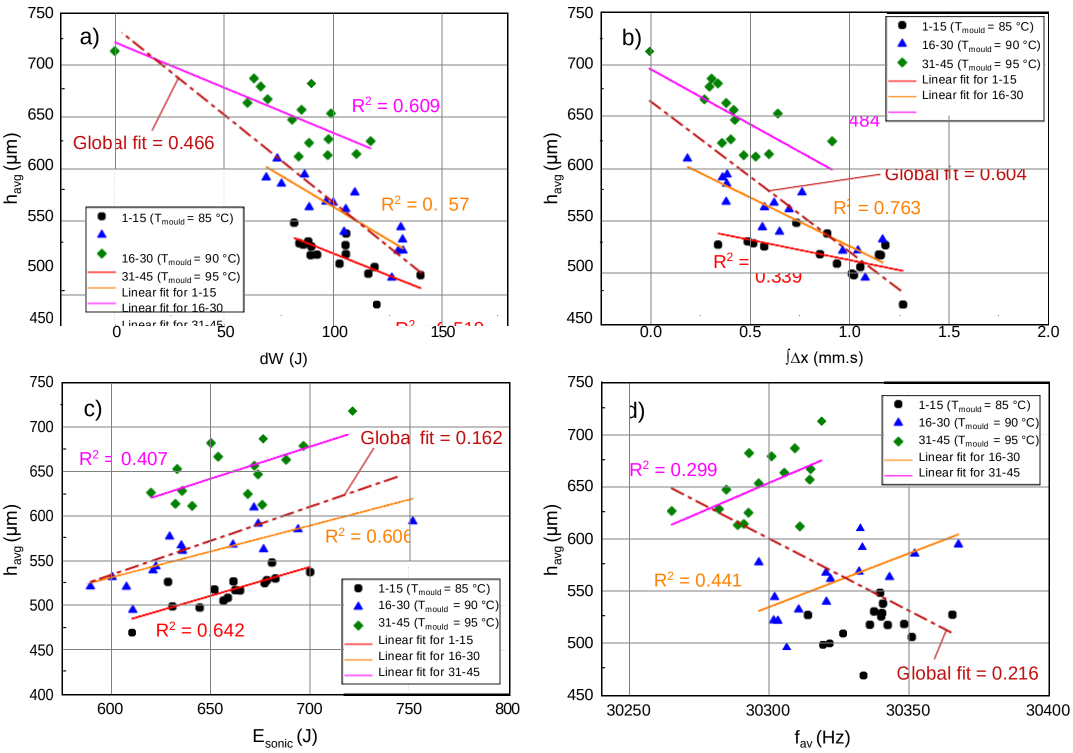

Figure 6-21. Scatter plots for process fingerprints vs $\mathrm{h_{avg}}$ from Batch-5

The data from Figure 6-21a show that fingerprints are extracted from power consumption data (dW and $\mathrm{E_{sonic}}$) yield the most consistent results in terms of predicting the microneedle height for the ranges 400-750 µm. This has been proved by reasonably high $\mathrm{R^2}$ values from dW where values of 0.757 and 0.609 have been found for higher mould temperatures which are of interest due to better replication of the microneedle features. $\mathrm{E_{sonic}}$ has been good at providing good correlation for different mould temperatures, however the global fit has resulted in an $\mathrm{R^2}$ of 0.162 down from ~0.722 which was found for Batch-u2 (Figure 6-21c). One of the effects here could be that the number of samples which is 15 down from 50 which might cause an effect on accumulation of the data. The second effect could be that when higher mould temperatures are used, occasionally lesser correlations have been observed generally for both PP and ABS. The reason for that behaviour could be the asymmetric flow front progression during filling which becomes more prominent at times when mould temperatures are increased.

According to Figure 6-21 it can be concluded that $\int \Delta \mathrm{x}$ which is extracted from the piston position data is a consistent process fingerprint for ultrasonic micromoulding where it usually yields R^2 values of above 0.5 Figure 6-21b. The global fit for $\int \Delta \mathrm{x}$ resulted in an R^2 of 0.604 which could be considered as a good indicator. Average sonication frequency (f_{av}) yielded lesser correlations for this particular experiment. However, there is a general trend in Figure 6-21d that higher mould temperatures cause the sonotrode to vibrate at lower sonication frequencies

6.4.2.2 Process fingerprints from thermal imaging

Thermal imaging acquisitions have been made with the same settings used for previous batches. Figure 6-22 represents process fingerprint data from thermal imaging vs $\mathrm{h}_{\mathrm{avg}}$.

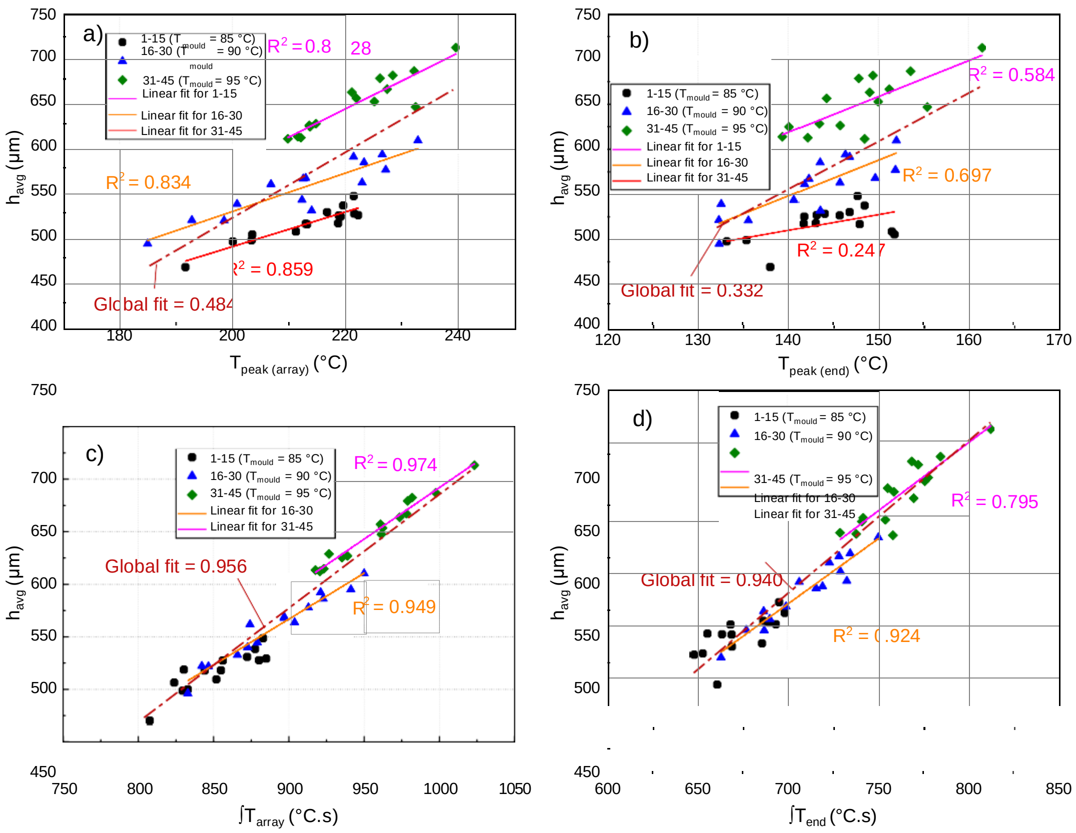

Figure 6-22. Scatter plots depicting correlations for h_{avg} vs $T_{p-array}$, T_{p-end}, $\int T_{array}$, $\int T_{end}$.

According to Figure 6-22a, $T_{peak-array}$ resulted in very good correlations when it is evaluated for different mould temperatures. However, the global fit has yielded an R^2 value of only 0.484. It has been also confirmed that the T_{p-end} is of less relevance to the microfeature replication for lower mould temperatures (Figure 6-22b). This effect can be explained by the faster cooling rates and solidification of the amorphous polymer while the flow front is still travelling towards the end of the cavity. However, 95°C can be regarded as a critical temperature for this particular microneedle design and material used as the R^2 values increased from 0.247 to 0.697 with only a 5°C mould temperature difference in the experiment.

$\int T_{array}$ has been particularly useful in providing an excellent linear correlation for both the global fit and different mould temperatures (Figure 6-22c). R^2 value for the global fit for the whole data for this particular fingerprint found to be 0.956, which is one of the highest in this work. The best correlations obtained from T_{mould} = 95°C can be explained with the filling behaviour and more homogenous melting of the amorphous ABS. Between the microneedle heights of 600 - 750 µm, the second taper present makes the filling process more viscosity dependant and as a result these better correlations have been achieved. The temperature integrals measured from the end of the cavity $\int T_{end}$ show a similar behaviour to the previous experiments and yielded excellent results (Figure 6-22d). However, it is clear that ROI which covers the 6x6 array region better information in terms of microfeature replication, as $\int T_{end}$ resulted in an R^2 of 0.795 for T_{mould} = 95°C.

6.4.2.3 Process fingerprints extracted from cavity pressure data

More consistent cavity pressure profiles had been expected as the melting of an amorphous polymer is more homogenous compared with a semi-crystalline material. However, the cavity pressure data from ultrasonic moulding of ABS has been seen to be quite inconsistent and unrepeatable at times, even compared with polypropylene experiments. Data given in Figure 6-23 depict cavity pressures from different cycles for particular mould temperatures of 85 and 95°C. 90°C has been omitted because of the proximity of the values.

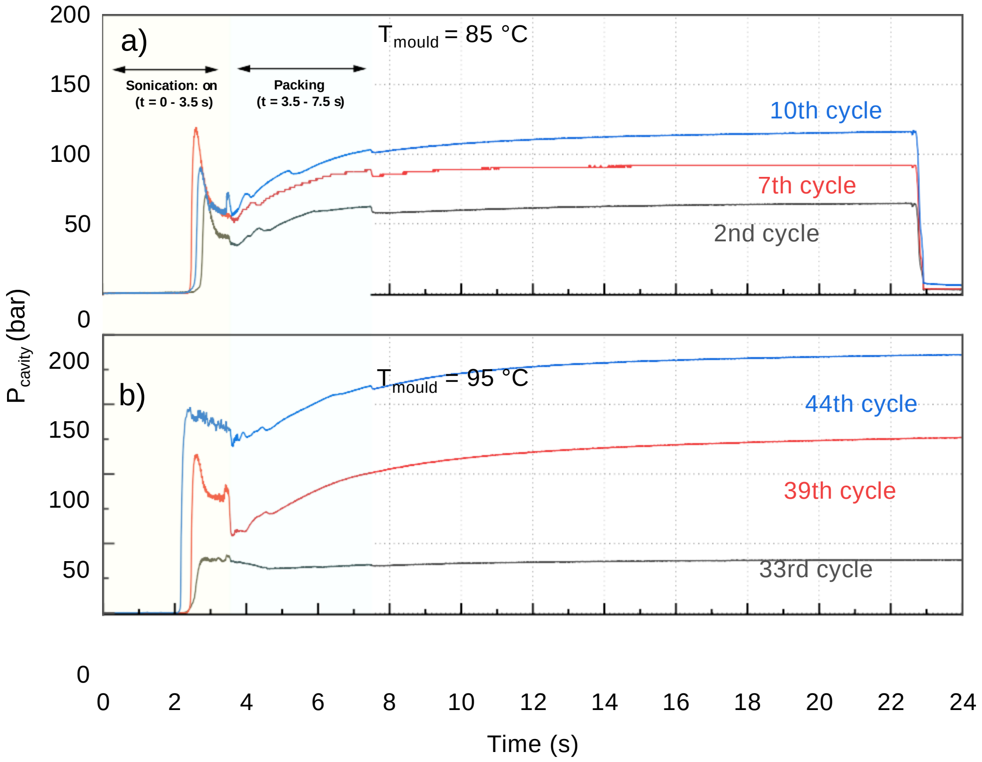

Figure 6-23. Cavity pressure profiles depicting the significant differences between cycles for T_{mould} = 85 (a) and 95°C (b).

According to the cavity pressure profiles given in Figure 6-23, the values are considerably different from each other, although same parameters have been used. The secondary peaks which had been seen for lower mould temperatures in PP experiments in the previous batch are not present for

ABS, however, secondary increase in pressure is still present. After the initial sharp increase in cavity pressure, a decrease follows and another significant increase can be seen. This behaviour is predictable for ABS, as there is an additional packing phase with 2000 N injection force right after the sonication, as indicated with coloured regions in Figure 6-23. However, the same effects regarding clamping force and shrinkage compensation processes likely to be present.

Another interesting feature in the cavity pressures for ABS is that the initial peaks which start around t = 2 - 3 s tend to lose their sharp decrease often times for T_{mould} = 95°C (Figure 6-23b). The sharp increase in cavity pressure often followed by a plateau. The reason for this behaviour could be that the sonication is still on and there is a sustained energy input on the material which is being injected and packed. This sustaining energy on the polymer melt prevents a sharp viscosity decrease near the pressure measuring pin, instead, a plateau is seen. This is highly likely since the plateau-like pressure profile lasts only until the end of sonication as indicated in (a) and (b) with a yellow region in Figure 6-23. Moreover, another feature in Figure 6-23a which supports this comment is that the pressure peaks near t=2.25 s show sharp decreases and plateau-like behaviour is not prominent for lower mould temperatures. For lower T_{mould}, it is expected and experienced in Chapter 5 that the cavity pressures decayed at a higher rate.

Significant differences in cavity pressures are also present in the profiles given in Figure 6-23b where the peak values changes between 40 - 150 bar for T_{mould} = 95°C. These could be attributed to the severe flashing effects that occur around the sonotrode where the molten polymer fills those gaps instead of imparting pressures on the cavity pressure measurement pin. For better understanding of cavity pressure behaviour, data have been given together with injection force and piston position in Figure 6-24 as have done before for PP experiments.

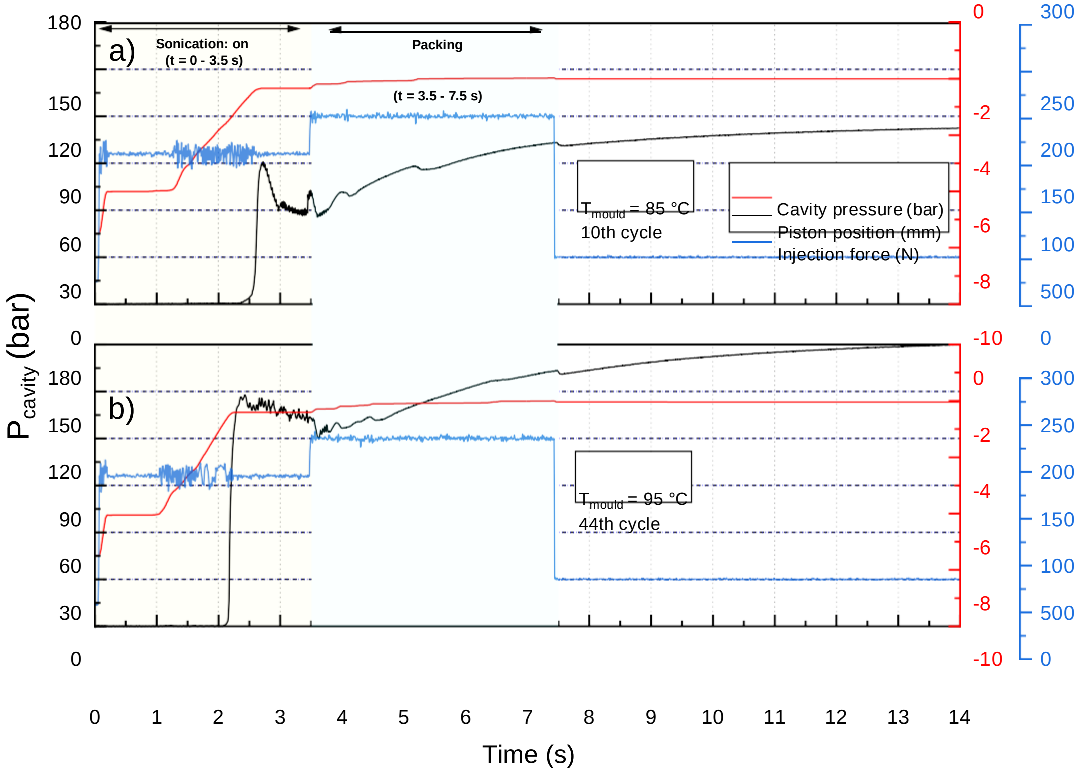

Figure 6-24. Process data for 10th and 44th cycles including piston position, injection force and cavity pressure.

Some of the local increases in cavity pressures in Figure 6-24 can be attributed to the behaviour of the melt and viscosity. Viscosity differences arise from the way of the melting, as it can differ at times because of the multi-layered stacks of disc shaped feedstock. After t = 7.5 s, where the packing phase ends, the load on the pressure transducer is still present and only a slight, instantaneous pressure decrease can be seen from both graphs. After this small decrease, the cavity pressure once again increases gradually, due to the explanations provided in 6.4.1.3. The same assumptions can be made in order to explain the reasons for seeing this behaviour. One of the reasons that could escalate this secondary increase in cavity pressure while moulding ABS is that the part has a certain decreasing temperature gradient from the sprue, through the runner and the main circular cavity after the part is filled, near t = 2 – 2.5 s. The material which forms the sprue is usually much hotter for ABS according to the gate temperatures extracted from thermal images because of its proximity to the ultrasonic horn which is confirmed by of its softness and deformability after ejection and inspection of the part by hand. The same is valid for the runner and the circular part where a certain viscosity which might allow packing of the material towards the end of the cavity where the pressure measurement pin is located. Also, a combination of a slight gap between the moulds and hot-injectable polymer melt, once again clamping force might be interfering with the cavity pressure readings.

Given in the following graph are the scatter plots for process fingerprints (P_c^{peak} and $\int P_c^{peak}$) versus average microneedle heights.

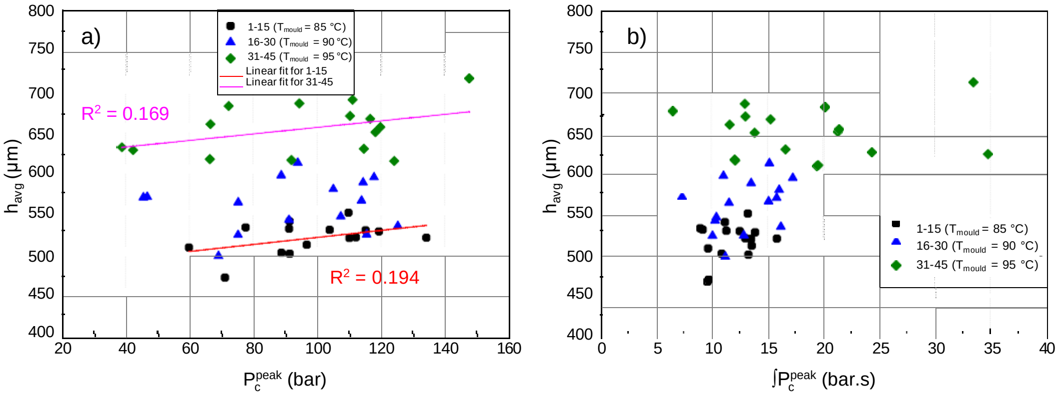

Figure 6-25. Scatter plots for cavity pressure fingerprints.

The data presented in Figure 6-25 for both process fingerprints show a scattered behaviour and do not show a clear correlation. A general positive trend is present for P_c^{peak}, however R^2 values for linear fits are very low. A similar behaviour is present for $\int P_c^{peak}$ where some accumulation of data points are seen. During the analysis of the data it was seen that some of the cavity pressure peaks exhibited a plateau behaviour and this is the reason for the extremely scatter behaviour of pressure integral values for T_{mould} = 95°C. The scattered behaviour of cavity pressure fingerprints correlate with the inconsistent cavity pressure profiles given in Figure 6-23.

6.4.3 Summary of ultrasonic micromoulding experiments including cavity pressure measurements

Two experimental batches for PP and ABS in this sub-section demonstrated the microfeature replication capability of the process using even higher mould temperatures used previously including cavity pressure data extraction from each cycle. Experiments form a continuation of the results from previous batches where lower mould temperatures were used. As a result, a range of mould temperatures experimented demonstrates here how the selected process fingerprints behave.

PP experiments with higher mould temperatures (90°C) in this batch have shown the best replication behaviour of this material amongst the experiments, including the conventional micromoulding. Although the random melting and unpredictable behaviour of PP has been discussed, piston position data yielded significant correlations for monitoring the process and predicting the microneedle heights, for higher mould temperatures in particular.

Cavity pressure measurements and fingerprints for PP experiments seem to be related to microreplication, however, scattered data have been seen for higher mould temperatures. Apart from the correlations, experiments with $\mathrm{T_{mould}}$ = 95°C which yielded an average needle height of ~850 μm have shown cavity pressure peak values between 65 - 100 bar which are significantly lower than the conventional micromoulding experiments. This feature definitely shows the advantage of having sonication after the packing and ultrasonic plasticisation of the polymer.

ABS has shown less favourable results regarding microfeature replication because of its higher viscosity compared with PP, however, has performed very well in the sense of process fingerprinting and correlation of process features and dimensional outcome of the parts. Thermal imaging data in particular exhibited very strong correlations to microneedle heights of the parts according to the $\mathrm{R^2}$ values. Moreover, piston position and sonication energy related process fingerprints also have shown correlations. This could be significant as the sonication energy and piston data can be taken directly from the machine without implementing additional sensor technologies which could be an advantage in terms of cost and labour.

It has been seen that cavity pressure fingerprints are not quite relevant to the final product quality for ABS, however, the data has shown interesting cavity pressure evolution throughout the process. Cavity pressure data is indeed very useful for identifying different stages and characterisation of the ultrasonic micromoulding process.

6.5 Summary

This chapter has presented an in-depth study for monitoring ultrasonic micromoulding using process fingerprinting methods alongside with assessment of microfeature replication capabilities of the technology. The work also presented the characteristics of ultrasonic micromoulding when using semi-crystalline and amorphous materials.

The rationale behind the selection of specific process fingerprints from machine data, thermal imaging and cavity pressure data have been explained and justified in detail. Piston position data have shown very good correlations for both semi-crystalline and amorphous materials. Thermal imaging is proven to be an excellent tool for both flow visualisation and temperature measurements for ultrasonic micromoulding. Cavity pressure data have also been very informative for identifying different stages and phenomena going on during the process.

Overall, better filling behaviour for PP has been achieved than ABS while using ultrasonic moulding. Moreover, ultrasonic micromoulding has been proved to be performing better while using PP with significant improvements in microneedle replication.

CHAPTER 7: Conclusions and Recommendations for Further Work

7.1 Introduction

This chapter summarises the work performed in this thesis to investigate conventional and ultrasonic micromoulding of thermoplastic microneedle arrays and process fingerprinting. The experimental findings and suitability of these two technologies as a manufacturing method of microneedles will be discussed. Experimental outcomes from both technologies are compared and contrasted. Suggestions and recommendations for further work are also provided.

7.2 Conventional micromoulding for manufacturing of thermoplastic microneedle arrays

Experiments performed using microneedle insert with a 6x6 configuration in a conventional micromoulding process presented a well-defined starting point for considering a pilot or mass production scenario when using thermoplastic materials. The main process features and characteristics have been discussed in detail using extensive process monitoring equipment attached to a state-of-the-art microinjection moulding machine. Material specific discussions are presented here.

7.2.1 Semi-crystalline (PP) microneedles

The results showed that microneedle cavity replication for PP does not depend on how extreme the process variables are. Rather, microneedle replication for PP was found to be distinctly influenced by its semi - crystalline nature where shrinkage effects become pronounced and manifest themselves on part quality. The typical achievable microneedle heights for PP were found to between 800 - 810 μm with good repeatability as suggested by a low coefficient of variances of ~0.5%.

The synchronised process data recorded from in-process sensors has provided a framework for understanding the physical aspects of a micromoulding cycle in detail. As far as the in-line process monitoring and process fingerprinting aspect are concerned, process fingerprints have not yielded any correlation in full-automatic mode. The experiments done in semi-automatic mode for PP however showed that switch-over and cavity pressure related process data could be of some relevance to the part quality.

7.2.2 Amorphous (ABS) microneedles

The experimental campaign for ABS showed that amorphous materials are more appropriate for manufacturing of thermoplastic microneedle arrays using conventional micromoulding. The main reasons for this result could be attributed to the low material shrinkage and material having a glass transition rather than a sharp melting point which is favourable for better packing of microneedle cavities.

The in-line process data was found to be relevant to the quality of the parts while using ABS. Good correlations have been found between injection - cavity pressures and dimensional outcome of the microneedles. Relevant data provided ways of understanding the filling and injection behaviour. Moreover, these correlations that have been found could be implemented in an in-line quality assurance procedure, where defective parts and outliers in dimensional quality thresholds can be identified.

One of the most significant outcomes in terms of microneedle quality in this work has been found in full-automatic experiments for ABS where an 886.7 μm average needle height has been found out of 50 samples with a coefficient of variance of 0.48%. Process fingerprints showed a scattered behaviour for these high - quality microneedles. It should be considered also that the microneedle cavities are nearly filled to their very sharp tips towards the end of the cavities, and one can comment that since it is being moulded at near its limits finding correlations also becomes even more difficult between process features and dimensional outcome of the needles. However, this is not significant from manufacturing point of view and this shows that the process is operating at its nearly highest level as suggested by the quality of the ABS microneedles.

Figure 7-1 shows SEM images taken from high - quality ABS microneedles manufactured using conventional micromoulding. The consistency in the filling of microneedle cavities can be clearly seen.

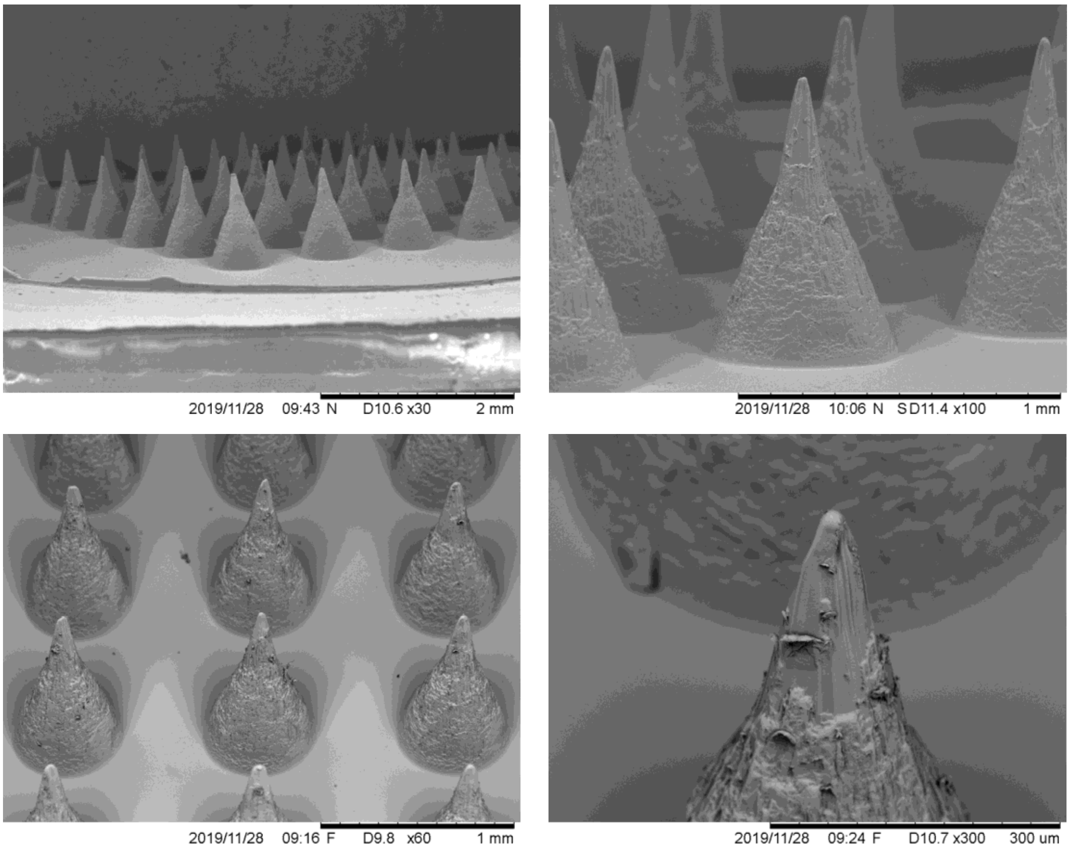

Figure 7-1. SEM images taken from ABS microneedles manufactured by conventional micromoulding.

7.3 Ultrasonic micromoulding for manufacturing of thermoplastic microneedle arrays

Similar to the approach taken in conventional micromoulding experiments, it has been necessary to find a suitable initial parameter set for ultrasonic micromoulding experiments from a process fingerprinting point of view. Moreover, limited literature and the complex nature of the simultaneous heating, melting and injection phases in this process have also been a challenge. Microneedles moulded in the 5x5 configuration with blunt tips have provided useful insights for initial experimentation where the needles have been replicated almost completely. Process data and fingerprinting attempts have been irrelevant to the part quality at this point of the experimental campaign. The experiment allowed the determination of process window for this component and provided insight on how the is behaving.

Process monitoring solutions and methods have been introduced for ultrasonic micromoulding in detail for the first time to the author’s knowledge although there has been some work done regarding thermal imaging of ultrasonic micromoulding flows from the group previously (Whiteside et al. 2016; Masato et al. 2018). However, these reports lack the usage of machine data and cavity pressure sensors where substantial information has been extracted within the scope of this work in order to characterise an ultrasonic micromoulding cycle.

7.3.1 Semi-crystalline (PP) microneedles

Ultrasonic melting and injection phases of a semi-crystalline material (PP) have been studied and characterised in detail. It has been found that substantially higher mould temperatures are needed for ultrasonic micromoulding compared with conventional technology to obtain a microneedle array with good quality. This is because the feedstock is being melted progressively and to keep the viscosity of the melt as low as possible while it progresses towards the runner and the gate.

Ultrasonic micromoulding of PP microneedles have been characterised by their variability and random filling behaviour. Even for the best experimental batch where 855.9 μm average needle height has been achieved for 15 parts, the coefficient of variance was recorded to be 2.13% which suggests a significant amount of variability is present cycle to cycle in comparison to conventional micromoulding results which yielded 0.45% of CoV. Thermal imaging data have shown local temperature differences which in turn cause local viscosity differences. When this particular batch is considered, ultrasonic micromoulding technology performed better than its conventional counterpart when using PP. Average needle heights of 855.9 and ~810 μm have been achieved for ultrasonic and conventional micromoulding respectively. The reason for this behaviour is that the sonication definitely prevents the abrupt solidification of semi-crystalline polymers and sustaining the ultrasonic energy after filling improves polymer replication significantly.

As far as the process fingerprinting concept is concerned, piston position information has been found to be the most consistent quality indicator. This has been experienced and proved throughout all the experiments, although a substantial amount of randomness in the shape and velocity of the flow front at different points in space and time have been recorded during moulding of PP. Hence, regardless of the random temperature distributions and asymmetric progression of the flow front, piston position could provide valuable information for in-line quality control of the microneedles in ultrasonic micromoulding.

The following Figure 7-2 shows details of the ultrasonically micromoulded PP microneedles.

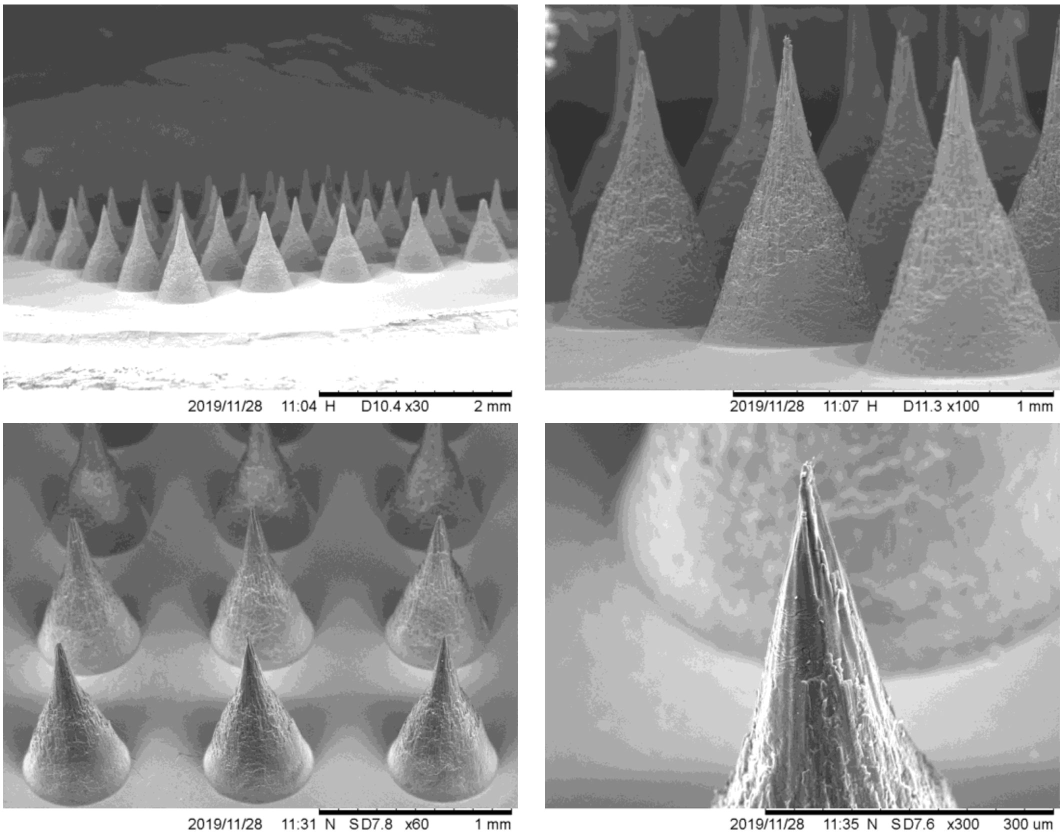

Figure 7-2. SEM images taken from ultrasonically micromoulded microneedles.

The SEM images in Figure 7-2 are in correspondence with the random temperature fields experienced during moulding of PP where extremely long and sharp needles are present as well as shorter and blunt - tipped needles within the same microneedle patch. Another significant result from this batch is the extremely pointy tips of the microneedles encountered at times (bottom right image - Figure 7-2). According to the scale, tip radius measures approximately 4.5 µm which is remarkable when a thermal process such as laser machining is considered since thermal machining processes usually result in severe machining marks and surface roughness.

7.3.2 Amorphous (ABS) microneedles

Replication of microneedle features using ABS has been a challenge in this work using ultrasonic micromoulding, where the high viscosity of the material resulted in difficulties during filling. Only a 650.8 μm average needle height was achieved even when using maximum mould temperatures.

Process fingerprints were found to correlate very well to the dimensional outcome of the microneedles when using ABS. Thermal imaging information in particular exhibited excellent linear correlations in predicting the needle height. Moreover, piston position information and sonication energy also resulted in very good linear correlations signifying how useful even standard machine data can be for process fingerprinting activities, without requiring additional sensor technologies and data management systems. Cavity pressure measurements have been very useful for characterising different aspects of the process. These measurements correlate with the power output, sonication frequency and piston position where behaviour of each of these channels was explained in detail.

7.4 Comparison of conventional and ultrasonic micromoulding

The findings of this thesis indicate that conventional micromoulding has been a more capable process moulding microneedles with amorphous materials (ABS) whereas ultrasonic micromoulding technology has been superior for moulding using semi-crystalline (PP) polymers.

The studies have shown a well-defined limit around 800 μm where the replication cannot be taken any further for PP while using conventional micromoulding. Whereas, at elevated mould temperatures ultrasonic micromoulding resulted in average needle heights of 855.9 μm, suggesting that sustaining the sonication energy definitely helps to overcome the negative effects of abrupt solidification. Relatively high cycle to cycle variability (CoV ~ 2%) in ultrasonic moulding experiments can be a negative, however, but there is still room for improving this aspect by further refinements that can be done in the machine design and the process.

Conventional micromoulding has been indisputably performed better over ultrasonic micromoulding when using an amorphous polymer. Deep microneedle cavities have been filled almost completely and resulting microneedles can be used for actual drug-delivery tests as they are very sharp at the tips and possess the required length.

Another very important outcome of this thesis has been the demonstration of the capability of ultrasonic micromoulding for producing parts with challenging micro-features at very low pressures as compared with conventional micromoulding. Figure 7-3 shows some of the significant results regarding typical cavity pressure values for both conventional and ultrasonic micromoulding processes.

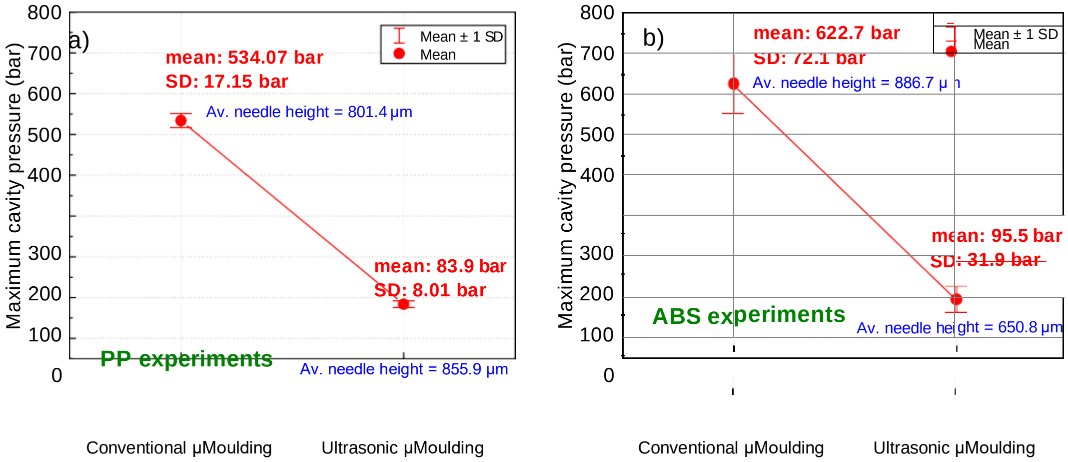

Figure 7-3. Graphs showing the typical cavity pressure values for conventional and ultrasonic moulding experiments. a) Polypropylene data, b) ABS data. 50 and 15 samples have been used in calculating the SD and means for conventional and ultrasonic micromoulding respectively.

For both materials, results have shown that ultrasonic micromoulding is being carried out at cavity pressures 6 times lower than conventional micromoulding has. Moreover, another significant result has been the very good replication for ultrasonic micromoulding for PP at very low pressures of 83.9 bar. Hence, this thesis has demonstrated that ultrasonic micromoulding is very capable of replicating microfeatures. The lower pressures required for manufacturing microparts in ultrasonic micromoulding is significant, as the technology requires less energy in the process for operation. Also, the operation at lower pressures will not require high-spec machine parts that are designed for high pressure-force machinery. This results in an overall reduction in the capital costs of the equipment and spare parts. Higher pressures usually correlate with higher energy consumption where ultrasonic micromoulding could be a more environmentally friendly option over conventional micromoulding. Moreover, conventional micromoulding use electrical heaters to keep the polymer in a molten state for hours which could result in higher energy consumptions in overall. Consequently, unique capabilities and potentials of ultrasonic micromoulding make it a good alternative for producing parts with micro-nano features.

7.5 Justification microneedle quality

A short discussion can be made here for elaboration of the high quality of the microneedles manufactured in this work, by emphasising the samples obtained from Batch-m4 (ABS) and Batch-u4 (PP - 90°C) which had 886.7 and 855.9 μm needle height with 11.58 and 8.25 μm tip radius (see Appendice-E and F). These considerably sharp tips achieved suggest that these needles can penetrate to the skin with considerably lower forces according to the literature. There are reports available that needle penetration forces as low as 0.17 N/needle with tip radius of 15 μm (Champeau et al. 2020). Moreover, an article discusses the drug transfer enhancements with needles as blunt as 32 μm in tip radius, which shows that even these blunt needles can open functional pores in the skin (Uppuluri et al. 2017). This means that the microneedles manufactured in this work meets the specifications required for making microneedles functional in the research community. It should also be pointed out that microneedles with tip radii going down to a few microns are very difficult to demould and handle in moulding processes where a careful balance between the needle height, tip radius and base diameter should be considered. Aforementioned reports also show that any microneedles having tip radii from a few microns up to 30 – 50 μm are of interest and functional, as far as different skin thicknesses and applications are concerned.

7.6 Global discussion

This work has presented a thorough study for manufacturing of thermoplastic microneedles using conventional and ultrasonic micromoulding technologies. Extensive process monitoring devices have been used for characterising the processes which forms a process fingerprinting framework for both micromoulding technologies.

Work done has covered also the challenging tool manufacturing stages of a microneedle product by evaluating different machining technologies. State-of-the-art laser machining has been shown to be very successful for obtaining very good quality microneedle cavities on tool steel surfaces with machining times as low as 40 minutes.

Specifications and requirements of a process monitoring framework for micromoulding processes have been covered in detail. Process data have been analysed in order to find and extract meaningful process fingerprints for conventional and ultrasonic micromoulding. Moreover, a quick and efficient method and equipment for evaluating microneedle heights has been introduced based on machine vision principles.

Experimental campaign covered the analysis of process data and interpretation, alongside with its relevance to the dimensional outcome of the microneedle arrays. Important relationships and correlations are presented for machine data and thermal imaging.

7.7 Key outcomes of this research

- Laser machining is shown to be an exceptionally viable of route for microneedle tool manufacture because of its speed and capability in machining high aspect ratio cavities.

- It is demonstrated that conventional micro-injection moulding process is an extremely repeatable and cost-effective method for manufacturing high-quality microneedle arrays for drug delivery.

- Ultrasonic micro-injection moulding is proven to be a highly capable manufacturing technique for microneedle production where it has significant advantages in energy consumption, capital cost, material savings and micromoulding of semi-crystalline polymers over conventional technology.

- Machine vision-based telecentric optical measurement systems provide excellent capability in dimensional quality assessment of microneedle arrays.

- Cost-effective in-line process monitoring procedures are presented where even as-supplied machine data from both conventional and ultrasonic micromoulding techniques are proved to be excellent quality indicators. The process fingerprints that are extracted from the process data can be used for implementing statistical quality control procedures and quality control thresholds for micro-scaled products. Moreover, the correlation of the process fingerprints to the dimensional outcome of micro-scaled products can be exploited for pass-fail procedures that can be implemented in manufacturing environments. This could also include usage of robots for handling the parts, which will provide automation and prevention of faulty samples going into the customer’s site or usage.

7.8 Suggestions for further work

1. Different microneedle cavity shapes can be explored and replication assessment can be carried out for a variety of polymers such as polycarbonate, liquid-crystal polymers, and biodegradable polymers such as polycaprolactone. Shallower, deeper or wider microneedles or microneedle-like structures are also of interest for trending topics such as sensor technologies and light - coupling applications for photovoltaics (Dottermusch 2019; Yang et al. 2019).

2. Although the telecentric optical measurement system provided excellent measurement capability based on machine vision principles and inspected thousands of microneedles in total in a quick way, improvements can be made in terms of sample mounting and alignment for increasing its accuracy. This will reduce the measurement errors and lead to better correlations between the process data and microneedle heights.

3. Previous work performed proved that interfacial heating is of great importance for ultrasonic melting and moulding of the polymer. Different feedstock shapes and amount of interfaces can be experimented for obtaining better replication efficiency with using similar process parameters (Gulcur et al. 2018).

4. The study of the wear behaviour of microneedle mould cavity walls can also be a very interesting research field which will shed light on the lifetime of these laser machined microneedle moulds.

References

Allen, E. A., O’Mahony, C., Cronin, M., O’Mahony, T., Moore, A. C. and Crean, A. M. (2016) Dissolvable microneedle fabrication using piezoelectric dispensing technology. *International Journal of Pharmaceutics* 500 (1), 1-10.

Babenko, M., Sweeney, J., Petkov, P., Lacan, F., Bigot, S. and Whiteside, B. (2018) Evaluation of heat transfer at the cavity-polymer interface in microinjection moulding based on experimental and simulation study. *Applied Thermal Engineering* 130, 865-876.

Baruffi, F., Calaon, M. and Tosello, G. (2018) Micro-Injection Moulding In-Line Quality Assurance Based on Product and Process Fingerprints. *Micromachines* 9 (6).

Baruffi, F., Gülçür, M., Calaon, M., Romano, J.-M., Penchev, P., Dimov, S., Whiteside, B. and Tosello, G. (2019) Correlating nano-scale surface replication accuracy and cavity temperature in micro-injection moulding using in-line process control and high-speed thermal imaging. *Journal of Manufacturing Processes* 47, 367-381.

Bediz, B., Korkmaz, E., Khilwani, R., Donahue, C., Erdos, G., Falo Jr, L. D. and Ozdoganlar, O. B. (2014) Dissolvable microneedle arrays for intradermal delivery of biologics: Fabrication and application. *Pharmaceutical Research* 31 (1), 117-135.

Bouchaud, J. and Dixon, R. (2015) *MEMS & Sensors – High Value MEMS Report.* https://technology.ihs.com/api/binary/519509?attachment=true Accessed 17.06.2019.

Cai, Y., Luo, X., Liu, Z., Qin, Y., Chang, W. and Sun, Y. (2019) Product and Process Fingerprint for Nanosecond Pulsed Laser Ablated Superhydrophobic Surface. *Micromachines* 10 (3), 177.

Champeau, M., Jary, D., Mortier, L., Mordon, S. and Vignoud, S. (2020) A facile fabrication of dissolving microneedles containing 5-aminolevulinic acid. *International Journal of Pharmaceutics* 586, 119554.

Chryssolouris, G., Stavropoulos, P. and Salonitis, K. (2015) Process of Laser Machining. In Nee, A. Y. C. (editor) *Handbook of Manufacturing Engineering and Technology.* London: Springer London. 1601-1628. https://doi.org/10.1007/978-1-4471-4670-4_74

Colavizza, E., Puliga, F. and Escudero, E. (2010) Sonoplast. "New process and machinery for microparts molding based on ultrasound excitation". *Annual Technical Conference - ANTEC, Conference Proceedings.* Vol. 1. https://www.scopus.com/inward/record.uri?eid=2-s2.0-77956701100&partnerID=40&md5=a7535ad63ab98dfc17c00612d3667251.

Curie, J. and Curie, P. (1882) Phénomènes électriques des cristaux hémièdres à faces inclinées. *J. Phys. Theor. Appl.* 1 (1), 245-251.

Davis, S. P., Landis, B. J., Adams, Z. H., Allen, M. G. and Prausnitz, M. R. (2004) Insertion of microneedles into skin: measurement and prediction of insertion force and needle fracture force. *Journal of Biomechanics* 37 (8), 1155-1163.

Demir, Y. K., Akan, Z. and Kerimoglu, O. (2013) Characterization of Polymeric Microneedle Arrays for Transdermal Drug Delivery. *PLoS ONE* 8 (10).

Dimov, S., Petkov, P., Lacan, F. and Scholz, S. (2011) Laser milling: Tool making capabilities. *30th International Congress on Applications of Lasers and Electro-Optics, ICALEO 2011.* https://www.scopus.com/inward/record.uri?eid=2-s2.0-82655170859&partnerID=40&md5=fd97f2d2cf44ed6bed59c2c9b2dcdd17.

Dorf, T., Ferrer, I. and Ciurana, J. (2018) Characterizing ultrasonic micro-molding process of polyetheretherketone (PEEK). *International Polymer Processing* 33 (4), 442-452.

Dottermusch, S. (2019) Micro-cone textures for improved light in-coupling and retroreflection-inspired light trapping at the front surface of solar modules. *Progress in photovoltaics* 27 (7), 593-602.

Drain, P. K., Nelson, C. M. and Lloyd, J. S. (2003) Single-dose versus multi-dose vaccine vials for immunization programmes in developing countries. *Bulletin of the World Health Organization* 81 (10), 726-731.

Fairbanks, H. V. (1974) Applying ultrasonics to the moulding of plastic powders. *Ultrasonics* 12 (1), 22-24.

Fischer, J. M. (2003) *Handbook of Molded Part Shrinkage and Warpage.* Handbook of Molded Part Shrinkage and Warpage.

Frankel, E. J. and Wang, K. K. (1980) Energy transfer and bond strength in ultrasonic welding of thermoplastics. *Polymer Engineering & Science* 20 (6), 396-401.

Giboz, J., Copponnex, T. and Mélé, P. (2007) Microinjection molding of thermoplastic polymers: A review. *Journal of Micromechanics and Microengineering* 17 (6), R96-R109.

Gill, H. S., Denson, D. D., Burris, B. A. and Prausnitz, M. R. (2008) Effect of microneedle design on pain in human volunteers. *Clinical Journal of Pain* 24 (7), 585-594.

Gooberman, G. (1968) *Ultrasonics Theory and Application.* English Universities Press Ltd.

Griffiths, C. A., Dimov, S. S., Brousseau, E. B. and Hoyle, R. T. (2007) The effects of tool surface quality in micro-injection moulding. *Journal of Materials Processing Technology* 189 (1-3), 418-427.

Griffiths, C. A., Dimov, S. S., Scholz, S., Hirshy, H. and Tosello, G. (2011) Process factors influence on cavity pressure behavior in microinjection moulding. *Journal of Manufacturing Science and Engineering, Transactions of the ASME* 133 (3).

Griffiths, C. A., Tosello, G., Dimov, S. S., Scholz, S. G., Rees, A. and Whiteside, B. (2015) Characterisation of demoulding parameters in micro-injection moulding. *Microsystem Technologies* 21 (8), 1677-1690.

Gulcur, M., Whiteside, B. R., Nair, K., Babenko, M. and Coates, P. D. (2018) Ultrasonic injection moulding of polypropylene and thermal visualisation of the process using a bespoke injection mould tool. *European Society for Precision Engineering and Nanotechnology, Conference Proceedings - 18th International Conference and Exhibition, EUSPEN 2018.* https://www.scopus.com/inward/record.uri?eid=2-s2.0-

85054508180&partnerID=40&md5=1685626ffd5922ac1817c7c325fc1dae.

Hamilton, J. D. (2011) *Fabrication and analysis of injection molded plastic microneedle arrays*. MSc. Georgia Institute of Technology. http://hdl.handle.net/1853/39481

Heckele, M. and Schomburg, W. K. (2004) Review on micro molding of thermoplastic polymers. *Journal of Micromechanics and Microengineering* 14 (3), R1-R14.

Henry, S., McAllister, D. V., Allen, M. G. and Prausnitz, M. R. (1998) Microfabricated microneedles: A novel approach to transdermal drug delivery. *Journal of Pharmaceutical Sciences* 87 (8), 922-925.

Holthusen, A. K., Riemer, O., Schmütz, J. and Meier, A. (2017) Mold machining and injection molding of diffractive microstructures. *Journal of Manufacturing Processes* 26, 290-294.

Janer, M., Plantà, X. and Riera, D. (2020) Ultrasonic moulding: Current state of the technology. *Ultrasonics* 102, 106038.

Jiang, B., Peng, H., Wu, W., Jia, Y. and Zhang, Y. (2016) Numerical simulation and experimental investigation of the viscoelastic heating mechanism in ultrasonic plasticizing of amorphous polymers for micro injection molding. *Polymers* 8 (5).

Jung, W. and Park, K. (2014) Selective ultrasonic imprinting for micropattern replication on predefined area. *Ultrasonics* 54 (6), 1495-1503.

Juster, H., van der Aar, B. and de Brouwer, H. (2019) A review on microfabrication of thermoplastic polymer-based microneedle arrays. *Polymer Engineering & Science* 59 (5), 877-890.

Kellomäki, M. and Törmälä, P. (1997) Ultrasonic moulding of bioabsorbable polymers and polymer/drug composites. *Journal of Materials Science Letters* 16 (21), 1786-1789.

Kolew, A., Münch, D., Sikora, K. and Worgull, M. (2011) Hot embossing of micro and sub-micro structured inserts for polymer replication. *Microsystem Technologies* 17 (4), 609-618.

Kukla, C., Loibl, H., Detter, H. and Hannenheim, W. (1998) Micro-injection moulding - the aims of a project partnership. *Kunststoffe Plast Europe* 88 (9), 6-7.

Kurt, M., Saban Kamber, O., Kaynak, Y., Atakok, G. and Girit, O. (2009) Experimental investigation of plastic injection molding: Assessment of the effects of cavity pressure and mold temperature on the quality of the final products. *Materials & Design* 30 (8), 3217-3224.

Larrañeta, E., Lutton, R. E. M., Woolfson, A. D. and Donnelly, R. F. (2016) Microneedle arrays as transdermal and intradermal drug delivery systems: Materials science, manufacture and commercial development. *Materials Science and Engineering: R: Reports* 104, 1-32.

Masato, D., Babenko, M., Shriky, B., Gough, T., Lucchetta, G. and Whiteside, B. (2018) Comparison of crystallization characteristics and mechanical properties of polypropylene processed by ultrasound and conventional micro-injection molding. *The International Journal of Advanced Manufacturing Technology* 99 (1), 113-125.

Michaeli, W., Kamps, T. and Hopmann, C. (2011) Manufacturing of polymer micro parts by ultrasonic plasticization and direct injection. *Microsystem Technologies* 17 (2), 243-249.

Michaeli, W. and Opfermann, D. (2006) *Ultrasonic plasticising for micro injection moulding.* Woodhead Publishing Limited.

Michaeli, W., Spennemann, A. and Gärtner, R. (2002) New plastification concepts for micro injection moulding. *Microsystem Technologies* 8 (1), 55-57.

Mirza, K. B., Zuliani, C., Hou, B., Ng, F. S., Peters, N. S. and Toumazou, C. (2017) Injection moulded microneedle sensor for real-time wireless pH monitoring. *Proceedings of the Annual International Conference of the IEEE Engineering in Medicine and Biology Society, EMBS.* https://www.scopus.com/inward/record.uri?eid=2-s2.0-85032195822&doi=10.1109/EMBC.2017.8036794&partnerID=40&md5=ecce5c79a65c1540b8d0156687110f77.

Mnkknen, K., Pakkanen, T. T., Hietala, J., Pkknen, E. J., Pkknen, P., Jskelinen, T. and Kaikuranta, T. (2002) Replication of sub-micron features using amorphous thermoplastics. *Polymer Engineering and Science* 42 (7), 1600-1608.

Nair, K. (2014) *Micro-injection moulded microneedles for drug delivery*. University of Bradford.

Nair, K., Whiteside, B., Grant, C., Patel, R., Tuinea-Bobe, C., Norris, K. and Paradkar, A. (2015) Investigation of plasma treatment on micro-injection moulded microneedle for drug delivery. *Pharmaceutics* 7 (4), 471-485.

Naitove, M. H. (2010) New machines & processes unveiled by Wittmann Battenfeld. *Plastics Technology* 56 (6), 13-16.

Nalluri, B. N., Uppuluri, C., Devineni, J., Nayak, A., Nair, K. J., Whiteside, B. R. and Das, D. B. (2017) Effect of microneedles on transdermal permeation enhancement of amlodipine. *Drug Delivery and Translational Research* 7 (3), 383-394.

Packianather, M., Griffiths, C. and Kadir, W. (2015) Micro injection moulding process parameter tuning. *Procedia CIRP.* Vol. 33. https://www.scopus.com/inward/record.uri?eid=2-s2.0-84939797372&doi=10.1016/j.procir.2015.06.093&partnerID=40&md5=df722b5dc6f9c0bc4dd9fe7dd9667705.

Paul, D. W. and Crawford, R. J. (1981) Ultrasonic moulding of plastic powders. *Ultrasonics* 19 (1), 23-27.

Prausnitz, M. R. (2004) Microneedles for transdermal drug delivery. *Advanced Drug Delivery Reviews* 56 (5), 581-587.

Prausnitz, M. R. (2017) Engineering microneedle patches for vaccination and drug delivery to skin. *Annual Review of Chemical and Biomolecular Engineering* 8, 177-200.

Ring, F. (2016) The Herschel heritage to medical thermography. *Journal of Imaging* 2 (2).

Romano, J. M., Gulcur, M., Garcia-Giron, A., Martinez-Solanas, E., Whiteside, B. R. and Dimov, S. S. (2019) Mechanical durability of hydrophobic surfaces fabricated by injection moulding of laser-induced textures. *Applied Surface Science* 476, 850-860.

Rouphael, N. G., Paine, M., Mosley, R., Henry, S., McAllister, D. V., Kalluri, H., Pewin, W., Frew, P. M., Yu, T., Thornburg, N. J., Kabbani, S., Lai, L., Vassilieva, E. V., Skountzou, I., Compans, R. W., Mulligan, M. J., Prausnitz, M. R., Beck, A., Edupuganti, S., Heeke, S., Kelley, C. and Nesheim, W. (2017) The safety, immunogenicity, and acceptability of inactivated influenza vaccine delivered by microneedle patch (TIV-MNP 2015): a randomised, partly blinded, placebo-controlled, phase 1 trial. *The Lancet* 390 (10095), 649-658.

Röhrig, M., Mail, M., Schneider, M., Louvin, H., Hopf, A., Schimmel, T., Worgull, M. and Hölscher, H. (2014) Nanofur for Biomimetic Applications. *Advanced Materials Interfaces* 1 (4).

Sacristán, M., Plantá, X., Morell, M. and Puiggalí, J. (2014) Effects of ultrasonic vibration on the micro-molding processing of polylactide. *Ultrasonics Sonochemistry* 21 (1), 376-386.

Sammoura, F., Kang, J., Heo, Y.-M., Jung, T. and Lin, L. (2007) Polymeric microneedle fabrication using a microinjection molding technique. *Microsystem Technologies* 13 (5), 517-522.

Sato, A., Sakaguchi, H., Ito, H. and Koyama, K. (2010) Evaluation of replication properties on moulded surface by ultrasonic injection moulding system. *Plastics, Rubber and Composites* 39 (7), 315-320.

Schauer, S., Schmager, R., Hünig, R., Ding, K., Paetzold, U. W., Lemmer, U., Worgull, M., Hölscher, H. and Gomard, G. (2018) Disordered diffraction gratings tailored by shape-memory based wrinkling and their application to photovoltaics. *Optical Materials Express* 8 (1).

Schneider, N., Zeiger, C., Kolew, A., Schneider, M., Leuthold, J., Hölscher, H. and Worgull, M. (2014) Nanothermoforming of hierarchical optical components utilizing shape memory polymers as active molds. *Optical Materials Express* 4 (9), 1895-1902.

Scholz, S. G., Kolew, A. and Griffiths, C. (2012) Laser structuring of metallic mold inserts by using µs, ns, and ps-laser Ablation. *Proceedings of SPIE - The International Society for Optical Engineering.* Vol. 8244. *https://www.scopus.com/inward/record.uri?eid=2-s2.0-84858675405&doi=10.1117/12.910006&partnerID=40&md5=7c0397fd1e4b8a592d4a80cf4f97fa62.*

Sha, B., Dimov, S., Griffiths, C. and Packianather, M. S. (2007) Micro-injection moulding: Factors affecting the achievable aspect ratios. *International Journal of Advanced Manufacturing Technology* 33 (1-2), 147-156.

Sonoplast project report. (2010) *https://cordis.europa.eu/project/rcn/93892_en.html* Accessed 17.02.2017.

SONORUS: New Machine for Microparts Moulding base on Ultrasound Excitation. (2011) *http://www.sonorusproject.eu/* Accessed 14.07.2019.

Spares, R., Whiteside, B. R. and Coates, P. D. (2009) High speed thermal imaging of micromoulding. *Annual Technical Conference - ANTEC, Conference Proceedings.* Vol. 5. *https://www.scopus.com/inward/record.uri?eid=2-s2.0-70450008441&partnerID=40&md5=7d3b816d632aa6771871acdf24515e71.*

Spares, R., Whiteside, B. R. and Coates, P. D. (2013) High speed thermal imaging of complex micromoulding flows. *Annual Technical Conference - ANTEC, Conference Proceedings.* Vol. 2. *https://www.scopus.com/inward/record.uri?eid=2-s2.0-84903527348&partnerID=40&md5=4adf44ff511fbe5dc091d01097c44718.*

Steglich, D., Lacan, F., Dessors, S., Eigenbrod, H., Moguedet, M. and Bambury, E. (2012) Optimising the Replication Quality of Polymer Injection-Moulded Microneedles on the IMPRESS Platform. (v), 978-981.

Sánchez-Sánchez, X., Hernández-Avila, M., Elizalde, L. E., Martínez, O., Ferrer, I. and Elías-Zuñiga, A. (2017) Micro injection molding processing of UHMWPE using ultrasonic vibration energy. *Materials and Design* 132, 1-12.

Tarbox, T. N., Watts, A. B., Cui, Z. and Williams, R. O., III (2018) An update on coating/manufacturing techniques of microneedles. *Drug Delivery and Translational Research* 8 (6), 1828-1843.

Tolunay, M. N., Dawson, P. R. and Wang, K. K. (1983) Heating and bonding mechanisms in ultrasonic welding of thermoplastics. *Polymer Engineering & Science* 23 (13), 726-733.

Tosello, G., Gava, A., Hansen, H. N. and Lucchetta, G. (2010) Study of process parameters effect on the filling phase of micro-injection moulding using weld lines as flow markers. *The International Journal of Advanced Manufacturing Technology* 47 (1), 81-97.

Ultrasion s.L website. (2019) http://ultrasion.eu/ Accessed 17.07.2019.

Uppuluri, C., Shaik, A. S., Han, T., Nayak, A., Nair, K. J., Whiteside, B. R., Nalluri, B. N. and Das, D. B. (2017) Effect of Microneedle Type on Transdermal Permeation of Rizatriptan. *AAPS PharmSciTech* 18 (5), 1495-1506.

van der Maaden, K., Jiskoot, W. and Bouwstra, J. (2012) Microneedle technologies for (trans)dermal drug and vaccine delivery. *Journal of Controlled Release* 161 (2), 645-655.

Vranić, E., Tucak, A., Sirbubalo, M., Rahić, O., Elezović, A. and Hadžiabdić, J. (2020) Microneedle-Based Sensor Systems for Real-Time Continuous Transdermal Monitoring of Analytes in Body Fluids. *CMBEBIH 2019.* Cham, 2020//. Springer International Publishing.

Wang, M., Hu, L. and Xu, C. (2017) Recent advances in the design of polymeric microneedles for transdermal drug delivery and biosensing. *Lab on a Chip* 17 (8), 1373-1387.

Wei, H., Wang, H., Xia, Y., Cui, D., Shi, Y., Dong, M., Liu, C., Ding, T., Zhang, J., Ma, Y., Wang, N., Wang, Z., Sun, Y., Wei, R. and Guo, Z. (2018) An overview of lead-free piezoelectric materials and devices. *Journal of Materials Chemistry C* 6 (46), 12446-12467.

Whiteside, B., Babenko, M., Tuinea-Bobe, C., Brown, E. and Coates, P. (2016) Ultrasonic injection moulding: A study of thermal behaviour and nanofeature replication. *Proceedings of the 16th International Conference of the European Society for Precision Engineering and Nanotechnology, EUSPEN 2016.* https://www.scopus.com/inward/record.uri?eid=2-s2.0-84984619801&partnerID=40&md5=cf069c46878f156d890ce3c551350c5d.

Whiteside, B. R., Brown, E. C., Ono, Y., Jen, C. K. and Coates, P. D. (2005a) Real-time ultrasonic diagnosis of polymer degradation and filling incompleteness in micromoulding. *Plastics, Rubber and Composites* 34 (9), 387-392.

Whiteside, B. R., Martyn, M. T., Coates, P. D., Allan, P. S., Hornsby, P. R. and Greenway, G. (2003) Micromoulding: Process characteristics and product properties. *Plastics, Rubber and Composites* 32 (6), 231-239.

Whiteside, B. R., Martyn, M. T., Coates, P. D., Greenway, G., Allen, P. and Hornsby, P. (2004) Micromoulding: Process measurements, product morphology and properties. *Plastics, Rubber and Composites* 33 (1), 11-17.

Whiteside, B. R., Spares, R., Brown, E. C., Norris, K., Coates, P. D., Kobayashi, M., Jen, C. K. and Cheng, C. C. (2008) Optical imaging metrology for micromoulding cavity flows and products. *Plastics, Rubber and Composites* 37 (2-4), 57-66.

Whiteside, B. R., Spares, R., Howell, K., Martyn, M. T. and Coates, P. D. (2005b) Micromoulding: Extreme process monitoring and inline product assessment. *Plastics, Rubber and Composites* 34 (9), 380-386.

Worgull, M. (2009) *Hot Embossing.* Hot Embossing.

Wu, W., Peng, H., Jia, Y. and Jiang, B. (2017) Characteristics and mechanisms of polymer interfacial friction heating in ultrasonic plasticization for micro injection molding. *Microsystem Technologies* 23 (5), 1385-1392.

Yang, Z., Xu, H., Huang, Y., Sun, J., Wu, D., Gao, X. and Zhang, Y. (2019) Measuring Mechanism and Applications of Polymer-Based Flexible Sensors. *Sensors* 19 (6).

Yole Développement (2015) *After fundraising, new collaborations and acquisitions, microfluidic players are in position: now, the game can start ...* Yole Développement Accessed 17.06.2019.

Yung, K. L., Xu, Y., Kang, C., Liu, H., Tam, K. F., Ko, S. M., Kwan, F. Y. and Lee, T. M. H. (2012) Sharp tipped plastic hollow microneedle array by microinjection moulding. *Journal of Micromechanics and Microengineering* 22 (1).

Zeng, K., Wu, X.-y., Liang, X., Xu, B., Wang, Y.-t., Chen, X.-q., Cheng, R. and Luo, F. (2014) Process and properties of micro-ultrasonic powder molding with polypropylene. *The International Journal of Advanced Manufacturing Technology* 70 (1), 515-522.

Zhang, H., Fang, F., Gilchrist, M. D. and Zhang, N. (2019) Precision replication of micro features using micro injection moulding: Process simulation and validation. *Materials & Design* 177, 107829.

Zhang, N., Chu, J. S. and Gilchrist, M. D. (2011) Micro injection molding: Characterization of cavity filling process. *Annual Technical Conference - ANTEC, Conference Proceedings.* Vol. 3. https://www.scopus.com/inward/record.uri?eid=2-s2.0-80051816038&partnerID=40&md5=64b3a95612c4046e889f19c5f4829226.

Zhang, N. and Gilchrist, M. D. (2012) Characterization of thermo-rheological behavior of polymer melts during the micro injection moulding process. *Polymer Testing* 31 (6), 748-758.

Zhang, N. and Gilchrist, M. D. (2014) Characterization of microinjection molding process for milligram polymer microparts. *Polymer Engineering and Science* 54 (6), 1458-1470.

Zhang, Z., Wang, X., Luo, Y. and Wang, L. (2010) Study on heating process of ultrasonic welding for thermoplastics. *Journal of Thermoplastic Composite Materials* 23 (5), 647-664.

Appendix A – Rheology data for polypropylene pellets

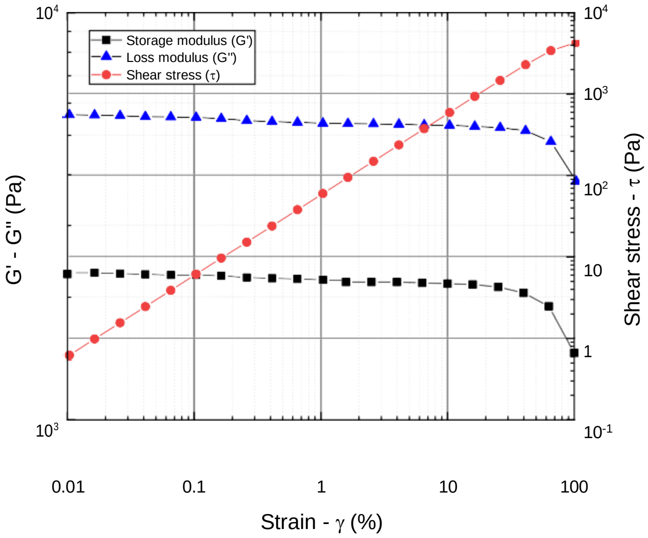

Graph showing amplitude sweep experiment carried out for pellet shaped polypropylene (PP, Ineos - GA12) feedstock at 240°C.

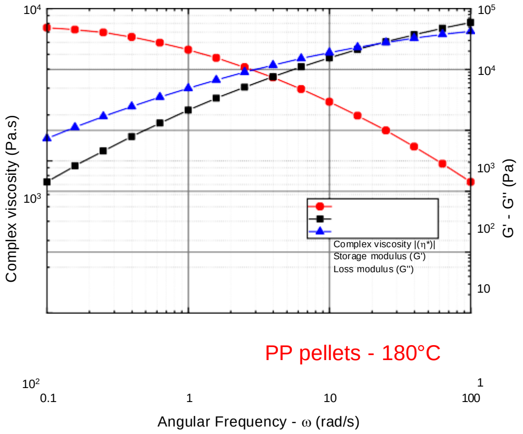

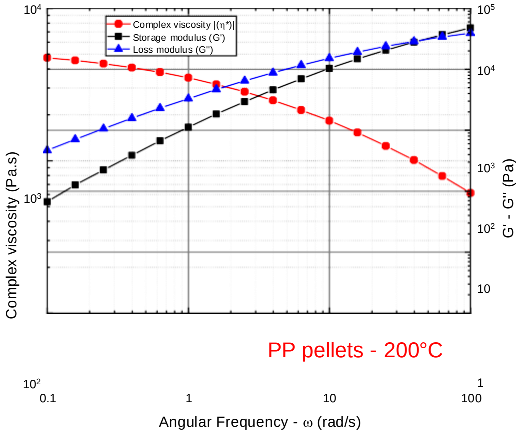

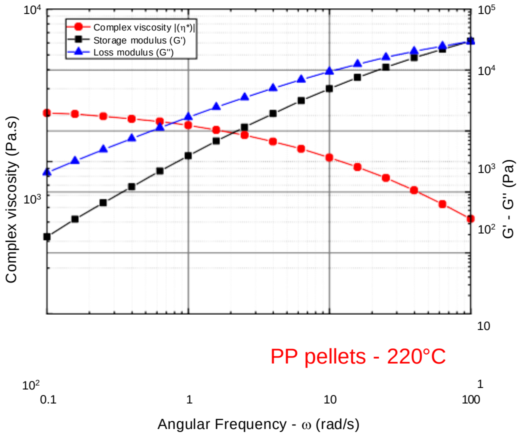

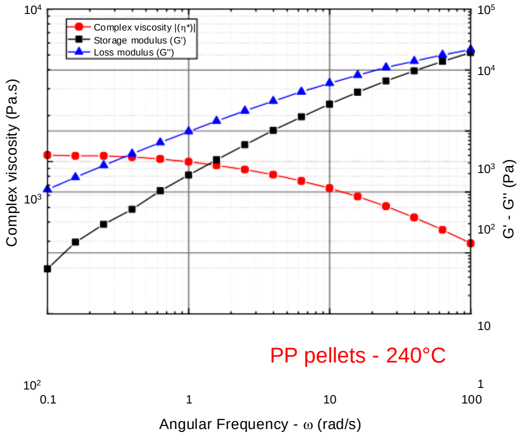

Graphs showing frequency sweep experiments for PP pellets at different temperatures (180, 200, 220, 240°C).

Appendix B – Rheology data for polypropylene discs

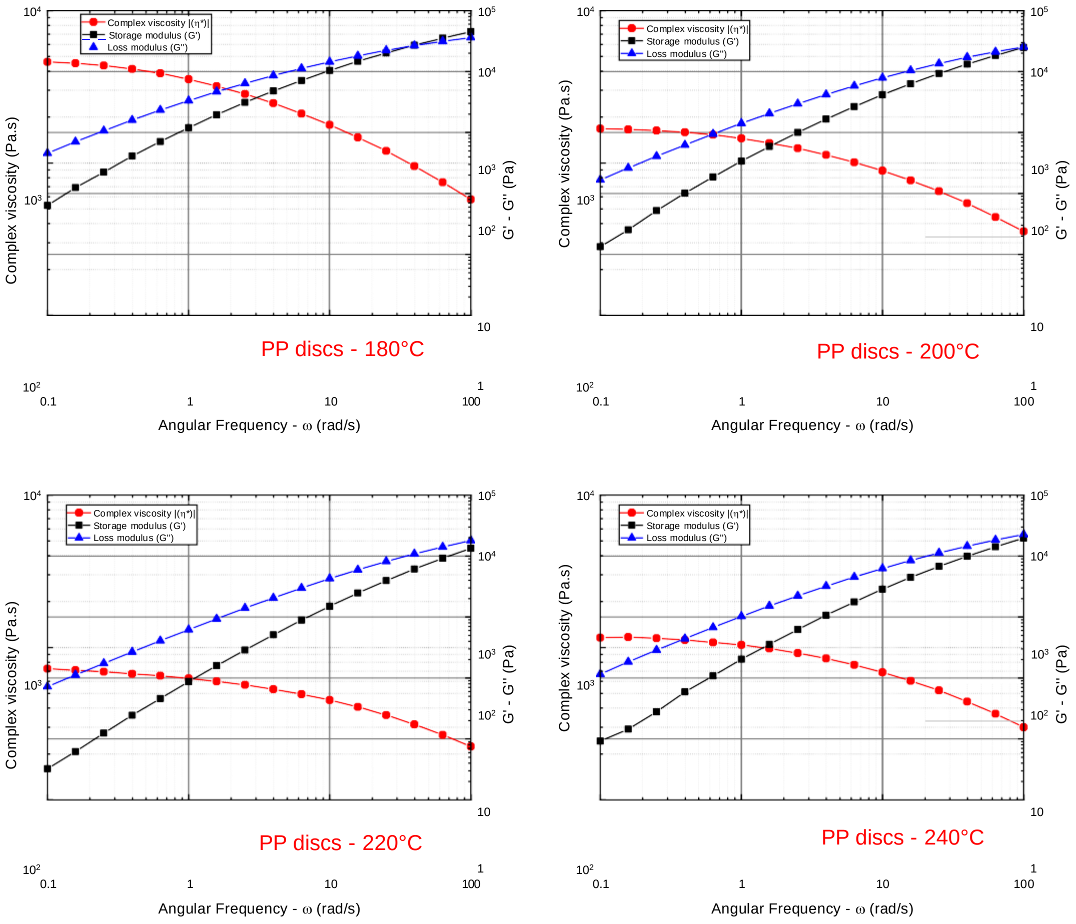

Graphs showing frequency sweep experiments for PP discs at different temperatures (180, 200, 220, 240°C).

Appendix C – Rheology data for acrylonitrile butadiene styrene (ABS) pellets

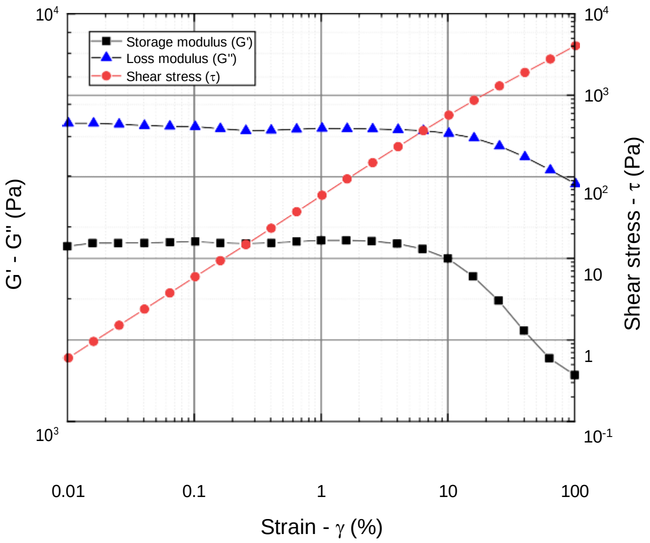

Graph showing amplitude sweep experiment carried out for pellet shaped acrylonitrile butadiene styrene (ABS, Sabic Cycolac - HMG94MD) feedstock at 240°C.

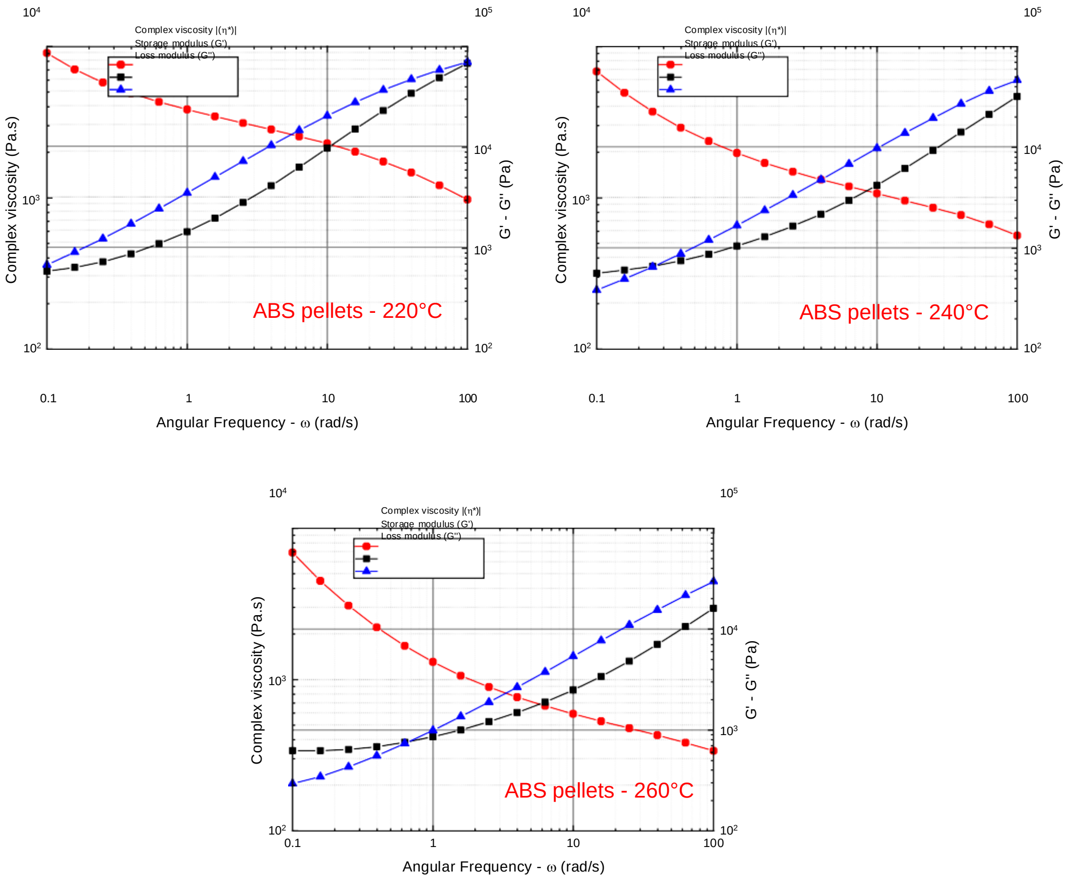

Graphs showing frequency sweep experiments for ABS pellets at different temperatures (220, 240, 260°C).

Appendix D – Rheology data for acrylonitrile butadiene styrene (ABS) discs

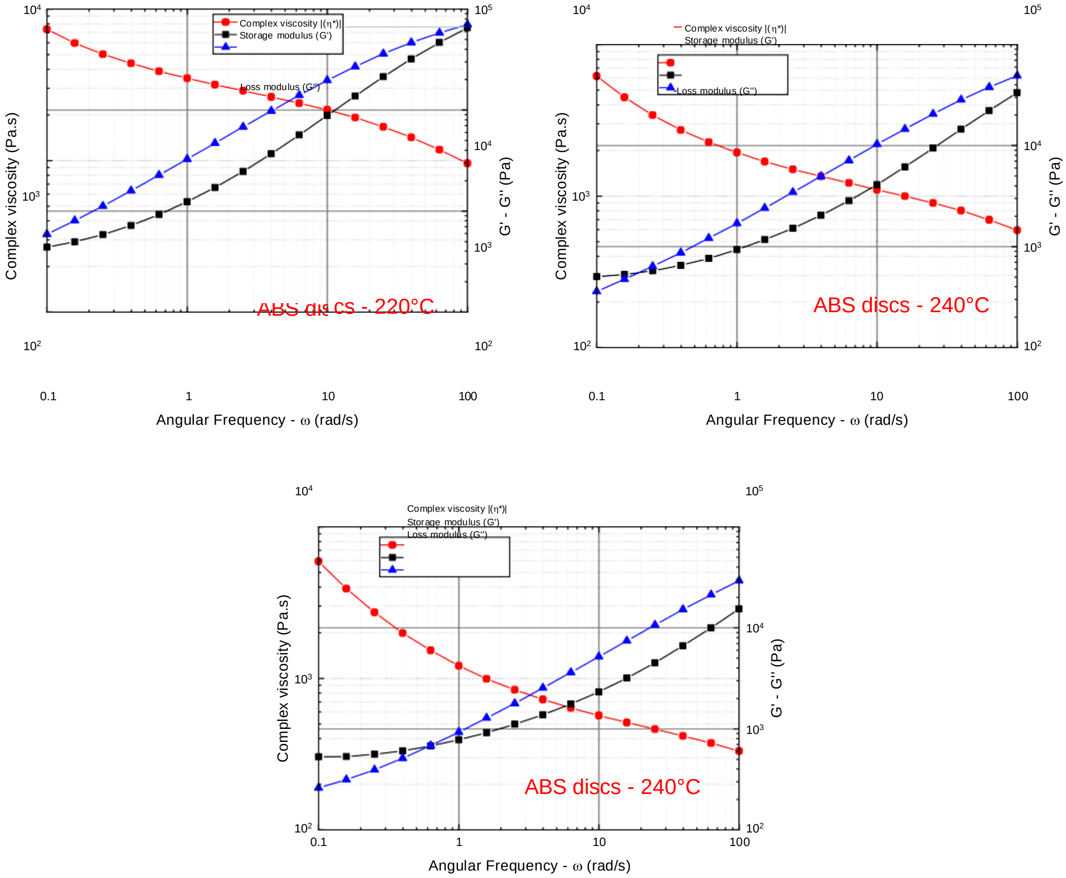

Graphs showing frequency sweep experiments for ABS discs at different temperatures (220, 240, 260°C).

Appendix E – Tip radius data for the experiments presented in Chapter 5

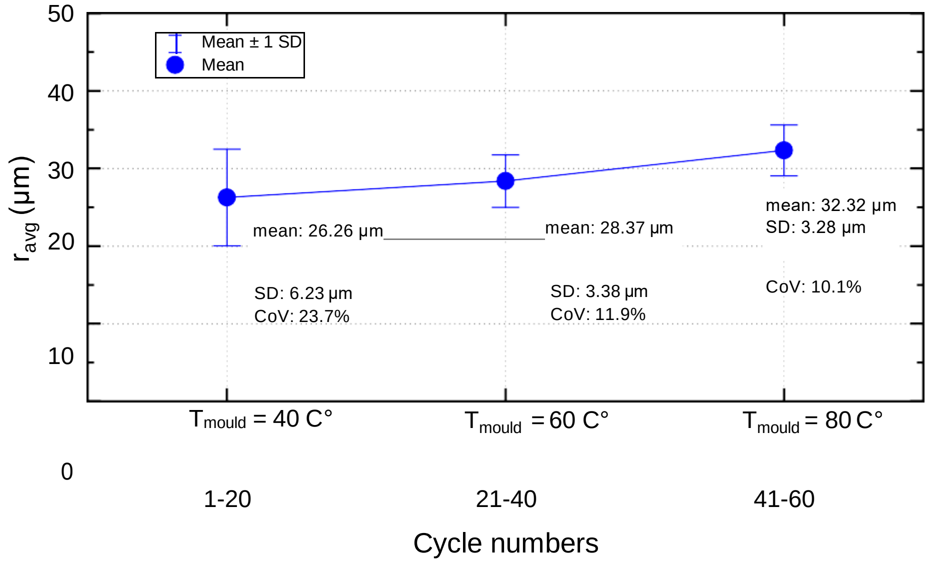

PP experiments (Batch-m1): Interval plots showing the SD, CoV and means of **average tip radius (r_{avg})** for cycles with different mould temperatures of 40, 60 and 80°C, respectively.

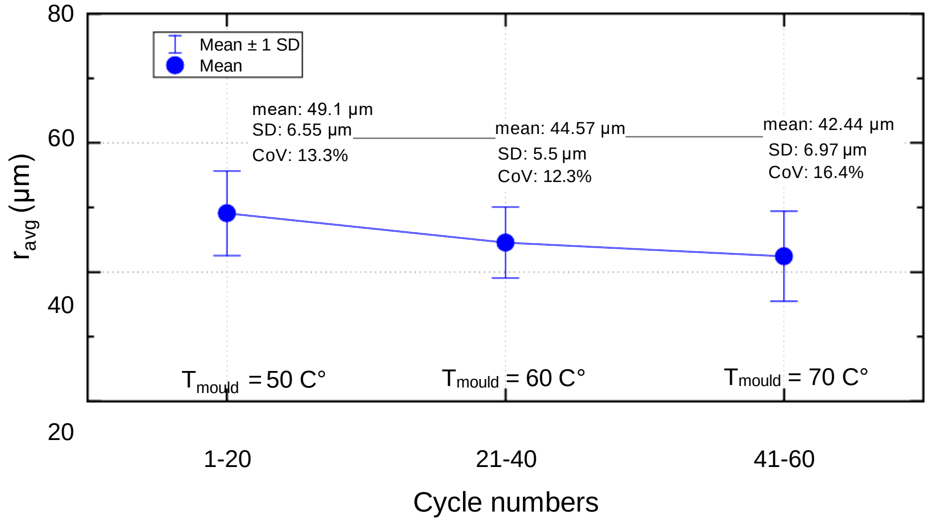

ABS experiments (Batch-2m): Interval plots showing the SD, CoV and means of average tip radius (r_{avg}) for cycles with different mould temperatures of 50, 60 and 70°C, respectively.

PP experiments (Batch-3m): Table showing tip radius measurement results from telecentric inspection system.

Average tip radius (r_{avg})	Standard deviation for h_{avg} (SD)	Coefficient of Variance for h_{avg} (CoV)
10.41 μm	1.58 μm	15.2 %

ABS experiments (Batch-4m): Table showing tip radius measurement results from telecentric inspection system.

Average tip radius (r_{avg})	Standard deviation for h_{avg} (SD)	Coefficient of Variance for h_{avg} (CoV)
11.58 μm	0.89 μm	7.7 %

Appendix F – Tip radius data for the experiments presented in Chapter 6

No tip radius data have been recorded for Batch-u1 since the measurements were done by manually and automatic acquisitions could not be used at the time.

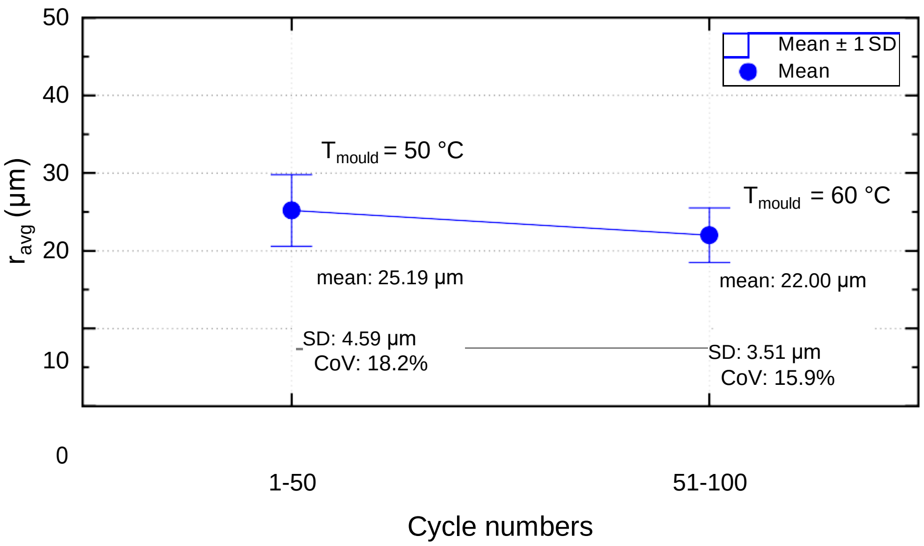

PP experiments (Batch-u2): Interval plot showing the SD, CoV and means of average tip radius (r_{avg}) for cycles with different mould temperatures of 50, 60°C.

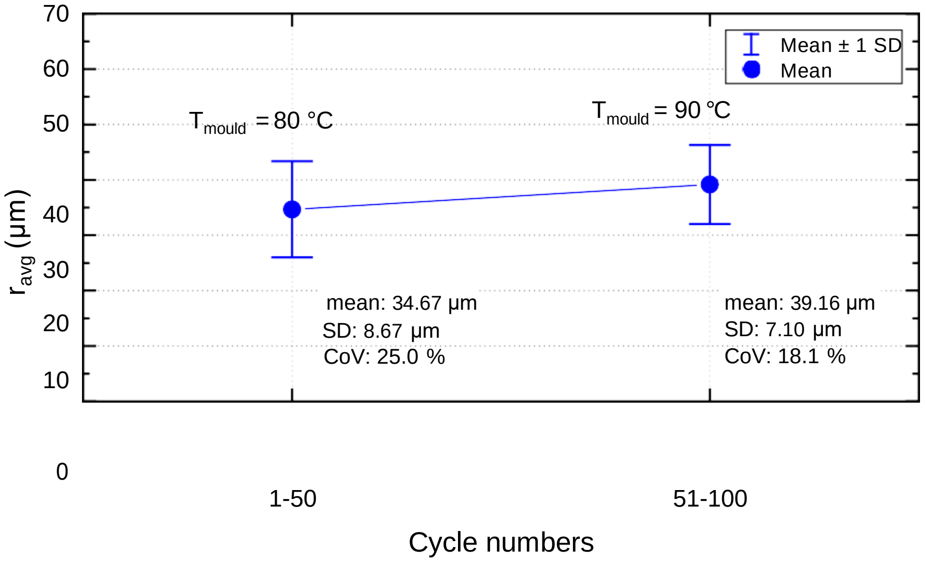

ABS experiments (Batch-u3): Interval plot showing the SD, CoV and means of average tip radius (r_{avg}) for cycles with different mould temperatures of 80 and 90°C, respectively. 36 and 46 samples have been used for creation of this data respectively for corresponding mould temperatures because of faults in edge detection in the measurement setup.

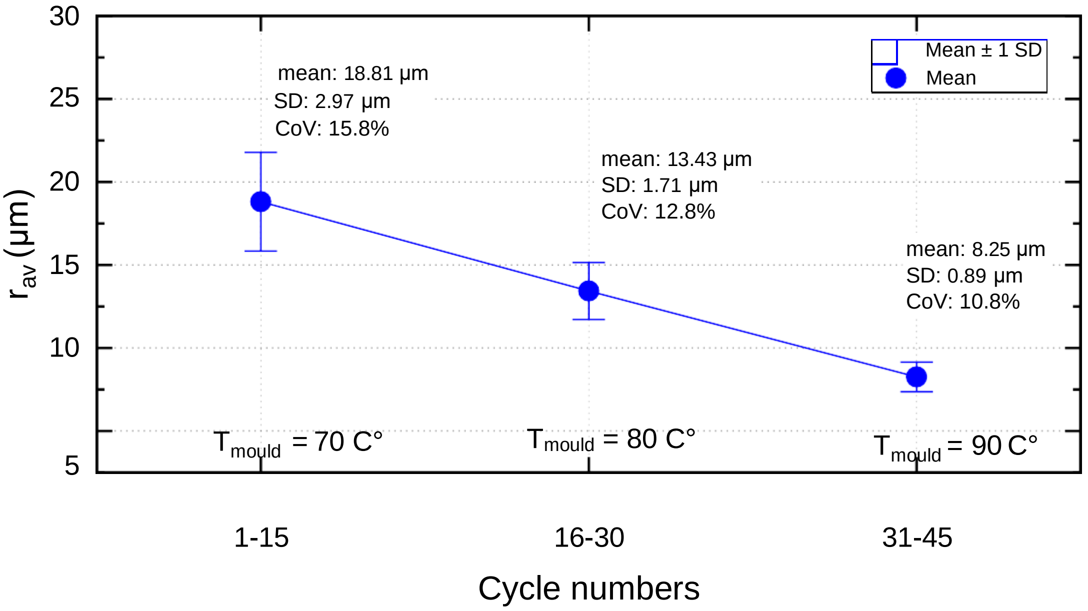

PP experiments (Batch-u4): Interval plot showing the SD, CoV and means of average tip radius (r_{avg}) for cycles with different mould temperatures of 70, 80 and 90°C, respectively. 15, 14 and 14 samples have been used for creation of this data respectively for corresponding mould temperatures because of faults in edge detection in the measurement setup.

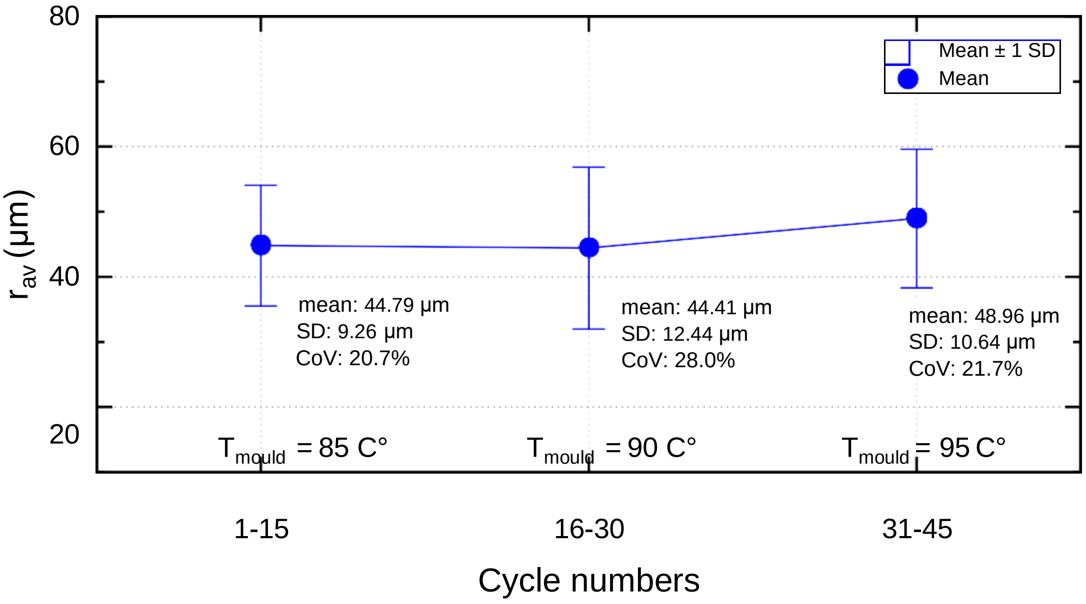

ABS experiments (Batch-u5): Interval plot showing the SD, CoV and means of average tip radius (r_{avg}) for cycles with different mould temperatures of 85, 90 and 95°C, respectively. 10, 10 and 15 samples have been used for creation of this data respectively for corresponding mould temperatures because of faults in edge detection in the measurement setup.

Appendix G – LabVIEW codes for data extraction

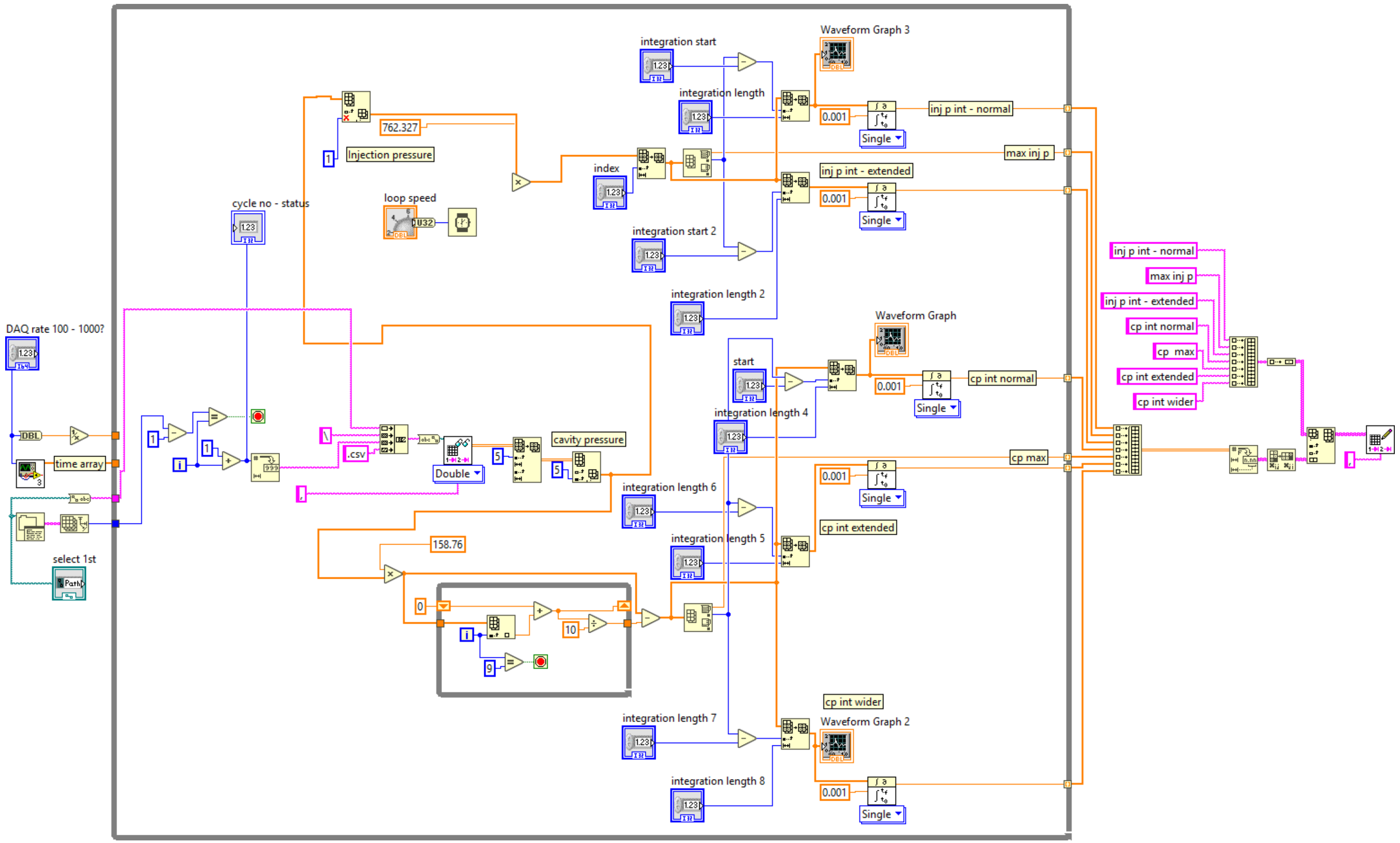

LabVIEW code written for pressure fingerprint extraction.

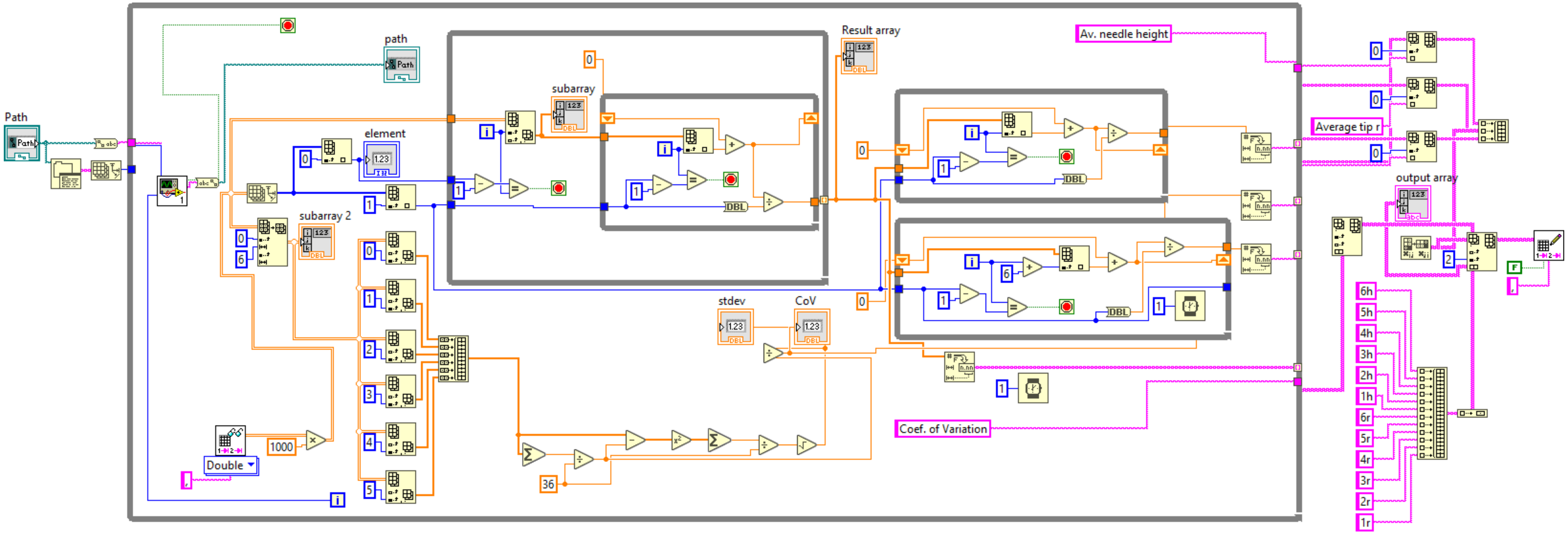

LabVIEW code written for microneedle measurement file analysis. Statistical terms and product data have been calculated using a while loop.

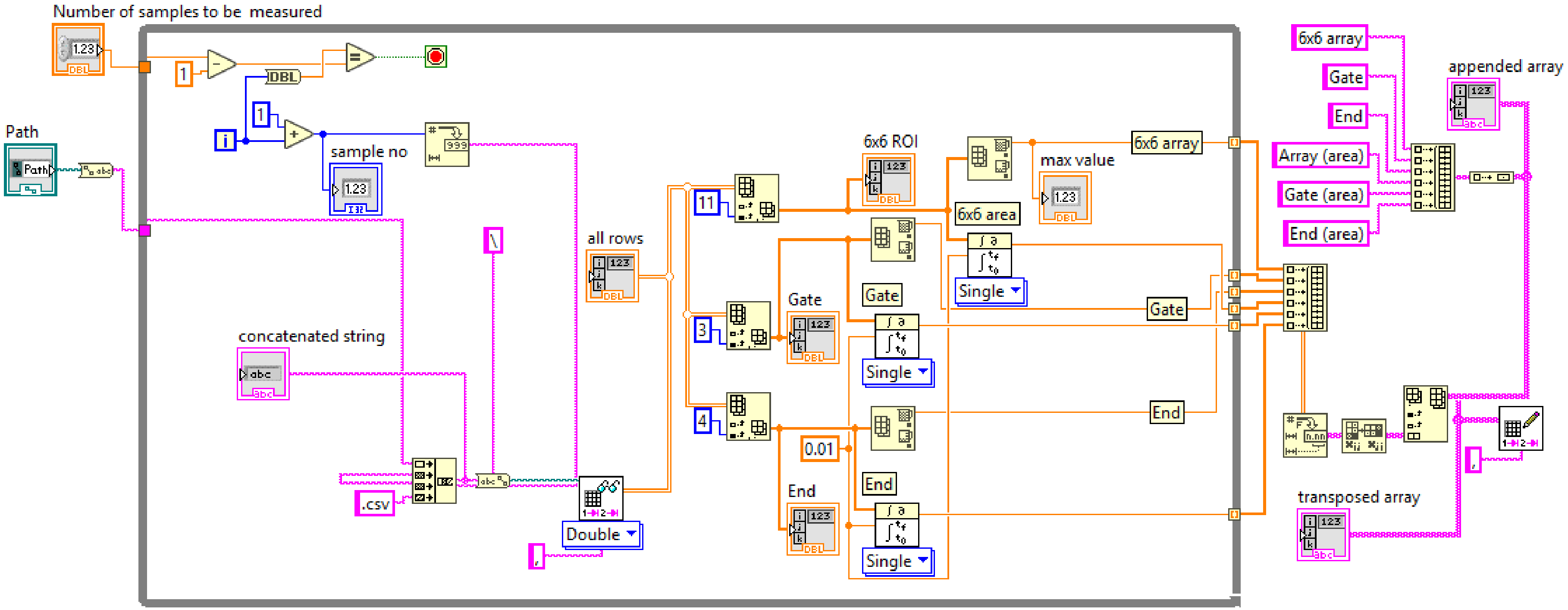

LabVIEW code written for thermal imaging process fingerprints.

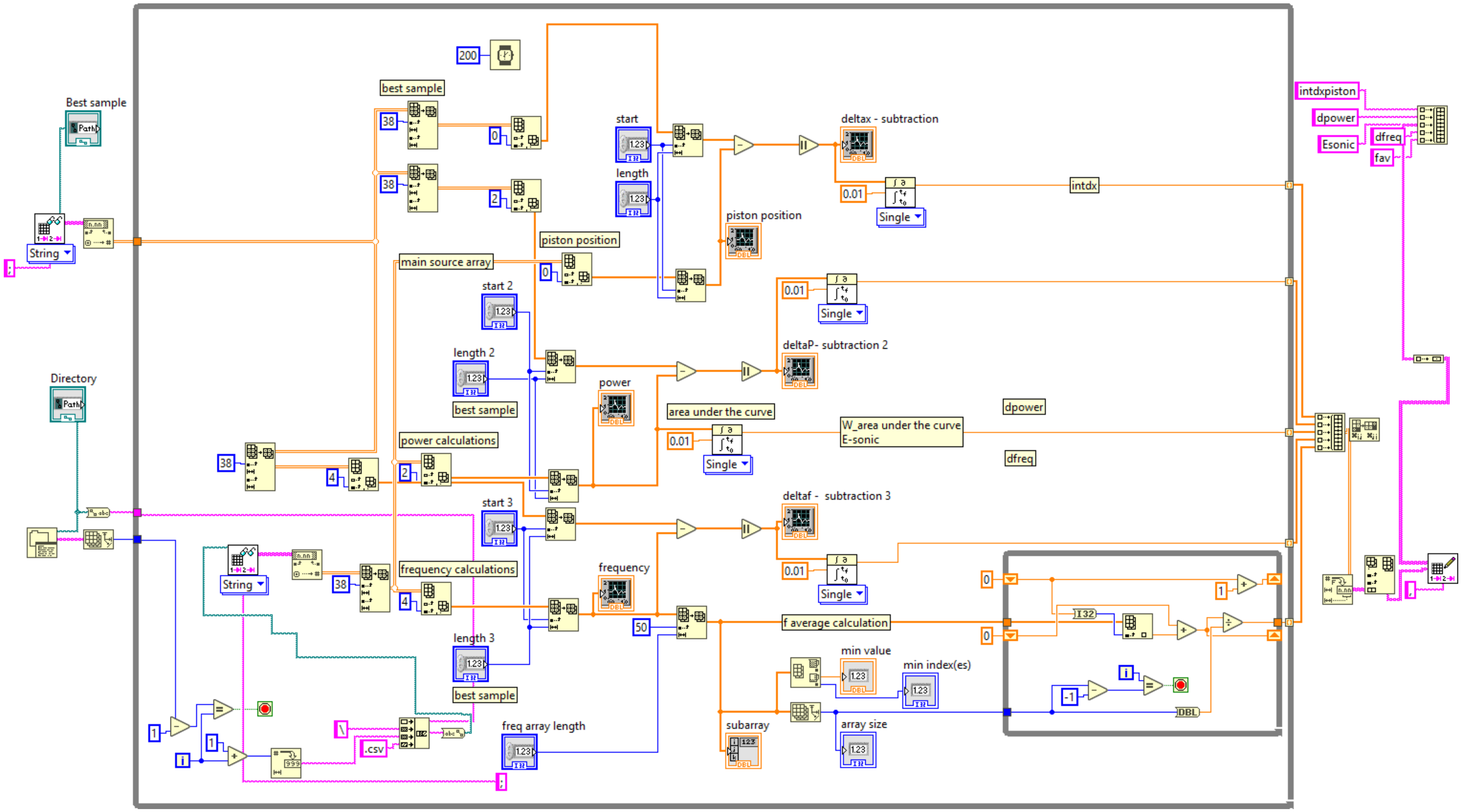

LabVIEW code written for ultrasonic micromoulding machine data process fingerprint extractions.

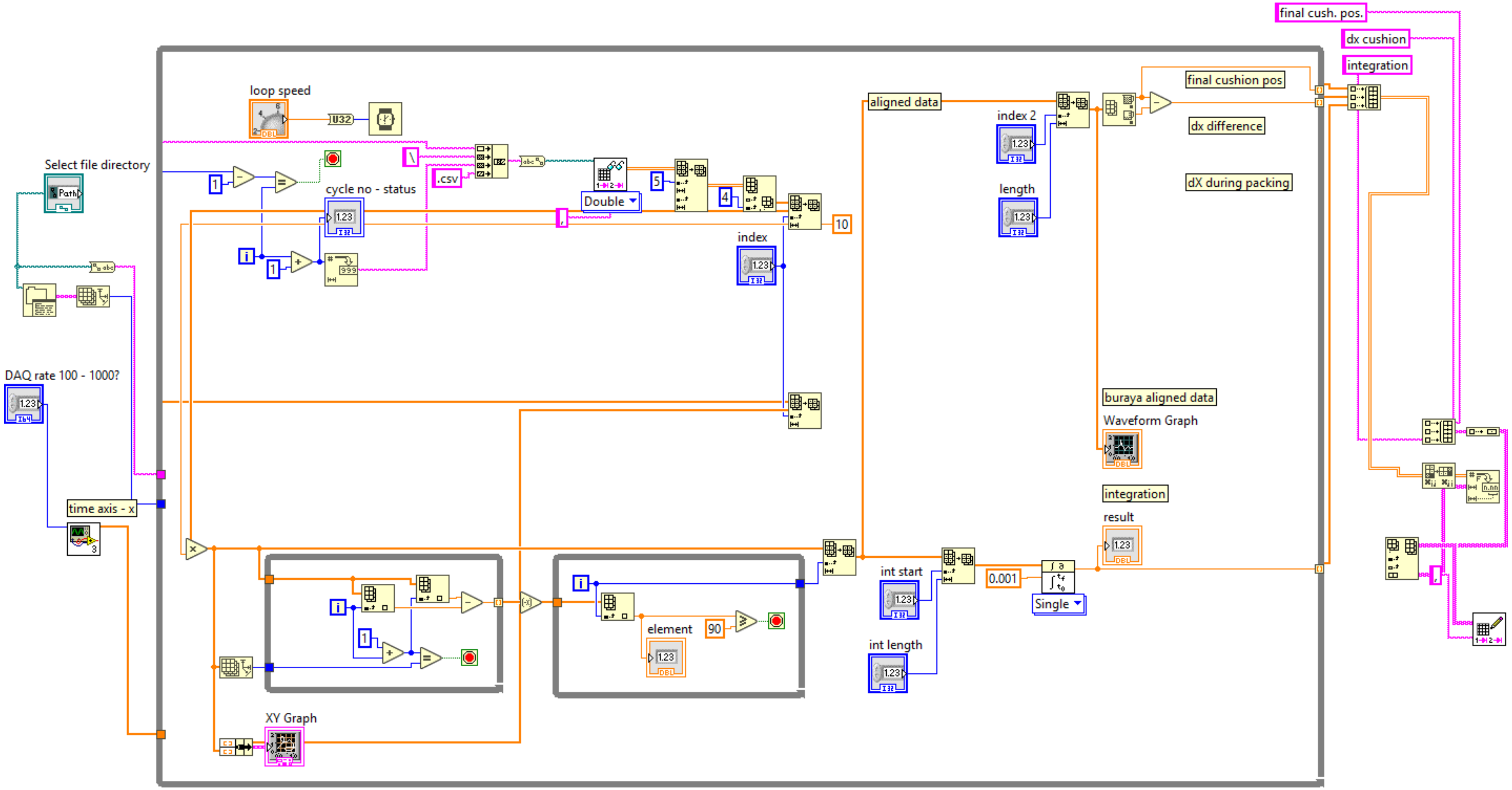

LabVIEW code written for laser/encoder position analysis.

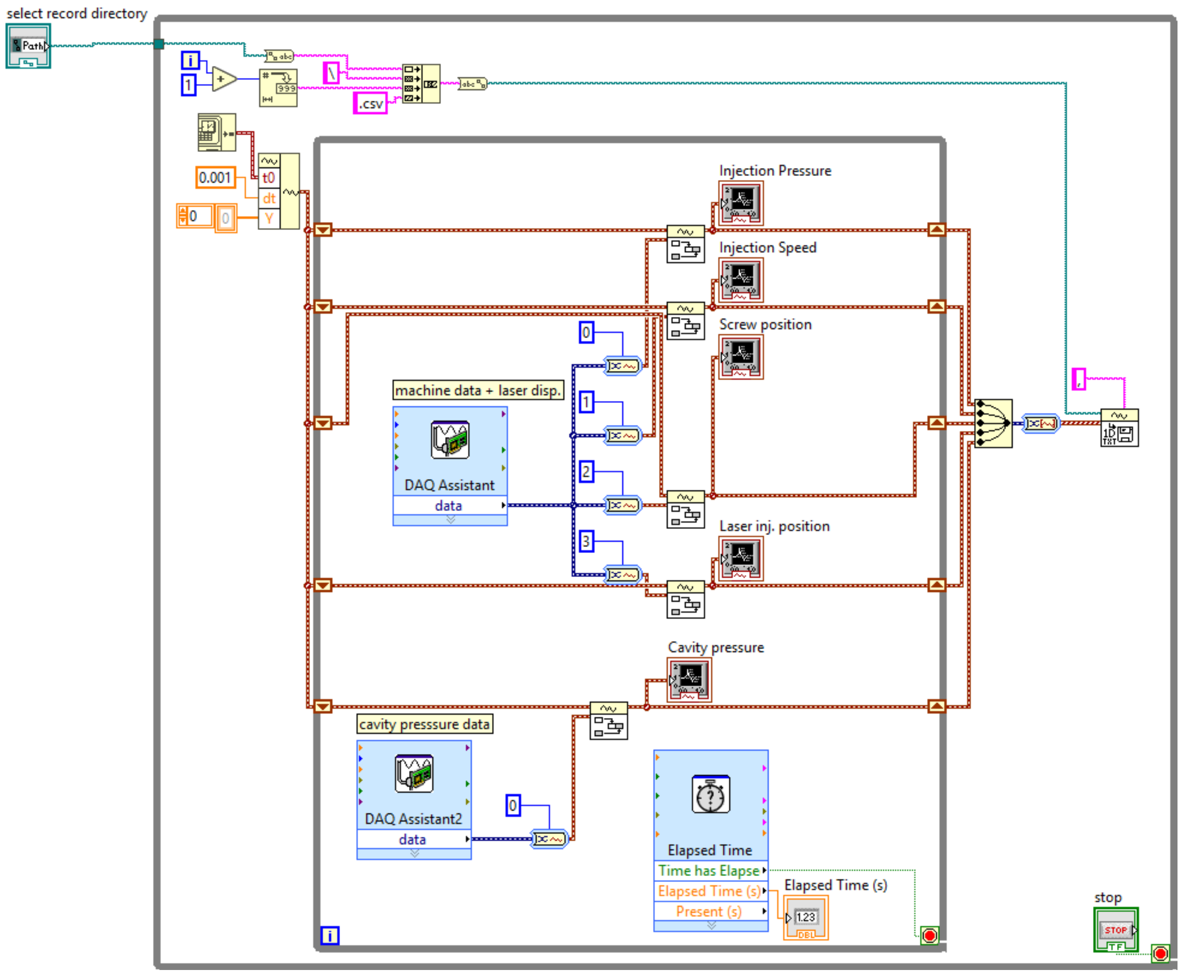

LabVIEW code used for data acquisition from Micropower 15.